Bond-selective and surface-site-specific dissociation of methane on platinum

Thèse N° 9530

Présentée le 31 mai 2019

à la Faculté des sciences de base
Laboratoire de chimie physique moléculaire
Programme doctoral en chimie et génie chimique

pour l'obtention du grade de Docteur ès Sciences

par

Ana GUTIÉRREZ GONZÁLEZ

Acceptée sur proposition du jury

Prof. J.-E. Moser, président du jury
Prof. R. Beck, directeur de thèse
Dr L. Juurlink, rapporteur
Prof. D. J. Auerbach, rapporteur
Dr M. Lingenfelder, rapporteuse

2019

ÉCOLE POLYTECHNIQUE
FÉDÉRALE DE LAUSANNE

To my parents and Marta,

for their daily words of encouragement over these four years.

To Julio,

for joining this adventure and being always by my side.

Abstract

I present a molecular beam study of methane dissociation on different surface sites of several platinum single crystal surfaces (Pt(111), Pt(211), Pt(210), Pt(110)-(2x1)). The experiments were performed in a molecular beam/surface-science apparatus that combines rovibrational state-selective excitation of reactants with detection of the reaction products by reflection absorption infrared spectroscopy (RAIRS), Auger electron spectroscopy (AES) and King and Wells (K&W) technique.

First, I explore how the barrier for methane dissociation depends on the Pt surface site (terrace, step, kink, and ridge atoms). For that, I compare the average reaction probabilities of methane on the different crystals using K&W. Moreover, I used the site-specific detection of chemisorbed methyl species by RAIRS to obtain the site-specific reactivity on steps, ridges and terraces. The highest methane reactivity and therefore the lowest barrier was observed for the surface atoms with the lowest coordination. The translational energy dependence of the reactivity shows clear evidence for a direct activated mechanism on all the surface sites studied. The decreasing catalytic activity for Pt atoms with increasing coordination number agrees well with theoretical predictions using first principles quantum theory calculations.

Second, I present the role of rovibrational excitation of the incident methane on the chemisorption on different surface sites. For CH_4, excitation of one quantum of the antisymmetric C-H stretch vibration (ν_3) was found to be less efficient than an equivalent amount of translational energy normal to the surface for promoting the dissociation on all the surface sites. The vibrational efficacy was seen to be lower for dissociation on the low coordinated sites, in accordance with calculations of transition state geometries. For CH_3D, the excitation of the antisymmetric C-H stretch vibration (ν_4) led to bond selectivity on the steps and terraces of the Pt(211) surface. These results show how careful control of the translational energy and rovibrational state of the incident CH_3D can be used for site-specific and bond-selective dissociation of methane.

As predicted previously by theory but not observed before experimentally, the C-H bond selectivity is shown to decrease with increasing translational energy.

Third, I explore the effect of surface temperature on the methane dissociation. The sticking coefficient for a direct chemisorption reaction such as CH_4 on Pt, might be expected to be independent of surface temperature, because the reaction happens very fast leaving very little time for the molecule to equilibrate with the surface. However, I observed an increase in methane reactivity with increasing surface temperature at low incident CH_4 energies. This observation is interpreted by a “loss of coordination” from the atoms displaced out of the plane due to their vibrational motion when the surface is heated.

The surface-site and quantum-state-specific data presented in this thesis are ideally suitable for testing theoretical models that aim to describe the methane-surface reaction at the microscopic level. Moreover, the characterization of different catalytically active sites for methane dissociation contributes to advancing the understanding of methane reactivity towards real catalytic conditions, where surfaces with several different atomic terminations are used.

Keywords

Methane, Pt(111), Pt(211), Pt(110)-(1x2), Pt(210), state and site-resolved reactivity, RAIRS, bond selectivity, surface science.

Version abrégée

Dans cette thèse, nous étudions la dissociation du méthane à l'aide de la technique des faisceaux moléculaires sur différents surfaces de divers monocristaux de platine (Pt(111), Pt(211), Pt(210), Pt(110)-(2x1)). Les coefficients de collage spécifiques à chaque site de surface ont été mesurés pour les différents isotopologues du méthane en utilisant un appareil à faisceau moléculaire/science de surface par spectroscopie de réflexion/absorption infrarouge (RAIRS) pour la détection sélective de l'espèce de méthyle chimisorbée produite. Les coefficients de collage spécifiques à l'état quantique pour les molécules de méthane dans des états rovibrationnels excités ont été obtenus par pompage infrarouge du méthane dans le faisceau moléculaire incident.

La détection sélective sur site d'espèces de méthyle chimisorbées par RAIRS nous permet premièrement d'analyser la dépendance entre la barrière de dissociation du méthane et le site dans la surface du Pt (terrasse, marche, décrochement et crête). La réactivité la plus élevée du méthane et, par conséquent, la barrière la plus basse ont été observées pour les atomes de surface dont la coordination était la plus faible. La dépendance énergétique translationnelle de la réactivité montre clairement la preuve d'un mécanisme d'activation directe dans tous les sites de surface étudiés. La diminution de l'activité catalytique des atomes de Pt avec l'augmentation de l'indice de coordination concorde bien avec les prédictions théoriques réalisées en utilisant des calculs *ab initio* de la théorie quantique.

Deuxièmement, nous nous sommes intéressés au rôle de l'excitation rovibrationnel du méthane incident sur la chimisorption dans différents sites de surface. Pour le CH_4, un quanta d'excitation de la vibration d'étirement antisymétrique C-H (ν_3) s'est révélé moins efficace que la même quantité d'énergie translationnelle perpendiculaire à la surface pour la dissociation sur tous les sites de surface. L'efficacité vibrationnelle a été perçue comme étant plus basse pour la dissociation sur les sites dont la coordination était plus faible, conformément aux calculs des géométries d'états de transition. Pour CH_3D, l'excitation de la vibration d'étirement antisymétrique C-H (ν_4) a conduit à une sélectivité de liaison sur les marches et les terrasses de la surface Pt(211). Ces résultats montrent comment le contrôle minutieux de l'énergie de translation et de l'état rovibrationnel du CH_3D incident peut être utilisé pour la dissociation du méthane sur des sites spécifiques et la coupure de liaisons sélectionnées. Comme prédit par la théorie auparavant, mais non observé expérimentalement jusqu'à présent : la capacité de sélection de la liaison C-H diminue avec l'augmentation de l'énergie de translation.

Troisièmement, nous avons étudié l'effet de la température de surface sur la dissociation du méthane. Nous avions anticipé que le coefficient de collage pour une réaction de chimisorption directe telle que CH_4 sur Pt était indépendant de la température de surface, étant donné que la réaction se produisait très rapidement, laissant très peu de temps à la molécule pour s'équilibrer à la surface. Cependant, nous avons observé une augmentation de la réactivité du méthane lorsque la température de surface augmente quand l'énergie incidente est faible. Cette observation est interprétée par une « perte de coordination » de la part des atomes déplacés hors du plan, en raison de leur mouvement vibratoire lorsque la surface est chauffée.

Les données présentées dans cette thèse sont idéales pour la vérification des modèles théoriques qui visent à décrire la réaction méthane-surface à l'échelle microscopique. En outre, la caractérisation de différents sites catalytiquement actifs pour la dissociation du méthane contribue à faire progresser la compréhension de la réactivité du méthane au regard des conditions catalytiques réelles, où les surfaces avec plusieurs terminaisons différentes sont utilisées.

Mots-clés

Méthane, Pt(111), Pt(211), Pt(110)-(1x2), Pt(210), sélectivité de liaison, réactivité résolue en état quantique, réactivité spécifique aux sites de surface, science de surfaces.

Resumen

En esta tesis se presenta un estudio sobre la disociación de metano en diferentes sitios de adsorción de diversas superficies de monocristales de platino (Pt(111), Pt(211), Pt(210), Pt(110)-(1x2)). Los experimentos mostrados en esta tesis han sido llevados a cabo en una máquina que combina la técnica de haces moleculares con técnicas de ciencia de superficies. En particular, compagina la capacidad de seleccionar el estado cuántico de las moléculas incidentes en la superficie, gracias al uso de láseres, con la detección de los productos de la disociación en la superficie usando espectroscopía de reflexión-absorción en el infrarrojo (RAIRS), espectroscopía electrónica Auger (AES) y la técnica de King y Wells (K&W).

Primero, se exploró la dependencia de la barrera energética de disociación de metano respecto del sitio de adsorción en la superficie (terrazas, escalones, kinks y crestas). Para ello, comparo la reactividad media del metano medida con K&W en las cuatro superficies. Además, uso la capacidad selectiva de RAIRS para distinguir el producto de la disociación de metano adsorbido en los diferentes sitios presentes en cada superficie. De esta manera, se obtienen las reactividades específicas en las terrazas, escalones y crestas. La reactividad de metano más alta, y por lo tanto la más baja barrera de disociación, se observa para los átomos de la superficie con menor coordinación, aunque la reactividad no es directamente proporcional al número de coordinación. Por otro lado, la dependencia de la reactividad con la energía cinética de las moléculas incidentes muestra claras evidencias de una reacción directa con una barrera de activación en todos los sitios de adsorción.

Segundo, presento el papel que desempeña la energía rovibracional de las moléculas de metano en la quimisorción en los distintos sitios de reacción. Para el isotopólogo CH_4, se observa que la excitación de un cuanto de la vibración C-H de tensión antisimétrica (ν_3) es menos eficiente que la misma cantidad de energía cinética en la promoción de la disociación de metano en todos los sitios de reacción. La eficiencia de la energía vibracional para promover la disociación en los sitios de adsorción con bajo número de coordinación es más baja que en aquellos con alto número de coordinación, de acuerdo con los cálculos de geometría del estado de transición. Para CH_3D, la excitación de la vibración de tensión antisimétrica de los enlaces C-H (ν_4) permite seleccionar el enlace disociado en los escalones y terrazas de la superficie de Pt(211). Estos experimentos muestran cómo el control minucioso de la energía cinética y el estado cuántico rovibracional de las moléculas de CH_3D pueden ser utilizados para especificar qué enlace de la molécula se disocia y dónde se adsorbe en la superficie. La capacidad de selección del enlace disociado en la superficie decrece a medida que la energía cinética aumenta, tal y como había sido predicho teóricamente pero nunca antes observado en un experimento.

Tercero, exploro el efecto de la temperatura de la superficie en la disociación de metano. En general, para una reacción directa como es la quimisorción de CH_4 en Pt, no se espera que los coeficientes de adsorción dependan de la temperatura de la superficie puesto que la reacción ocurre de manera muy rápida sin que haya suficiente tiempo para que las moléculas se equilibren con la superficie. Sin embargo, yo observo un aumento en la reactividad del metano asociado a un aumento en la temperatura de la superficie. Esta observación es interpretada como una “pérdida temporal” de la coordinación de los átomos de la superficie que son desplazados fuera del plano de la superficie debido a un aumento de su energía vibracional al calentar la muestra.

En general, los datos obtenidos durante esta tesis doctoral son muy adecuados para la validación de modelos teóricos que tratan de describir la reacción de metano en platino a una escala microscópica. Además, la caracterización de los sitios de reacción activos catalíticamente contribuye al avance de nuestro conocimiento de la reactividad de metano hacia condiciones catalíticas reales en las que se usan superficies con diferentes terminaciones atómicas.

Palabras clave

Metano, Pt(111), Pt(211), Pt(110)-(1x2), Pt(210), selectividad de enlace, reactividad resuelta por estado cuántico, reactividad específica a sitios de reacción, ciencia de superficies.

List of Abbreviations

AES	Auger Electron Spectroscopy
AIMD	Ab-Initio Molecular Dynamics
BOA	Born Oppenheimer Approximation
CN	Coordination Number
DFT	Density Functional Theory
IR	InfraRed
IVR	Intramolecular Vibrational Redistribution
K&W	King and Wells
LEED	Low Energy Electron Diffraction
MEP	Minimum Energy Path
PES	Potential Energy Surface
QCT	Quasi-Classical Trajectories
QM	Quantum Mechanics
QMS	Quadrupole Mass Spectrometer
RAIRS	Reflection Absorption Infrared Spectroscopy
RPH	Reaction Path Hamiltonian
SVP	Sudden Vector Projection
TOF	Time of Flight
TPD	Temperature Programmed Desorption
TS	Transition State
UHV	Ultra High Vacuum
XPS	X-ray Photoelectron Spectroscopy
ZPE	Zero Point Energy

Contents

Abstract ... **i**

Version abrégée ... **iii**

Resumen ... **v**

List of Abbreviations ... **vii**

Contents ... **ix**

Chapter 1 Introduction ... **1**

1.1 Motivation ... 1

1.2 Evolution of gas-surface dynamics experiments ... 3

1.2.1. Mode or state specificity ... 6

1.2.2. Bond selectivity ... 7

1.2.3. Steric effects ... 8

1.3 Dynamical models for methane chemisorption ... 9

1.4 Goals and outline of this thesis ... 12

Chapter 2 Experimental setup ... **15**

2.1 Overview ... 15

2.2 Molecular beam/surface-science apparatus ... 16

2.2.1. Supersonic expansion and molecular beam speed characterization ... 18

2.2.2. Molecular beam flux ... 20

2.2.3. Sample manipulator and sample preparation ... 22

2.2.4. Detection Methods ... 28

2.3 Laser setup ... 38

2.3.1. Optical Parametric Oscillator ... 38

2.3.2. Frequency stabilization 40

2.3.3. Rovibrational excitation by Rapid Adiabatic Passage 43

2.3.4. Determination of the excited state population in the molecular beam 44

Chapter 3 Influence of the surface atomic structure on the reactivity of methane on Pt 49

3.1 Introduction 49

3.2 CHD_3 reactivity on different facets of Pt measured by K&W detection 54

3.2.1. Angle dependence of the S_0 of CHD_3 on Pt(211) 60

3.3 Site-specific detection of CH_4 dissociation using RAIRS 64

3.3.1. RAIR spectra: site-specific detection of chemisorbed methyl on Pt surfaces 64

3.3.2. Coverage dependence of the RAIRS spectra and uptake curves 71

3.3.3. Calibration of RAIRS intensities 74

3.3.4. Site-specific sticking coefficients 79

3.4 The electronic structure factor: *d*-band theory 84

3.5 Quantum state- and surface-site-specific sticking coefficients for $CH_4(\nu_3)$/Pt 87

3.6 Summary 91

Chapter 4 Bond selective dissociation of methane isotopologues on Pt(111) and Pt(211) 95

4.1 Introduction 95

4.2 Bond selective chemisorption of methane isotopologues on Pt(111) 101

4.2.1. RAIRS detection of isotopologues of methyl species. 102

4.2.2. A new strategy for the calibration of RAIRS intensities. 103

4.2.3. Laser-off results 106

4.2.4. Laser-on results 112

4.3 Bond and site selective dissociation of CH_3D on Pt(211) 117

4.3.1. RAIRS detection of methyl isotopologues on the steps and terraces of Pt(211) 117

4.3.2. Bond selectivity on Pt(211) 123

4.3.3. Degree of bond selectivity 124

4.4 Implications of bond selectivity 127

4.5 Summary 130

Chapter 5 Surface temperature dependence of methane activation on Pt surfaces 131

5.1 Introduction 131

5.2 Low incident energy regime – T_S dependence on S_0 (CH_4 (ν_3))/ Pt(111) 133

5.3 High incidence energy regime & surface carbon migration at high T_S 142

5.4 Summary 146

Chapter 6 Summary and outlook 149

References 161

Appendix 173

List of Figures 175

List of Tables 185

Acknowledgements 187

Curriculum Vitae 191

Chapter 1 Introduction

1.1 Motivation

Heterogeneous catalysis is well known for its tremendous impact in our society and is considered the basis of the chemical industry[1,2]. Some examples are the Haber-Bosch process for the production of synthetic fertilizers[3], the Fischer-Tropsch reaction for the generation of various hydrocarbons that can act as source of chemicals and fuels[4], and the catalytic conversion of exhaust gasses (HC, NO_X, CO) to reduce automotive pollution[5].

Steam methane reforming is another very important example of a heterogeneously catalyzed reaction with great importance for the chemical industry. It consists of transforming methane and water into a mixture of hydrogen and carbon monoxide:

$$\mathrm{CH_4} + \mathrm{H_2O} \rightarrow \mathrm{CO} + 3\mathrm{H_2} \tag{1.1}$$

This reaction constitutes the principal industrial source for the production of molecular hydrogen[2] which is then used in ammonia synthesis by the Haber-Bosch process, for combustion in fuel cells and many other applications. One of the first steps and also the rate limiting factor to achieve steam methane reforming is the dissociation of methane. Methane is a very stable molecule, and its dissociation requires a substantial amount of energy (~416 kJ/mol[6]). In order to decrease the activation energy for dissociation and thus increase the rate of the steam reforming reaction, a solid catalyst is used so the methane dissociatively chemisorbs on the surface catalyst.

To produce hydrogen with more energy efficiency and less cost, there is a continuous search for better catalysts. However, since no predictive theoretical model for the dissociative chemisorption of methane is currently available, the search for better catalysts has to be done mostly by trial and error. This process is time consuming and expensive and it would be beneficial to replaced it by a direct search *in silico* using first principles theory of chemical reaction at interfaces.

Our approach for studying methane chemisorption on the surface of the metal catalyst is based on performing highly controlled experiments in which we define as many of the parameters of the molecule-surface collision as possible, as schematically represented in Figure 1-1. These parameters include the translational energy of the incident methane (E_{trans}), the rotational and vibrational quantum state of the incident molecule (ν, J), the reactant alignment relative to the surface as well as properties of the surface such as its structure and composition or temperature (T_S).

The highly specific data produced by our experiments are ideally suited to test theoretical models because they avoid extensive averaging of the theoretical results over many rotational and vibrational quantum states. Through a close collaboration between experiment and theory, we aim to accurately model the methane-surface interaction, thus allowing a more efficient search for new catalysts.

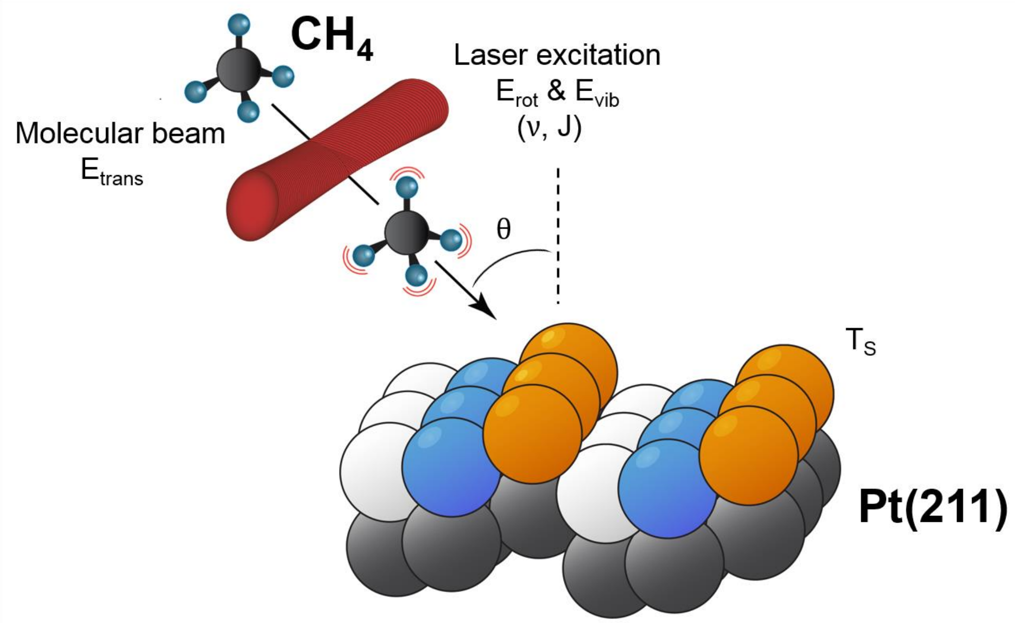

Figure 1-1. Cartoon of a CH_4 molecule striking a Pt(211) surface that is composed of different types of surface atoms. Some of the parameters that influence the probability of adsorption are indicated: the translational energy (E_{trans}), the rotational and vibrational quantum number (ν, J), the angle of incidence (θ), or the surface temperature (T_S).

1.2 Evolution of gas-surface dynamics experiments

Studies of methane reactivity have progressed significantly during the last decades giving important insights into gas-surface interactions[7–11]. This progress is in part due to experimental and technical advances, which have allowed for a more precise control of the translational energy and quantum state of the molecules that interact with the surface.

One significant advance was the introduction of the molecular beam. Before its introduction, bulb experiments were performed[12,13], where the translational, vibrational and rotational energy of the gas are thermally equilibrated. The use of supersonic expansions to generate molecular beams allows the preparation of reactants with translational energy that is variable over a large hyperthermal range and with a well-defined, narrow translational energy distribution. The supersonic expansion also provides efficient cooling of the rotational degrees of freedom[14] of the reactants and isolates the expanding gas in a collision free environment.

Rettner, Pfnür, and Auerbach reported the first molecular beam-surface reactivity measurement of methane dissociation on W(110), and found that translational energy directed normal to the surface promoted the reaction whereas the parallel component of the energy did not induce dissociation[15]. Furthermore, the authors varied the nozzle temperature and used variable seeding to gain independent control of vibration and translation. Following this and previous bulb-experiment results, they proposed a model based on the equal participation of all vibrational modes and an approximate equivalence of vibrational and translational energy in their ability to promote dissociative chemisorption[16].

However, in the experiments of Rettner *et al.*[15], the population of the reactant's vibrational levels was almost unchanged from thermal equilibrium at the specific nozzle temperature since this type of energy is not efficiently cooled in a supersonic expansion[14]. Therefore, only the averaged reactivity over the thermally populated vibrational states could be determined in these studies.

This limitation was overcome with the introduction of laser excitation, which allows the preparation of reactants in a specific vibrational and rotational quantum state over a wide range of incident kinetic energies. Juurlink *et al.*[17] published the first study that showed the role of a specific vibrational mode of a polyatomic molecule in promoting dissociation on a surface. Studying the reaction between methane and Ni(100), they found a 1600-fold increase in reactivity when exciting the ν_3 C-H antisymmetric stretching mode of CH_4 in comparison with the results obtained for CH_4 molecules in the ground state. Despite this enhancement, they demonstrated that translational energy remains more effective in promoting reactivity than vibrational excitation of ν_3. Thus, the *vibrational efficacy* for ν_3, $\eta(\nu_3)$, which is a measure of how efficient this vibrational energy mode is in overcoming the reaction barrier compared to an equivalent amount of translational energy normal to the surface, is less than unity.

This ability to measure the individual energetic contribution from particular degrees of freedom of the molecule provides very valuable information about the potential energy surface (PES). In 1972, Polanyi[18] proposed a model that relates the energy consumption of the chemical reaction and the energy disposal in the final products to the location of the barrier on the PES. Based on bimolecular reactions ($A + BC \rightarrow AB + C$), he categorized the reactions depending on where the saddle point connecting reactants and products (i.e. the *transition state*) is placed. This is schematically represented on Figure 1-2. In these plots, the potential energy is represented by contours as a function of the interatomic distance between the reactant BC (r_{BC}) and the product AB (r_{AB}).

The reaction is considered to have an “early barrier” when the transition state is positioned in the entrance channel. In this case, r_{BC} is in its equilibrium position at the transition state location. As a result, adding vibrational energy to the BC reagent and therefore stretching the B-C bond does not promote the reaction very efficiently. In this case, translational energy is expected to be more efficient than vibrational energy.

On the contrary, in the case of a “late barrier” where the r_{BC} is already stretched at the transition state, placing vibrational energy on the B-C bond is predicted to promote the reaction efficiently. The reason for this promotion is the fact that vibration adds progress along the reaction pathway. In other words, this vibration places energy into the *reaction coordinate* (RC) which can be considered as a special coordinate that connects reactants with products through the transition state.

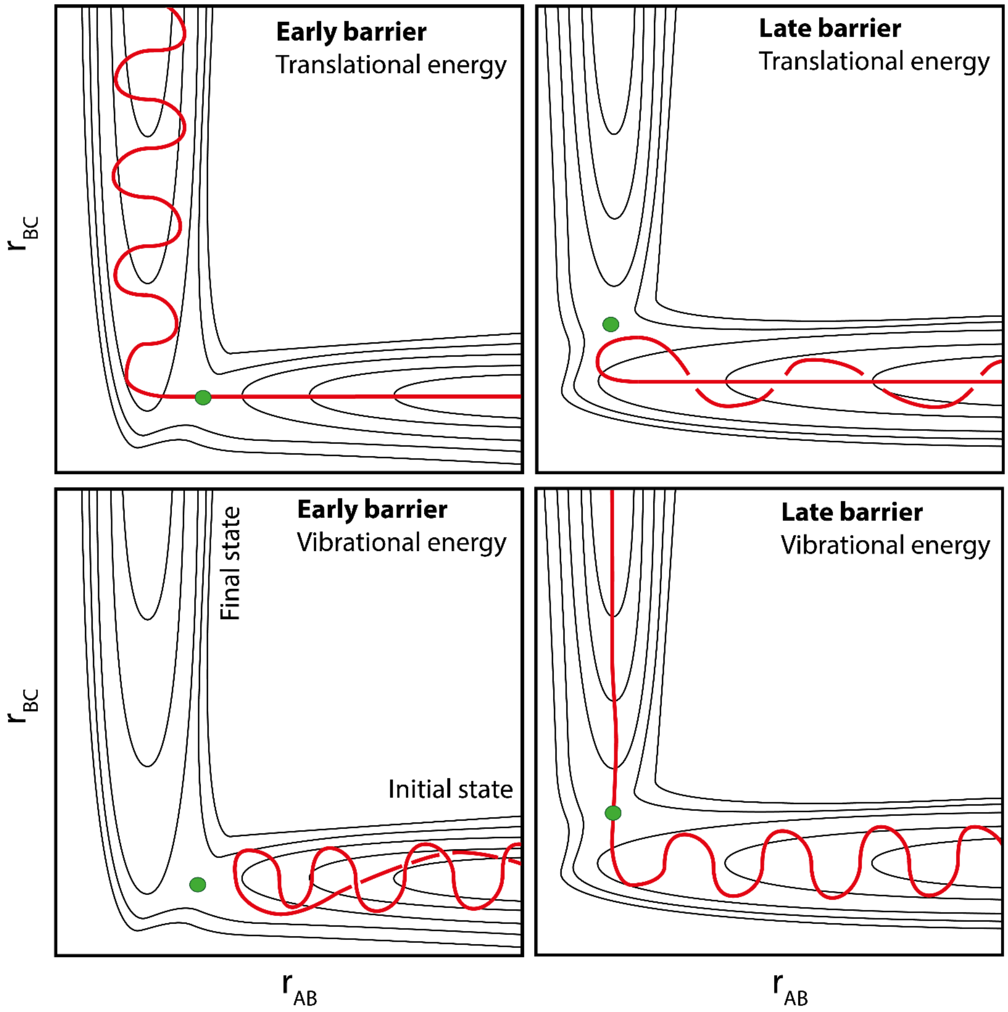
Early barrier
Translational energy
Late barrier
Translational energy
Early barrier
Vibrational energy
Final state
Initial state
Late barrier
Vibrational energy
r_BC
r_BC
r_AB
r_AB

Figure 1-2. Schematic contour plots of the PES for the $A + BC \rightarrow AB + C$ reaction as a function of the interatomic distance of the reagent BC and the product AB. The saddle points are represented by solid green circles. The initial and final states are indicated in the bottom right plot. Adapted from [9].

However, Polanyi's rules were originally intended to describe reactions of a diatomic molecule with an atom in the gas phase. Reactions of polyatomic molecules with surfaces are inherently more complicated, in part due to the increased number of vibrational modes that a polyatomic molecule presents and the many degrees of freedom associated with the surface atoms. For example, different vibrational modes of CH_4 have been demonstrated to promote the CH_4/Ni(100) reaction differently. While the antisymmetric stretch ν_3 vibrational mode of CH_4 was observed to be less efficient than translational energy in promoting the chemisorption reaction[17], Maroni *et al.*[19] found a vibrational efficacy for the symmetric stretch ν_1, $\eta(\nu_1)$ of 1.4. This means that energy specifically placed in the ν_1 mode is 1.4 times more efficient than translational energy in promoting the reaction. Thus different vibrational modes, even having similar energies as it is the case for the ν_1 and ν_3 normal modes of CH_4, can promote the reaction differently.

1.2.1. Mode or state specificity

The fact that two different, isoenergetic vibrational modes promote a reaction differently is an effect called *state* or *mode specificity,* and it was first demonstrated for a chemisorption reaction in 2003 in our group[20] for the reaction of CH_2D_2 with Ni(100). In these experiments, the reactivity of CH_2D_2 prepared in two isoenergetic states, $2\nu_6$ and $\nu_1+\nu_6$, on a Ni(100) surface was measured. Within a local mode basis, these two states can be written as $|20>$ and $|11>$ respectively; the former representing two quanta of CH stretch in a single bond and the latter representing one quantum of C-H excitation in each of the two C-H bonds. The results showed that the reaction probability for CH_2D_2 excited with two quanta of excitation in a single bond was up to 5 times higher than having one quantum of vibrational excitation in each of the two C-H bonds, demonstrating that two states with the same amount of vibrational energy can have different reactivities.

Mode specificity was subsequently demonstrated in several other molecule-surface systems[19,21]. The reaction of methane on Pt(110)-(1x2) was found to be mode specific by comparing the vibrational efficacy of four different vibrational eigenstates consisting of different amounts of bend and stretch excitation[21]. And more recently, mode specific dissociation has been observed for two methane isotopologues (CH_2D_2 and CH_3D) when they interact with Pt(111)[22]. In this work, the symmetric stretch vibration is shown to be more reactive than the antisymmetric C-H stretching. The observation of mode specificity in a chemical reaction is evidence against a statistical reaction mechanism that can be described by a statistical rate theory such as Rice-Ramsberger-Kassel-Marcus (RRKM)[23].

In contrast, the experimental results agree well with theoretical calculations performed by Guo and coworkers using their so-called Sudden Vector Projection (SVP) model[24]. The SVP model was proposed with an intent to generalize Polanyi's rules to polyatomic reactions where the incident molecule has more than one vibrational mode and is designed to predict differences in vibrational efficacy between the modes. The model is called “sudden” because it assumes that the reactive collision time is much shorter than that required for intramolecular energy redistribution (IVR) to occur within the reactant molecules before the dissociation occurs. In this sudden limit, the efficacy of a vibrational mode is quantified as the projection of the reactant vibrational mode vector with the vector of the reaction coordinate at the transition state. The larger the projection of the initial state onto the reaction coordinate at the transition state, the greater is the predicted vibrational efficacy.

Using their SVP model, Guo and coworkers have qualitatively reproduced the mode specificity observed in the reaction of methane on Ni and Pt surfaces[22,25]. Also, this insightful model agrees well with the larger enhancement of the CH_4 reactivity by the stretch vibrations of methane relative to the bending modes[25,26] observed experimentally[21,27].

1.2.2. Bond selectivity

Preparation of methane reactants in a single vibrational and rotational state has been also used to explore the possibility of selectively breaking a particular bond in the dissociative chemisorption reaction. This is referred to as *bond selectivity* and it is one of the topics investigated in this thesis. A more complete overview of bond selectivity, from its first demonstration in gas phase reactions to its observation on gas-surface reactions, is presented in the introduction of Chapter 4.

The first evidence of bond selectivity in a gas-surface reaction was reported by Killelea *et al.* in 2008[28]. They demonstrated bond selective dissociation of CHD_3 on Ni(111) using recombinative desorption of adsorbed methyl products with sub-surface D atoms. Vibrational excitation with one quantum of ν_1, the unique C–H stretch in CHD_3, enhanced the C–H cleavage channel by at least 2 orders of magnitude compared to the statistical 1/3 CD_3/CHD_2 branching ratio observed without C–H stretch excitation.

Li *et al.*[29] extended the bond selective chemisorption study to all three partially deuterated methanes (CH_3D, CH_2D_2, and CHD_3) on Pt(111) using reflection absorption infrared spectroscopy (RAIRS) as the product detection method. RAIRS can be used to distinguish the different isotopologues of the methyl species on Pt(111), formed as the nascent dissociation products of the methane chemisorption. Their results show that a single quantum of C–H stretch excitation is sufficient to make the dissociation of all three partially deuterated methane isotopologues fully bond selective.

1.2.3. Steric effects

Yoder *et al.*[30,31] studied the dependence of the alignment of CH_4 and CHD_3 on their reactivities on Ni(100). They used linearly polarized infrared excitation to align the angular momentum and the vibrational transition dipole moment of both methane isotopologues, and showed that the reactivity was highest when the vibrational amplitude is aligned parallel to the plane of the surface.

All these three observations (mode specificity, bond selectivity and steric effects) give very valuable information about the reaction dynamics and the timescales of the gas-surface reaction. They clearly indicate that when the methane molecule dissociates on the surface, it retains a memory of the rovibrational state in which it was excited. In consequence, IVR between the different bonds of the incident molecule is absent or at least incomplete on the timescale of the collision. Moreover, as noted previously, the experimental observations described above exclude any statistical rate theory from correctly describing the chemisorption of methane on a metal catalyst since these theories consider that different types of energy all promote reaction equally[32,33].

Statistical theories assume that IVR within the collision complex formed by the reactant molecule and several surface atoms takes place faster than the reaction between the molecule and the surface, resulting in a complete randomization of the vibrational energy before the bond breaking takes place. Therefore, a statistical theory predicts that the reaction rate (i.e. *sticking coefficient*) depends only on the total internal energy of the reactant and exclude any mode specificity and bond selectivity.

State resolved experiments have shown that the methane-metal surface reaction can only be accurately described by dynamical models which assume that the reactivity and outcome of the methane-surface interaction depends on the precise nature of the vibrational mode of the incident molecule. These dynamical models aim to treat explicitly all degrees of freedom of the system and calculate the motion of all the atoms during the molecule-surface interaction based on the PES using either classical or quantum dynamics.

1.3 Dynamical models for methane chemisorption

Dynamical calculations have greatly evolved in the last years, from considering the CH_4 molecule as a quasi-diatomic R-H molecule to reduce the dimensionality of the system[34] to being able to consider the full 15 degrees of freedom of the CH_4 molecule in the interaction with the metal[35,36]. In addition, the quantum state resolved experiments described above are ideally suitable for testing these dynamical models since they avoid averaging over a large number of rotational and vibrational quantum states.

Since throughout this thesis I often compare my experimental observations with theoretical predictions obtained by different dynamical models, here I will explain, briefly and in simple terms, the different dynamical theories used to date by different theory groups to describe the chemisorption of methane on a metal surface.

All of these theoretical approaches assume the Born-Oppenheimer approximation (BOA) and use density functional theory (DFT) to calculate the electronic energy. For that, they employ exchange correlation functionals at the generalized gradient approximation (GGA) or semi-empirical exchange correlation functionals. Once the electronic structure is calculated and the PES is obtained for various nuclear configurations, the nuclear dynamics are run on the calculated PES. Depending on the nature of the dynamical calculations, we can divide the dynamical models presented here into those that follow quasi-classical trajectory (QCT) calculations and those that perform quantum mechanical (QM) wavepacket calculations to obtain the dynamics.

The first set of theories are considered as “quasi-classical” because they follow the dynamics considering classical Newtonian forces acting on the nuclei, but at the same time they include some quantum mechanical effects such as the *zero point energy* (ZPE) of the molecules. The groups of Kroes and Busnengo perform such quasi-classical calculations.

Busnengo *et al.*[37,38] calculate the Born-Oppenheimer potential energy surface (PES) for various nuclear configurations using DFT and they analytically parametrize this potential to obtain a PES represented by a continuous function (the *reactive force-field*). Using this pre-calculated PES, they run the nuclear dynamics assuming classical mechanics. An advantage of this approach is that the last step, the integration of the nuclear equations of motion, is fast and therefore relatively cheap. For this reason, they can run a large amount of trajectories (~$1\cdot10^6$) with long integration times (~100 ps), achieving good statistics. A drawback of this method is that any error in the parametrization of the PES leads to inaccuracies in the calculations.

Another approach is to perform ab-initio molecular dynamics (AIMD). Following this method, Kroes and coworkers[35,39–43] avoid calculating the entire PES beforehand. Instead, the forces acting on the molecule are calculated "on the fly" by solving the electronic Schrödinger equation. By calculating only the regions of the PES that are sampled along the reaction path, they reduce the computational cost and they are able to consider all the molecular and also surface degrees of freedom. While this procedure adds very valuable information on the surface dynamics, the AIMD calculations are computationally very expensive. This limits the number of trajectories that can be calculated (~$1\cdot10^3$ trajectories) and the integration times (1 ps). With a limited total number of trajectories (reactive and nonreactive) one cannot simulate sticking coefficients of less than about 1% using the AIMD approach.

Among the drawbacks of quasi-classical dynamical calculations are the neglect of tunnelling, which restricts the application of these models to incident energies above the minimum barrier, the "ZPE violation", and the so-called "artificially-induced IVR". The "ZPE violation" refers to the fact that classical mechanics allow the ZPE to "leak" into unbound degrees of freedom, leading to products whose internal energy is lower than their ZPE, which is forbidden by quantum mechanics. Similarly, quasi-classical dynamics break another postulate of quantum mechanics: a molecule that is excited to a particular eigenstate of a system, without any perturbation, remains in that state as time elapses; it is a *stationary state*. However, in quasi-classical dynamics, the flow of energy from an eigenstate into other states of similar energy can easily happen even if the molecule is unperturbed. This effect is called "artificially induced-IVR". In order to avoid it, Kroes and coworkers perform calculations for molecules excited to vibrational modes that are localized and off-resonance with other vibrations. For example, in this thesis experimental results are compared with AIMD calculations for ν_1-excited CHD_3 where the vibrational energy is localized on the C-H bond.

Alternatively, Bret Jackson developed a quantum dynamical treatment of methane chemisorption using their reaction path Hamiltonian (RPH) approach[36,44–48]. First, using DFT, they calculate the minimum energy path (MEP) which connects reactants with products and they assume that any motion orthogonal to this path is harmonic. Then, they perform quantum dynamics by propagating wave packets on that MEP.

Figure 1-3 displays the frequencies of the 9 vibrational modes of CH_4 as well as modes corresponding to rotation and translational motion along the reaction path (*s*). As the molecule approaches the transition state at *s*=0, the ν_1 normal mode of CH_4 reduces its frequency (it *softens*). This mode softening is associated to a localization of the vibrational energy in the reactive bond: as the molecule approaches the surface, the reactive bond weakens until it breaks. Following this, the ν_1 vibration of CH_4 is thus localized on the reacting C-H bond, while ν_3 vibration is localized on the CH_3 methyl fragment since it does not suffer from mode softening. Therefore, vibrational energy in the ν_1 is expected to promote the CH_4/Pt(111) reaction more efficiently than ν_3 excitation, as it was previously observed for Ni(100)[19]. The RPH model also includes the possibility of vibrationally non-adiabatic crossings between different vibrational modes. For example, a molecule excited in the 3´ state of Figure 1-3 can suffer a transition to the 4' state, then to 5´, etc. Hence, the initial vibrational energy in ν_1 is converted into motion along the reaction path.

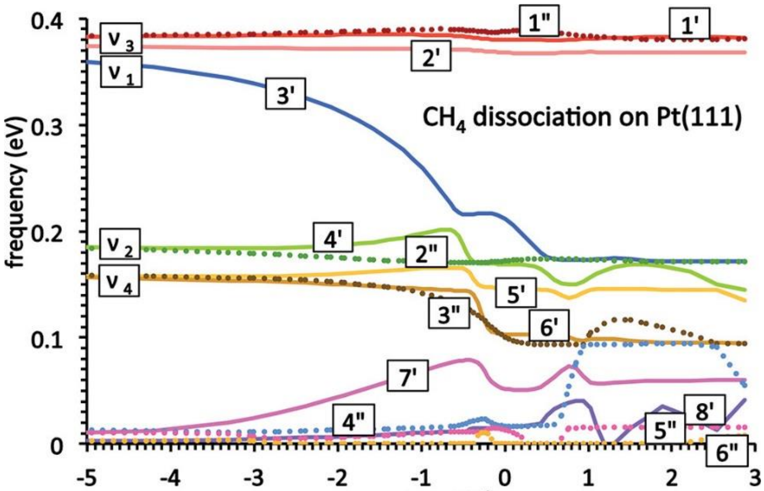

Figure 1-3. Frequencies of the 9 vibrational modes of CH_4 (the triply degenerate antisymmetric stretch, ν_3, the symmetric stretch, ν_1, the doubly degenerate bend, ν_2, and the triply degenerate bend, ν_4) and other five modes corresponding to rotational and translational motion along the reaction path (s). s=0 corresponds to the transition state. Reproduced with permission from[49].

Through his quantum approach, Jackson captures the vibrational energy flow between the different degrees of freedom during the gas-surface interaction. As the molecule approaches the surface, it suffers from the so-called *surface-induced IVR*: the vibrational modes of the isolated molecule are no longer eigenstates of the combined Hamiltonian of the molecule-surface complex. As a consequence, the energy initially placed in those modes evolves in time due to the interaction with the surface. Therefore, even though mode specificity and bond selectivity clearly show that IVR is not complete on the time-scale of the reaction, surface-induced IVR is responsible for the flow of energy from vibrational normal modes of the isolated molecule into localized energy on the reacting C-H and non-reacting (CH_3) bonds.

1.4 Goals and outline of this thesis

Most of the studies reviewed above have focused on the study of the role of translational and the vibrational mode of the incident gas-methane molecule. However, to date, less attention has been paid to the surface itself, even though it is well known that real catalysts used in industry expose different low and high coordinated reaction sites. For this reason, and in an attempt to move our studies a step toward surfaces that resemble the surface of a real catalyst, I explore in my thesis the effect of the surface structure by performing quantum state resolved and surface site resolved experiments.

This thesis has the following structure:

Chapter 2 describes the molecular beam/surface-science apparatus and the infrared laser setup used for this thesis work.

Chapter 3 presents a study of the influence of the surface structure on the dissociative chemisorption of methane. Methane dissociation was studied on several platinum surfaces cut along different crystallographic planes. The chapter is divided in two parts differing in the detection technique that I used (King and Wells and RAIRS). Using King and Wells reactivity measurements, I compare the site-averaged reactivity of the Pt(111), Pt(211), Pt(110)-(1x2) and Pt(210) surfaces. Then, I demonstrate the ability of RAIRS to perform surface site-specific measurements of methane dissociation on Pt(211) and Pt(110)-(1x2). For the first time, we report a quantum-state resolved study of the dissociation of methane on different Pt surface sites. The effect of translational energy and ν_3 vibrational excitation of CH_4 in promoting the dissociation of CH_4 on the different surface sites is also explored.

In chapter 4, I present a bond selective study on the Pt(111) and Pt(211) surfaces. On Pt(111), an extension of Chen's bond selectivity study over a range of incident translational energies was performed. I also show a comparison of the reactivities of CH_3D, CH_2D_2, and CHD_3 both in the ground state and prepared with a single quantum of C-H stretch vibration. In the second part of this chapter, I report the first combined study of bond- and surface-site selective dissociation of methane (CH_3D) chemisorption on a Pt(211) surface.

Chapter 5 investigates the effect of surface temperature on the dissociation of methane on Pt(111) and Pt(110)-(1x2) surfaces for different incident kinetic energies and using different techniques for the detection of the chemisorbed species.

Finally, in chapter 6, the most important findings of this work are summarized and I present some suggestions for future experiments.

Chapter 2 Experimental setup

2.1 Overview

The experiments presented in this thesis were performed using a molecular beam/surface-science apparatus designed and built during the PhD work of Li Chen. An extensive description of the design and operation of this apparatus is presented in his dissertation[50] as well as in a previous publication[51]. Here, I will discuss the most relevant features of the machine and mention the changes made during my PhD work.

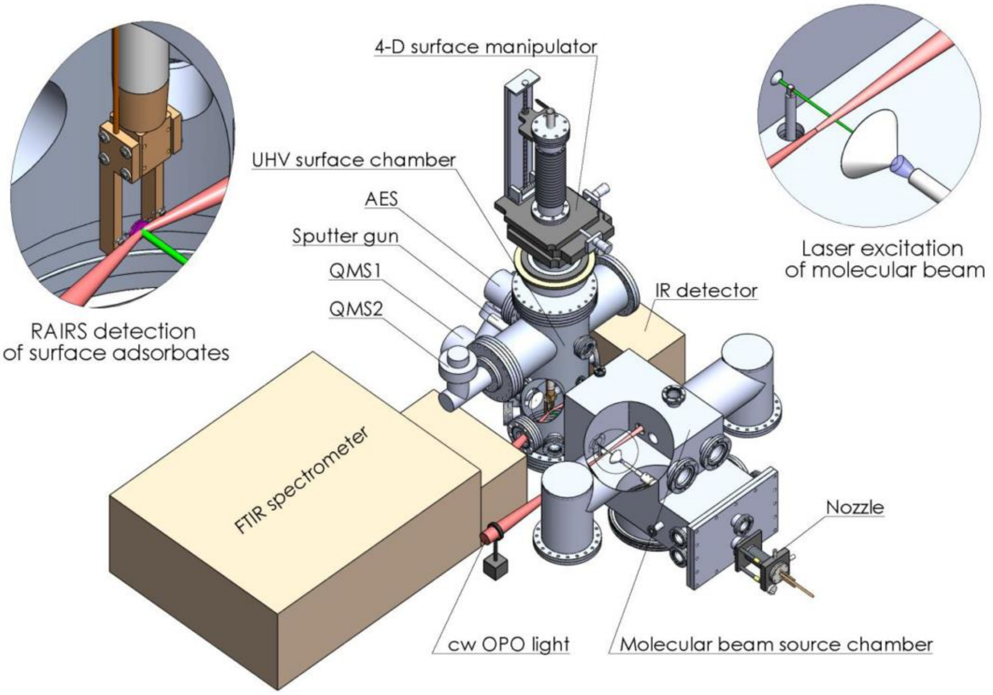
4-D surface manipulator
UHV surface chamber
AES
Sputter gun
QMS1
QMS2
RAIRS detection of surface adsorbates
Laser excitation of molecular beam
IR detector
FTIR spectrometer
Nozzle
cw OPO light
Molecular beam source chamber

Figure 2-1. SolidWorks 3-D model of the molecular beam/surface-science apparatus. Taken from [50].

Figure 2-1 shows a SolidWorks 3-D model of the apparatus. Briefly, it consists of a triply differentially pumped molecular beam source coupled to an ultra-high vacuum (UHV) chamber with a base pressure of $5{\cdot}10^{-11}$ mbar where the gas-surface interaction takes place. A continuous molecular beam is generated by skimming a supersonic jet expansion of the methane gas mixture. This expansion is formed in a stainless steel nozzle, and it allows to prepare the incident molecules with a narrow translational energy distribution and to cool the rotational degrees of freedom. The velocity distribution of the molecular beam is measured by a time-of-flight (TOF) method using a chopper wheel in combination with an on-axis quadrupole mass spectrometer (QMS).

Quantum state-resolved measurements can be performed by exciting the incident molecules to a specific ro-vibrational state using an optical parametric oscillator (OPO). A room temperature pyroelectric detector is installed in the third pumping stage and can be translated into the molecular beam path in order to detect the flux of vibrationally excited molecules in the beam.

Once the molecules enter into the UHV chamber, they collide with the surface sample. The UHV ensures the surface cleanliness during the experiments. In my thesis, different Pt crystals were studied: Pt(111), Pt(211), Pt(110)-(1x2), and Pt(210) whose structure is explained in detail latter in this chapter. The detection of the methane-surface reaction products can be performed by different techniques: Reflection Absorption Infrared Spectroscopy (RAIRS), King and Wells (K&W) beam reflectivity, Auger Electron Spectroscopy and Temperature Programmed Desorption (TPD).

In the remainder of this chapter, I will explain in more detail the essentials of this machine and the methods used for the detection and how they complement each other.

2.2 Molecular beam/surface-science apparatus

The molecular beam/surface-science apparatus consists of a molecular beam source with three pumping stages couple to an ultra-high vacuum (UHV) chamber where the sample is located. A schematic section view of the machine is presented in Figure 2-2. The pumps used and typical vacuum conditions in each stage are shown in Table 2-1. During the course of my PhD work, the pump on the UHV chamber has been exchanged with a corrosion resistant pump. Both turbomolecular drag pumps used in the UHV chamber are presented in Table 2-1.

As it is represented in Figure 2-2, a separation valve isolates the third (P3) and forth (P4) from the first (P1) and second (P2) chambers. This valve, which is open to let the molecular beam enter into the UHV chamber, also allows venting the first and second chambers without breaking the UHV vacuum in P4. During my thesis, I changed the design of this separation valve. Details about the design and working principle of the new separation valve are presented in Appendix A.

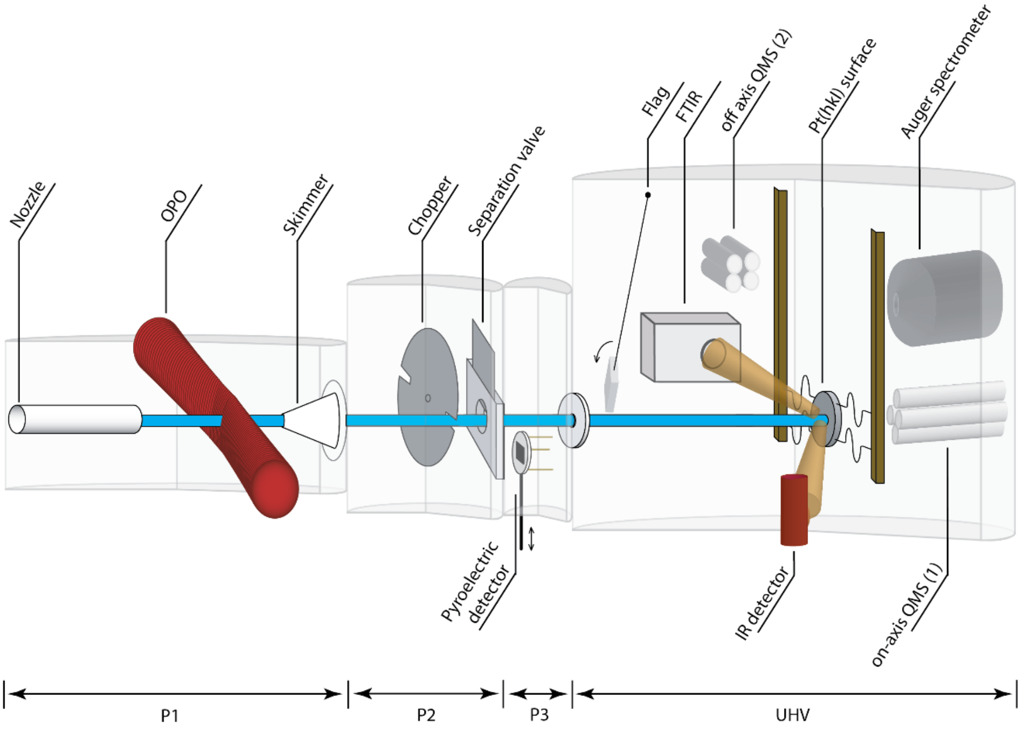
Nozzle
OPO
Skimmer
Chopper
Separation valve
Flag
FTIR
off axis QMS (2)
Pt(hkl) surface
Auger spectrometer
Pyroelectric detector
IR detector
on-axis QMS (1)
P1
P2
P3
UHV

Figure 2-2. Schematic overview of the molecular beam/surface-science apparatus. In the first chamber, P1, the supersonic jet expansion is produced and skimmed. In the second chamber, P2, a chopper wheel modulates the molecular beam for TOF measurements using the on-axis QMS (1). In the third chamber, P3, a pyroelectric detector that can be translated into the molecular beam to measure the excited fraction of molecules by the OPO light source. Finally, the molecular beam enters into the UHV chamber and collides with the sample surface where the adsorbed dissociation products can be detected by RAIRS, AES, K&W (using QMS(2) in combination with the flag) or TPD (using QMS(2)).

Stage	Pump model	Pumping speed S (N_2, L/s)	Base Pressure (mbar)
Source	Pfeiffer TPH 2301 P	1900	$2 \cdot 10^{-7}$
2nd stage	Pfeiffer TMU 521 P	510	$5 \cdot 10^{-8}$
3rd stage	Pefiffer TMU 520 P	500	$7 \cdot 10^{-10}$
UHV	Pfeiffer TMU 1000 (old)	800	$5 \cdot 10^{-11}$
	Pfeiffer TMU 1001 (new)	920	

Table 2-1. Overview of the turbomolecular pumps used in the molecular beam/surface-science apparatus and typical vacuum conditions.

2.2.1. Supersonic expansion and molecular beam speed characterization

A continuous supersonic jet expansion is produced by expanding the methane mixture from stagnation pressure P_N (1-4 bar) inside the nozzle through a 50 µm orifice diameter into the vacuum of the source chamber. The molecular beam is formed when the jet expansion passes through a skimmer (Beam Dynamics, Model 2) that is placed inside the *zone of silence* of the jet expansion[52].

The supersonic expansion is used to create a molecular beam where the sample molecules are moving with well defined, supersonic velocity under collision free conditions. This is done by passing the molecules from a high pressure region into vacuum through a small orifice where many collisions (10^2-10^3) occur. In these collisions, the random thermal motion of the molecules is converted into a directed flow with a well-defined and narrow speed distribution. For methane, the number of collisions experienced during the jet expansion are sufficient to cool the rotational degrees of freedom[14]. Assuming ideal gas mixtures, the maximum or terminal velocity of the molecular beam is given by:

$$v_\infty = \sqrt{\frac{2k_B}{\langle m\rangle}\frac{\langle\gamma\rangle}{\langle\gamma\rangle - 1}T_N} \tag{2.1}$$

Where k_B is the Boltzmann constant, $\langle m\rangle = \sum_i X_i m_i$ is the average molecular mass of the gas mixture composed of i constituents with X_i molar fraction, and $\langle\gamma\rangle = \sum_i X_i\gamma_i$ is the molar average ratio of the heat capacities C_p/C_v. The incident translational energy of the molecules can be modified either changing $\langle m\rangle$

in eq. (2.1) by seeding methane in different gases (He, Ne, Ar…) or by changing the seeding ratio, or varying the nozzle temperature (T_N).

The nozzle, mounted on a three-axis manipulator, can be translated in order to change the distance between the nozzle and the skimmer from 15-65 mm. Translation in the other two axis, perpendicular to the molecular beam direction, allows optimizing the nozzle position so that the gas flow that passes through the skimmer into the first differentially pumping stage is maximized. A detailed description of the nozzle design used in these experiments is presented in Chen's thesis[50]. Briefly, it consists of two concentric tubes connected by a front plate where a hole is drilled into a thin wall. By passing current through the concentric tubes, most of the power is dissipated in the thin wall because of its highest electric resistance. Therefore, we locally heat the tip of the nozzle where the supersonic expansion is produced, thus increasing the beam speed. A Sorensen DCS8-125E DC power supply that provides 0-8 V and 0-125 A is used to provide the DC current. A chromel-alumel (K-type) thermocouple is spot-welded to the front of the nozzle to control the temperature. The nozzle temperature is adjusted by controlling the heater supply by a proportional-integral-differential (PID) temperature controller (SRS PCT-10). The nozzle is cooled down by passing water through a cooper-cooling coil that is wrapped around the nozzle mount.

The velocity distribution of the molecular beam is measured by a time-of-flight (TOF) method using a chopper wheel in combination with an on-axis quadrupole mass spectrometer (QMS (1) in Figure 2-2). For these velocity measurements, the sample crystal is moved out of the molecular beam path so the chopped beam enters directly into the ion source of the on-axis QMS (1). This method consists of measuring the time it takes for a package of molecules produced by chopping the molecular beam to arrive to the detector of the QMS(1), that is placed at a known distance from the chopper. The on-axis QMS (Pfeiffer, QMA 400, QMH 410-2 and QMG 421) is set so the analyzer transmits only the mass-to-charge ratio (m/z) of interest. The chopper wheel (5" diameter, 0.1 mm thickness), installed in P2, contains two 2 mm wide slits cut symmetrically. An optocoupler is installed at 180° from the molecular beam path so it detects when the molecular beam passes through a slit. The packages of molecules are produced when the chopper wheel is spun, usually at 200Hz, by a water-cooled brushless electric motor (Maxon) controlled by a EPOS2 software. Every time a package of molecules is produced, the optocouple provides a reference trigger to a multichannel analyzer (MCA-3/P7882) which stores the number of ion pulses measured by the secondary electron multiplier (SEM) detector of the QMS according to their delay time. The measured TOF distributions are converted to translational energy distributions using a deconvolution of the chopper function. A complete description of the TOF calibration is described in Chen's thesis[50]. Table 2-2 contains typical translational energies for different nozzle temperatures and gas mixtures.

Gas mixture	T_N (K)	E_{trans} (kJ/mol)
1% CH_4 in H_2	300	52
1% CH_4 in H_2	800	130
3% CH_4 in He	300	25
3% CH_4 in He	800	65
3%CH_3D in He	500	44

Table 2-2. Some examples of molecular beam conditions used through this thesis work.

Since vibrational cooling in the supersonic expansion is not efficient, the thermal population of vibrationally excited modes can be calculated from Boltzmann statistics using the vibrational partition function.

2.2.2. Molecular beam flux

The flux density of molecules impinging on the surface is given by[53]:

$$flux = \frac{\Delta P\ S}{k_B\ T_g\ A} \tag{2.2}$$

where ΔP is the methane partial pressure rise in the UHV chamber when the molecular beam is introduced, S is the experimentally determined pumping speed of the UHV chamber for CH_4, A is the cross sectional area of the molecular beam that we determined by AES, and T_g is the temperature of the gas in the UHV chamber which is assumed to be room temperature.

The methane partial pressure rise is measured using the QMS(2) in Figure 2-2 (Pfeiffer, QMA 400, QMH 400-5 and QMG 422 with a grid ion source). In order to convert the QMS ion signal (A) to pressure (mbar), a calibration was performed. For CH_4, this calibration consists of introducing a molecular beam of pure CH_4 into the UHV chamber and measuring with QMS(2) the ion signals due to CH_4 and its fragments (m/z=16, 15, 14, and 13). At the same time, the total pressure rise (in mbar) is recorded with a Pfeiffer IKR11 cold cathode ion gauge and corrected with the ionization efficiency of methane (0.7). This procedure is repeated for different pressure rises in the UHV chamber. Figure 2-3 shows the corrected pressure from the reading of the cold cathode gauge *vs* the QMS signal from the sum of the methane fragments. The slope of the line is the proportionality constant between CH_4 pressure and QMS signal that can be used to convert the QMS signal to partial CH_4 pressure when using a gas mixture of CH_4.

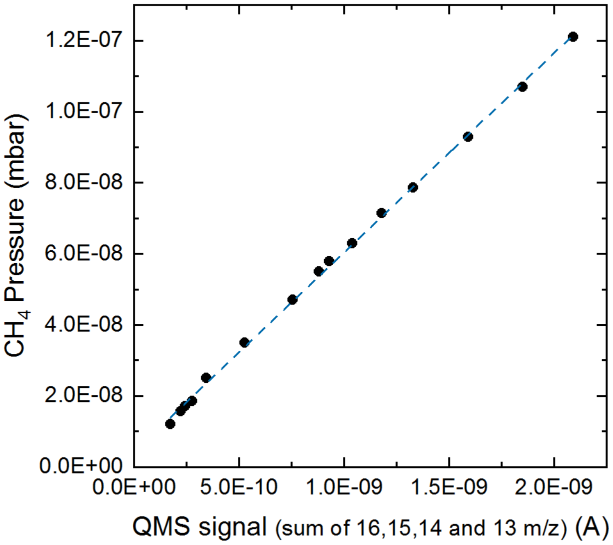

Figure 2-3. QMS signal calibration in terms of CH_4 partial pressure using a pure CH_4 molecular beam. The slope of the linear regression (56 mbar/A) is used to convert between the QMS signal and CH_4 partial pressure.

The effective pumping speed of the UHV turbo pump was experimentally determined by measuring the pump-out time of the UHV chamber. A pure CH_4 molecular beam was introduced into the UHV chamber and the methane partial pressure was measured with the QMS(2). After a certain time, the molecular beam was turned off rapidly by rotating the chopper wheel to block the molecular beam in the second differential pumping stage. The partial pressure decreases exponentially with time, as it is presented in Figure 2-4. The pumping speed is equal to the volume of the UHV chamber (26 L) divided by the time it takes for the pressure to decrease a factor of 1/e.

During my PhD work in date, I had to change the UHV turbomolecular pump because the original pump TMU 1000 failed. The new pump (TMU 1001) uses a different protection grid than the old one with a lower conductance (1952 l/sec for the new pump compared to 3051 l/sec for the old pump). For this reason, the effective pumping speed of the chamber decreased from 520 L/s to 306 L/s after these changes.

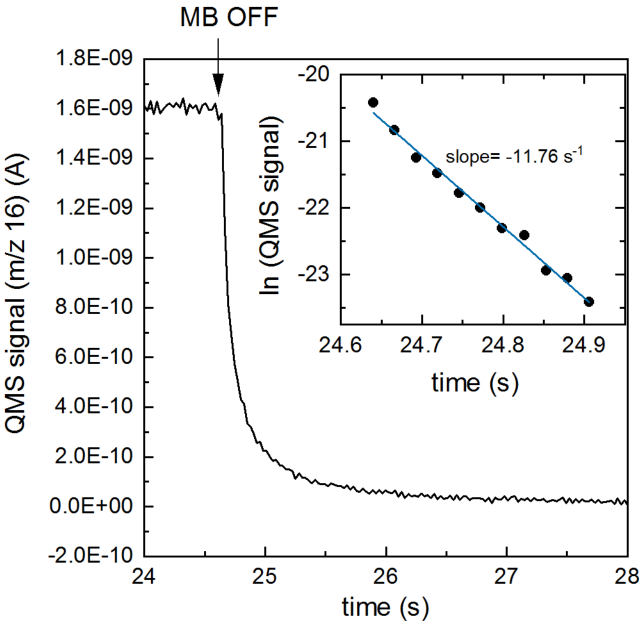

Figure 2-4. Measurement of the pump-out time for CH_4. QMS signal decays exponentially as a function of time once the molecular beam is turned off. Inset shows the linear fitting for the ln(QMS) vs time. The inverse of the slope, 85 ms, is the pump-out time.

Another modification performed during these four years is the addition of two new holes (of Ø=0.5 and 1 mm) to the chopper wheel besides the 2 mm slits. This allows to change the molecular beam spot size and therefore the incident flux of molecules without modifying the stagnation pressure.

2.2.3. Sample manipulator and sample preparation

Figure 2-5 a) shows a photograph of the same mounting inside the UHV chamber. The sample is mounted between two 0.38 mm tungsten wires on a home-made liquid nitrogen cryostat that is supported on a commercial *XYZθ* 4-axis manipulator (Omniax).

Both tungsten wires are attached to two copper arms which are connected to a liquid nitrogen dewar for cooling of the surface to about 80-90 K depending on the thermal contact between the cryostat and the surface. The surface temperature is measured by a *K*-type thermocouple that is either inserted into a

0.5 mm hole in the side of the crystal or directly spot-welded on the side of the crystal. The surface can be heated to above 1200 K by passing current (supplied from a Sorensen DCS8-125E DC power supply) through the tungsten wires. A PID temperature controller (SRS PCT-10) is used to stabilize the temperature to within 0.1 K and also to apply linear temperature ramps for temperature programmed desorption (TPD) measurements. Figure 2-5 b) shows the sample glowing when heated to T_S= 1100 K.

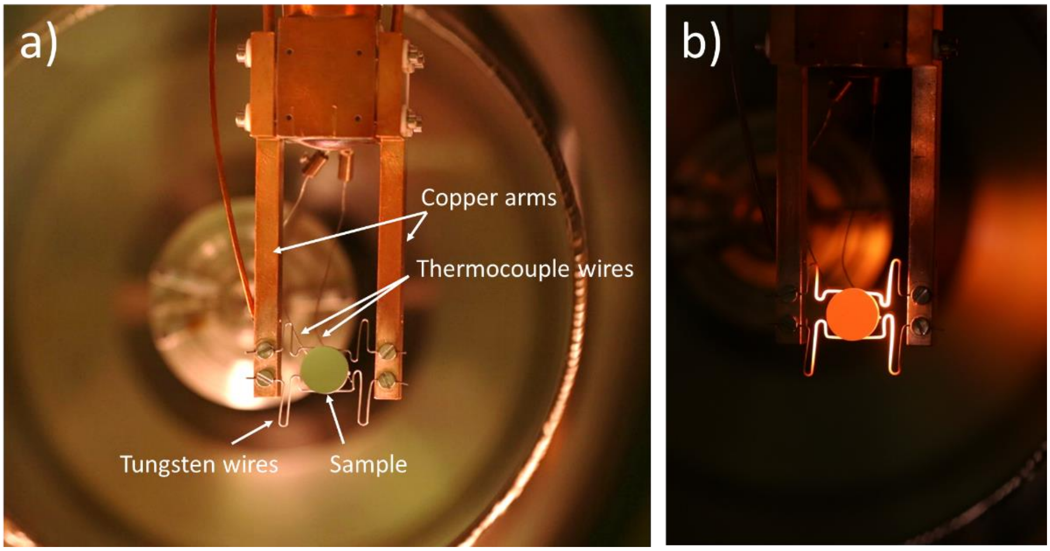

Figure 2-5. Photograph of the sample mount inside the UHV chamber (a)), and of the sample glowing when it is being heated at a surface temperature of 1100 K (b)).

All the Pt samples used in this thesis work were purchased from Surface Preparation Labs in Holland. The Pt(111), Pt(110)-(1x2) and Pt(210) surfaces used in this thesis work had a diameter of 10 mm and were cut to within 0.1° of the (111), (110) and (210) planes respectively, providing an upper limit to the unwanted defects of 0.17%. The Pt(211) crystal was cut and polished on the front (10 mm) and on the back (12 mm) of the crystal. A small miscut angle of 0.05° and 0.075° on both surfaces yield a lower limit to unwanted defects of 0.09% and 0.13% respectively. When the 10 mm side of the crystal was used, the single crystal was held in a tantalum support between the two tungsten wires. When the 12 mm surface side of the crystal was used, the crystal surface was directly mounted between the two tungsten wires.

The surface cleaning procedure involves argon ion sputtering, oxygen treatment and annealing. Between each experiment, the surface was cleaned by exposing the crystals to $5\cdot10^{-8}$ mbar of O_2 at T_S=700-900 K for 5 min. This removes the C adsorbed on the surface by oxidation to CO and CO_2. Once the pressure in the UHV chamber decreased to $\sim10^{-10}$ mbar, the crystal was annealed at T_S=1100 K-1200 K for 2-5 min. At the end of each day, cleaning by Ar^+ sputtering and annealing was used. For that, Ar^+ at 1 kV and 2 μA were bombarded at normal incidence on the surface crystal at an argon pressure of $1\cdot10^{-7}$ mbar using a commercial ion gun[1]. The Pt(210) surface was cooled down at a cooling rate of 2 K/s to avoid undergoing a roughening transition that could lead to a rough surface with no periodic structure[54].

The cleanliness of the surface was verified with AES to check that no detectable (<1% ML) trace of carbon or oxygen was present on the surface after the cleaning procedure. Figure 2-11 shows AES spectra taken before and after cleaning the surface. Ideally, we would use Low Energy Electron Diffraction (LEED) to confirm the surface reconstruction after the annealing of the samples. However, a LEED setup is not available in our current apparatus. Instead, we made used of well-established cleaning procedures for the different Pt surfaces that were tested with LEED[55–57]. Furthermore, we also recorded RAIR spectra for CO adsorption with our RAIRS setup, which has been widely used as a sensitive probe for detects on Pt surfaces. This method allowed us to confirm that our surfaces have the expected structure (i.e. that for example the Pt(211) has only step and terrace sites, and no other defects such as kinks are present on the surface).

In the case of the Pt(210) surface, the structure after Ar^+ sputtering and annealing was checked by inspection of a LEED pattern in the second surface science apparatus that we have in our lab (the “old scattering” machine). The surface was installed using a special mount and the LEED pattern after our typical cleaning procedure was measured. AES was used to confirm the surface cleanliness. Figure 2-6 shows a photograph of a LEED pattern of the clean Pt(210) surface. The LEED pattern matches well with that of a clean and reconstructed Ir(210)[58]. No streaking of the peaks that could correspond to irregular steps are observed.

---

[1] During my PhD work, the Ar^+ sputter ion gun was changed from the Omicron ISE100 to a STAIB NIQ1-S.

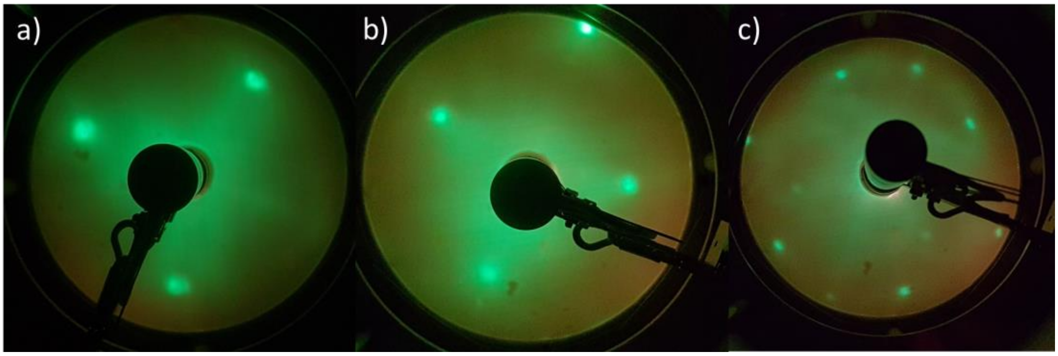

Figure 2-6. LEED images of the Pt(210) sample at different electron energies: a) 53 eV, b) 65 eV, and c) 95 eV.

2.2.3.1. Surface structure

One of the goals of my thesis is the study of the influence of the surface structure on the chemisorption of methane on Pt surfaces. To achieve this, I used several Pt crystals cut along different crystallographic directions, thereby creating different surface structures.

Platinum crystallizes in a face-centered cubic structure (fcc). As shown in Figure 2-7, in the conventional cubic cell, this *Bravais* lattice, has four lattice points (1/8 x 8 from the contribution of the corner lattice points + 1/2 x 6 from the contribution of the face lattice points). Every atom in the bulk has 12 neighbor atoms and therefore the coordination number (CN) of the Pt atoms in the bulk is CN=12.

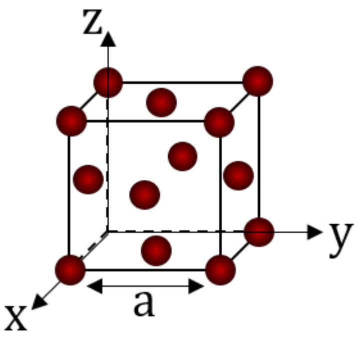

Figure 2-7. Sketch of a fcc conventional cubic cell. “a” refers to the conventional lattice parameter, which for Pt is 3.92 Å[59].

The difference between the Pt(111), Pt(211), Pt(110)-(1x2) and Pt(210) surfaces is the plane along which the crystal is cut. Figure 2-8 shows the different planes. On the second layer in Figure 2-8, only the atoms that are located in the (111) (a), (110) (b), (211) (c), and (210) (d) planes are shown. The planar density on the (111), (110), and (210) planes can be calculated by dividing the number of atoms that are centered in these planes divided by the area of the planes in the conventional cubic cell. For example, there are (1/2 x 1 + 1/4 x 2) atoms that are centered on the (210) plane. The experimental value for the conventional lattice parameter is 3.92 Å[59]. Therefore, the planar density for the topmost atomic layer of Pt(210) (composed of kinks) is $5.82 \cdot 10^{18}$ ridge atoms/m^2. On the Pt(211), as it can be seen in Figure 2-8, the atoms in the (211) plane in the conventional cell fall in a line and are not enough to reproduce the entire lattice structure. In this case, the calculation of the planar density using this method requires the consideration of more than one conventional cell (or, alternatively, the primitive cell).

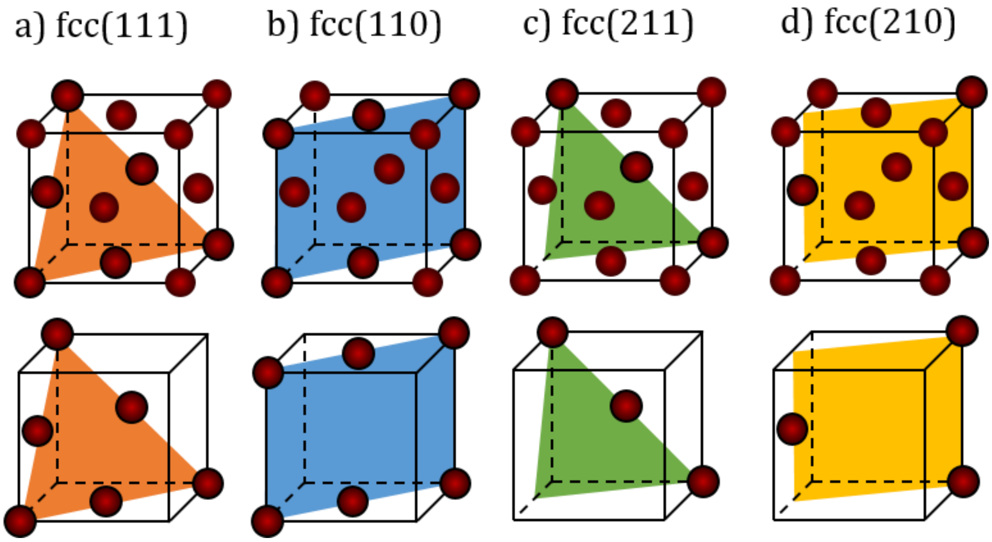

Figure 2-8. Sketches of different planes along which Pt was cut to obtain the Pt(111), Pt(110), Pt(211) and Pt(210) surfaces. On the second layer, only the atoms that are centered on the specified planes are shown.

The Pt crystal surfaces are shown schematically in Figure 2-9. The Pt(111) surface has very little corrugation and all surface atoms are equivalent; we denote these surface atoms as part of “111 terraces”. The Pt(211), also indicated as [3x(111)+(100)] following the Van Hove-Somorjai notation[60], consists of three-atom-wide terraces with (111) structure followed by one-atom-high steps with (100) character. The three different surface atoms are labeled as step, terrace, and corner sites. The Pt(210)= [2x(100)+(110)] consists of two-atom-wide terraces of (100) symmetry and monoatomic steps with (110) character. The atoms on this surface are labeled as kink, middle and bottom atoms. Unlike the Pt(111), Pt(211) and Pt(210), the Pt(110) surface undergoes a (1x2) missing-row reconstruction that leads to a more corrugated structure consistent of alternating ridges and valleys[61]. Three different types of Pt atoms are exposed by this surface: ridge, facet and valley atoms.

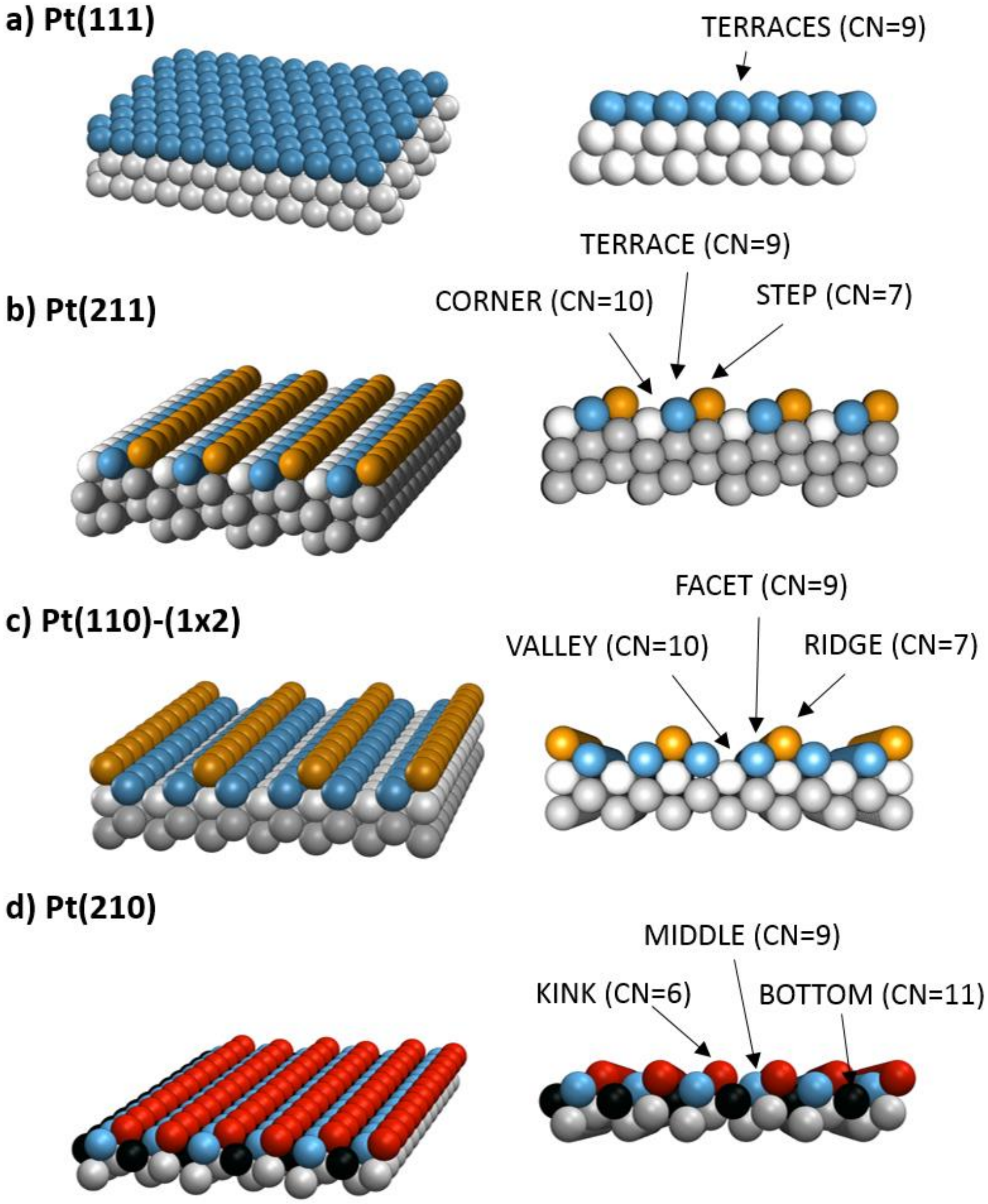
a) Pt(111)
TERRACES (CN=9)
TERRACE (CN=9)
b) Pt(211)
CORNER (CN=10)
STEP (CN=7)
FACET (CN=9)
c) Pt(110)-(1x2)
VALLEY (CN=10)
RIDGE (CN=7)
d) Pt(210)
MIDDLE (CN=9)
KINK (CN=6)
BOTTOM (CN=11)

Figure 2-9. Models of the a) Pt(111), b) Pt(211), c) Pt(110)-(1x2), and d) Pt(210) with the different surface sites labeled in the side view of the surfaces with the corresponding coordination numbers.

As it can be observed in Figure 2-9, on the corrugated Pt(211), Pt(110)-(1x2) and Pt(210) surfaces, not only the topmost atomic layer is exposed. Through this thesis work, I use the term monolayer (ML) to define the surface coverage. 1 ML coverage refers to each of the Pt atoms on the surface being bond to an adsorbate. Therefore, all the different types of surface atoms on each of the Pt surfaces and their fractional occurrence needs to be consider to calculate the density of surface atoms and thus the ML definition on each of the surfaces. Table 2-3 shows, for each Pt surface, the surface atom density and the fractional occurrence of each of the Pt atoms.

Surface	Surface atom	f^{site}	CN	Site density (x10^{18} atoms/m^2)	Surface atom density (x10^{18} atoms/m^2)
Pt(111)	terrace	1	9	15.0	15.0
Pt(211)	step	1/3	7	5.3	15.9
	terrace	1/3	9	5.3	
	corner	1/3	10	5.3	
Pt(110)-(1x2)	ridge	1/4	7	4.6	18.4
	facet	1/2	9	9.2	
	valley	1/4	11	4.6	
Pt(210)	kink	1/3	6	5.8	17.4
	middle	1/3	9	5.8	
	bottom	1/3	11	5.8	

Table 2-3. Summary of the surfaces used in this thesis, the different surface atoms that each of the surface exposes with their fractional occurrence (f^{site}) and coordination number (CN), the density of each of the surface atoms and the total surface atom density.

2.2.4. Detection Methods

2.2.4.1. Temperature Programmed Desorption

Temperature Programmed Desorption (TPD) has been widely used to perform chemisorption studies on metal surfaces[62]. This technique consists of recording the partial pressure of the desorbing species with a QMS while a linear temperature ramp program is applied to the surface. Information about the desorption activation energy, the reaction order for desorption and even of the amount of adsorbate present on the surface can be extracted from a TPD trace.

In this thesis work, TPD was not used to quantify the products of the dissociation. Instead, it was used to control the desorption temperatures of some contaminants on the sample such as H_2 or CO. In this way, some of the experiments, for example those performed using H_2 as a seeding gas, where performed at surface temperatures that are well above the desorption temperature of H_2, ensuring that the hydrogen from the molecular beam does not block any sites on the Pt surface.

2.2.4.2. King and Wells method

The King and Wells (K&W) method allows to measure absolute sticking coefficients (i.e. no calibration is needed). The off-axis QMS(2) in Figure 2-2 is used to monitor the parent mass of the species of interest. Figure 2-10 a) presents a typical K&W measurement trace from the QMS. In this case, the reactivity of CHD_3 on the Pt(110)-(1x2) was being studied. Therefore, the methane isotopologue parent mass at 19 amu was monitored. The time axis has been shifted so that at t=0 the molecular beam directly hits the crystal. In the beginning, before the molecular beam enters into the UHV chamber, there is no significant signal for mass 19. At t=-57 s, the separation valve between P2 and P3 is opened, and the molecular beam enters the UHV chamber. For the first 57 s (between t=-57 and 0 s), a teflon flag is inserted in the path of the molecular beam so the molecules scatter from this inert flag. At t=0 s, the beam flag is raised by a UHV compatible stepper motor controlled by a Labview program. By opening the flag, we let the molecules to hit directly the Pt(110)-(1x2) surface. Any sticking of CHD_3 on the surface results in a drop (ΔP) of the 19 amu QMS signal. The pressure drop decreases with time as the surface is being passivated by the dissociation products. After 15 s deposition, the beam flag blocks the beam again, and at t=64 s the molecular beam is switched off by closing the separation valve between P2 and P3.

The time dependent sticking coefficient S(t) is given by:

$$S(t) = \frac{\Delta P(t)}{P} \tag{2.3}$$

where $\Delta P(t)$ is the change in the partial pressure of mass 19 in the QMS for t>0 when the flag is open and P is the increase in the partial pressure of mass 19 when the molecular beam enters the UHV chamber. Figure 2-10 b) shows the correspondent $S(t)$ for the QMS trace shown in Figure 2-10 a). $S(t)$ traces were fit using a double exponential decay to extrapolate the initial sticking coefficient S_0 at t=0. The reason for this double exponential fitting is explained in more detail in chapter 5. Briefly, the reason is that the dissociative chemisorption of methane on the Pt surfaces at a range of surface temperatures between 500 and 800 K was shown to be governed by two processes: a fast initial dissociation of the CH_4 and a slower growth of carbon particles on the surface[63]. A double exponential fitting for the $S(t)$ is meant to take into account both processes:

$$S(t) = A_1 e^{-k_1 t} + A_2 e^{-k_2 t} \tag{2.4}$$

where $A_1 + A_2 = S_0$ is the initial sticking coefficient, and k_1 and k_2 account for the rate at which the sticking coefficient decreases.

An advantage of using K&W is that is self-calibrated. However, in our current setup the detection limit for S_0 measurements using K&W is about 1%. Therefore, energetic beams seeded in hydrogen that lead to S_0> 1% were used for the K&W experiments that I described in chapters 3 and 5.

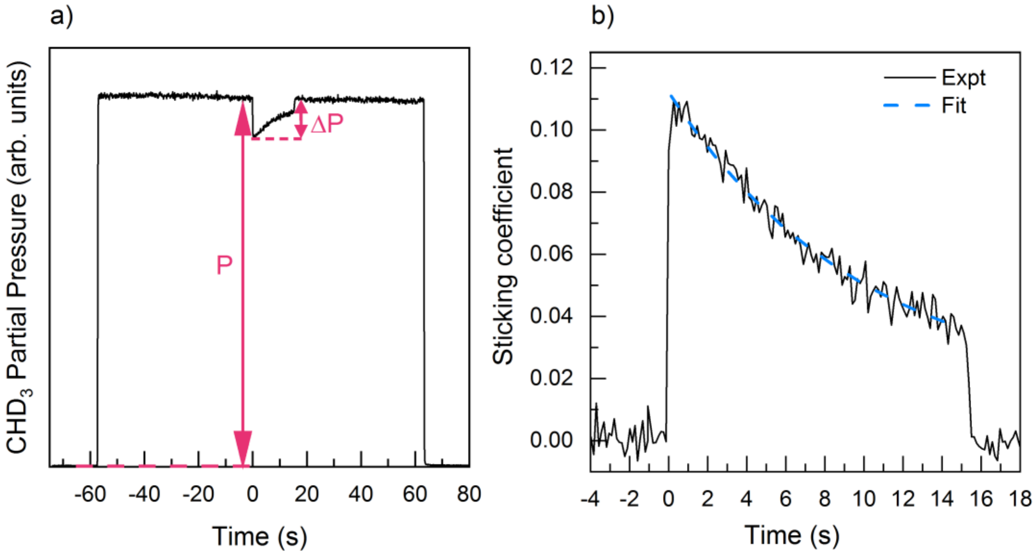

Figure 2-10. a) King and Wells QMS trace for the dissociative chemisorption of CHD_3 on Pt(110)-(1x2) at 123 kJ/mol and a surface temperature of 650K. b) Time dependence of the sticking coefficient. The dashed blue corresponds to the fit to the data with a double exponential using equation (2.4).

2.2.4.3. Auger Electron Spectroscopy

Auger Electron Spectroscopy (AES) is a well-known chemical surface analysis tool[64]. The surface is bombarded with a beam of high kinetic energy electrons (3-5 keV) that are accelerated onto the surface. These electrons ionize the surface atoms by removing a core electron from level *W*, leaving behind a hole. This empty electron position is filled by an electron from a higher energy level (*X*), and in this process the excess of energy between level W and X is transferred to a third electron at level *Y* that is emitted. This last emitted electron is an *Auger* electron coming from a *WXY* transition.

The experimental setup described here is equipped with a Auger electron spectrometer with a cylindrical mirror analyzer from Perkin Elmer. A RDB PCI card is used for the data acquisition. During this thesis work, AES was used to confirm the cleanliness of the surface after our cleaning procedures. Using an electron current of 1.2 μA and ramping the analyzer energy in steps of 1 eV with a dwell time of 750 ms, the minimal coverage of C that our AES set up can measure is about 1.5% ML. Therefore, we can confirm that after our cleanliness procedure, the C coverage on the surface is less than 1.5% ML of C.

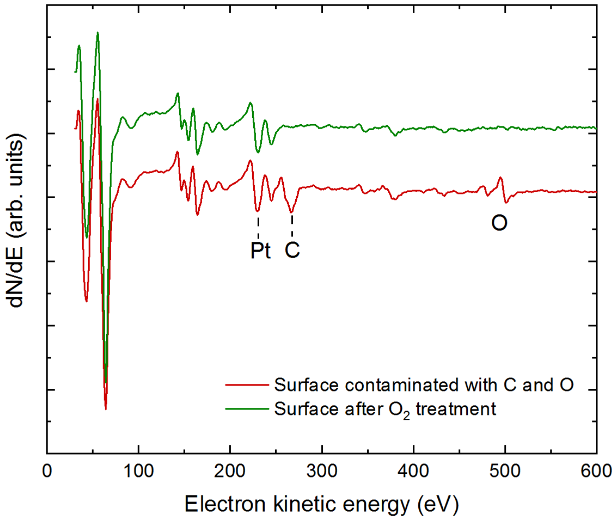

Figure 2-11. Auger electron spectra measured on Pt(211). In red, AES spectrum taken on the surface contaminated with carbon and oxygen; In green, AES of a clean surface after cleaning in a O_2 atmosphere at T_S= 700 K.

Figure 2-11 shows typical AES spectra for the surface covered with C, O and a clean surface. The peaks that match in both spectra correspond to different Pt transitions. The transitions due to O and C are labeled. After heating the surface with an O_2 partial pressure of $5\cdot10^{-8}$ mbar, both the oxygen and carbon on the surface disappear (green spectrum) leaving a clean Pt surface.

AES was also used to detect carbon after methane depositions. In this case, the amount of carbon (C) on the surface was determined by the ratio between the transition of C shown in in Figure 2-11 and the only transition of Pt that is labeled in Figure 2-11. This Pt transition, at 239 eV, is chosen as representative of Pt because it appears at a similar energy to that of C (272 eV) in the AES spectrum. This avoids recording a very long scan that could induce to some contaminants on the surface as well as electron beam induced chemistry[50]. Figure 2-12 shows a typical Auger profile of a carbon "spot" after a deposition of methane on the Pt(111) surface with 8% ML of carbon coverage.

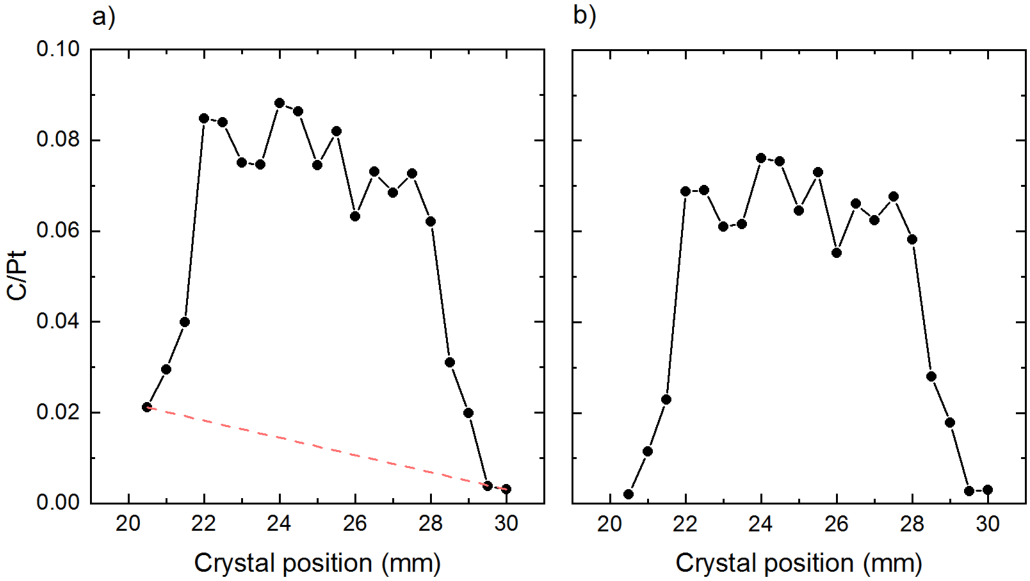

Figure 2-12. a) Example of an Auger profile measured following a CH_4 deposition on Pt(111). The red dashed line shows the carbon background generated from the UHV background contamination and the electron gun. b) Auger profile obtained after background subtraction of the AES profile shown in a).

2.2.4.4. Reflection Absorption Infrared Spectroscopy

Reflection Absorption Infrared Spectroscopy (RAIRS), also referred to as Infrared Reflection Absorption Spectroscopy (IRAS), consists of measuring the vibrational absorption spectra of the adsorbates on the surface in the mid infrared region. Briefly, as shown schematically in Figure 2-2 and Figure 2-13, infrared light from a thermal source is reflected off the metallic sample surface at grazing incidence and focused onto a suitable infrared detector. In the presence of adsorbates on the surface, a decrease in the reflected infrared intensity is observed due to infrared active vibrations of any adsorbates on the surface. Thus, this technique provides information about the molecular structure of the adsorbates on the surface.

A RAIR spectrum is obtained as the ratio of a sample spectrum recorded with the adsorbate covered surface and a background spectrum recorded with a clean surface. Since it does not interfere with the chemisorption reaction, RAIRS can be used to record infrared spectra during the molecular beam exposure and therefore to record the uptake of reaction products of the chemisorption reaction. The ability to perform the detection throughout the molecular beam exposure is an advantage compared to other invasive surface analysis techniques such as AES, because it allows to record the full uptake of the chemisorption products in a single experiment. Another advantage of RAIRS with respect to K&W or AES is the possibility to distinguish between different deuterated methyl species on the surface[29]. This feature is used to perform bond selectivity studies on Pt(111) and Pt(211) in chapter 4. In this thesis (chapter 3 and 4), I also demonstrate the ability of RAIRS to distinguish between methane chemisorption products on different sites of Pt surfaces, opening up new possibilities for the site-specific study of methane chemisorption on corrugated surfaces. All these features and advantages make RAIRS a very powerful tool to perform gas-surface reaction studies.

- Our setup

The FTIR VERTEX 70V spectrometer from Bruker used in these experiments has been described in detail in the dissertation of Chen[50]. Here, I will give a short introduction of some key concepts behind RAIRS and I will show how I optimized some parameters to increase the signal to noise in our measurements. Figure 2-13 shows the optical layout of our RAIRS setup. A Globar source (S_1) is used as the mid-infrared radiation (MIR) source. The light, passes through a Rocksolid™ interferometer that induces a periodically varying path length difference between two beams from the MIR source produced by a beam splitter (BS). Both IR beams, containing all wavelengths, are recombined and detected in the form of an interferogram that is then Fourier transformed into an absorption spectrum. A liquid N_2 cooled Indium Antimonide (InSb) detector with a spectral range between 1850-10000 cm^{-1} was used in position D_1 in Figure 2-13.

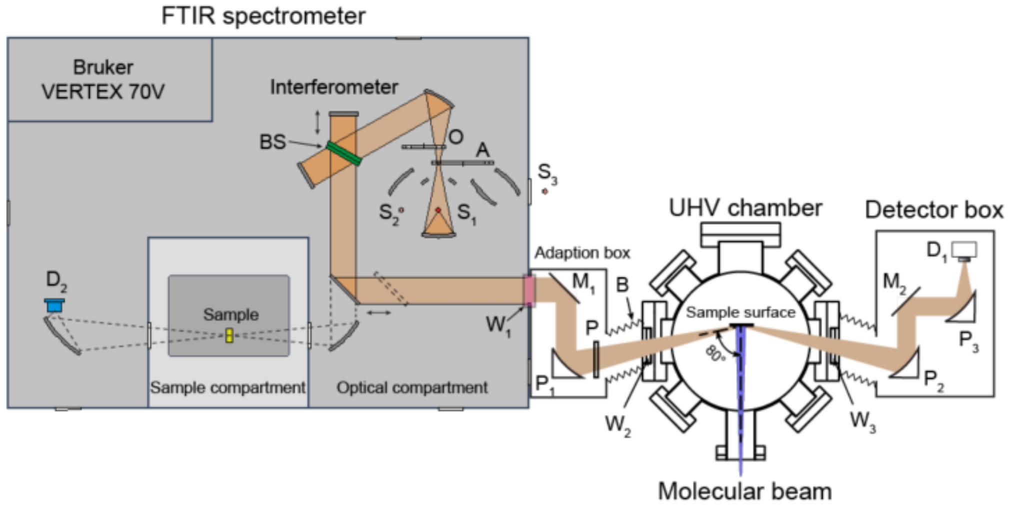
FTIR spectrometer
Bruker VERTEX 70V
Interferometer
BS
O
A
S_3
S_2
S_1
UHV chamber
Detector box
Adaption box
D_1
M_1
B
M_2
D_2
Sample
P
W_1
Sample surface
80°
P_3
P_2
P_1
Sample compartment
Optical compartment
W_2
W_3
Molecular beam

Figure 2-13. Optical layout of the RAIRS setup. S_1: MIR Globar source; A: Aperture wheel; BS: Beam Splitter; W_1, W_2 and W_3: KBr windows; M_1 and M_2: gold-coated plane mirrors; P_1,P_2 and P_3: praboloidal mirrors; P: wire-grid linear polarizer; B: bellows; D_1: InSb IR detector.

- Surface selection rule

As it is indicated in Figure 2-13, the IR light is incident at 80° with respect to the surface normal. The reason for this geometry is that the absorption of IR radiation by the adsorbates is enhanced at near grazing incident angles. This can be understood by considering the electrical field of the incident and reflected beams. At the point of contact with the surface, the net electric field amplitude of the s-polarized (perpendicular to the plane of incidence) IR radiation is zero (see Figure 2-14). Therefore, only the p-polarized radiation (parallel to the plane of incidence) will interact with the surface adsorbates. Solving Maxwell's equations, one can prove that the electric field amplitude of the p-component reaches a maximum near grazing incidence. Since the light intensity is proportional to the square of the amplitude of the electric vector, grazing incidence gives the best detection sensitivity. This brings us to the so-called *surface selection rule* for reflection IR spectroscopy. A molecule is excited when its dipole moment interacts with the electrical field of the IR light. Since only the p-component of the radiation presents a component of the electric field at the surface, only active vibrations that have a component of the dipole moment perpendicular to the surface can be detected using RAIRS. Furthermore, as it is represented in Figure 2-14 c) the interaction of the vibrational dipole moment with its image dipole moment on the metal surface leads to a constructive interference for dipole moments perpendicular to the surface plane, and to destructive interference for dipole moments parallel to the surface plane.

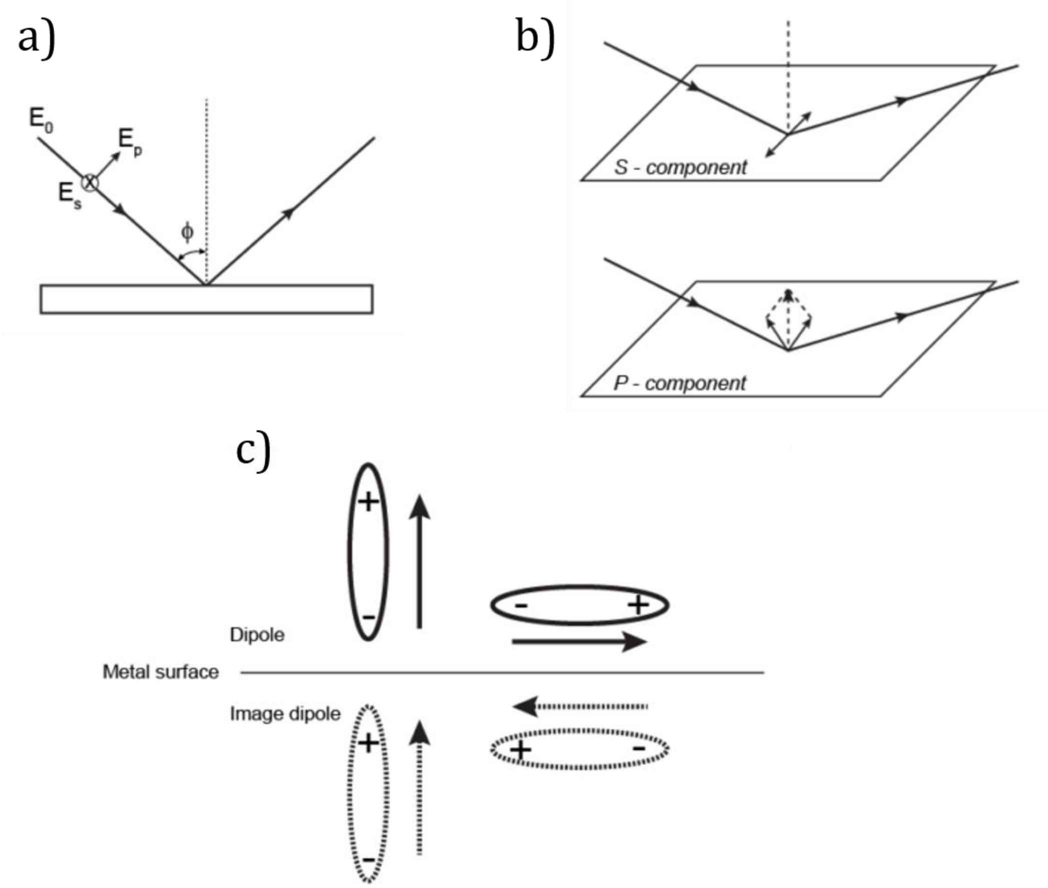

Figure 2-14. a) Schematic representation of the plane of incidence and the definition of the s and p polarized radiation; b) Destructive and constructive interference for the s and p components of the electric field at the surface; c) Illustration of the surface selection rule: the interaction of the vibrational dipole moment with its image dipole moment on the metal surface leads to a destructive interference for dipole moments parallel to the surface plane.

This surface selection rule is also directly related to the sensitivity of the RAIRS technique. The measured absorption peak intensity in RAIRS strongly depends on the transition dipole moment of the detected vibration at the surface. Therefore, for molecules with a strong transition dipole moment perpendicular to the surface, as it is the case of CO(ads) on Pt, the detection limit is low[50,65]. For example, Chen quantified the RAIRS detection limit of our setup for CO(ads) detection to be 0.02% ML for a 35 second measurement time and a spectral resolution of 4 cm^{-1}. For chemisorbed methyl groups (CH_3(ads)) on Pt(111), whose transition dipole moment is approximately 50 times weaker than that of CO, the detection limit of our setup was estimated to be about 1% ML. As it is presented in chapter 3, the transition dipole moment for methyl adsorb on different surface sites is different due to different geometries of the adsorbate. Therefore, the RAIRS sensitivity can vary for the detection of the methyl adsorbed on different surface reaction sites.

- Signal to noise

The signal to noise ratio (SNR) of a RAIR spectrum is determined as:

$$SNR = \frac{U(\nu)\ \Theta\ \Delta\nu\ t^{\frac{1}{2}}\ D^{*}\ ʒ}{A_{D}^{1/2}} \tag{2.5}$$

where $U(\nu)$ is the spectra brightness determined by the blackbody radiation of the MIR source, Θ is the optical throughput, $\Delta\nu$ is the spectra resolution, t is the measurement time, D^{*} is the detector sensitivity, $ʒ$ is the detector efficiency and A_D is the active area of the detector. Having a fixed source and detector, there are three parameters that we can optimize in order to improve our SNR: the measurement time, the optical throughput and the spectra resolution. All three can be modified using the OPUS software that controls our VERTEX FTIR. The resolution was fixed to 4 cm^{-1} and not changed during the experiments presented in this thesis since it was enough to resolve all the detected peaks.

In FTIR, a 100% transmission line is usually used to determine the SNR. The 100% line consists of a spectrum measured from the ratio of two identical spectra. In this case, signal is 100% and noise is calculated from RMS. Figure 2-15 shows the SNR (1/RMS) for several measurement times and two different optical throughputs. The measurement time is modified by changing the number of sample scans to average. As expected, the longer the measurement time, the lower the noise of the spectrum.

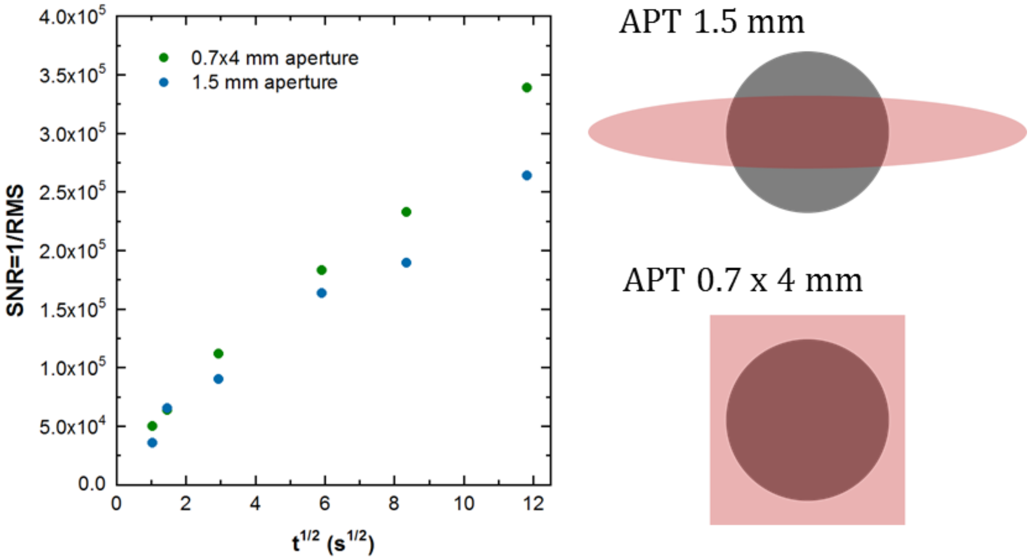

Figure 2-15. SNR from 100% line measurements as a function of $t^{1/2}$, being t the measurement time. Two different apertures (A in Figure 2-13) for the IR beam were used. The IR beam shapes on the sample surface for both apertures are shown on the right.

The optical throughput, Θ, determines the power received at the detector. In our setup, the throughput is limited by the sample surface area or the FTIR aperture (shown as A in Figure 2-13). Different shapes and sizes of apertures can be chosen. In this thesis, two different apertures were used: the “APT Ø1.5 mm” which leads to an ellipsoidal IR beam shape on the surface of 27x4.5 mm; and the “APT 0.7x4 mm” that produces a rectangular IR beam on the surface of 13x12 mm dimensions. The latter is more sensitive to misalignment effects but it was found to reduce the noise in the spectrum as it is shown in Figure 2-15. For this reason, it was used in experiments where the signal of the adsorbates on the surface was small due to their weak dipole moment.

For those experiments for which improving the SNR was necessary, I took a long background scan (for about 20 min, with 8192 scans) and I flashed the surface once the background spectrum was recorded to desorb possible contaminants that could adsorb on the surface during the background measurement time. The surface was then cooled back to the desired temperature of the experiment and the deposition was started. During the experiment, depending on the rate of the adsorbate uptake, I averaged between 256-512 scans to have a RAIR spectrum every ~35-70 seconds. Once saturation coverage was achieved, a final sample spectrum was recorded by averaging 8192 scans to achieve a high SNR spectrum.

2.3 Laser setup

An essential part of our experimental setup is the use of coherent light sources to prepare the methane reactant in the molecular beam in a specific rovibrational quantum state. For that, we use a commercial tunable, single mode, continuous-wave optical parametric oscillator (Aculight Argos System). In our setup, the incident molecules can be excited either before or after the molecules pass through the skimmer. In all the laser-on experiments presented in this thesis the excitation was performed before the skimmer, as it is shown in Figure 2-2.

2.3.1. Optical Parametric Oscillator

During this thesis work, I used an Argos model 2400 cw-OPO C module produced by the Lockheed Martin Aculight Corporation, with a tuning range of 2500-3125 cm^{-1}, which covers the IR active fundamental C-H stretches of all methane isotopologues.

Optical parametric oscillators are based on a second order nonlinear process that involves the mixing of three electromagnetic waves. A single input photon ("pump") is split into two generated photons ("signal" and "idler") when passing through a nonlinear optical crystal. The only two restrictions on the combination of frequencies of the generated photons is that phase matching is achieved and that conservation of energy is preserved:

$$\omega_{pump} = \omega_{signal} + \omega_{idler} \tag{2.6}$$

Figure 2-16 shows schematically the pump source, which is a distributed feedback (DFB) fiber laser centered at 1064 nm. This single mode DFB fiber with a bandwidth of <100 kHz and generated by Yb-doped fiber laser, seeds a 20 W fiber amplifier (IPG Photonics). The pump light is then transmitted to the OPO through a polarization preserving armored fiber cable that is coupled to the OPO cavity.

The OPO cavity consists of a nonlinear optical crystal placed inside an optical resonator. The "signal" wave is resonant in the optical cavity while the "idler" wave make a single pass through the crystal. In this case, the nonlinear crystal is a periodically poled lithium niobate crystal (PPLN). Efficient parametric generation of IR light requires phase matching between the pump, signal and idler waves through the nonlinear crystal medium. Phase matching refers to fixing the relative phase of the electromagnetic waves as they propagate through the crystal. In our OPO, quasi-phase matching is achieved thanks to the periodic pooling of the crystal. Moreover, this periodic pooling is engineered in a “fan-out” pattern that alters the periodicity of the poling across the crystal and thereby allows tuning of the generated photon frequency by translating the crystal. Single-mode operation of the OPO is ensured by an intracavity etalon with a free spectral range of ~ 13 cm^{-1} mounted to a galvanometer.

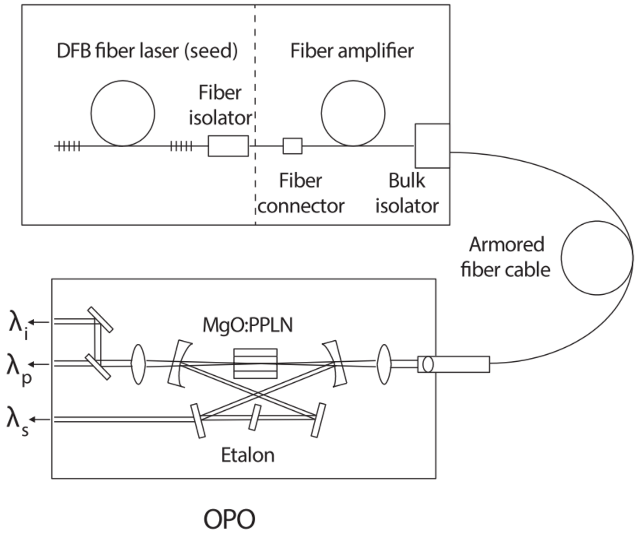

Figure 2-16. Schematic of the Argos 2400 SF tunable light source. See text for details. Drawing provided by Lockheed Martin Aculight.

During the experiments performed in this thesis, I only used the “idler” beam to excite the reactants in the molecular beam. In order to tune the wavelength of the idler beam to match the desired rovibrational state wavelength to excite, three mechanisms were used providing different levels of tuning:

1. Course tuning (~ 13 cm^{-1} steps) is achieved by translation of the non-linear crystal perpendicular to the beam axis. By doing so, different poling periods of the engineered crystal are sampled and so phase matching is achieved for different combinations of frequencies.

2. Intermediate tuning (~ 1 cm^{-1} steps) is accomplished by modifying the angle of the intracavity etalon in the cavity.

3. Fine tuning is attained by applying an external voltage (0-150 V) to a piezo electric element (PZT) that is connected to the seed laser fiber. This voltage induces a strain in the seed laser fiber that allows to tune

continuously the idler frequency over a range of ~100 GHz (~3.33 cm^{-1}).

2.3.2. Frequency stabilization

In our experiments, the IR excitation frequency needs to stay resonant with the narrow rovibrational transitions in the molecular beam (FWHM of 1-3 MHz) for extended periods of time (~1 hour), which is not possible unless an active frequency stabilization is used. Otherwise, the OPO idler frequency drifts several MHz per minute (and hundreds of MHz per hour) because of temperature fluctuations or changes in the air pressure in the laboratory.

Two different methods for frequency stabilization were used for the work presented in this thesis: Lamb Dip locking and transfer cavity stabilization. Lamb dip locking has been used for some years in our group and has been described in detail previously[66]. The transfer cavity stabilization was first implemented by van Reijzen during his thesis[67] and it has been improved and discussed in detail recently in Werdecker's dissertation[67,68]. Therefore, both principles are only briefly described here.

2.3.2.1. Lamb dip locking

This method consists of stabilizing the OPO idler frequency to a Doppler-free saturation hole burned into the center of a Doppler broadened absorption line of methane in a static cell.

For that, a small fraction (~100 mW) of the laser output is sent through a static gas cell filled with 20-50 μbar of the methane isotopologue gas under investigation, and then retro-reflected. By detecting the reflected beam intensity as the OPO is tuned over a particular transition (ω_0), a Doppler-broadened absorption profile with a narrow dip (Lamb Dip) in the center is observed. The Lamb dip can be understood in a simple way: when the laser is detuned from ω_0 to ω_L, the incident wave can be absorbed by molecules traveling with a velocity component in the axis of the laser beam of $v_x = (\omega_L - \omega_0)\, c/\omega_0$. In the same way, the refected wave can be adsorbed by molecules traveling with $v_x = -(\omega_L - \omega_0)\, c/\omega_0$. This yields to a Doppler broadened profile as the one shown in Figure 2-17. For $\omega_L = \omega_0$, both the incident and the reflected beams are adsorbed by the molecules moving perpendicular to the laser beam ($v_x = 0$). Therefore, only molecules with zero velocity in the direction of the laser beams experience twice the laser intensity. If the laser power is sufficiently high to saturate the transition, a decrease in the adsorption signal is observed due to a bleaching of the lower level population. The width of this Doppler-free Lamb Dip is typically 2-3 MHz due to transit time, power and pressure broadening[66].

The frequency of the Lamb dip corresponds to the Doppler-free molecular adsorption frequency needed to excite the molecular beam(ω_0) with a perpendicular laser crossing. Thus the Lamb dip can be used to stabilize the OPO idler output frequency to better than 1 MHz using lock-in techniques (Laselok system). The lock-in technique produces a derivative shape of the Lamb dip which is used as an error signal for the stabilization in a PID controller to provide feedback to the tuning input of the pump laser.

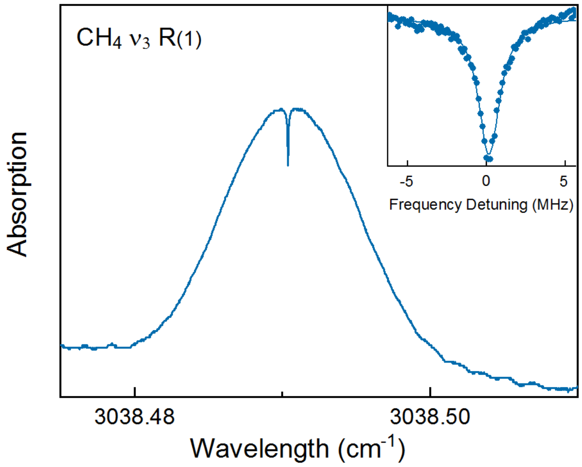

Figure 2-17. Doppler broadened profile of the R(1) transition of the ν3 antisymmetric stretch transition of CH_4 with the Lamb dip in the center (at 3038.491 cm^{-1}). The gas cell was filled with 30 µbar of CH_4. Inset: Magnification of the Lamb dip. In this case, the x axis is expressed in terms of the frequency detuning $\omega_L - \omega_0$.

This stabilization method has been used to lock the idler frequency for many hours[66]. An important disadvantage of Lamb dip locking is that it can only be used to lock on rovibrational transitions if the lower level of the transition is sufficiently populated in the gas cell as room temperature. Furthermore, the transition needs to have a sufficiently large transition dipole moment (Einstein coefficients of at least 1 s^{-1}) in order to be saturated in a static gas cell with typically 100 mW of IR light. The rovibrational transitions excited for this thesis work could all be locked using Lamb dip cell. However, due to a rearrangement in the optical table layout, part of the experiments performed in this thesis were done using another stabilization technique: the transfer cavity.

2.3.2.2. Transfer cavity stabilization

This method consists of stabilizing the OPO idler beam frequency by comparing its frequency with that of a temperature stabilized helium-neon (HeNe) laser with a drift of less than 1 MHz/hr. This frequency comparison is achieved by sending both the HeNe laser and a small portion of the OPO idler output through a Fabry-Pérot cavity which contains one mirror mounted on a piezo electric actuator so that the cavity length can be varied by the application of a high voltage ramp. As shown in Figure 2-18, both the IR and the HeNe laser are transmitted by the cavity and separated by a germanium window and detected by two different photodiodes. Scanning the cavity length produces periodic transmission peaks for both lasers. Since a confocal cavity was used, a constructive interference was achieved if:

$$4n(\lambda)L = m\lambda \qquad\qquad m = 0, 1, 2, \dots \tag{2.7}$$

being λ the wavelength, L the cavity length, $n(\lambda)$ the refractive index of the intra-cavity medium. Each of the transmission peaks corresponds to a cavity mode labeled as m and k for the IR and HeNe lasers respectively in Figure 2-18. The relative position of the IR and HeNe fringes depends on the wavelength of both lasers. The wavelength of the HeNe laser is stable, so any change in the relative position between two fringes of the IR and HeNe lasers (ΔL_{mk}) is due to the drifting of the IR frequency. Therefore, by stabilizing ΔL_{mk} using lock-in techniques, the frequency of the OPO laser could be stabilized.

The frequency stability of the OPO idler using the transfer cavity has been shown to be as good as that using the Lamb dip[68]. This stabilization method also offers as an advantage that it requires only very little IR power (< 1 mW) and can be applied to excite also hotband transitions from levels that have no thermal population at room temperature. Werdecker realized an offset scanning technique using the transfer cavity locking which allows scanning of the idler frequency with MHz resolution[68].

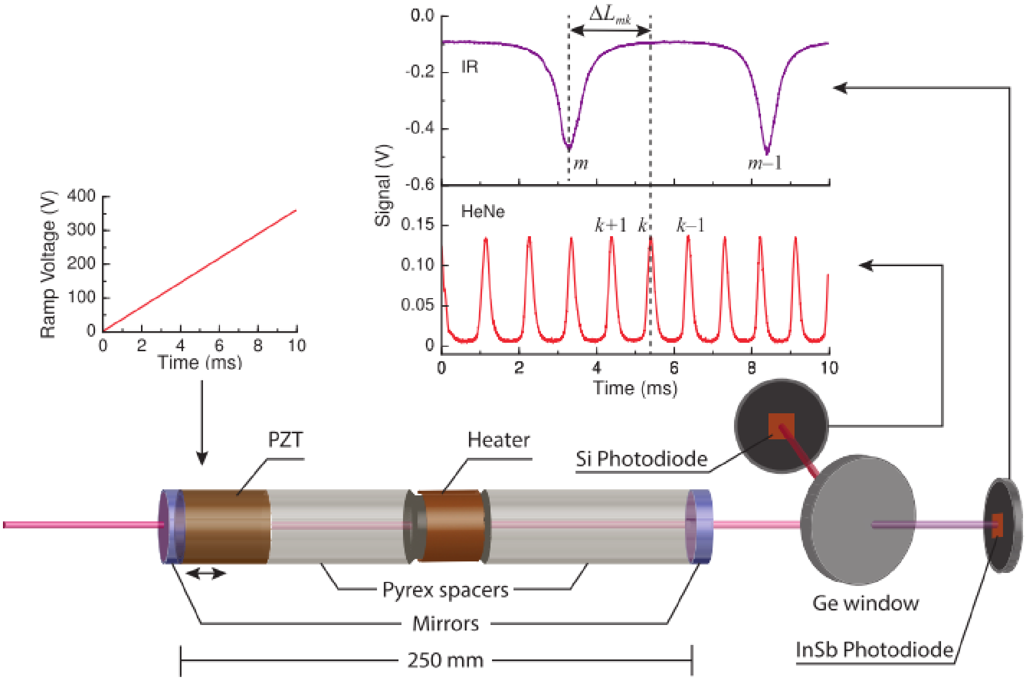
0.0
ΔL_{mk}
-0.2
IR
-0.4
m
m–1
-0.6
Signal (V)
HeNe
k+1
k
k–1
0.15
0.10
0.05
0
0
2
4
6
8
10
Time (ms)
Ramp Voltage (V)
400
300
200
100
0
0
2
4
6
8
10
Time (ms)
PZT
Heater
Si Photodiode
Pyrex spacers
Mirrors
250 mm
Ge window
InSb Photodiode

Figure 2-18. Schematic drawing of the transfer cavity setup. The IR and HeNe lasers are aligned through the confocal Fabry-Pérot cavity. The cavity length is scanned by periodically applying a voltage ramp to the PZT mount of one cavity mirror. After passing through the cavity, the IR and visible beams are separated and detected by two different photodiodes. The relative position between two fringes of the IR and HeNe laser are measured by a LabView program and used to correct for any drift in the wavelength of the IR laser. Taken from [68].

2.3.3. Rovibrational excitation by Rapid Adiabatic Passage

With the OPO idler frequency locked to the desired transition, the preparation of the molecules in the specific rovibrational state was achieved using rapid adiabatic passage (RAP). The theory of RAP is beyond the scope of this thesis work. The interested reader is referred to the theses of Yoder[66], and Werdecker[68] and a publication by Chadwick *et al.*[69] where a theoretical description of RAP and its implementation in our experiment is described in detail.

Briefly, RAP uses a frequency-chirped laser field to completely invert the population of a two-level system. Without using RAP, even an intense, coherent and resonant radiation field would lead only to saturation of a 2-level system with 50% population transfer to the excited level. This is due to the average excitation probabilities for molecules having slightly different velocities within the finite velocity spread of the molecular beam, and experiencing different Doppler shifts. In contrast, RAP achieves an inversion of the population by proper focusing of the laser beam with a cylindrical lens that creates curved wavefronts of the laser field. These curved wavefronts lead to a Doppler tuning effect when the molecular beam crosses the focused laser beam. If properly adjusted and with enough laser power, this frequency sweep leads to a complete population inversion between two quantum states coupled by a nonzero transition dipole moment.

RAP has been proven to transfer all the population from the ground state into the excited state by performing a two-lasers bleaching experiment[69]. In this experiment, a first laser was sent to excite the molecules to a particular transition from the initial state (v=0, J”) to the final state (ν’, J”+1). After this initial excitation, a second laser crossed the molecular beam and its frequency was locked to excite a transition from (v=0, J”) to (ν’, J”-1). By recording the flux of excited molecules using a pyroelectric detector, it was demonstrated that the first laser removed most of the population from the initial state, leaving no molecules for the second laser to excite and demonstrating the inversion of the population.

2.3.4. Determination of the excited state population in the molecular beam

The determination of the excited state population in the state prepared molecular beam is needed for the measurement of state resolved sticking coefficients. This is determined by recording the power dependence of the signal of a room temperature pyroelectric detector inserted into the molecular beam (Figure 2-2). This detector is only sensitive to changes in temperature, which requires modulation of the excitation laser by an electromechanical shutter. By chopping the OPO beam used for vibrational excitation with a fast shutter (2 Hz), the pyroelectric detector signal detects only the vibrationally excited molecules in the continuous molecular beam.

In order to quantify the fraction of excited molecules in the beam, two different methods can be used. One is based on the fact that the excitation fraction is proportional to the IR pumping efficiency and the population of the initial state:

$$f_{exc} = f_{rot} \cdot f_{vib} \cdot f_{RAP} \tag{2.8}$$

where $f_{rot} \cdot f_{vib}$ account for the fraction of molecules in the lower state, and f_{RAP} is the IR pumping efficiency obtained using RAP.

f_{RAP} can be calculated by recording laser fluence curves of the pyroelectric detector signal. For this, the pyroelectric detector signal is detected by a lock-in amplifier as a function of the laser power, which is changed by rotating a λ/2 waveplate that varies the power transmitted by a linear polarizer. Two examples of fluence curves for two different rovibrational transitions of CH_4 are shown in Figure 2-19. As the laser power increases, the pyroelectric detector signal increases and if complete population inversion occurs the pyroelectric detector signal approaches an asymptote that is independent of the transition dipole moment and proportional to the population of the rotational level. From the fluence curve, the fraction of the population transferred can be calculated as the ratio of the pyroelectric signal at the laser power used for the experiments and the asymptote determined from the fit of the fluence curve.

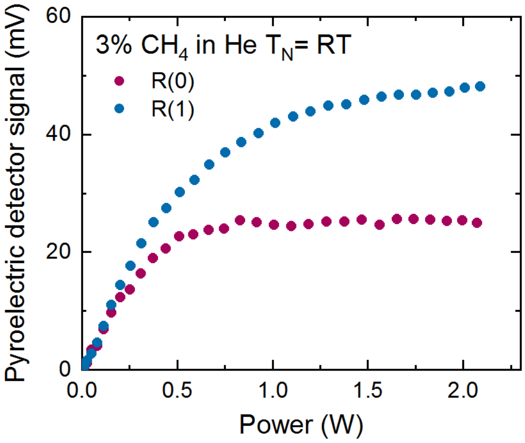

Figure 2-19. Fluence curves for the ν_3 R(0) and R(1) transitions for a 3% CH_4 in He mixture.

f_{vib} is the fraction of molecules in the initial vibrational state. This is calculated from Boltzmann statistics assuming that the temperature of the nozzle is the same as the temperature of the molecules since vibrational cooling in a supersonic expansion is inefficient[14].

f_{rot} is the fraction of molecules in the lower rotational level. Rotational cooling in a supersonic expansion is very efficient and so, in this case we cannot assume that the temperature of the nozzle is equal to the rotational temperature of the beam. In order to obtain f_{rot}, two methods have been used in our group:

a) The first one has been explained in detail in Chen's thesis[50]. It is based on recording fluence curves for several transitions involving different initial J levels. The relative rotational populations for different J levels are obtained by the ratios of the asymptotes of the fluence curves. These relative populations can be directly compared with theoretically calculated relative populations at different rotational temperatures (T_{rot}). In this way, the T_{rot} of the molecules and therefore the population (f_{rot}) of the different J levels at that T_{rot} are obtained.

b) This method makes use of the fact that the pyroelectric detector signal is proportional to the population of the excited molecules. The procedure consists of measuring fluence curves for transitions involving J levels from the same symmetry species. We record as many fluence curves as J levels populated (i.e. until we arrive to a J level that is not populated and therefore we do not detect any signal in the pyroelectric detector). Then, all the values from the asymptotes of the pyroelectric signals for all the J levels studied are added. That sum corresponds to the theoretical fraction of molecules that owe this symmetry (for example, CH_4, F symmetry = 9/16). By doing so, we have a direct calibration that brings us from the asymptote of the pyroelectric detector signal for a transition from a particular J level to the population in that J level (f_{rot}).

However, both methods above explained are quite time consuming. Alternatively, I assumed that the pyroelectric detector signal is proportional to the flux of excited molecules:

$$V = \alpha \cdot f_{exc} \cdot flux \tag{2.9}$$

where V is the pyroelectric detector signal and α is the constant that relates the pyroelectric detector signal and the excited flux of molecules. The proportionality constant α was obtained by calculating the f_{exc} using the method b) explained above and the flux of molecules for a reference (ref) state. The excited fraction for any other state is given by:

$$f_{exc} = \frac{V}{flux} \frac{flux(ref)}{V(ref)} f_{exc}(ref) \tag{2.10}$$

In this way, the calculation of f_{rot}, f_{vib}, and f_{RAP} is avoid. In order to confirm that the pyroelectric detector signal is proportional to the excited flux of molecules, the excitation fraction was calculated using the traditional (equation (2.8)) and this new method (equation (2.10)) for several transitions, nozzle temperatures and different gas mixtures. Figure 2-20 compares the excitation fraction obtained by both methods. The reference transition in equation (2.10) was taken to be the R(1) transition for a T_N RT using a pure CH_4 molecular beam. The values obtained using both methods are in reasonably good agreement. Furthermore, the agreement obtained for the 1% CH_4 in H_2 at T_N= 500 K indicates that, within the kinetic energy range studied, the pyroelectric signal responses linearly with incident energy.

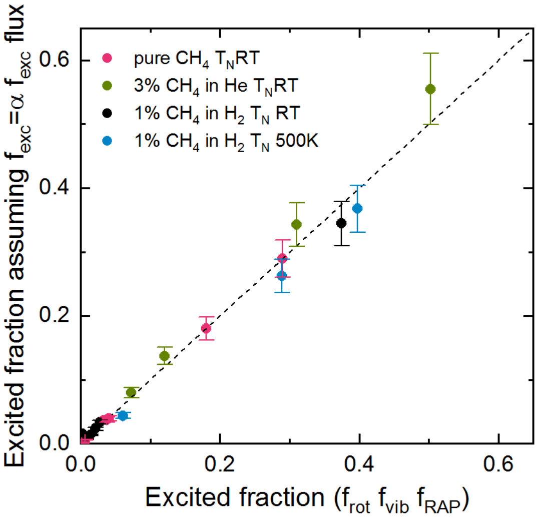

Figure 2-20. A comparison of the excited fraction determined using equation (2.8) and calculated assuming that the pyroelectric detector signal is proportional to the flux of excited molecules using equation (2.10). For each of the gas mixtures and nozzle temperatures, the excited fraction for transitions involving different initial J levels are shown.

Chapter 3 Influence of the surface atomic structure on the reactivity of methane on Pt

3.1 Introduction

The motivation behind this chapter is well summarized in the following quotation by the Nobel Laureate G. Ertl and coworkers[70]:

> "*The notion of "active sites" is fundamental to heterogeneous catalysis… …many catalytic surfaces are not uniformly active but exhibit activity only at sites distinguished by a special arrangement of the surface atoms…. However, the exact nature of the active sites and hence the mechanism by which they act are still largely a matter of speculation".*

Thus, the importance of the surface reaction site in heterogeneous catalysis has been evident for decades. However, the majority of the surface science studies have been performed on single crystals cut along high symmetry crystallographic directions, which may not be representative of the surface of real catalysts. This structural difference between the atomically smooth single crystals used in surface science and the real catalysts that expose different orientations with defects such as steps, vacancies or kinks is known as the "structure gap"[71–73]. Figure 3-1 illustrates an idealized catalytic nanoparticle that exhibits different facets and forms different sites such as corners, steps, and terraces[74].

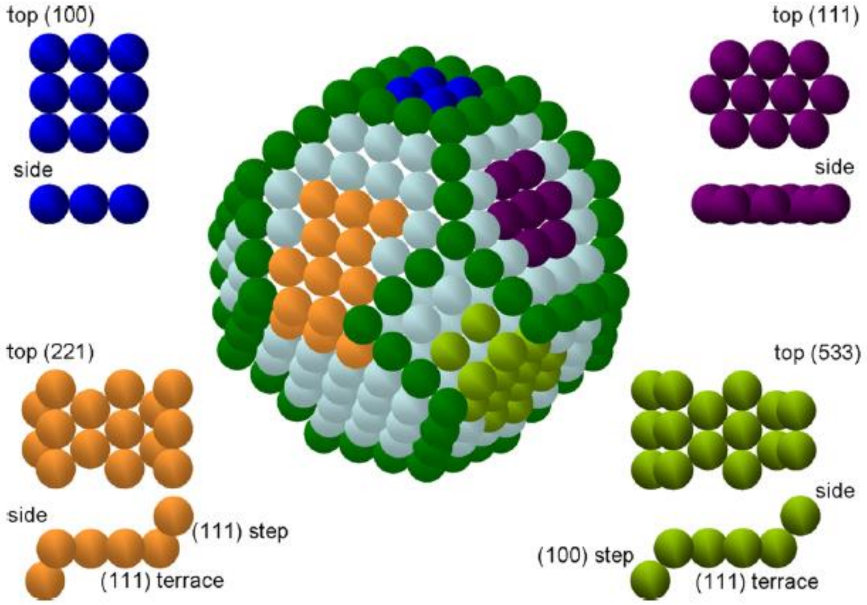

Figure 3-1. (*center*) Sketch of an idealized metallic catalytic nanoparticle. (*outer*) Top and side views of small parts of atomic arrangements on low- and high- Millex indices single crystal surfaces. Reproduced with permission from[74].

One way to start closing this structure gap is to study the role of specific sites on a catalytically active surface by performing experiments on single crystals cut along different low- and high-Miller-indices that expose different types of high and low coordinated sites for adsorption. Following this approach, several studies concerning the role of different surface sites have been perform for chemical reactions involving H_2[74–82], O_2[55,83,84], CO[85–87], NO[88–90] and N_2[91,92]. Another approach that uses curved single crystal samples exposing different step types and densities[93] has been employed to study reactions involving H_2[40,55], O_2[55], H_2O[94] and CO[95,96].

A complete review of all of these studies is beyond the scope of this thesis. However, they are mentioned here, since they constitute experimental proof of different reactivities observed for different reaction sites on a particular surface even if these experiment do not concern the dissociation of methane which is the topic of this thesis. The dissociation of methane has been widely studied on low index single crystals and very few studies concerning the dissociation of methane on "defected surfaces"⁽²⁾ can be found.

---

(2) By "defected surfaces" I refer to surfaces cut along low symmetry crystallographic directions and exposing low coordinated sites such as steps or kinks.

One of the first such studies concerning methane dissociation on a stepped surface was reported by Gee *et al.*[97] who probed methane dissociation on a Pt(533) surface which consists of a periodic array of (111) terrace and (100) step sites. Their experimentally obtained CH_4 sticking coefficients on the Pt(111) and Pt(533) are shown in Figure 3-2 as a function of incident energy. By comparing the reactivity of CH_4 on the stepped Pt(533) with that on the flat Pt(111) they observed a higher dissociation probability on the stepped surface, which they attributed to the presence of the (100) steps. However, the product detection methods that they used (King & Wells method[98] and O_2 titration) were not surface-site-specific and only measured total reactivity averaged over all surface sites present on the sample. In order to extract the reactivity of the step sites, the authors had to assume equal reactivity for the terrace sites on Pt(533) and Pt(111) which is not necessarily correct[55].

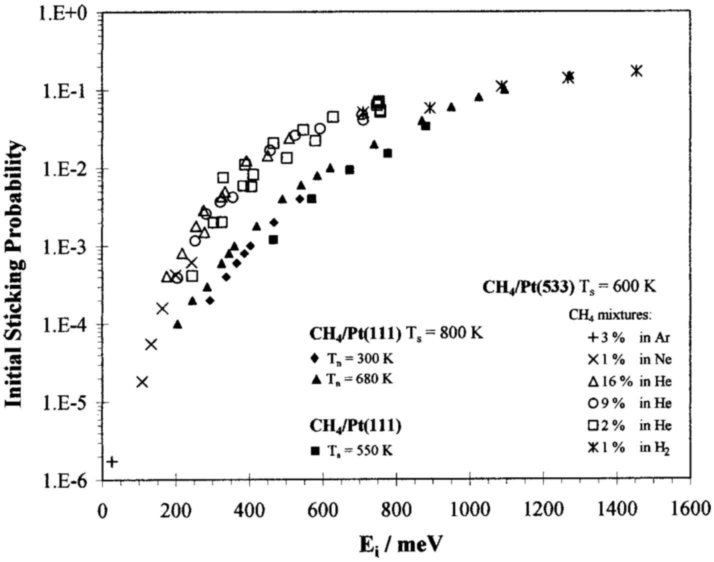

Figure 3-2. Initial sticking coefficient as a function of incident energy for CH_4 dissociation: on Pt(533) at T_S=600 K (empty symbols and crosses), and on Pt(111) at T_S=550 K and T_S=800 K (filled symbols). Reproduced with permission from[97].

Papp *et al.*[99] studied methane dissociation on the stepped surfaces Pt(355) and Pt(322) using X-ray photoelectron spectroscopy (XPS). Both surfaces consist of five atoms wide (111) terraces separated by (111) and (100) steps, respectively. Methane reactivity was measured by recording carbon XPS line profiles following methane dissociation on Pt(111), Pt(355) and Pt(322). The XPS signal was deconvoluted into a series of peaks to resolve the contribution from terrace and step sites as well as due to C-H fragments produced by the intense

X-ray radiation. Comparison of the signal ratios for the CH_3 peaks assuming identical vibrational fine structure for the terraces of the three surfaces indicated a similar reactivity for the step and the terrace sites, in contradiction with the study of Gee *et al.*[97] Figure 3-3 shows the relative initial sticking coefficients for CH_4 on the three surfaces. On the stepped surfaces, methyl was found to occupy mostly the steps of the surface with about only 10-20% of the methyl coverage being adsorbed on the terraces (inset of Figure 3-3). Assuming a similar reactivity for the terraces of the stepped surfaces and the terraces of the flat Pt(111) surface, the authors concluded that the higher coverage on the steps sites was due to a rapid diffusion to the step sites of the methyl groups initially formed on terrace sites.

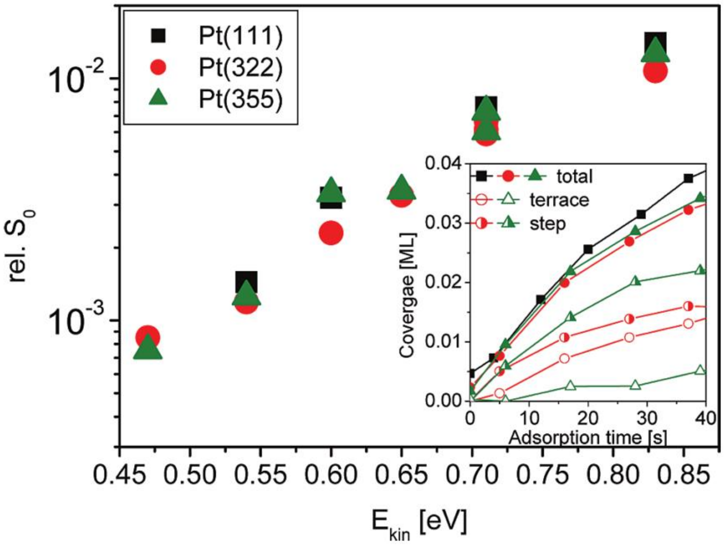

Figure 3-3. Relative initial sticking coefficient as a function of incident kinetic energy for CH_4 dissociation on Pt(355), Pt(322) and Pt(111) at T_S=125 K. The inset shows the coverage on the steps and terraces as a function of adsorption time for an incident kinetic energy of methane of 0.54 eV. Reproduced with permission from[99].

The reactivity of methane on the highly corrugated Pt(110)-(1x2) surface was also investigated before. This surface undergoes a missing row reconstruction leaving rows of ridge atoms followed by valleys in a (1x2) structure. Methane dissociation on this surface was reported to occur via two different pathways[100,101]. At low incident energies (<10 kJ/mol), a precursor mediated mechanism was observed where the molecule initially loses some normal momentum and becomes trapped in a physisorbed precursor state. The molecule then diffuses on the surface and, if it finds a reactive site, subsequent dissociation happens on that surface site. If not, the molecule desorbs. A precursor mediated reaction is typically identified by an increase in the reactivity with decreasing incident energy. At higher incident energies (>10 kJ/mol), methane was found to react via a direct activated mechanism where the molecule dissociates immediately after impinging the surface if it has enough energy to overcome the activation barrier.

A study of the incident angle dependence of the reactivity of CH_4 on Pt(110)-(1x2) was performed in our group using the AES and K&W method as detection techniques[101]. From the polar and azimuthal angle dependence of the reactivity, the authors concluded that the reactivity of CH_4 on the ridges was higher than in the valleys.

Lastly, methane activation and dehydrogenation was studied on Pt nanoparticles supported on a CeO_2 film on Cu(111)[102]. A lower activation barrier for dissociation was observed on the Pt nanoparticles which expose several low coordinated sites. More facile dehydrogenation of the surface reaction products in comparison with experiments performed on Pt(111) single crystals was found.

The discrepancy between the first two studies presented above by Gee *et al.*[97] and Papp *et al.*[99] together with the lack of further studies concerning the role of "defect sites" on the dissociation of methane motivates a systematic study of the mechanism for the dissociation of methane on differently coordinated surface sites. During my thesis, I studied the dissociative chemisorption of methane on Pt(111), Pt(211), Pt(110)-(1x2), and Pt(210) surfaces, exposing several different types of adsorption sites (terraces, steps, ridges, corners, valleys and kinks).

The results shown in this chapter are divided in two parts depending on the detection technique used:

1) First, I present a comparison of the absolute initial sticking coefficients for CHD_3 dissociation on the four surfaces measured by the K&W method. Since this technique is not surface-site-specific, the experiment measures the average reactivity over the different reaction sites. On the Pt(211), a study of the dependence of the initial reactivity on the angle of incidence of CHD_3 with respect to the macroscopic surface allows to attribute a different barrier for dissociation on the step and terrace sites of the surface.

The experimental results are compared with the calculated initial sticking coefficients obtained from ab-initio molecular dynamics calculations.

Part of this study has been published as part of our collaboration with the group of Prof. Geert Jan-Kroes who perfoms ab-initio molecular dynamics[41,103,104].

2) In the second part of this chapter, a study of the dissociation of methane on the different surfaces using RAIRS is shown. I present RAIRS as a site-specific detection technique that allows for site-specific reaction probability measurements. The role of rovibrational excitation of CH_4 on the dissociative chemisorption on the different surface sites is presented.

   The study described in this part of the chapter has been also published in collaboration with the group of Prof. Bret Jackson[105] and Prof. Fabio Busnengo[106].

3.2 CHD_3 reactivity on different facets of Pt measured by K&W detection

The initial reactivity of CHD_3 on different platinum surfaces was measured using the K&W method. Figure 3-4 shows the initial sticking coefficient for CHD_3 dissociation on Pt(111), Pt(211), Pt(110)-(1x2), and Pt(210) as a function of incident translational energy. For these experiments, mixtures of 1-2% CHD_3 in H_2 were used in order to access incident kinetic energies in the range of 50-140 kJ/mol for nozzle temperatures from 300 – 800 K. At these energies, the initial sticking coefficients exceed 1%, which is near the detection limit for the K&W method in our setup. The surface temperature was kept at T_S=650 K for Pt(211), Pt(110)-(1x2), and Pt(210) and T_S=500 K on Pt(111). At these temperatures, the initially formed methyl species quickly dehydrogenate leaving C atoms on the surface, and H and D atoms leave the surface by recombinative desorption. Sticking coefficient measurements for CH_4 dissociation on Pt(111) in the same incident kinetic energy range have shown that the reactivity does not depend on surface temperatures between 500 K and 800 K[63]. Therefore, the difference in T_S between the Pt(111) and the other three surfaces is not expected to affect nor explain the reactivity trends that we observe in Figure 3-4.

To better visualize the trends in S_0 as a function of incident E_{trans}, the S_0 data points shown in Figure 3-4 were fit using S-shaped reactivity curves:

$$S_0 = \frac{A}{2}\left[1 + erf\left(\frac{E_{trans} - E_0}{W}\right)\right] \tag{3.1}$$

Where A is the asymptote, E_0 is the average barrier height for the dissociation and W is the width of the distribution of barrier heights assumed to be Gaussian. None of these parameters was fixed in the fitting. Table 3-1 shows the A, E_0, and W values that gave the best fit to the experimental data points.

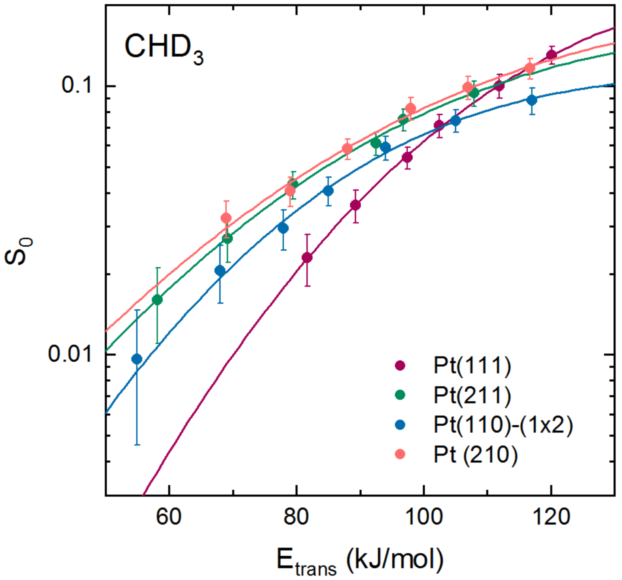

Figure 3-4. Comparison of the sticking coefficients measured using the K&W method for CHD_3 on Pt(111) (T_S 500 K, purple), Pt(211) (T_S 650 K, green), Pt(110)-(1x2) (T_S 650 K, blue) and Pt(210) (T_S 650 K, pink).

	Pt(111)	Pt(211)	Pt(110)-(1x2)	Pt(210)
A	0.25±0.03	0.17±0.05	0.11±0.08	0.17±0.04
W (kJ/mol)	36±3	49±9	39±3	54±9
E_0 (kJ/mol)	120±4	103±13	92±3	100±9

Table 3-1. Summary of the values obtained for A, W and E_0 in equation (3.1) that gave the best fit to the experimental data points.

Figure 3-4 shows a strong increase in the CHD_3 reactivity with increasing incident energy, indicating a direct dissociation mechanism on the four surfaces in this range of energies. At incident translational energies E_{trans}< 100 kJ/mol, the reactivity is highest on Pt(210) and Pt(211), followed by Pt(110)-(1x2). The flat Pt(111) surface is the least reactive one. This indicates a lower barrier for dissociation on the less coordinated atoms of the Pt(210), Pt(211) and Pt(110)-(1x2) surfaces. At higher incident kinetic energies (E_{trans}> 100 kJ/mol), the relative reactivity changes and the Pt(111) surface shows the highest sticking coefficient. A possible explanation for this observation is discussed below.

Bisson *et al.*[101] compared the reactivity for CH_4 on Pt(110)-(1x2) and Pt(111) at T_S=600 K using AES as a detection technique. Their results showed a higher sticking coefficient for the highly corrugated surface for incident translational energies up to 70 kJ/mol, in agreement with our results. Anghel *et al.*[107] calculated the energetics of the transition states of CH_4 chemisorption on Pt(110)-(1x2) and found that upon dissociation, the ridge atom was the most stable site for CH_3(ads). Using their Reaction Path Hamiltonian (RPH) model, Jackson and coworkers[45] predicted a lower barrier for dissociation on the ridge sites of Pt(110)-(1x2) by about 20 kJ/mol compared to the Pt(111) terraces.

Recently, the sticking coefficients for CHD_3 on Pt(111), Pt(211), Pt(110)-(1x2) and Pt(210) were calculated using ab-initio molecular dynamics (AIMD) by Chadwick *et al.*[41,104]. A comparison between the experimental and theoretical initial sticking values is presented in Figure 3-5. For CHD_3 dissociation on Pt(111) and Pt(211) (Figure 3-5 a) and b)), the experimental and calculated S_0 values agree within chemical accuracy (i.e. the difference between the computed probabilities and the experimental curve along the energy axis is less than 4.2 kJ/mol). On the Pt(211) surface, AIMD calculations predict the CHD_3 molecules to react predominantly at the step sites. The minimum barrier for dissociation on the steps was calculated to be 53.9 kJ/mol, in contrast with the higher value calculated for the terraces of the Pt(211) (96.4 kJ/mol) and the terraces of the Pt(111) (78.6 kJ/mol). Moreover, dissociation on the more coordinated corner sites was not observed in the AIMD calculations. The calculated barriers for dissociation on the different surface sites are presented in Table 3-2.

Surface	Site	E_b (kJ/mol)
Pt(111)	Terrace	78.6
Pt(211)	Step	53.9
	Terrace	96.4
Pt(110)-(1x2)	Ridge	65.7
	Facet	96.6
Pt(210)	Kink	39

Table 3-2. Computed lowest activation barriers E_b using the SRP32-vdW functional for different sites of the Pt(111), Pt(211), Pt(110)-(1x2) and Pt(210) surfaces.

On the Pt(110)-(1x2) surface, the main dissociation site is predicted to be the least coordinated ridge atom, with a calculated barrier of 65.7 kJ/mol, followed by the facet atom, with a barrier of 96.6 kJ/mol. On this surface, agreement between theory and experiment is good only if the calculated S_0 by AIMD include contribution from the "trapped trajectories" in the reactivity. Figure 3-5 c) shows the experimental S_0 values as well as the calculated S_0 including (empty circles) and excluding (empty stars) reactivity from the trapped trajectories. In the calculations, the trajectories were propagated for a maximum time of 1 ps and considered as reactive if the dissociating bond exceeded 3 Å. If the height of the CHD_3 molecule above the (110)-(1x2) plane was larger than 6.5 Å with the center of mass velocity pointing away from the surface, the trajectory was considered to be non-reactive (scattered). If none of these possibilities were observed, the molecule was assumed to be trapped on the surface. The calculated S_0 points shown by empty circles in Figure 3-5 c) assume that all the CHD_3 molecules "trapped" on the surface end up dissociating, while the S_0 points represented by empty stars do not consider any contribution from these trajectories.

As shown in Figure 3-5 c), the contribution from the "trapped trajectories" brings the experimental and calculated reactivities into better agreement, especially at the lowest incident energies. For the two highest incident energies, where the calculated trapping probability is lower, the experimental and calculated S_0 excluding contribution from trapped trajectories values are in good agreement.

Such trapping mediated dissociation has been observed previously on Pt(110)-(1x2) at much lower incident energies (E_i<10 kJ/mol) for two surface temperatures (400 K[100,101] and 600 K[101]). In both cases, the sticking coefficient was seen to increase with decreasing incident energy. This trapping mediated mechanism has been attributed to energy transfer from translational motion normal to the surface to motion along the surface[108].

Performing AIMD calculations, Migliorini *et al.*[108] showed that energy transfer to parallel motion is more efficient on a corrugated surface than on a flat surface. On Pt(211), the authors showed that CHD_3 molecules hitting the step and not dissociating on direct impact, can undergo energy transfer to parallel motion and start travelling in the direction perpendicular to the step edge. In this way, the CHD_3 molecules can explore the surface, and if they find a reactive site or favorable orientation, they can go on to dissociate. Initially the authors propagated the trajectories for 1 ps as Chadwick *et al.*[104] did on Pt(110)-(1x2). However, when they extended the trajectories for 2 ps, Migliorini *et al*. observed that half of the trapped molecules desorb from the surface and no trapped molecules had reacted within the extra 1 ps that they extended their calculations. Therefore, a large portion of the trapped trajectories observed by Chadwick *et al.* on Pt(110)-(1x2) will most likely desorb from the surface, and the S_0 represented as empty circles in Figure 3-5 are just an upper limit of the calculated S_0 for CHD_3 on Pt(110)-(1x2).

On the Pt(210) surface (Figure 3-5 d)), the agreement between the theory and the experiment is poor. Theory predicts a higher reactivity due to the kink atoms, where the barrier for dissociation is calculated to be 39 kJ/mol. However, the experimental sticking coefficients for Pt(210) and Pt(211) fall within the experimental error. This experimental observation indicates that either the reactivity on the kinks of Pt(210) and on the steps of Pt(211) is similar, or that the “middle” atoms on the Pt(210) surface have a much higher barrier for dissociation than the terraces of Pt(211).

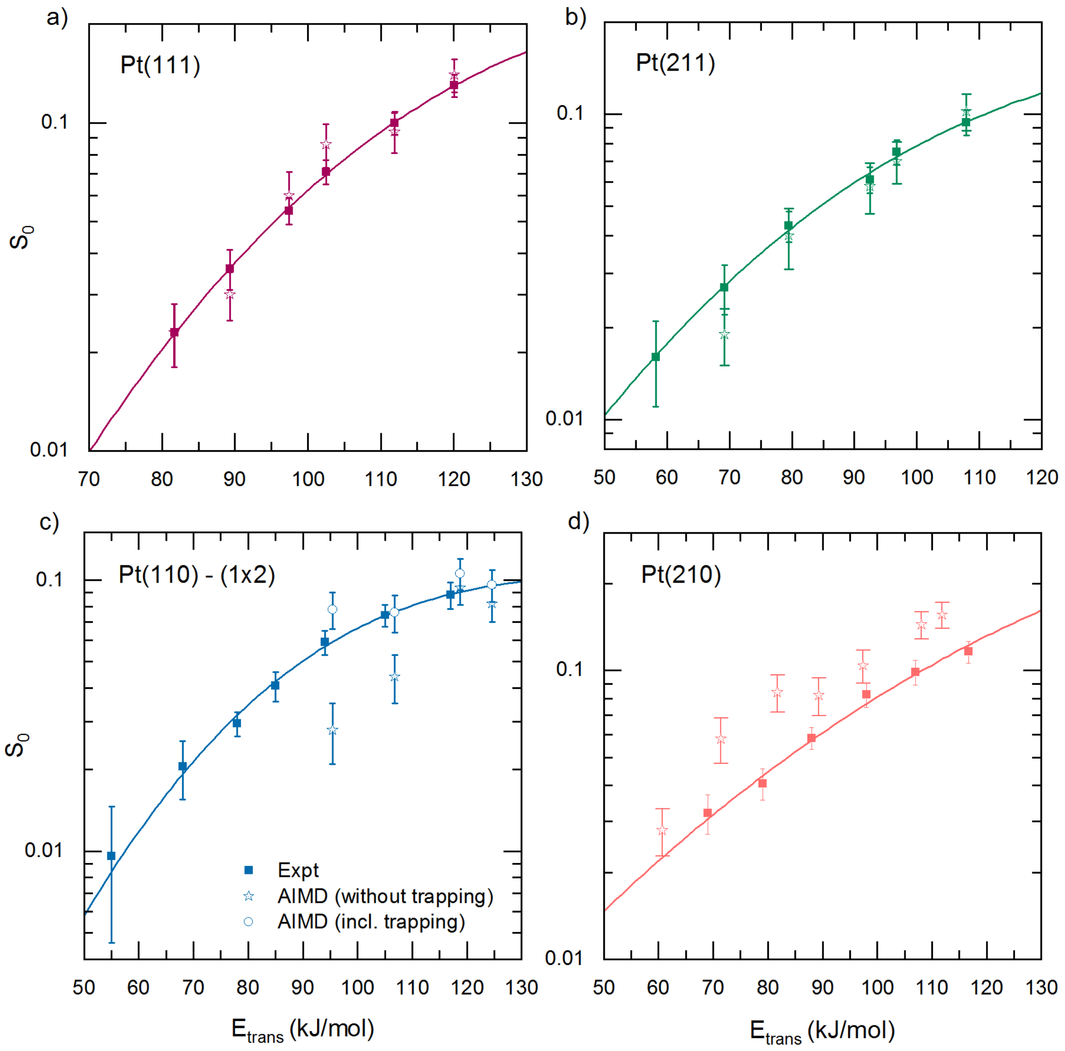

Figure 3-5. Comparison of the sticking coefficients from K&W experiments (filled symbols) and from AIMD calculations (empty symbols) for CHD_3 dissociation on a) Pt(111), b) Pt(211), c) Pt(110)-(1x2) and d) Pt(210) On the Pt(110)-(1x2) surface AIMD S_0 including (empty circles) and excluding (star symbols) reactivity from "trapped trajectories" is presented.

By comparing the calculated barriers for dissociation on the different surface sites (Table 3-2) and the density of each type of site on the surface, we can explain the trends observed in Figure 3-4 (except for Pt(210) where theory and experiment do not agree). At incident translational energies lower than 100 kJ/mol, CHD_3 dissociates most readily on the steps of the Pt(211) surface which have a lower dissociation barrier than the terrace atoms. The barrier for dissociation on the ridge atoms of the Pt(110)-(1x2) surface is calculated to be 11.8 kJ/mol higher than for the steps on Pt(211), explaining why the Pt(110)-

(1x2) surface is less reactive than the Pt(211). Furthermore, the number of ridge atoms on the Pt(110)-(1x2) is lower than the step atoms on the Pt(211), supporting the lower S_0 of Pt(110)-(1x2) in comparison with Pt(211). The Pt(111) surface is the least reactive surface, since its terrace atoms show a higher barrier for dissociation than both the ridge and step atoms on the Pt(110)-(1x2) and Pt(211) surfaces, respectively.

At higher incident energies than 100 kJ/mol, dissociation starts to occur on the higher barrier sites of the Pt(110)-(1x2) and Pt(211) surfaces. The lowest activation barrier for CHD_3 dissociation on the terraces of the Pt(211) surface is calculated to be 96.4 kJ/mol, and 96.6 kJ/mol on the facets of the Pt(110)-(1x2) surface.

No dissociation is predicted by DFT on the valley and corner sites since those sites are associated with a large barrier for dissociation[41,104,109]. For example, Jackson *et al.* predicted a barrier for CH_4 dissociation of 183 kJ/mol on the corners of the Pt(211) surface[105]. Therefore, molecules incident on these high barrier sites will scatter rather than dissociate, thus limiting the average reactivity of the whole surface since it reduces its “active area”. However, on Pt(111) all surface atoms are identical, with a minimum barrier for dissociation of 78.6 kJ/mol over the top site of a surface atom. Its higher density of “reactive atoms” (terraces) explains the higher reactivity of this surface at the highest incident energies presented in Figure 3-4.

3.2.1. Angle dependence of the S_0 of CHD_3 on Pt(211)

On the flat Pt(111)[110], Ni(111)[111], and Pd(111)[112] surfaces, the CH_4 sticking coefficient was observed to scale with the translational energy normal to the macroscopic surface ($E_i cos^2\theta_i$). However, deviations from such “normal energy scaling” were observed for the dissociation of methane on Pt(110)-(1x2)[101,113]. In their study, Bisson *et al.*[101] explored the role of both the polar and the azimuthal incident angle on the dissociation probability of CH_4. They observed that when methane was incident parallel to the ridges of the Pt(110)-(1x2) surface, mostly the normal incident energy contributed to the reactivity (normal incident scaling). However, when the methane velocity was directed perpendicular to the ridges of the surface, the reactivity decreased less quickly with increasing polar angle θ than predicted by normal energy scaling. The authors attributed this observation to a higher reactivity of the ridges compared with the facet atoms. With increasing θ, the incident methane collides preferentially with the ridge sites where the activation barrier is the lowest, being the facet and valley atoms shadowed by the ridges.

The angular distribution of the sticking probability of CH_4 was measured on Pt(533) by Gee *et al.*[97] In their study, the authors found that the sticking coefficient does not follow normal energy scaling. Instead, S_0 decreases more slowly as the incident CH_4 is directed toward the (100) steps in contrast with incidence toward the (111) terraces of the surface. By assuming the same reactivity on the terrace atoms of the Pt(533) and the Pt(111), Gee *et al.* deconvoluted the contribution to the S_0 from the steps and from the terraces. A significantly broader angular dependence of the S_0 associated with the (100) steps than the (111) terraces was observed, which was attributed to the fact that the step atoms are more exposed than the terraces.

During my thesis, I measured the reactivity of CHD_3 on Pt(211) as a function of the polar (θ) angle of incidence. Figure 3-6 shows the Pt(211) surface illustrating the azimuthal and polar angles of incidence. The azimuthal angle was kept Φ=0. Thus, varying the polar angle of incidence (θ) corresponds to the molecule being directed toward the (111) terraces ($\theta_i<0$) or toward the (100) steps ($\theta_i>0$)

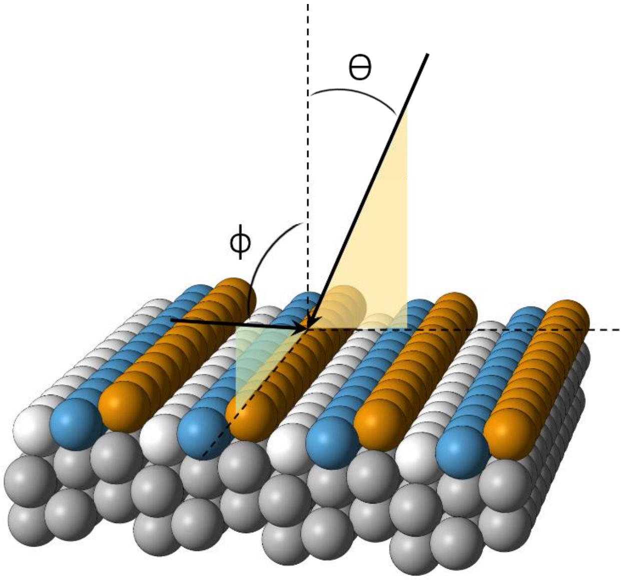

Figure 3-6. Schematic illustration of the Pt(211) surface indicating the polar (Θ) and azimuthal (ϕ) angle. For the experiments presented here, only the polar angle of incidence was modified, keeping ϕ=0 so the plane of incidence is perpendicular to the step rows.

For all measurements, the surface temperature was T_S=650 K and the incident kinetic translational energy was fixed at 96.8 kJ/mol. The initial sticking coefficients as a function of polar angle θ are presented in Figure 3-7. The dashed line shows a $cos^2\theta_i$ distribution and the arrows indicate the angles of incidence for which methane is directed normal to the (111) (θ=-19.5°) and the (100) (θ=35.3°) microfacets.

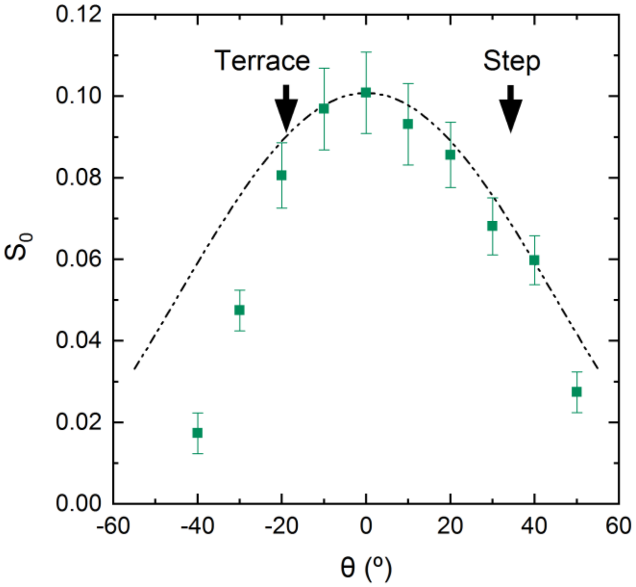

Figure 3-7. Sticking coefficients as a function of polar angle of incidence measured using K&W for CHD_3 dissociation on Pt(211) at incident translational energy of 96.8 kJ/mol and T_S 650 K.

S_0 drops more quickly when the polar angle of incidence is changed toward the direction normal to the terraces of the surface (θ_i<0). A similar angle dependence was observed for the dissociation of CH_4 on Pt(533)[97]. The fact that the step atoms are more exposed makes them more accessible at different polar angles of incidence, thereby increasing their cross section seen by the molecular beam. Therefore, one might expect a slower variation of the initial sticking coefficient for the steps with incident angle. Moreover, a shadowing of the terraces by the steps may contribute for positive angles of incidence similar to what was observed for Pt(110)-(1x2)[101].

The experimental results shown in Figure 3-7 were compared with theoretical predictions by AIMD[103]. In order to disentangle the contributions leading to the trend observed in Figure 3-7 (different cross section, shadowing effects and/or different reactivities of terraces and steps), for each surface site, the number of incident trajectories was compared with the number of dissociative trajectories resulting in calculated site-specific dissociation probabilities. Figure 3-8 a) shows the fraction of trajectories that impact closest to the step (red), terrace (blue) and corner (green) atoms as a function of the polar angle of incidence. Very few molecules collide near the hidden (shadowed) corner atoms. In contrast, the more exposed step atoms are accessible at all the incident angles, dominating at $\theta_i>0$ at which they slightly shadow the terrace sites.

Figure 3-8 b) shows the fraction of trajectories leading to dissociation on the step and terrace atoms at the different polar angles of incidence. No "reactive trajectories" were observed closest to the corner surface atoms and thus their contribution is not shown in Figure 3-8 b). At all angles of incidence, the dissociation is dominated by the step atoms. Only at about θ_i=-40°, the steps and terraces show the same reactivity within the error bars.

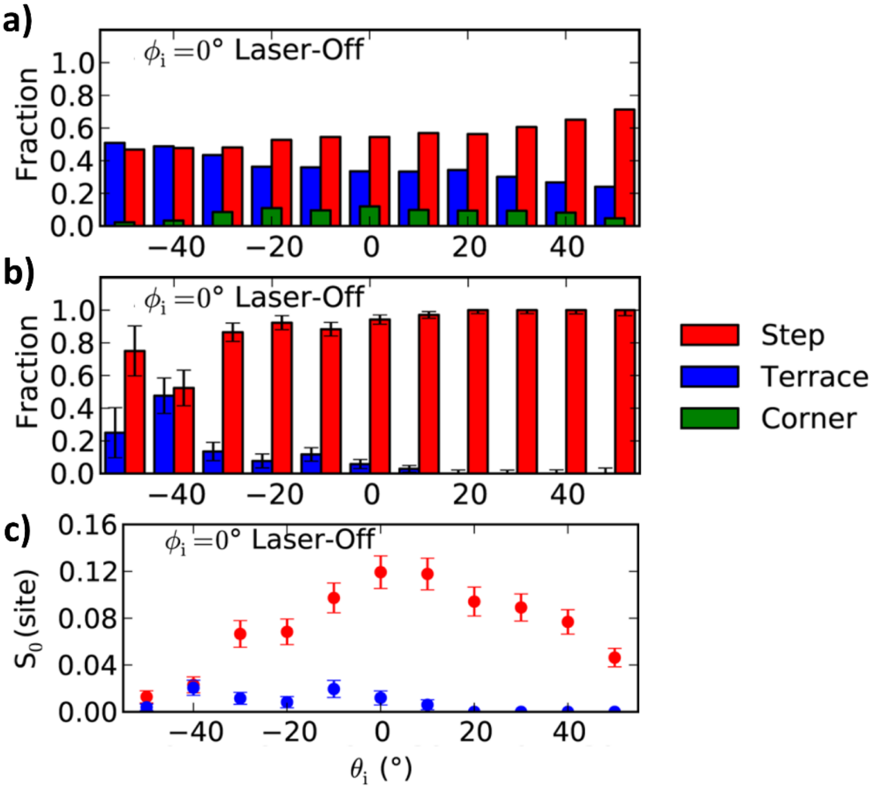

Figure 3-8. a) Fraction of CHD_3 molecules that impact closest to the step (red), terrace (blue) and corner (green) sites of the Pt(211) surface; b) Fraction of molecules that lead to dissociation of CHD_3 on the step and terrace sites; c) Calculated site-specific sticking coefficient for CHD_3 on the step and terrace sites. Reproduced from [103].

By dividing the number of trajectories leading to dissociation on each site by the number of trajectories impinging on these particular sites, the site-specific sticking coefficients were calculated. Thus, these calculated site-specific sticking coefficients account for any differences in active cross section seen by the incident molecules or shadowing effects. Figure 3-8 c) displays these site-specific reactivities on the terrace and step atoms as a function of polar angle of incidence. As it is shown, the steps are predicted to dominate the reactivity for all angles of incidence, except at θ_i=-40°. However, the reactivity at this angle of incidence is too low to have good statistics. In addition, an asymmetry is observed for the S_0 (step), with the sticking coefficient decreasing less quickly at positive angles of incidence. This asymmetry in the S_0(step) was attributed to different activation barriers at different locations around the step atom. Taken together, these theoretical observations predict that the experimental S_0 presented in Figure 3-7 are mostly contribution from dissociation on the step sites, and that a small shadowing effect happens and favors dissociation on the step sites although it does not explain the asymmetry observed in S_0, which is attributed to different activation barriers around the step atom.

3.3 Site-specific detection of CH_4 dissociation using RAIRS

So far, I have presented a comparison of the methane reactivity on different platinum surfaces measured using the K&W method. However, K&W does not allow for site-specific detection of the adsorbates on the surface. Therefore, it only allows for a comparison of the average reactivity on the different surfaces.

In this sub-chapter, I will introduce RAIRS as a site-specific detection technique for methane dissociation on platinum surfaces and I will show how it can be used to measure the site-specific sticking probabilities of methane on the different sites of Pt(211) and Pt(110)-(1x2) surfaces.

3.3.1. RAIR spectra: site-specific detection of chemisorbed methyl on Pt surfaces

Figure 3-10 presents RAIR spectra following molecular beam deposition of CH_4 on Pt(111), Pt(211), and Pt(110)-(1x2). The incident translational energy of the methane molecules was 65 kJ/mol on Pt(111) and Pt(211) and 62 kJ/mol on Pt(110)-(1x2) and the surface temperature was 120 K in all three experiments.

On the Pt(111) surface at low surface temperature, CH_4 is known to dissociative directly on impact by cleaving a single C-H bond resulting in chemisorbed CH_3(ads) and H(ads)[29,51,114]. DFT calculations predict that the dissociation takes place over a top site on Pt(111) with the CH_3(ads) bound on the top site and H(ads) in a hollow site. Figure 3-9 show the calculated transition state and product state configuration for CH_4 dissociation on Pt(111).

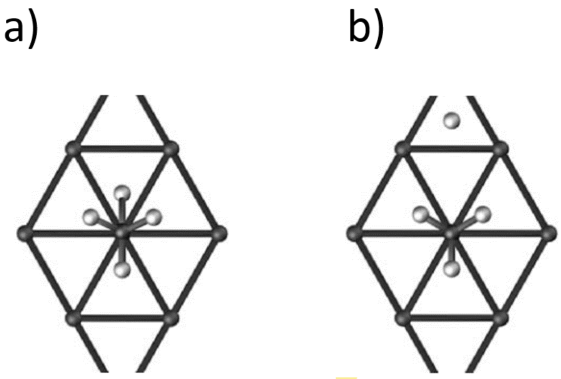

Figure 3-9. Configurations for the transition state (a)) and product state of minimum energy (b)) for dissociation of CH_4 on Pt(111). Reproduced with permission from[45].

Temperature programmed reaction measurements showed that the CH_3(ads) is stable up to T_s=200 K[115] on the terrace sites of Pt(111). For T_S>200 K dehydrogenation leads to CH(ads) on the hollow sites[116]. Figure 3-10 a) shows the RAIR spectrum for the symmetric C-H stretch vibration of CH_3(ads) on Pt(111) with a single peak at 2881 cm^{-1}.

Dissociation of methane on the stepped Pt(211) surface yields a RAIR spectrum with two peaks in the C-H stretch region at 2886 cm^{-1} and at 2903 cm^{-1}. Comparison with the spectrum shown in Figure 3-10 a) taken for deposition on Pt(111) leads us to assign the 2886 cm^{-1} to CH_3(ads) on the terrace site and the 2903 cm^{-1} peak to CH_3(ads) on the step site. The absence of a third peak that could be assigned to CH_3(ads) on the corner sites is consistent with a much higher barrier for dissociation on these sites, calculated by DFT as 183 kJ/mol[109]. A confirmation of the assignment of CH_3(ads) on the step and terrace sites is presented below. Also, the observed vibrational frequencies are given with their assignments in Table 3-3.

Figure 3-10 b) also shows a peak at 2979 cm^{-1} which we assign to the antisymmetric C-H stretch of CH_3(ads) on the steps sites. On the terrace sites, this vibration is not observed due to the surface selection rule for RAIRS which states that only adsorbate vibrations with a transition dipole component along the surface normal can be detected[117]. For CH_3(ads) on a terrace site, with a local symmetry of C_{3v}[118], there is no dipole moment component along the surface normal for the antisymmetric C-H stretch mode. However, for CH_3(ads) on the step sites, a small tilt angle of the methyl group's C_{3v} axis away from the microscopic surface normal could lead to a small dipole component along the surface normal.

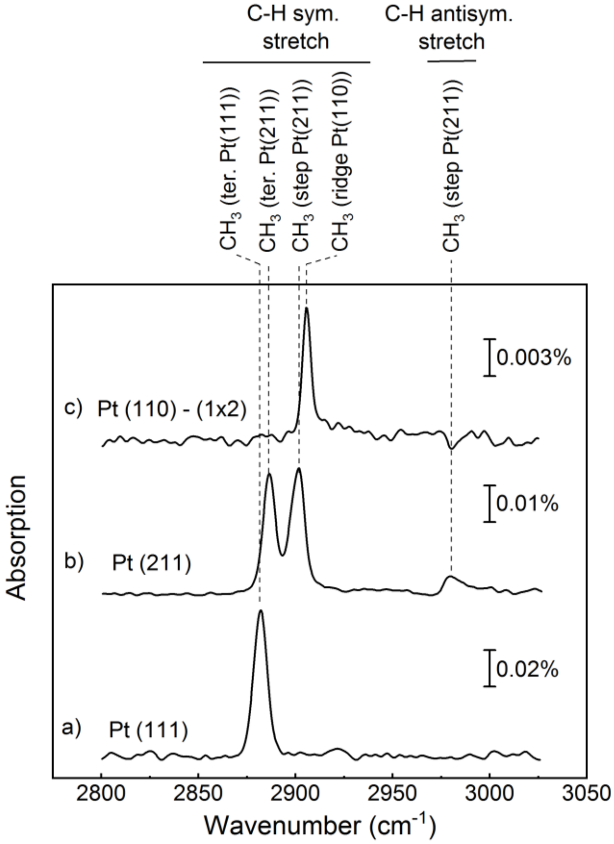

Figure 3-10. RAIRS detection of CH_3 adsorbed on a) Pt(111), b) Pt(211) and c) Pt(110)-(1x2) at T_S=120 K. CH_3(ads) was generated by dissociative chemisorption of CH_4 with incident translational energies in the range of 62-65 kJ/mol.

A RAIR spectrum for the dissociation of methane on the highly corrugated Pt(110)-(1x2) surface is displayed Figure 3-10 c). A single RAIRS peak is detected at 2905 cm^{-1} which is assigned to the symmetric stretch vibration of

CH_3(ads) on the ridge atoms of the Pt(110)-(1x2) surface since we expect the ridge atoms to be the most reactive ones on this surface[101]. The assignment to CH_3(ads) on the ridge atoms of Pt(110)-(1x2) is consistent with the assignment of the 2903 cm^{-1} peak to CH_3(ads) on the step atoms of Pt(211), since the two sites have the same coordination number of 7. Previous studies for CO adsorption have shown that the singleton frequency of CO(ads) on Pt is a linear function of the coordination number of the substrate atom where the CO molecule is adsorbed[119].

Surface	Site	Frequency (cm^{-1})	Mode assignment
Pt(111)	Terraces	2881	Symmetric C-H stretch
Pt(211)	Terraces	2886	Symmetric C-H stretch
	Steps	2903	Symmetric C-H stretch
		2979	Antisymmetric C-H stretch
Pt(110)-(1x2)	Ridges	2905	Symmetric C-H stretch

Table 3-3. Assignments of RAIRS peaks observed for nascent methyl products of CH_4 dissociation on Pt(111), Pt(211), and Pt(110)-(1x2) at T_S=150 K. Peak frequencies are taken from spectra in Figure 3-10.

A confirmation of the peak assignments for CH_3(ads) on the step and terrace sites was obtained by passivating the step sites with CO(ads). CO adsorption on platinum surfaces has been extensively studied using RAIRS and its vibrational frequencies on different surface sites are well-known[85,95,120,121]. Figure 3-11 shows a series of spectra taken during deposition of CO at different exposures. Both, the region of the spectra associated with bridging CO and CO adsorbed on the top sites of steps and terraces are shown.

At low coverages, a single peak appears at 2064 cm^{-1}, corresponding to CO adsorbed on top of a step atom (“atop-CO”). With increasing coverage, this peak shifts to higher frequencies and it reaches a maximum frequency of about 2078 cm^{-1}. Simultaneously, other peaks appear in the spectrum: the atop-CO bonded to the terrace site, which at first appears as a shoulder of the step peak, at 2091 cm^{-1}, and two other peaks associated to bridge-CO bonded to steps and terraces (at 1883 and 1894 cm^{-1}). With further increasing the coverage, the peak assigned to atop-CO on the terrace grows, while the peak associated with atop-CO on the step decreases in height and becomes wider. The assignment of these four peaks is in good agreement with previous studies[85].

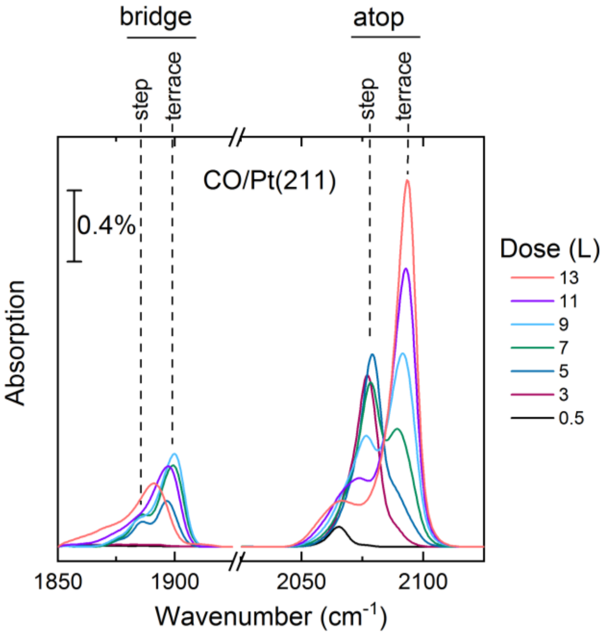

Figure 3-11. RAIR spectra following adsorption of CO on Pt(211) at T$_S$=150 K at different doses (in Langmuir).

For both, atop- and bridge-CO configurations, the step peak appears red-shifted with respect to the terrace peak. This frequency order has been explained before based on the different electronic properties that the terraces and the steps present[122,123]. Due to a different electron charge distribution in the vicinity of the atomic steps of the surface, the steps are positively charged with respect to the terraces. Therefore, there is a rather strong localized electric field parallel to the surface which yields to a lateral surface Stark effect acting on molecules adsorbed near these defects. In the case of CO, this Stark effect gives rise to a split in the $2\pi^*$ molecular orbitals that are degenerate, turning into a filling of this orbital by charge electron transfer from the metal valence band ("backdonation mechanism"). Since the $2\pi^*$ molecular orbitals have an antibonding nature, a large filling of these orbitals upon chemisorption weakens the C-O bond, yielding a lower frequency on the steps than on the terraces.

Spectra following annealing of the Pt(211) surface previously dosed with CO at 150 K is presented in Figure 3-12. Spectra were obtained after heating the surface to the specified temperatures and cooled down to 150 K to measure a spectrum. Up to T$_S$=180 K, the peak assigned to atop-CO bonded to the terrace increases its intensity and shifts to lower frequencies. This effect has been observed before[85] and attributed to ordering of the CO molecules bonded to the terraces. After heating to 250-300 K, only the peaks assigned to atop- and bridge-CO adsorbed on the steps are observed due to the desorption of the more weakly bound CO on the terraces.

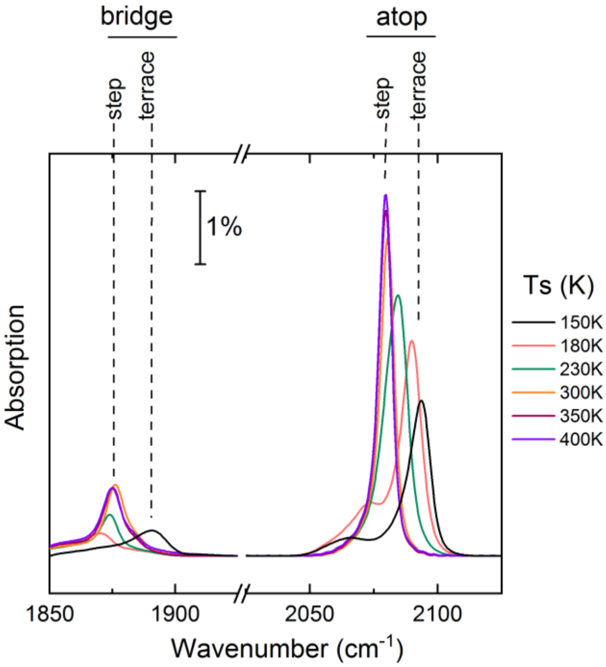

Figure 3-12. RAIR spectra following annealing to different surface temperatures after saturation of the Pt(211) surface with CO at T_S=150 K.

By heating the surface to T_S=400 K after CO saturation, I managed to prepare the Pt(211) surface with the more reactive steps being passivated with CO yet leaving the terraces clean. After this preparation, the surface was exposed to a molecular beam of 3% CH_4 in He at E_{trans}=65 kJ/mol. Figure 3-13 shows the spectrum obtained after 45 min deposition of the molecular beam of methane. For comparison, a spectrum obtained after a deposition under the same molecular beam conditions but on a clean Pt(211) surface is displayed. The selective detection of the peak previously assigned to CH_3 adsorbed on the terrace sites confirms the frequency assignment for CH_3 on step and terrace sites.

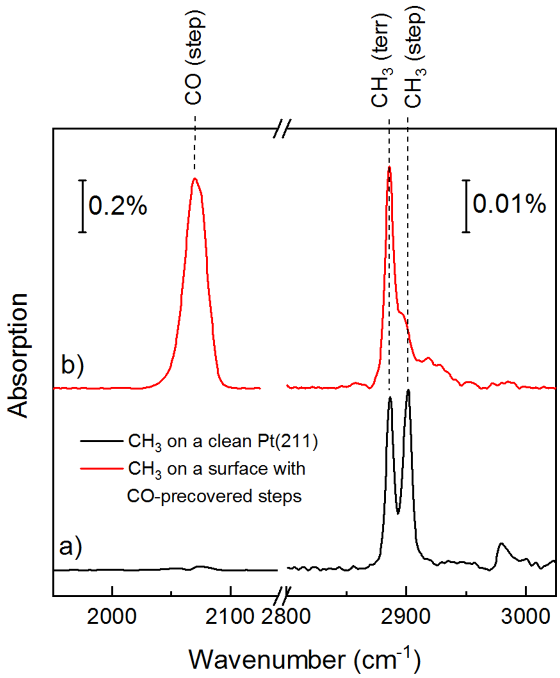

Figure 3-13. RAIR spectra following 45 min deposition of a 3% CH_4 in He molecular beam at E_{trans}=65 kJ/mol at T_S=150 K: a) on the Pt(211) whose steps were previously passivated with CO, b) on a clean Pt(211) surface.

As it is presented in Table 3-3, the symmetric C-H stretch of CH_3(ads) on the steps is blue-shifted by 17 cm^{-1} with respect to CH_3(ads) on the terraces. In the case of CO, as it is mentioned above, the order in the frequencies for CO adsorbed on the steps and on the terraces is the opposite to that observed for CH_3. Naively, one could expect the same order for CH_3: if the carbon atom is more strongly adsorbed to the step Pt atom that to the terrace Pt atom, the C-H vibration would be expected to be weaker, yielding a lower C-H stretch frequency for CH_3(ads) on the steps than on the terraces.

The groups of Prof. Fabio Busnengo, Prof. Bret Jackson and Prof. Geert-Jan Kroes have used DFT calculations to predict the vibrational frequencies for CH_3(ads) on steps and terraces. DFT predicts a lower vibrational frequency for the symmetric C-H stretch mode of CH_3(ads) adsorbed on the steps than for adsorption on the terrace sites, opposite to what we observe in our experiment. Moreover, Busnengo and coworkers predict CH_3(ads) on the steps and ridges of Pt(211) and Pt(110)-(1x2) to be less stable than CH_3(ads) on the terrace sites with calculated dissociation barriers of 22 kJ/mol and 80 kJ/mol for CH_3(ads) on step and terrace sites, respectively. Based on these results, Busnengo *et al.* suggest that CH_2(ads) is the stable dissociation product of methane on the steps and ridges at surface temperatures of T_S=120-150 K. The instability of CH_3(ads) could be due to rapid diffusion of the adsorbed methyl species along the steps and ridges, allowing CH_3 to reach bridge sites, where they could dehydrogenate into CH_2(ads) with an activation barrier of 16 kJ/mol. This leads Busnengo *et al.* to suggest that the stable products of methane dissocation on Pt(211) are CH_3 adsorbed on the top-terrace sites and CH_2 adsorbed on the bridge-step sites. DFT predicts a higher symmetric C-H stretch frequency for CH_2(ads) on the steps than for CH_3(ads) on the terrace sites as long as there are two H atoms adjacent to the CH_2(ads) on the steps. While this seems like an interesting example of self-organization of molecular species on a stepped single crystal surface, there are still some inconsistencies between this hypothesis and our experimental results. Further theoretical and experimental investigation are needed in order to arrive at a definite answer why the observed RAIRS frequencies are not reproduced by DFT calculations.

3.3.2. Coverage dependence of the RAIRS spectra and uptake curves

Since RAIRS does not interfere with the chemisorption reaction, it can be used to monitor uptake curves for the methane dissociation products during the molecular beam deposition. Figure 3-14 a) shows the evolution of the RAIR spectra with increasing incident dose for a 3% CH_4 in He molecular beam at 62 kJ/mol incident energy on the Pt(211) surface. Each spectrum is an average of 1024 scans with 4 cm^{-1} resolution which takes about 2.5 min to record.

Figure 3-14 b) shows the integrated peak area for the CH_3 adsorbed on the step and terrace sites of Pt(211) as a function of incident dose of CH_4. From both Figure 3-14 a) and b) we note a faster adsorption of methane on the steps than on the terraces, indicating a higher reactivity on the lower coordinated step sites. This is consistent with calculated barrier heights for dissociation of CH_4 on steps and terraces of Pt(211) and thereby provides further confirmation of our assignment of CH_3(ads) vibrational frequencies on step and terraces sites.

The incident dose of CH_4 on the Pt surface was calculated as the product of the flux (equation (2.2)) and the exposure time. In order to express the dose in monolayers (ML), the surface atom density of the different surfaces was taken into account (1.5 10^{15} Pt atoms/cm^2 on Pt(111), 1.59 10^{15} Pt atoms/cm^2 on Pt(211) and 1.84 10^{15} Pt atoms/cm^2 on Pt(110)-(1x2)).

The data points in the uptake shown in Figure 3-14 b) were fit using a modified Langmuir fitting model[124]. This model assumes that there is no interaction between the incident molecules and the surface adsorbates. Therefore, the probability that a molecule dissociately adsorbs on the surface is proportional to the initial reaction probability (S_0) multiplied by the number of available or "free" sites on the surface:

$$\frac{d\theta}{d\varepsilon} = S_0(1 - n_s\theta)^{\xi} \tag{3.2}$$

where θ is the coverage, ε is the dose, n_s is the number of sites blocked by each adsorbate on the surface, and ξ is the number of free sites that the new methane molecule needs to dissociate. The initial sticking coefficient corresponds to the initial slope of the uptake curve.

Previously, ξ was considered equal to 2, since two surface sites are needed for the dissociation of each methane molecule into adsorbed methyl and hydrogen fragments. However, we found that $\xi = 2$ does not provide the best fitting for the measured RAIRS uptake curves.

On the Pt(211), the fits on each site were done independently, assuming that the CH_3(ads) uptake on the steps was not influenced by the CH_3(ads) on the terraces and vice versa. On both step and terrace sites of Pt(211), as well as on the ridges of Pt(110)-(1x2), the best fit was obtained for $\xi = 1$. The first explanation that comes to mind is that it may be that the H(ads) does not adsorb on any of those sites and therefore only one site is needed for the CH_3(ads) to dissociate. However, DFT calculations predict the most stable site for H(ads) on Pt(211) to be the bridge site between two step atoms. Hence, either the CH_3(ads) on the step "kicks" the H(ads) out of the step during the reaction, or the higher reactivity on the steps allows for having a step atom bonded to a H atom and a CH_3(ads).

On the Pt(111), the best fit was achieved when using $\xi = \mathrm{n_s}$ (i.e. the number of sites blocked by each adsorbate on the surface is the same as the number of free sites that the new methane molecule needs to dissociate). By having n_s as the power, we account for the fact that whilst there may be two free adjacent sites on the surface, the molecule may not adsorb. The molecule may need more free sites on the surface due to, for example lateral repulsions between CH_3 adsorbates. The number of free sites that the incident molecule needs to dissociate can also change with incident translational energy, leading to an increase in saturation coverage with increasing translational energy[125].

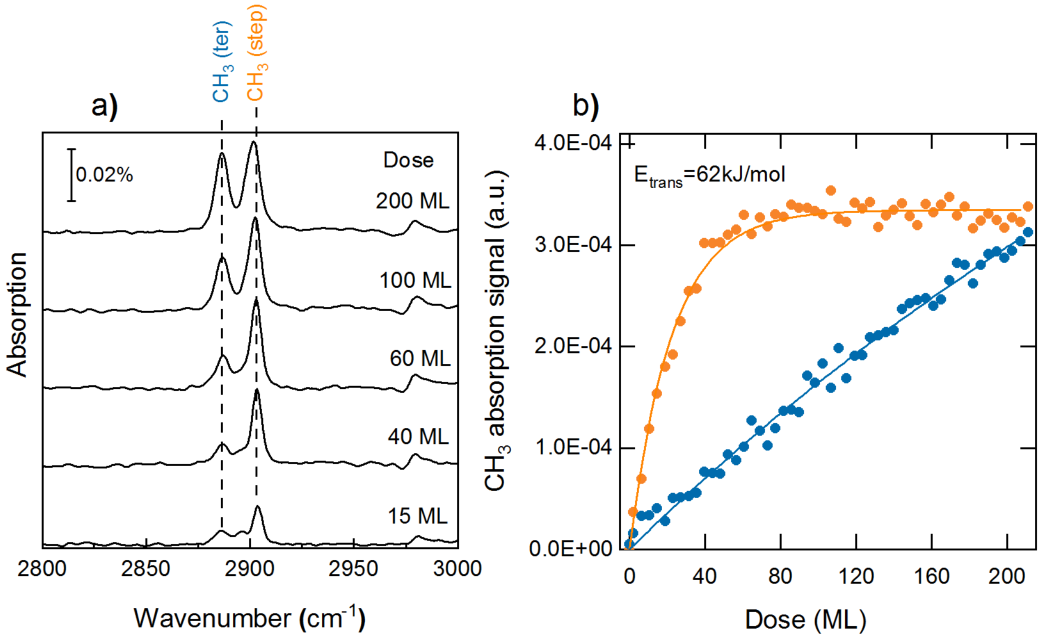

Figure 3-14. a) RAIR spectra taken during exposure of the Pt(211) surface at different incident doses of CH_4 at E_{trans}=65 kJ/mol and T_S=120 K. b) Uptake curves for CH_3(ads) on the steps (orange) and on the terraces (blue). The solid lines are fits to the data obtained using eq. (3.2) with $\xi = 1$.

In order to test if CH_3(ads) diffusion occurs at T_S=120 K on Pt(211) as proposed by Papp *et al.* for Pt(533) and Pt(322)[99], Pt(211) was exposed to a molecular beam with incident translational energy E_{trans} = 56 kJ/mol. At this incident energy, CH_3(ads) uptake is detected only on the steps, confirming the lower barrier for methane dissociation on these sites. After 15 minutes deposition at E_{trans} = 56 kJ/mol and with the steps now saturated with CH_3(ads), the molecular beam deposition was stopped for 2 minutes. If dissociation would also occur on the terraces at E_{trans} = 56 kJ/mol but rapid diffusion causes the CH_3(ads) to move to the step sites as proposed by Papp *et al.*[99], we would expect to detect an increase in terrace peak height once the steps are saturated. This was not observed. As shown in Figure 3-15, the terrace peak only starts to grow after the incident energy is raised to E_{trans} = 65 kJ/mol. Therefore, this experiment excludes the possibility for diffusion at T_S=120 K which is consistent with a calculated barrier of 64 kJ/mol[105] by DFT for methyl diffusion from the terraces to the steps.

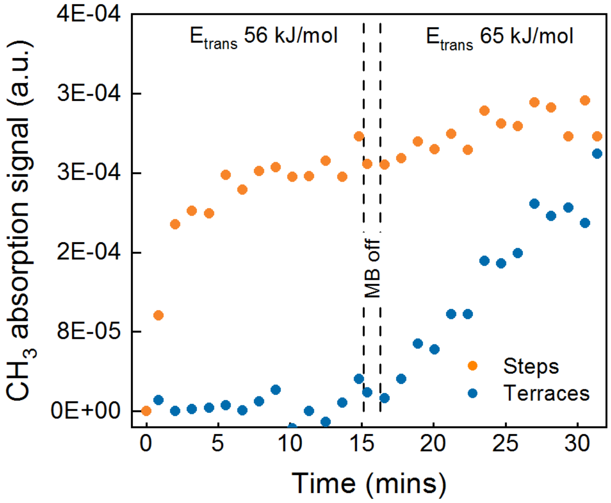

Figure 3-15. RAIRS uptake curve for methane dissociation on the terraces (blue) and steps (orange) at T_S=120 K. During the first 15 min, the incident CH_4 had an incident energy E_{trans}=56 kJ/mol and CH_3 is detected only on the steps. The molecular beam was then stopped and the incident energy was increased to E_{trans}=65 kJ/mol. At this incident energy, CH_3 is observed also on the terraces.

3.3.3. Calibration of RAIRS intensities

An important aspect of RAIRS is that the measured absorption peak intensity depends on the transition dipole moment of the detected vibration at the surface. The surface dipole selection rules states that the absorption is proportional to the component of the transition dipole moment normal to the surface. For this reason, a determination of the coverage of a particular species on the surface requires a calibration between the adsorbate coverage and the RAIR absorption signal for the vibrational mode of interest. In this chapter, I focus on the dissociative chemisorption of methane on different sites of platinum surfaces. Thus, a calibration of the RAIRS absorption signal for the corresponding methyl product CH_3 on each site is necessary in order to obtain the coverage from the RAIR spectra. Moreover, since the geometry of CH_3 adsorbed on the different surface sites is likely to be different, the magnitude of the transition dipole moment of a particular vibration of CH_3 on different sites is different.

The CH_3 symmetric stretch vibration displayed in Figure 3-10 was chosen to monitor the reaction since it is the most sensitive vibration of CH_3(ads) detected with RAIRS. Below, I present the calibration performed on the different sites of the surfaces individually as two different methods were used to obtain the calibrations.

3.3.3.1. RAIRS calibration for CH_3(ads) on Pt(111)

The calibration from CH_3(ads) RAIRS absorption signal to C coverage on the Pt(111) surface was performed using Auger Electron Spectroscopy (AES) detection.

The main idea of this calibration is represented in Figure 3-16. First, the C/Pt AES signal ratio was calibrated in terms of coverage with a known saturation coverage of carbon on the Pt(111) surface. For this purpose, we used a self-limiting reaction (C_2H_4 chemisorption on Pt(111)) which produces a well-known saturation coverage of 0.5 monolayers (1 $ML=1.5\cdot10^{15}$ Pt atoms/cm^2) of carbon on a Pt(111) surface at 140 K[126]. With the surface positioned in front of the AES analyzer, we leaked C_2H_4 in the UHV chamber at a pressure of $3.3\cdot10^{-8}$ mbar and recorded AES spectra every 15 s. After each AES scan, the surface was moved with respect to the Auger electron beam in steps of 0.5 mm to reduce the contribution from any carbon generated by the electron gun. Figure 3-17 shows how the C/Pt ratio increases with C_2H_4 dose until it reaches a plateau at about 1.5 L dose. The C/Pt data points were fit using a modified-Kisliuk model[127]. C_2H_4 is known to react on Pt(111) both via precursor-mediated adsorption and Langmuir-type adsorption kinetics[128,129]. From this fitting function, we obtain a C/Pt AES signal ratio of 0.4 for the plateau, which corresponds to the well-known 0.5 ML Carbon saturation coverage. Therefore, a value of 0.80 ± 0.01 is used to convert from C/Pt ratio to carbon (methyl) coverage.

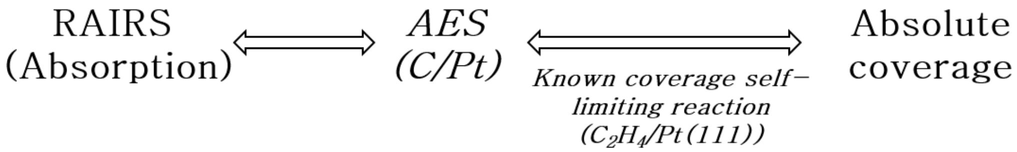

Figure 3-16. Steps of the calibration needed to convert our RAIR signal to absolute coverage.

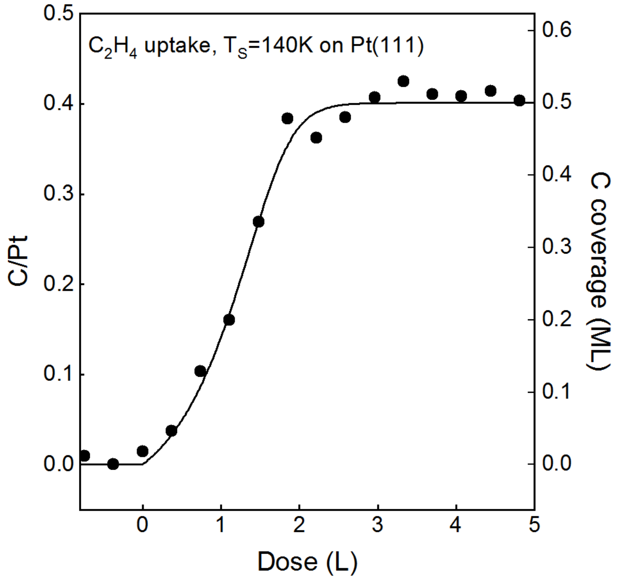

Figure 3-17. AES peak-to-peak ratio C(272 eV)/Pt(237 eV) as a function of C_2H_4 dose on Pt(111) at T_S=140 K. The solid line is a fit of the data based on a modified-Kisliuk model that gives a C/Pt at the plateau of 0.4 which corresponds with the known 0.5 ML carbon saturation coverage (right axis).

Once the AES signal was calibrated in terms of carbon coverage, we proceeded to the RAIRS absorption signal calibration by recording the RAIR spectra and the C/Pt Auger ratio in the same experiment. For this, we performed several depositions of a molecular beam of CH_4 each leading to a different carbon coverage produced by different incident molecular beam energies.

Figure 3-18 shows the RAIR spectra (a)) and uptake curves (b)) as well as the Auger carbon spots (c)) after several depositions performed at different incident energies and therefore leading to different amounts of CH_3 on the surface. To determine the conversion factor from peak height to coverage, a straight line was used for the fitting (Figure 3-18 d)). This linear dependence is justified by the weak transition dipole of the symmetric C-H stretch mode of CH_3. The absorption peak height to coverage conversion factor is calculated as the linear fit gradient divided by 0.80 to account for the conversion between C/Pt and carbon coverage, yielding a factor of 249 ± 28 that we need to multiply to the peak height in order to get the coverage in ML.

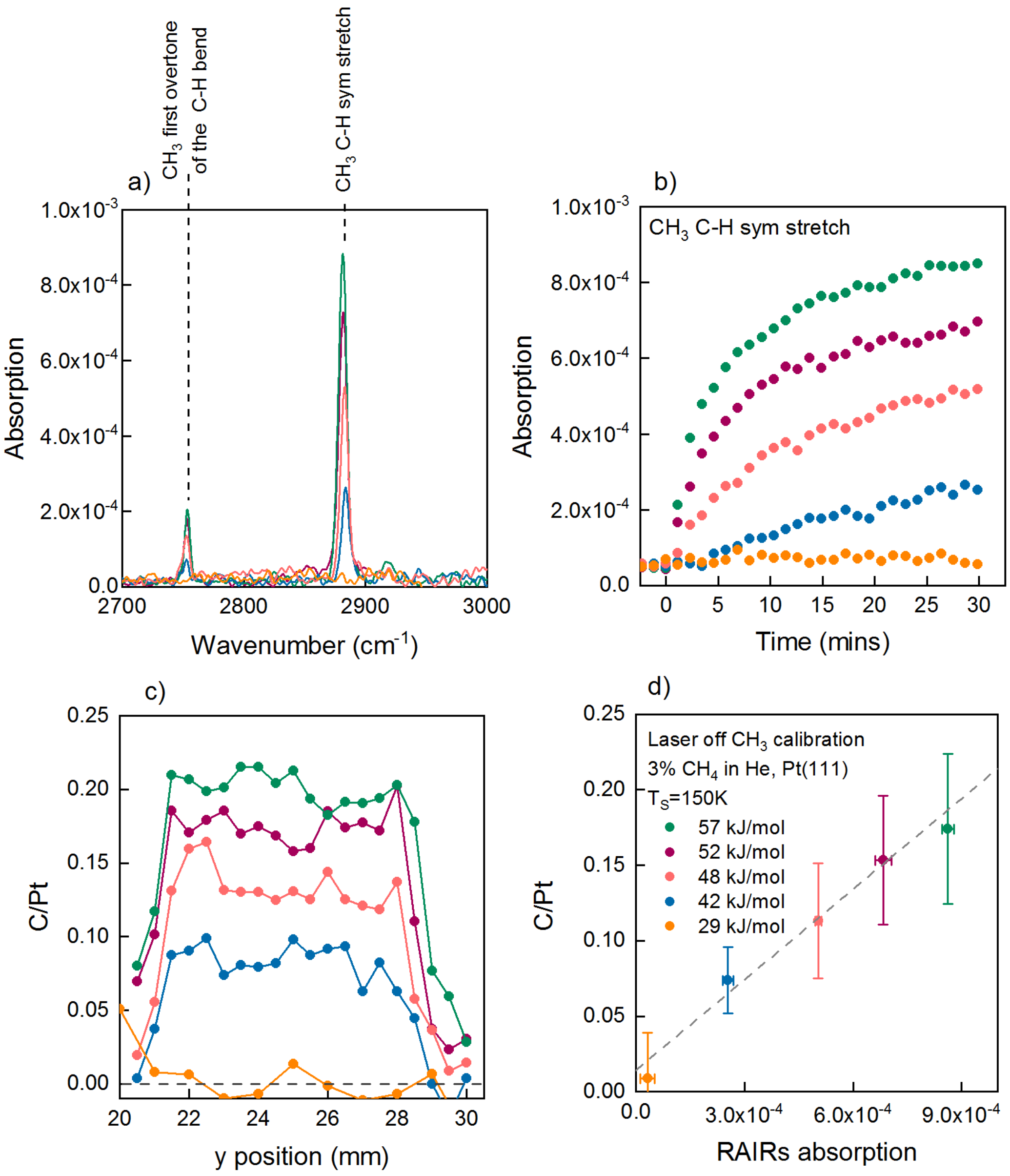

Figure 3-18. CH_3 RAIRS calibration on Pt(111): a) The final RAIR spectra for different incident doses, each of them obtained by averaging 4096 scans; b) CH_3 uptake curves recorded during the depositions; c) Auger scans taken after every deposition measurement; d) C/Pt AES signal ratio *vs* RAIRs absorption peak signal for the CH_3 symmetric stretch peak at 2881 cm^{-1}.

3.3.3.2. RAIRS calibration for CH_3(ads) on Pt(110)- (1x2)

The calibration for the CH_3 RAIRS signal on the ridges was performed using the K&W method. Figure 3-19 shows the K&W trace and the CH_3(ads) uptake curve measured on Pt(110)-(1x2) at E_{trans} = 62 kJ/mol and T_S = 120 K. Both traces were measured simultaneously. Using the K&W method, we obtained an absolute measurement of the initial sticking coefficient [63,98]. In the case of RAIRS, the same value of the sticking coefficient should be extracted from the initial slope of the Langmuir fitting model using equation (3.2). Therefore, using the absolute S_0 obtained using K&W, the factor needed to convert the absorption signal into coverage can be extracted from the scale needed to bring the initial slope of the RAIRS uptake to the actual absolute S_0 obtained using K&W. This procedure was repeated 4 times, and the average result was used to convert from CH_3 absorption signal to coverage. The conversion factor is presented in Table 3-4.

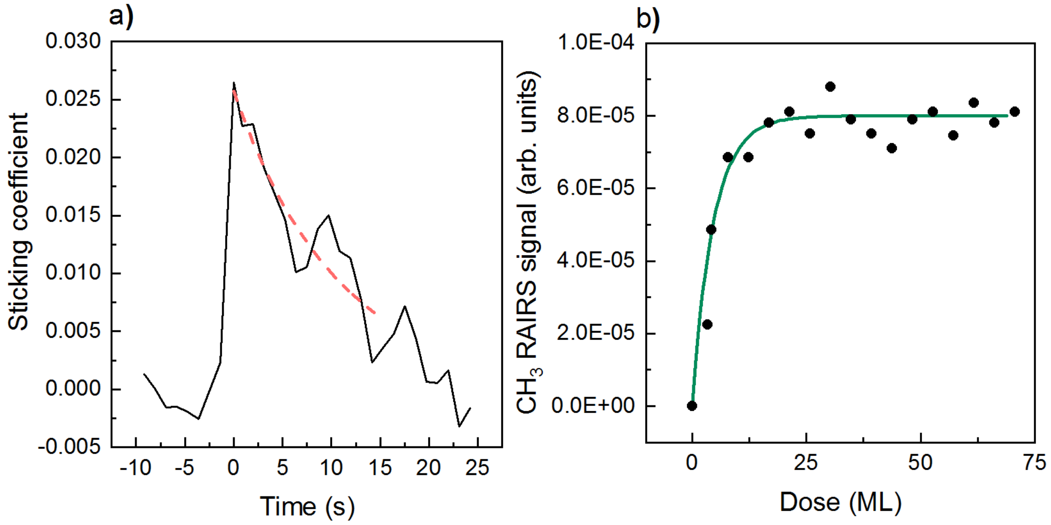

Figure 3-19. The dissociation of CH_4 at E_{trans}=62 kJ/mol on Pt(110)-(1x2) at T_S=120 K was studied by K&W and RAIRS in the same experiment: a) shows the time dependence trace of the Sticking coefficient measured by K&W. The dashed red line corresponds to the fit to the data using a double exponential decay; b) RAIRS uptake curve fit using equation (3.2).

3.3.3.3. RAIRS calibration for CH_3(ads) on Pt(211)

The CH_3(ads) RAIR signal on the step sites of Pt(211) was calibrated using K&W following the same procedure as for Pt(110)-(1x2). Monitoring the deposition by K&W and RAIRS simultaneously at E_{trans}=65 kJ/mol and T_S=150 K and assuming that the contribution from dissociation on the terrace sites to the S_0 measured with K&W was negligible, the calibration factor was obtained.

The conversion factor for CH_3(ads) on the terraces of the Pt(211) surface was assumed to be the same as for CH_3 adsorbed on the Pt(111) surface. However, the energetics of methane chemisorption on the terraces of Pt(211) and Pt(111) are different. Therefore, an error may be included in this calibration. For this reason, I tried to improve the calibration for CH_3 on the terraces of Pt(211) by using AES. However, the detection limit for AES was not good enough to allow for a CH_3 calibration on the terrace sites.

The calibration factors used for Pt(111), Pt(211) and Pt(110)-(1x2) are shown in Table 3-4. It can be seen that RAIRS is more sensitive to CH_3 vibration on the terrace sites in comparison with the step and ridge sites, indicating a smaller component of the transition dipole moment perpendicular to the surface when the CH_3 is adsorbed on the step and ridge atoms.

Surface	Site	Calibration factor (ML/Absorption unit)
Pt(111)	Terrace	248
Pt(211)	Terrace	234
	Step	1462
Pt(110)-(1x2)	Ridge	1872

Table 3-4. Conversion factors from CH_3 absorption signal (using the peak height of the CH_3 symmetric stretch peak) to coverage (in ML, taking into account the different surface atom densities of the different surfaces).

3.3.4. Site-specific sticking coefficients

Due to the site-specific detection capabilities of RAIRS, the "site-specific initial sticking coefficients (S_0^{site})" were measured for the terrace sites on Pt(111) and Pt(211) as well as the steps of the Pt(211) surface and the ridges of the reconstructed Pt(110)-(1x2) surface. We define the site-specific sticking coefficient as the reaction probability for a molecule incident on a specific site of the surface. Therefore, when converting the total measured sticking coefficient to the site-specific sticking coefficient one needs to take into account the fractional density of the specific type of surface site (step, terrace, ridge…). For example, while on Pt(111), the fractional area of terrace sites is 1, on Pt(211) the fractional area of the terrace sites is only 1/3 because there are also an equal number of step and corner sites. The total sticking coefficient can be expressed as:

$$S_0(total) = \sum_i \rho_i S_0^i \tag{3.3}$$

where ρ_i is the fractional density of the i surface site and S_0^i the site-specific initial sticking coefficient on that site.

The definition of site-specific initial sticking coefficients allows for comparison of the specific reactivity of different surface sites. In order to determine the surface-site-specific sticking coefficients from the site-specific RAIRS uptake curves, the fractional incident dose on each of the different surface sites was taken into account. To do so, the total incident dose on the surface calculated from equation (2.2) was converted to the fractional dose on each site. On the Pt(211) surface, the fractional dose on each site (step, terrace and corner) was assumed to be 1/3 of the total incident dose since the surface layer consists of these three types of atoms in equal proportion. On the Pt(110)-(1x2) surface, the incident dose on the ridge atoms was assumed to be 1/4 of the total incident dose.

Figure 3-20 shows a comparison of the S_0^{site} values for the different sites on the three different Pt surfaces as a function of incident translational energy. To better visualize the trend in S_0 as a function of incident energy, the S_0 points were fit using equation (3.1).

For all the incident energies studied, we observed the highest reactivity for the lowest coordinated step and ridge sites. On Pt(211), DFT studies predicted a barrier for CH_4 dissociation on the terraces of 84 kJ/mol, while on the step sites the lowest barrier for dissociation was found to be 42 kJ/mol, result that agrees very well with these experimental observations[105].

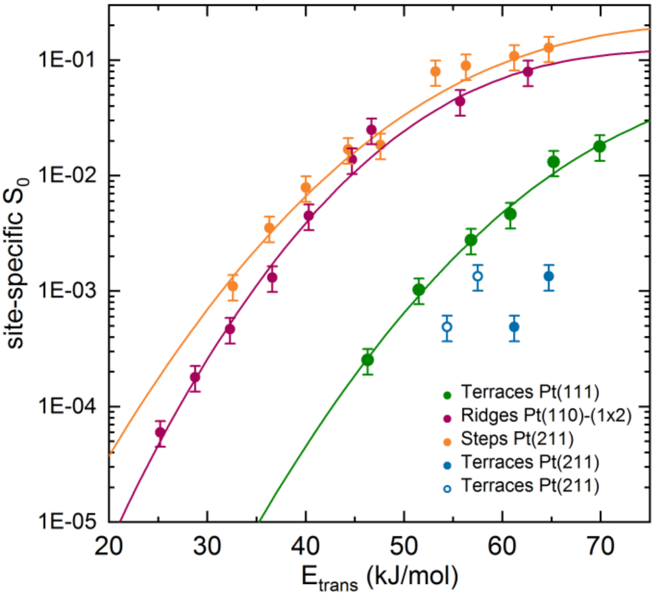

Figure 3-20. Site-specific initial sticking coefficient S_0 vs. incident translational energy (E_{trans}): terrace sites of Pt(111) (T_S=150 K, green), the ridges of the Pt(110)-(1x2) surface (T_S=120 K, red), and the steps (orange) and terraces (blue) of the Pt(211) surface (T_S=120 K). The solid symbols are S_0 as a function E_{trans} measured normal to the macroscopic surfaces. The open symbol S_0 vs. E_{trans} normal to the (111) terrace of the Pt(211) surface which are tilted by 19.5° relative to the 211 crystal plane. The solid lines corresponds to the fit to the experimental data points obtained using equation (3.1.)

We find the Pt(110)-(1x2) ridge sites to have a slightly lower sticking coefficient than the step sites on Pt(211), being the reactivity a factor of ~2 higher on the step sites, while both have the same coordination number CN=7. This is in qualitative agreement with theoretical results previously reported[45,104,105]. By fitting the measured kinetic energy dependence of the site-specific sticking coefficients S_0 both for the steps and the ridges using equation (3.1) with a constant asymptote A and width W for the distribution of barrier heights (0.17 and 15 respectively), we obtain an average E_0 activation barrier height of about 3 kJ/mol higher for the ridges than for the steps. This difference in the average barrier height obtained experimentally is smaller than the difference in the minimum barriers for dissociation on the steps and ridges calculated by DFT. Chadwick *et al.*[104] predicted a 10 kJ/mol higher barrier for CHD_3 dissociation on the ridges than on the steps. Jackson and coworkers have reported higher minimum PBE barriers on the ridges by 21.7 kJ/mol than on the steps[45,105].

At the beginning of this chapter, I reported a comparison between the experimental sticking coefficients for CHD_3 on Pt(110)-(1x2) measured at T_S=650 K using the K&W method and the ones predicted by ab initio quasi-classical trajectory calculations. Both experiment and theory agree very well at high incident energies but disagree for incident energies lower than 110 kJ/mol. Good agreement was found between the calculated and measured reactivities at the low energies as long as some contribution to the dissociation from molecules trapped on the surface was included in the theoretical sticking coefficients.

This trapping mediated channel on Pt(110)-(1x2) could explain why the measured reactivities on this surface are larger than predicted by theory and why the difference between the sticking coefficients for the steps and the ridges is smaller than that predicted by DFT. However, the existence of trapping mediated dissociation could not be confirmed by our experiments. The lifetime of physisorbed CH_4 on Pt(110)-(1x2) at T_S=120 K is around 32 ms[104]. Taking into account the flux of incident molecules on the surface, we expect to have less than 0.8% of a ML of CH_4 on the surface at any given second, assuming that all the CH_4 in the molecular beam would physisorb on the surface, which is not realistic. Assuming that only a small fraction of the indicent CH_4 would trap on the surface, most probably the limits of detection of our RAIRS setup would not allow us to observe CH_4 as the precursor for CH_3 dissociation on the Pt(110)-(1x2) surface.

Another interesting feature visible in Figure 3-20 is the different reactivity of the terraces of the flat Pt(111) surface and the terraces of Pt(211) which was assumed to be the same in previous studies[97,99]. Although the coordination number is the same for the terraces on both surfaces, the Pt(111) terraces show a higher reactivity. A possible reason for this discrepancy is the different normal incident energies onto the terraces of Pt(111) and Pt(211) surfaces. Since the (111) microfacets of the Pt(211) surface are tilted with respect to the macroscopic (211) surface plane by 19.5°, the incident normal energy onto the 211 terraces is lower by a factor of $\cos^2(19.5°) = 0.63$ compared to the 111 terraces for a molecular beam incident normal the macroscopic surface plane. Using this correction for the local normal incident energy, I obtained the open symbols shown in Figure 3-20, which bring the S_0 on the terraces of the Pt(211) surface closer to the S_0 on the terraces of Pt(111). The remaining horizontal offset between the data points for Pt(111) and the corrected S_0 values for the terraces of Pt(211) is approximately 5 kJ/mol.

A higher barrier for dissociation on the terraces of the Pt(211) has been also predicted by DFT calculations: Jackson and coworkers[105] predicted a 17 kJ/mol higher barrier on the terraces of Pt(211) while Busnengo *et al.*[106] obtained a difference between both barriers of 3 kJ/mol. Moreover, Busnengo suggests that the relatively small difference between the activation energies that he finds on the two terrace sites is likely due to a compressive strain effect. The average distance between the terrace atoms and their nearest neighbors on Pt(211) is 2% smaller than for the terrace atoms on Pt(111), due to the stepped (211) surface relaxation. According to the *d*-band model, which I will explain below, such a compressive strain produces a downshift of the *d*-band center for metal atoms with more than half-filling of the *d*-band like Pt which in turn causes a decrease of reactivity.

Overall, these results demonstrate that the coordination number of the surface atoms where adsorption takes place is not the only factor which determines the site-specific reactivity and that the local environment surrounding the surface site also plays a role. Calle-Vallejo *et al.*[130] proposed the use of the generalized coordination number (CN) that takes into account the coordination number of the nearest neighbor atoms. Therefore, this number can take into account the main difference between the (111) terrace of the stepped and the flat surfaces as well as the difference between the steps on Pt(211) and the ridges of Pt(110)-(1x2). However, the generalized coordination number is higher on the terraces of the Pt(111) surface (CN =7.5) than on the terraces of the Pt(211) (CN =7.33), and it is also higher on the steps of Pt(211) (CN =5.5) than on the ridges of the Pt(110)-(1x2) (CN =5.16). Therefore, a higher reactivity would be expected on the terrace sites of the Pt(211) than on the terrace sites of Pt(111), and a higher reactivity would be expected on the ridges of Pt(110)-(1x2) than on the steps of Pt(211) opposite to the experimental results observed here.

3.4 The electronic structure factor: *d*-band theory

This section is meant to explain in a very concise and simple way the *d*-band theory that can be used to explain the results observed in this chapter in a qualitative way.

The effective medium model[131] approximates the interaction between the adsorbate and the surface as the sum of three components: the core-core repulsion, the interaction of the adsorbate with the *s*- and *p*-bands of the metal and the interaction of the adsorbate with the *d*-band of the metal. The first term can be accurately approximated by a core-core potential. In their model, Hammer and Nørskov[132] consider that the s and p states would lead to a broadening and a shift of the atomic level to lower energies. They considered that the contribution from these states can be modelled by the interaction of the adsorbate with an uniform electron gas (*jellium model*). They predict that the trends in the reactivities can be understood by looking at the interaction between the molecule energy levels and the metal *d*-bands of the surface. In particular, the *d*-band model suggests considering the interaction between the molecule energy levels and the center of the *d*-band of the surface.

Figure 3-21 shows a schematic drawing of the interaction between a molecule and a surface using their *d*-band model. The interaction with the *d*-band of the metal splits the atomic level into a bonding and anti-bonding state with respect to the surface-molecule bond. If the bonding and anti-bonding states are occupied, the total energy is raised and the interaction would be repulsive. On the other hand, if the Fermi level is below the anti-bonding state, this state won't be (fully) occupied, resulting in an attractive molecule-surface interaction. It is therefore the position of the Fermi energy level that dictates if the anti-bonding state is fully, partially occupied or empty and so if the reaction is repulsive or attractive.

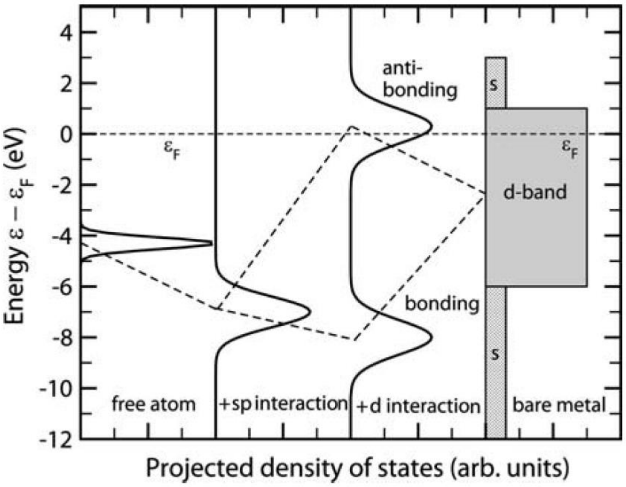

Figure 3-21. Schematic drawing of the interaction of an atomic level with the metallic states of a transition metal surface. The atomic level is broadened and shifted down due to the interaction with the s and p states (*jellium model*). The interaction with the center of the *d*-band splits the atomic level into a molecule-surface bonding and anti-bonding contributions. Reproduced with permission from[133].

The *d*-band model can be also applied to justify the differences in reactivity observed on stepped surfaces[134,135]. In a simple tight-binding picture, the effect of having low coordination sites on the surface is to decrease the width of the *d*-band. Let us then imagine the implication of this reduction in the bandwith of the *d*-band for a late transition metal with a more than half-filled *d*-band like platinum. If the center of the *d*-band is kept fixed, the occupation of the *d*-band increases due to the reduction of the bandwidth that brings the whole band below the Fermi energy level. However, the number of d-electrons must be conserved obeying the charge conservation. Therefore, the center of the *d*-band needs to shift up so the number of occupied states is constant, as it is shown in Figure 3-22.

The shift-up of the center of the *d*-band yields a higher anti-bonding molecule-surface orbital, which will be less occupied that in the case of a flat surface whose *d*-band center is lower. Hence, adding lower coordinated sites on the surface of a late-transition metal is predicted by the *d*-band model to increase the binding energy of the adsorbates on these sites. According to the Brønsted-Evans-Polanyi relationship[136,137], this increase in the binding energy of the adsorbates on the low coordinated sites causes a decrease in the barrier height for dissociation on these sites.

On platinum, the binding energies of several undercoordinated Pt_x atoms deposited on a Pt(111) surface were measured using high energy resolution core level photoelectron spectroscopy[138]. The lower the coordination of the Pt atoms, the lower the binding energy measured relative to the bulk core energy position on Pt(111). By combining these experimental binding energies with DFT calculations, the authors showed a linear relation between the *d*-band center shift and the atomic coordination number for the different undercoordinated Pt_x atoms.

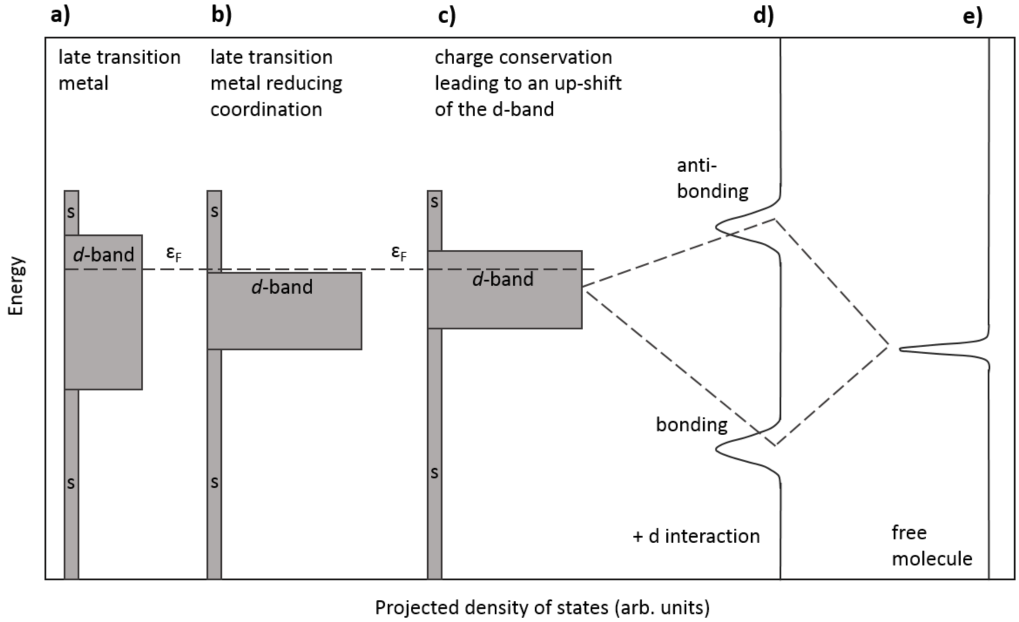
a)
b)
c)
d)
e)
late transition metal
late transition metal reducing coordination
charge conservation leading to an up-shift of the d-band
anti-bonding
bonding
s
d-band
ε_F
Energy
+ d interaction
free molecule
Projected density of states (arb. units)

Figure 3-22. Schematic illustration of the effect of reducing the coordination of the surface atoms. From the right to the left: a) a more than half-filled *d*-band; b) the reduced width of the *d*-band due to the lower coordination of the surface atoms; c) up-shift of the *d*-band because of charge conservation; d) the molecule-surface bonding and anti-bonding orbitals; e) a free molecule orbital.

Interestingly, on early transition metal surfaces with a less than half-filled *d*-band, the opposite effect is predicted[135]. A narrowing of the *d*-band due to low coordinated sites would induce a shift-down of the center of the *d*-band because of charge conservation. This would induce a lowering in the anti-bonding molecule-surface orbital and therefore a filling of this orbital that would turn into a more repulsive interaction than on the flat surface.

This model has been used to qualitatively understand the trends in the reactivity of transition metal surfaces. However, there are some cases where the position of the center of the band does not correlate with the reactivity of the surface as it was found recently for the interaction of H_2 on a Cu(211) surface where the steps were found to be less reactive than the terraces[40].

Here we can use it to explain in a qualitative way why the reactivity on the less-coordinated ridges or steps is higher than on the more coordinated terraces. An interesting experiment that we could perform in the future in our lab is the comparison of the reactivity of low and high coordinated sites on an early transition metal such as tungsten, where the low coordinated sites are expected to be less reactive than the high coordinated sites.

3.5 Quantum state- and surface-site-specific sticking coefficients for $CH_4(\nu_3)$/Pt

In this section, I present state- and site-resolved initial sticking coefficients for the dissociative chemisorption of CH_4 on Pt(110)-(1x2) and I compare the role of rovibrational laser excitation of the incident methane on the chemisorption on different surface sites of Pt(111), Pt(211), and Pt(110)-(1x2).

Previous quantum state resolved studies have investigated the effect of rovibrational excitation on the reactivity of CH_4 on Ni(100)[17,20,139], Ni(110)[31], Ni(111)[31,140,141], Pt(111)[51,125,141], and Pt(110)-(1x2)[21] surfaces. Among these studies, it has been demonstrated that the ability of vibrational energy to promote the dissociation of methane strongly depends on the vibrational mode in which the molecules are excited (i.e. *mode specificity*). For instance, excitation of the symmetric C-H stretch normal mode ν_1 of CH_4 has been shown to be more efficient in promoting dissociation than excitation of the antisymmetric C-H stretch normal mode ν_3 for the CH_4 dissociation on Ni(100)[17,19], even though the two modes contain nearly the same vibrational energy. This mode specific CH_4 reactivity was predicted by Halonen *et al.*[142] on the basis of a vibrationally adiabatic model that simulates the normal mode evolution of CH_4 as a function of surface distance using a model potential for the molecule/surface interaction. The ν_1 symmetric C-H stretch normal mode far from the surface transforms by the interaction with the surface into a localized stretch vibration of the C-H bond that points toward the surface. On the other hand, CH_4 initially excited to the antisymmetric stretch mode ν_3 evolves into a C-H stretch vibration localized in the CH_3 group pointing away from the surface. Based in such "*surface-induced vibrationally adiabatic intramolecular vibrational energy redistribution (IVR)*", the authors predicted that ν_1 excitation of CH_4 should lead to a larger dissociation probability than excitation of ν_3.

The effect of excitation of $2\nu_3$, the first overtone of the antisymmetric C-H stretch vibration of CH_4, for promoting dissociation on Pt(111) and Ni(111) was measured and compared for the two surfaces[141]. The ground-state reactivity on Ni(111) was found to be approximately 3 times lower than on Pt(111) and the reactivity of $CH_4(2\nu_3)$ was observed to be larger on Ni(111) than on Pt(111). Previous experiments by Luntz and Bethune[110] also observed a higher vibrational efficacy of thermally populated states in a hot nozzle on Ni(111) than on Pt(111). These observations have been explained by the structure of the transition state. The transition state for CH_4 dissociation on Ni(111) shows a more elongated reactive C-H bond than on Pt(111)[143]. By exciting the overtone of the stretch vibration and therefore elongating the C-H bonds, the vibrational energy is placed very efficiently in the reaction coordinate for dissociation on Ni(111). This transition state geometry is typical from a late barrier[18]: a later barrier for dissociation of CH_4 on Ni(111) than on Pt(111) would explain why vibrational energy is more efficient than translation in promoting dissociation on Ni(111).

Here, I report the first state resolved measurements of the $CH_4(\nu_3)$ reactivity on Pt(110)-(1x2). Figure 3-23 shows the state- and surface-site resolved sticking coefficients $S_0(\nu_3)$ at T_S=120 K, as well as the laser-off sticking coefficient.

For the laser-on experiments, since not 100% of the incident molecules are excited, one needs to take into account the excitation fraction in order to extract the state-resolved S_0 using:

$$S_0^{\nu_3} = \frac{S_0^{laser-on} - S_0^{laser-off}}{f_{exc}} + S_0^{v=0} \tag{3.4}$$

Where $S_0^{laser-on}$ and $S_0^{laser-off}$ are the sticking coefficients measured in the experiments with and without laser excitation at the same incident translational and rotational energy. $S_0^{v=0}$ is the vibrational ground state (v=0) reactivity and f_{exc} is the vibrational excitation fraction of the molecular beam measured using the pyroelectric detector as it is described in chapter 2.

$S_0^{laser-off}$ is the contribution from the ground state population (v=0) and from all the thermally excited vibrational states in the molecular beam. Therefore, $S_0^{laser-off}$ is an upper limit for $S_0^{v=0}$. For all the translational energies presented here, the $S_0^{laser-off}$ is less than 5% of $S_0^{laser-on}$. Therefore, I assumed that the contribution from $S_0^{v=0}$ is negligible in equation (3.4).

As shown in Figure 3-23, excitation of the ν_3 stretch mode enhances dramatically the reactivity of CH_4 on the Pt(110)-(1x2) surface. The experimental data points were fit using S-shaped reactivity curves using equation (3.1). In order to compare the extent to which this type of vibrational energy promotes reactivity with respect to translational energy, I calculated the vibrational efficacy using:

$$\eta(\nu_3) = \frac{(E_0^{laser-off} - E_0^{\nu_3})}{E_{\mathrm{vib}}(\nu_3)} \tag{3.5}$$

where $E_0^{laser-off}$ and $E_0^{\nu_3}$ are the average activation barriers determined by the S-shaped fitting curves to the laser off and state-resolved sticking coefficients shown in Figure 3-23. The A and W parameters in equation (3.1) were fixed to 0.2 and 16.2 kJ/mol respectively. $E_0^{laser-off} - E_0^{\nu_3}$ corresponds to the horizontal offset between the two S-shaped curves. Adding 17.3 kJ/mol of translational energy promotes the reactivity by the same amount as adding 36 kJ/mol in the ν_3 vibrational mode. The efficacy of this vibrational state is therefore $\eta(\nu_3) = 0.48$.

Here it is worth mentioning that the fit shown in Figure 3-23 for the state-resolved data (in red) does not seem to capture the trend as well as it does for the laser off data. This is due to the enforced curvature having A and W fixed for both sets of data. Any difference in the effective barrier height distribution for the state-resolved and the ground state due to the sampling of a different part of the PES would lead to different shapes in the S_0 curves and could explain this observation.

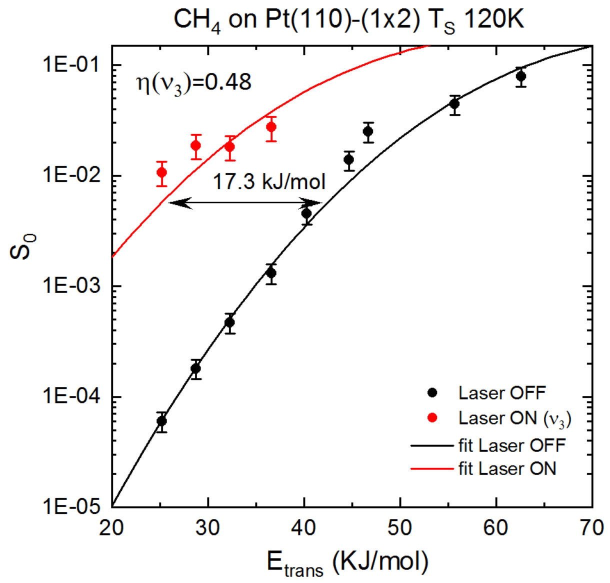

Figure 3-23. State-resolved sticking coefficients for CH_4 prepared with a single quantum of ν_3 (red symbols) and under laser-off conditions (black symbols) for dissociation on the ridges of Pt(110)-(1x2).

Previously in our group, Bisson *et al.*[101] reported the effect of $2\nu_3$ excitation on the dissociative chemisorption of CH_4 on Pt(110)-(1x2). An efficacy of $\eta(2\nu_3) = 0.47$ was found for the overtone of the antisymmetric stretch of methane. A lower efficacy for the overtone with respect to the fundamental stretch vibration ν_3 was observed before for Ni(111)[140,141] and Pt(111)[51,141]. This observation was rationalize by the fact that the total energy of $2\nu_3$ exceeds the reaction barrier and thus its vibrational efficacy decreases. In other words, promotion of reactivity by rovibrational excitation is expected to be more efficient at energies below the barrier for dissociation. However, for Pt(110)-(1x2) I observe a similar efficacy for the fundamental stretch ν_3 than that measured before for the overtone $2\nu_3$.

Following the same procedure explained below for Pt(110)-(1x2), Chadwick measured the ν_3-efficacy on the step and terrace sites of Pt(211)[105]. Table 3-5 shows a comparison of the experimentally obtained efficacies on the different surface sites. As it is explained below, this comparison of the effect of ν_3 excitation on the dissociation on different surface sites yields very valuable information about the transition state geometry and barrier height for methane dissociation on each site.

The general trend is for the efficacy to decrease with decreasing coordination number of the surface site. One possible interpretation for this difference in efficacy is the lower barrier height on the low coordinated sites. For example, at 60 kJ/mol, the addition of 36 kJ/mol of vibrational energy to the molecule makes a big difference in the reactivity for the terraces because the reaction on the terraces is "starving for energy". However, on the steps or ridges, the addition of vibrational energy is not so important because the translational energy is enough to overcome the barrier for dissociation.

Another interpretation is based on the transition state structure. On the Pt(211), DFT calculations of the transition state structure performed by the group of Bret Jackson[109] show that the reactive C-H bond is more stretched for dissociation on the terrace site (1.525 Å) than on the step site (1.480 Å). Therefore, adding energy into the ν_3 vibration can be expected to be more efficient for dissociation on the terrace than on the step site, since this vibrational mode places energy into the reaction coordinate by stretching the reactive C-H bond.

Using the sudden vector projection model[144], theoretical efficacies for several vibrational modes of CH_4 on different surfaces were calculated[42]. The theoretical efficacy was calculated as the squared ratio between the overlap of the initial vibrational mode vector with that of the molecule at the TS and the overlap of translation vector normal to the surface with the molecule at the TS. Even though the agreement between the experimental and theoretical efficacies is poor, the SVP model predicts a lower efficacy for ν_3 on the Pt(110)-(1x2) than on the Pt(111) surface, in agreement with our results.

Surface	Site	$\eta(\nu_3)$
Pt(111)	Terrace	0.68
Pt(211)	Terrace	0.59
	Step	0.45
Pt(110)-(1x2)	Ridge	0.48

Table 3-5. Vibrational efficacies of ν_3 vibration for the dissociation of CH_4 on different surface sites of Pt(111), Pt(211) and Pt(110)-(1x2) surfaces.

3.6 Summary

The influence of the surface structure on the dissociative chemisorption of methane on Pt surfaces has been investigated experimentally, by measuring both the averaged surface reactivity by the K&W method and by surface-site-specific reactivity measurements using site-specific RAIRS detection. Methane dissociation was studied on the Pt(111), Pt(211), Pt(110)-(1x2), and Pt(210), surfaces that expose different sites such as terraces, steps, corners, ridges, valleys, and kinks.

Using the K&W method, the total CHD_3 dissociation probability, summed over all the sites present on a particular surface was measured on the different surfaces. The experimental results were compared to calculations perfomed using AIMD by Kroes and coworkers in order to test the ability of AIMD to predict the methane reactivity with chemical accuracy. At incident energies below 100 kJ/mol, the reactivity of the more corrugated surfaces was higher (Pt(210)>Pt(211)>Pt(110)-(1x2)>Pt(111)); this order is reversed at incident energies higher than 100 kJ/mol (Pt(111)≃Pt(210)>Pt(211)>Pt(110)-(1x2)). The less coordinated kinks, steps and ridges dominate the reactivity at low incident energies, with the kinks and the steps being more reactive than the ridge atoms, in accordance with theory predictions. At high energies, the "active area" of the surface dominates the reactivity. For example, the Pt(211) surface consists of steps, terraces and corners, being the corner sites hardly reactive, with a barrier for dissociation predicted by DFT of 184 kJ/mol[105]. On the Pt(110)-(1x2) surface, the same effect happens with the valley atoms. Therefore, 1/3 of the surface area in the case of Pt(211) and 1/4 in the case of Pt(110)-(1x2) is not expected to be "active" for the methane to dissociate. However, the Pt(111) surface presents 100% of the sites as terraces, whose barrier for dissociation is higher than on kinks, steps or ridges, but much lower than for the corners or valleys. Hence the Pt(111) shows a higher reactivity at the highest incident energies studied here.

The reactivity of CHD_3 on Pt(211) was studied as a function of incident polar angle. The sticking coefficient was seen to decrease sharply when the angle of incidence was changed from normal incidence to the surface toward normal incidence to the terraces of the surface. The results are explained by a small shadowing effect from the more exposed steps to the terraces together with a distribution of different activation barriers around the step atom.

In the second part of the chapter, I introduce RAIRS as a site-specific detection technique able to distinguish between CH_4 dissociation on the different sites of the Pt(111), Pt(211) and Pt(110)-(1x2) surfaces. Following the assignment of the various peaks observed in the RAIR spectra and calibration of their transition dipole moment, the CH_4 reactivity on the different sites was quantified.

The order in the site-specific reactivity measured with RAIRS is $S_0^{step\ Pt(211)} > S_0^{ridge\ Pt(110)} > S_0^{terr\ Pt(111)} > S_0^{terr\ Pt(211)}$, in agreement with theoretical calculations. The reactivity does not scale with the coordination number since the terraces of Pt(111) and Pt(211), and the steps and ridges of the Pt(211) and Pt(110)-(1x2) do not present the same reactivity. Neither the generalized coordination number can explain the trends observed in the reactivity. The *d-band* model is shortly presented as a model that predicts in a qualitative way why the low coordinated sites of late-transition metals like Pt decrease the barrier for dissociation.

Finally, I present state-resolved sticking coefficients for $CH_4(\nu_3)$ on Pt(110)-(1x2) and I compare the efficacy of ν_3 excitation on the reaction of CH_4 on the different sites of Pt(111), Pt(211) and Pt(110)-(1x2). Even though the excitation of the antisymmetric stretch of CH_4 enhances dramatically the reaction, the translational energy is found to be more efficient in promoting the dissociation of CH_4 on all different sites. The efficacy of ν_3 excitation scales on the different sites as: $\eta_{\nu_3}^{terr\ Pt(111)} > \eta_{\nu_3}^{terr\ Pt(211)} > \eta_{\nu_3}^{ridge\ Pt(110)} > \eta_{\nu_3}^{step\ Pt(211)}$. The difference between the efficacy of ν_3 excitation on the different sites is explained by the differences in the barrier height and the geometry of the transition state.

Chapter 4 Bond selective dissociation of methane isotopologues on Pt(111) and Pt(211)

4.1 Introduction

Being able to control the branching ratio of a chemical reaction with several possible channels has been a long-standing goal in chemistry both for practical reasons and due to the theoretical insight that the study of bond selectivity can offer[145]. Different methods for achieving bond selectivity in chemical reactions using laser radiation have been proposed and demonstrated including femtosecond pulse timing[146], phase control via interfering excitation pathways[147], and vibrational mediated reaction control[148]. In this thesis, I will focus on the last strategy, which has been used to achieve bond selective chemistry in unimolecular dissociation[149], bi-molecular reactions in the gas phase[150–157], and in gas-surface reactions[22,28,29].

The basic idea of bond selectivity via vibrational excitation consists on depositing vibrational energy in a particular bond of a polyatomic molecule so only that specific bond of the molecule breaks and thus alters the outcome of the chemical reaction. A simple sketch of the definition of bond selectivity is depicted in Figure 4-1. However, as it was already published in 1991 by the group of Richard N. Zare[151], three factors conspire against bond selectivity:

1) *"The difficulty of preparing a molecule in a selected vibrational level.*
2) *The time scale that vibrational energy remains localized in a well-defined motion (vibrational mode) once the molecule is excited.*
3) *The efficacy with which vibrational motion of a polyatomic molecule promotes bond-specific bimolecular reaction."*

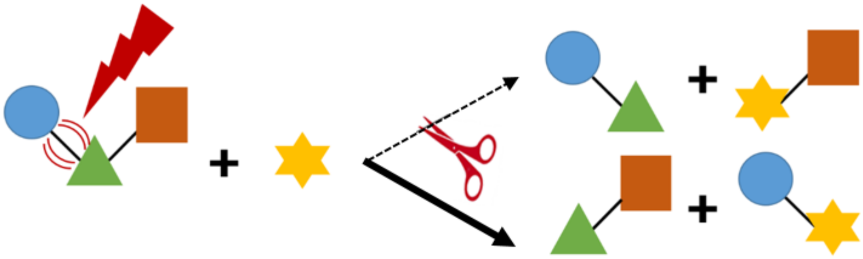

Figure 4-1. Schematic of a bond selective bimolecular reaction. A particular bond of the polyatomic reactant molecule is vibrationally excited. This localized excitation leads to the breaking of that particular excited bond during the reaction, inhibiting the other channel of the reaction to occur.

Overcoming these three factors, Crim and coworkers published in 1989 the first evidence for a vibrational mediated photodissociation reaction[149]. By selectively exciting the O-H stretching vibration in HOD before its photodissociation induced by a second laser, they observed a preferential production of the OD product upon photolysis. Full O-H bond selectivity was observed by exciting the water molecule to an overtone of the O-H stretching vibration.

Soon after, they expanded bond selectivity to studies of gas-phase chemical reactions. Sinha *et al.*[150] reported vibrational bond selectivity for the bimolecular gas-phase reaction of HOD molecules with H atoms. Their results, together with experiments performed by Bronikowski *et al.*[151], showed that vibrational excitation of the O-H bond in HOD leads almost exclusively to the H_2+OD product channel, while excitation of the O–D stretch produced mainly HD+OH products.

In subsequent work, these two groups broadened the bond selective studies to the reaction between methane isotopologues with chlorine atoms and they reported bond selectivity for both C-H and C-D cleavage channels for CH_3D[152–154] and CH_2D_2[155,156] as well as an enchanced cleavage of the C-H bond for CHD_3[156]. These results were interpreted with a simple spectator model in which every bond of the reactant behaves as an isolated oscillator: vibrational excitation of the reactive bond increases its probability for dissociation but leaves the unreactive bond unaffected. Therefore, this model does not account for intramolecular vibrational redistribution (IVR) in the molecule because the bonds are supposed to be local and uncoupled. However, this model has been shown to break down in the reaction between CHD_3 and Cl, in which IVR was observed[157]. In particular, a comparison between the H+CHD_3 and Cl+CHD_3 reactions showed that energy redistribution is more pronounced in the chlorine reaction, where the incident atom approaches slower and couples more strongly during the course of the reaction. The detection of CHD_2 products in their ground state after the interaction between C-H excited CHD_3 molecules and Cl atoms suggested that vibrational energy must flow from the C-H bond into translation of the escaping product fragments or into vibrational excitation of the DCl product. IVR can therefore prevent bond selectivity since the extra energy deposited in an initial bond (C-H in this case) can flow into other degrees of freedom, including the C-D bonds.

Studies of vibrational bond selectivity were subsequently extended to gas-surface reactions for methane chemisorption on nickel and platinum surfaces. One might expect that bond selectivity is more difficult to achieve at the gas-surface interface because of its increased complexity (many more degree of freedom are available for energy to flow into) compared to an isolated atom-molecule system. In addition to surface induced IVR[158], the metal provides phonon and electron-mediated quenching channels that can compete with the reaction and may prevent bond selectivity[159]. Therefore, the length of time that the molecule spends close to the surface, the IVR rate and the rate of quenching by the surface determines the extent of energy flow prior to reaction.

Despite these complications, bond selectivity has been observed in gas-surface reactions, with the first evidence reported by Killelea *et al.* in 2008[28]. They demonstrated bond selectivity in the dissociation of CHD_3 on Ni(111) by combining bond selective vibrational excitation with isotope-resolved detection. Their method, illustrated in Figure 4-2, consists of titrating the surface-bound methyl species with subsurface D atoms prepared prior to the CHD_3 deposition and the quantification of the CD_4:CHD_3 product ratio using a mass spectrometer. By selectively exciting the ν_1 C-H stretch vibration of the molecule, they observed a CD_4:CHD_3 product ratio of >30:1, in contrast with the 1:3 product ratio obtained when no laser excitation was used and an isoenergetic ensemble of CHD_3 was studied.

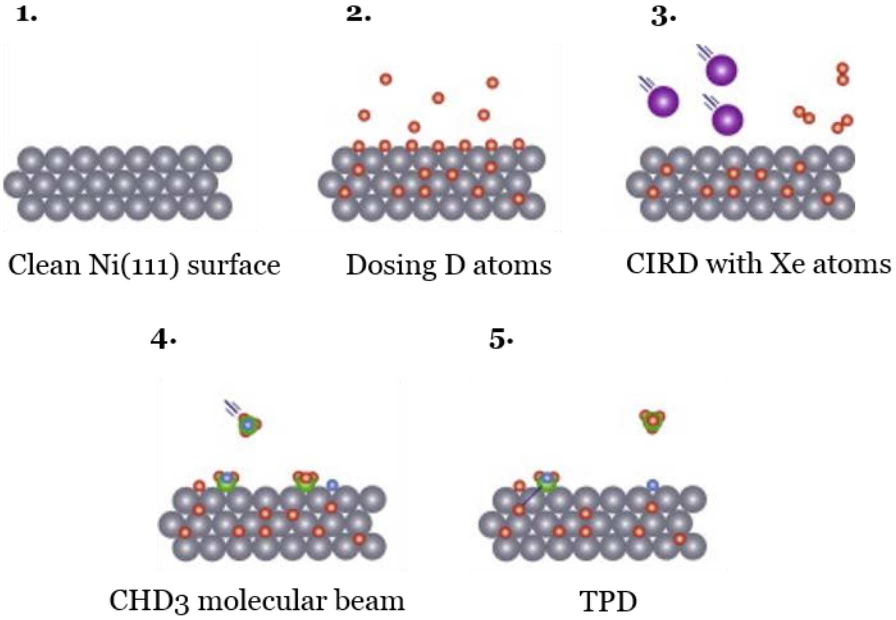

Figure 4-2. Illustration of subsurface D titration method for quantifying bond selectivity. 1) clean Ni(111) surface (side view), 2) D atoms occupy surface and subsurface sites, 3) Xe atoms induce recombinative desorption of surface-bound D leaving a clean surface, 4) CHD_3 impinges on the surface and some CHD_3 molecules dissociative chemisorb, 5) Temperature Programmed Desorption measurement of deuterated adsorbed methyl species. Reproduced with permission from [160].

However, their titration method is limited to a small range of surface samples due to the subsurface atom preparation. Also, it cannot be applied to the rest of the partially deuterated methane isotopologues. For example, in the case of the dissociation of CH_2D_2, detection of m/z=18 in the TPD could come from two different sources: CH_2D_2 as a result of the recombination of the C-D cleavage product (CH_2D) with a D atom, and also from CD_3 because of fragmentation in the mass spectrometer of the CHD_3 formed by recombination of the C-H cleavage product (CHD_2) with a D atom. In order to overcome these limitations, Li Chen, a former member of our group implemented Reflection Absorption Infrared Spectroscopy (RAIRS) for the detection of surface adsorbates, a more general technique that allows the study of a wide range of molecule-surface systems[50,51].

Using RAIRS detection of the methyl products, Chen *et al*. demonstrated that a single quantum of C-H stretch excitation is sufficient to make the dissociation reaction of the partially deuterated methane isotopologues (CH_3D, CH_2D_2 and

CHD_3) fully bond selective[29]. While a combination of incident translational energy and thermal vibrational excitation produced a nearly statistical distribution of C-H and C-D bond cleavage, he observed that laser excitation of the incident molecules to an infrared active C-H normal mode (ν_4 for CH_3D, ν_6 for CH_2D_2 and ν_1 for CHD_3) leads exclusively to C-H bond cleavage products. The same amount of total energy was available in both the laser-off and laser-on experiments by reducing the incident kinetic energy in the laser-on experiments to ensure that any difference in reactivity was not due to a different total energy but because of the nature of the energy. Figure 4-3 shows the RAIR spectra measured after 80 minutes molecular beam deposition on Pt(111) at 150 K for CH_3D, CH_2D_2 and CHD_3. The reaction of C-H stretch excited methane isotopologues (in red) is characterized by a complete absence of C-D bond cleavage products, while in the laser-off deposition (in black), surface methyl products from both channels are detected.

Two of those systems (CH_3D and CH_2D_2 on Pt(111)) were revisited by Hundt *et al.*[22] who in addition to the antisymmetric C-H stretch normal modes (ν_4 for CH_3D, ν_6 for CH_2D_2) investigated previously by Chen *et al*, excited also the symmetric C-H stretch normal modes (ν_1 for CH_3D, ν_1 for CH_2D_2) and reported the simultaneous observation of both bond selectivity and mode specificity. Hundt demonstrated that excitation of the symmetric stretches again yields full bond selectivity, which agrees with theoretical calculations done by Guo *et al.* using the sudden vector projection model (SVP)[24].

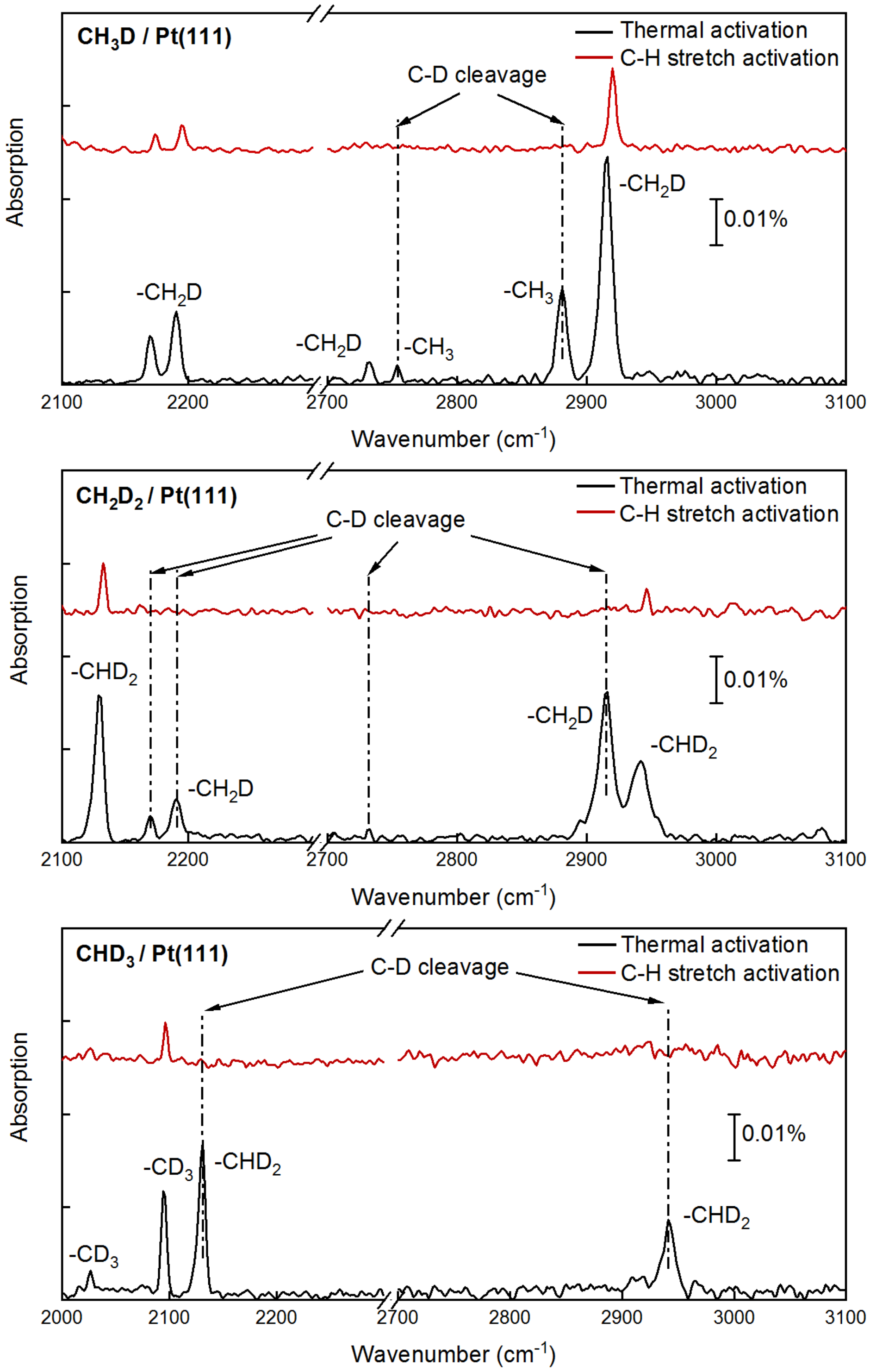

Figure 4-3. RAIR spectra measured after 80 minutes molecular beam deposition on Pt(111) at T_s 150 K for CH_3D, CH_2D_2 and CHD_3. The black lines correspond to molecules with high kinetic energies (but without laser excitation) and the red lines to C-H stretch vibrationally excited molecules. Adapted from[50].

The results shown in this chapter build on this previous reviewed work and their presentation is divided in two parts:

1) A extended study of the bond selectivity of CH_3D, CH_2D_2 and CHD_3 on a Pt(111) surface over a range of kinetic energies is presented. Also, a comparison of the reactivities of the three isotopologues for molecules both without laser excitation and prepared with a single quantum of C-H stretch vibration was studied as a follow-up to the results already presented by Li Chen in his dissertation[50].

2) In the second part of this chapter, I report the first combined study of bond- and surface-site selective dissociation of methane chemisorption. As it has been introduced, bond selectivity has been previously studied on flat surfaces (Ni(111) and Pt(111)). Here, I used the ability of RAIRS to distinguish between methyl products adsorbed on different sites of the Pt(211) surface to investigate the degree of bond selectivity on the steps and terraces of this surface as a function of translational energy.

   The study described in the second part of this chapter has been published[161] in the Journal of Chemical Physics.

4.2 Bond selective chemisorption of methane isotopologues on Pt(111)

As described in the introduction, Chen was able to show how a single quantum of C-H stretch excitation is sufficient to make the dissociation of all three methane isotopologues fully bond selective on a Pt(111) surface[29]. However, Chen's bond selectivity study was performed only at a single kinetic energy of the incident molecules. As far as I know, there is no experimental report of the dependence of the translational energy on the bond selectivity on a gas-surface system. Shen *et al.*[37,38] have reported a theoretical study which predicts a loss of bond selectivity as a function of increasing kinetic energy of the incident molecule. By performing quasi-classical trajectory (QCT) calculations, they also predict changes in the reactivity of methane due to the successive replacement of H atoms by D atoms in the CH_4 molecule both in the ground state and for vibrationally excited molecules. In this context, Chen showed in his dissertation a preliminary study of the relative reactivity of the four methane isotopologues. As he wrote in his thesis, he left as a *future experiment a complete and more detailed study of the dependence of the sticking coefficient on kinetic energy for both molecules in the ground state and vibrationally excited molecules*. For this reason, this section builds on his previous work.

4.2.1. RAIRS detection of isotopologues of methyl species.

When a partially deuterated methane isotopologue (CH_3D, CH_2D_2 or CHD_3) dissociatively chemisorbs on a platinum surface, there are two possibilities for the reaction: either the C-H or the C-D bond can break. Previously in our group, RAIRS was demonstrated to be a powerful technique to distinguish between the different products on the surface[29,50,51]. Confirming the capabilities of RAIRS, spectra following deposition of the four methane isotopologues on Pt(111) were re-measured. Figure 4-4 shows the products of the dissociation in the RAIR spectra for several methane isotopologues and gives the peak assignments for the different methyl products species. The results shown in Fig. 4-4 agree well with the spectra previously reported by Li Chen. For further details about the peak assignments, please refer to Table 4-4 and Chen's thesis[50].

As we can see in Figure 4-4, CO adsorption is observed on the Pt(111) surface due to a CO impurity in the molecular beam and from the UHV background. In all the measurements presented here the contamination was less than 1% of a monolayer at the end of the deposition experiments.

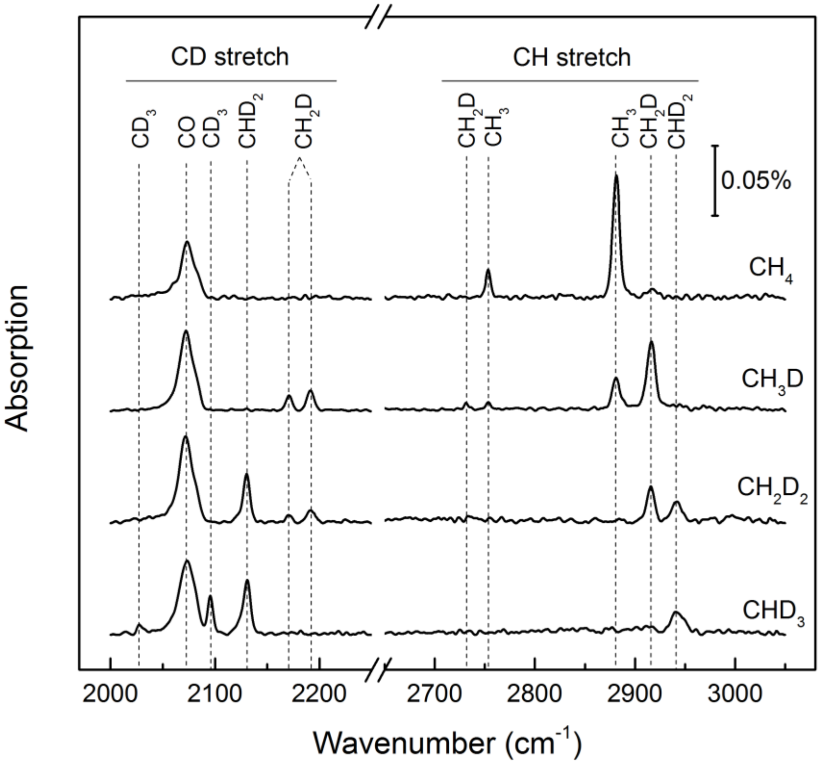

Figure 4-4. RAIRS of methane isotopologues on Pt(111) at T_S=150 K. All the spectra were taken after 60 min deposition at T_N=700 K. The kinetic energies for the different species were: 57 kJ/mol (CH_4), 60 kJ/mol (CH_3D), 58 kJ/mol (CH_2D_2) and 66 kJ/mol (CHD_3).

4.2.2. A new strategy for the calibration of RAIRS intensities.

In order to quantify the extent of bond selectivity and calculate sticking coefficients for the different methane isotopologues, a calibration for the corresponding methyl products (CH_3, CH_2D, CHD_2 and CD_3) on the surface was needed.

Chen presents in his thesis[50] a calibration for the RAIR peak signal in terms of surface coverage for different methyl isotopologues. His method consisted on first getting a calibration factor for the CH_3 peak intensity after CH_4 molecular beam depositions by using AES following the procedure explained in section 3.3.3.1. Then, following deposition of CH_3D, where both CH_3(ads) and CH_2D(ads) methyl products are chemisorbed on the surface, he obtained the calibration factor for CH_2D(ads). For that, he recorded RAIR spectra and measured the C/Pt Auger ratio after several CH_3D depositions. Since in the first step of his calibration he had already obtained the calibration factor for CH_3(ads) he calculated the fraction of C coming from CH_3(ads) after deposition of CH_3D. The remainder C measured with AES was therefore coming from CH_2D(ads). By comparing the CH_2D peak intensity and the C coverage associated with CH_2D(ads), he obtained the calibration factor for CH_2D(ads). In this way, following depositions for the rest of the isotopologues, he determined the RAIRS calibration factors for all the methyl products.

However, following this procedure, any error introduced in the calibration of CH_3 is added to the calibration of CH_2D, and the error in both CH_3 and CH_2D calibration are both introduced in the CHD_2 calibration, etc. In order to reduce those errors, we performed a “laser-on” calibration. The main idea is to deposit only one methyl product on the surface at a time to get the calibration for each specific product independently. Using the laser to excite the C-H bond of CH_3D, CH_2D_2 and CHD_3 and measuring RAIR spectra for each deposition, we can confirm that the deposition of C-H stretch excited CH_3D, CH_2D_2 and CHD_3 yields only adsorbed CH_2D, CHD_2 and CD_3 products respectively. In this way, we used the C-H bond selectivity observed before[29] as a tool for the calibration.

As an example of the calibration for a particular methyl species on the surface, Figure 4-5 shows the calibration obtained for the CH_2D RAIRS peak at 2918 cm^{-1}, which corresponds to the C-H stretch vibration of the adsorbate on the surface. For this calibration, CH_3D molecules in the incident beam were excited to the ν_4 antisymmetric C-H stretch vibration, yielding only CH_2D products on the surface. The resulting coverage was varied by performing experiments at different incident translational energies and by performing experiments for different incident doses.

Figure 4-5 a) shows RAIR spectra after several depositions of stretch excited $CH_3D(\nu_4)$ on the Pt(111) surface. I detected four bands assigned to C-D stretch (peaks at 2172 and 2191 cm^{-1}), the first overtone of the C-H bend (2731 cm^{-1}) and the C-H stretch (at 2917 cm^{-1}). I chose the C-H stretch at 2917 cm^{-1} as representative of the CH_2D(ads) on the surface because it has the highest transition dipole moment of the four bands. The peak height was obtained using function J from the Bruker software OPUS.

Figure 4-5 c) shows the AES C/Pt profiles following each deposition. The C/Pt ratio was plotted as a function of RAIRS absorption, as we can see in Figure 4-5 d). To determine the conversion from peak height to coverage, a straight line was used for the fitting. Absorption peak height to coverage conversion factors for the different methyls are shown in Table 4-1. The given values are calculated as the linear fit gradient divided by 0.8 to account for the conversion between C/Pt and carbon coverage.

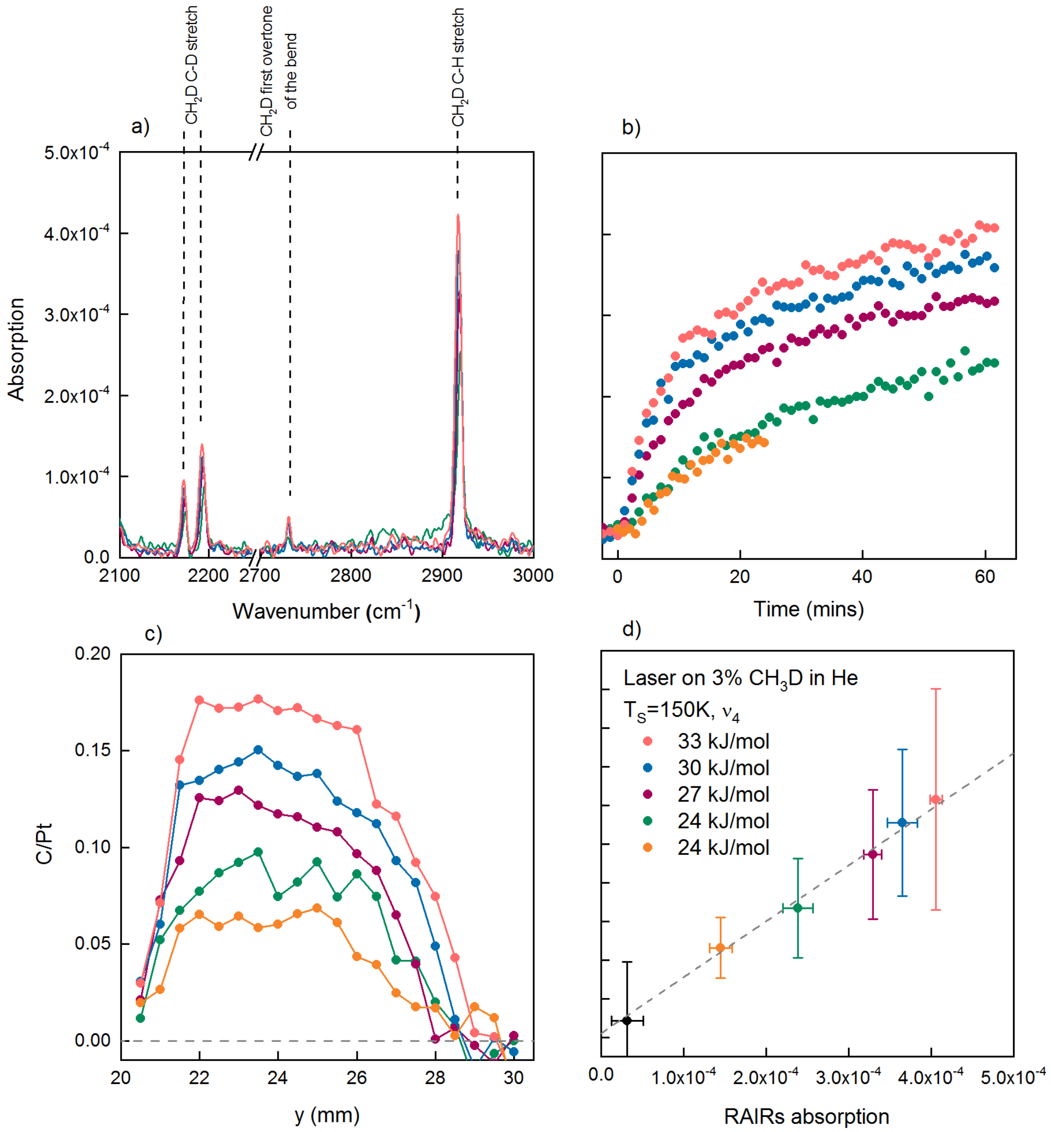

Figure 4-5. CH_2D RAIRS calibration measurements: a) The final RAIRS spectra for different incident doses, each obtained by averaging 4096 scans; b) CH_2D uptake curves recorded during the deposition following the growth of the C-H stretch; c) Auger scans taken after every deposition measurement; d) C/Pt AES signal ratio *vs* RAIRs absorption peak signal for the C-H stretch peak at 2917 cm^{-1} peak.

	Calibration factor (ML/absorption unit)	Chen's calibration factor (ML/absorption unit)
CH_3 (C-H sym stretch)	248	242
CH_2D (C-H stretch)	360	362
CHD_2 (C-D stretch)	455	406
CD_3 (C-D sym stretch)	268	226

Table 4-1. Measured absorption peak height to coverage factors obtained from the calibration measurements. The calibration factors obtained previously by Li Chen are also shown, being both calibrations in agreement with a maximum deviation of 18% for the CD_3 calibration factor.

4.2.3. Laser-off results

The dissociative chemisorption of the three partially deuterated methanes (CH_3D, CH_2D_2 and CHD_3) was studied for a range of translational energies (47-66 kJ/mol). The incident translational energy of the molecules was increased by raising the nozzle temperature which also increases the thermal vibrational energy of the molecules. C-H and C-D cleavage are observed at all the translational energies studied for the laser-off depositions. Examples of spectra following deposition of the three partially deuterated methanes and CH_4 are displayed in Figure 4-4.

4.2.3.1. Branching ratios

By measuring RAIR spectra during the deposition of the methane molecules on the Pt(111) surface, it is possible to record uptake curves for the C-H and C-D cleavage channels by integrating the peaks of interest. Examples of uptake curves are shown in Figure 4-6. The absorption peak heights were converted to carbon coverage by using the calibration presented above. The analysis of the CD_3 peak was slightly more complicate due to the spectral overlap with the CO peak in the RAIR spectra due to a CO contamination. In order to remove the influence from the CO adsorption, the two peaks where fit by Gaussians in the region between 2040 and 2120 cm^{-1}. As mentioned above, the contribution from the CO contamination was less than 1% of a monolayer at the end of all of these measurements and therefore it should not significantly perturb the uptake of the methyl species of interest through site blocking.

The uptake curves for the total coverage shown in Figure 4-6 were fit using a modified Langmuir model for dissociative adsorption using:

$$\frac{d\theta}{d\varepsilon} = S_0(1 - n_s\theta)^{n_s} \tag{4.1}$$

where θ is the methyl coverage, ε is the incident dose of molecules, S_0 is the initial sticking coefficient and $1/n_s$ is the saturation coverage. The exponent is taken as n_s to account for the change in the number of sites that the adsorbed methyl blocks on the surface with incident translational energies, which leads to an increase in saturation coverage with increasing translational energy[125]. After fitting the total coverage, the C-H and C-D cleavage channel uptakes were fit as a fraction of the total uptake to get a saturation coverage of each species. The branching ratio was then calculated as the ratio between the saturation coverages of the two dissociation channels.

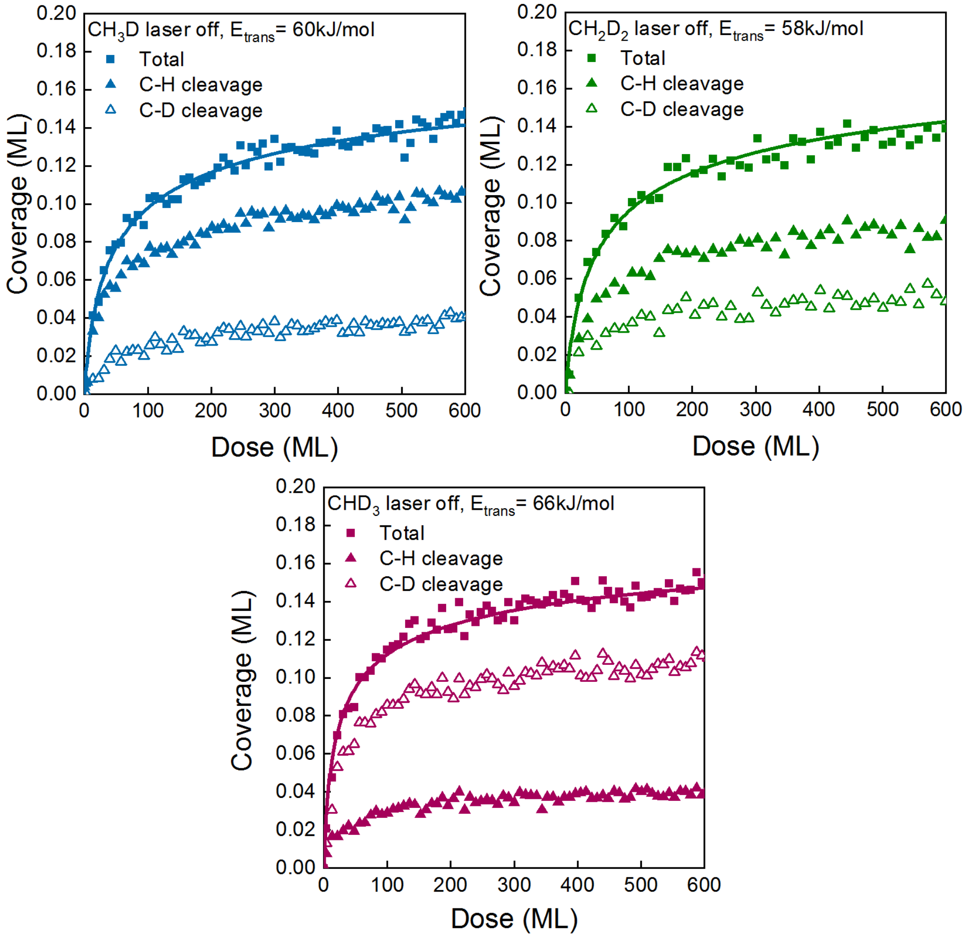

Figure 4-6. RAIRS uptakes for the dissociation of CH_3D, CH_2D_2 and CHD_3 measured at 60, 58 and 66 kJ/mol of translational energy respectively. The open triangles show the uptake for the C-D cleavage product and the filled triangles the one for the C-H cleavage product.

Figure 4-7 shows the branching ratios for C-H and C-D cleavage as a function of incident translational energy for the three partially deuterated methanes. For the three methane species, the relative yield of C-H cleavage asymptotically approaches the statistical ratio (25% for CHD_3, 50% for CH_2D_2 and 75% for CH_3D) with a slight preference for the C-H bond cleavage that is more pronounced at low incident energies. This effect can be attributed to the differences in the Zero Point Energies (ZPE) of the C-H and C-D bonds. The higher ZPE for the C-H bond leads to a lower barrier for C-H cleavage than for C-D cleavage, yielding a preferential cleavage for the C-H channel. At higher translational energies, steric factors dominate: in the case of CHD_3, the C-H bond has 25% chances to impinge the surface with its C-H bond towards the surface, while the C-D bonds have 75% of being one of the bonds placed towards the surface when the reaction occurs. This is why the branching ratio for this molecule approaches C-H/C-D=0.25. The same argument applies for the other two deuterated methanes.

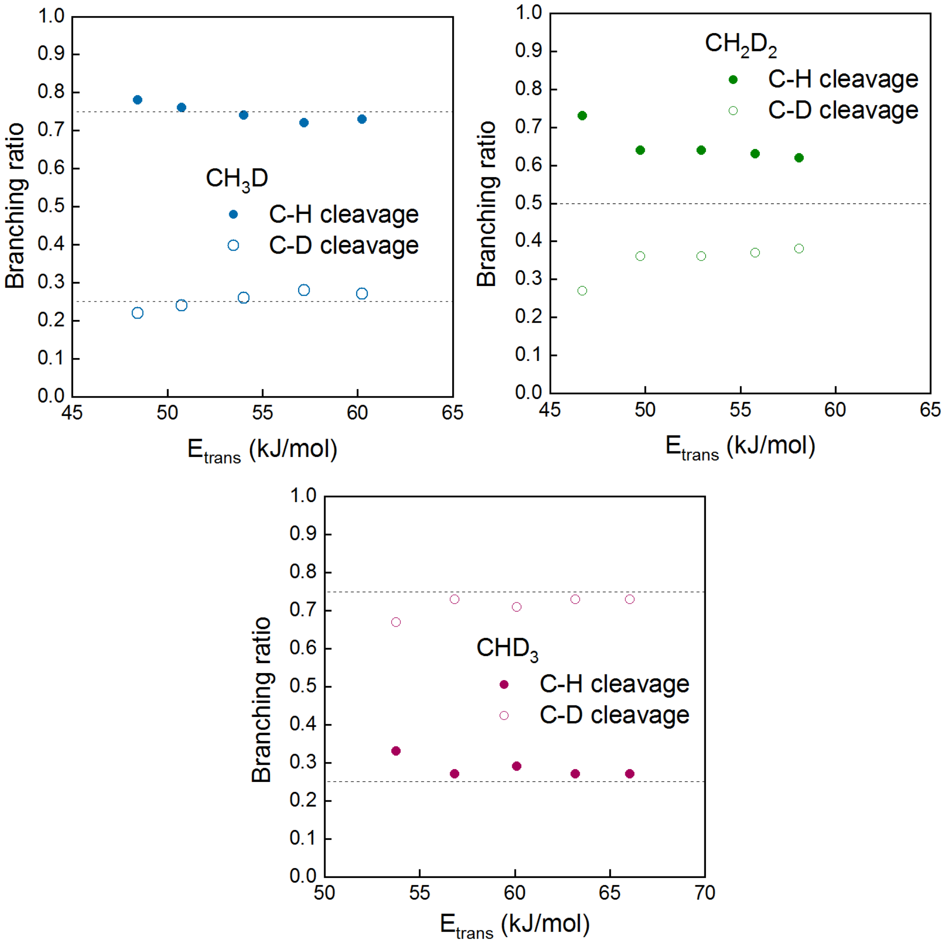

Figure 4-7. Branching ratios as a function of translational energy for CH_3D, CH_2D_2 and CHD_3. The dashed lines in each plot show the values that correspond to the statistical branching ratio.

This result agrees well with previous experimental results for the reaction between CHD_3 and Ni(111) where Killelea *et al.*[28] found an enhancement of the C-H cleavage at low energies. For the same system, using their Reaction Path Hamiltonian (RPH) model[36], Jackson and coworkers predicted a ZPE-corrected barrier for C-H cleavage 0.05 eV lower than for C-D cleavage[162]. Thus, the C-H bond is predicted to be more reactive than the C-D bond and they expected the ratio of C-H:C-D cleavage to be higher than statistical at low kinetic energies. Their predictions for the ground state and three different vibrationally excited states are shown as the solid lines in Figure 4-8. In the same figure, in circles, we can see the branching ratios reported by Guo and coworkers[25]. Contrary to what we observed, the quasi-classical approach followed by Guo predicts a slight preference toward the C-D bond cleavage at lower incident energies.

This prediction, still not understood at present, contradicts the energetic balance. On the other hand, QCT calculations by Nattino *et al.*[43] for the dissociation of CHD_3 on Pt(111) and by Shen *et al.*[38] and Lozano *et al.*[37] for all the partially deuterated isotopologues of methane on Pt(111) predicted an enhancement of C-D cleavage over the C-H at high energies where the branching ratio would be expected to be statistical.

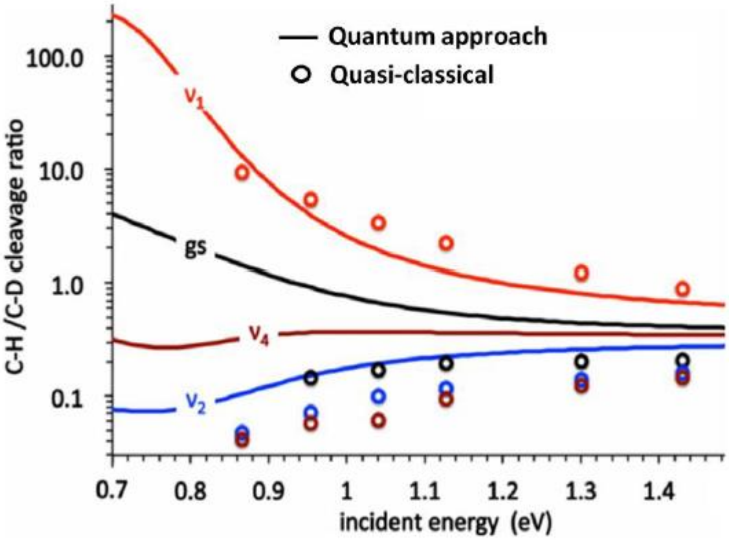

Figure 4-8. C-H:C-D branching ratio for CHD_3 molecules in either the ground state (gs) or one of the vibrational states indicated. ν_1 is the C-H symmetric stretch normal mode, ν_2 the C-D symmetric stretch and ν_4 corresponds to the C-D antisymmetric stretch. The lines correspond to a quantum approach[36] while circles are results from quasi-classical calculations[25]. Figure adapted with permission from[46].

4.2.3.2. Sticking coefficients

From the uptake experiments presented in the previous paragraphs, the initial reactivities were obtained as the initial slope of the uptake curves fit using equation (4.1). In Figure 4-9, S_0 is plotted as a function of incident translational energy for CH_4, CH_3D, CH_2D_2 and CHD_3. To better visualize the trend in S_0 as a function of inicident translational energy, the data S_0 points were fit using S-shaped reactivity curves. Figure 4-9 shows how the reactivity of the isotopologues decreases with increasing deuteration due to the difference in zero point energies of the C-H and C-D bonds leading to a preferential cleavage of the C-H bond.

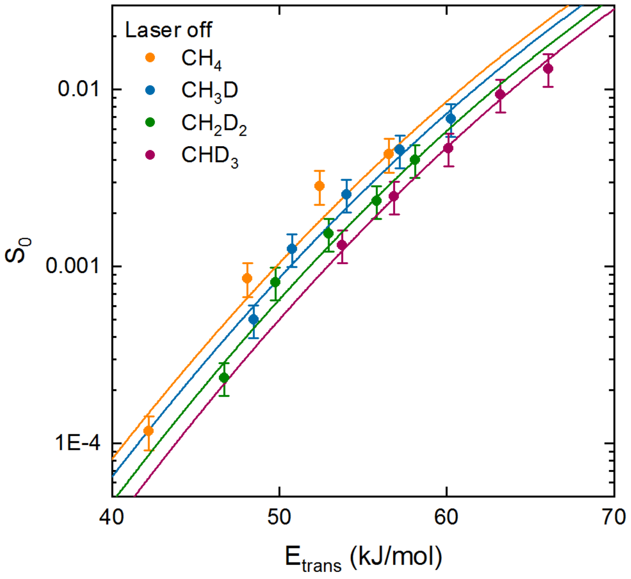

Figure 4-9. Sticking coefficients obtained for laser-off experiments for CH_4 (black), CH_3D (blue), CH_2D_2 (green) and CHD_3 (red) on Pt(111) at T_S=150 K.

The ratio of the initial sticking probabilities $S_0(CH_4)/S_0(CHD_3)$ is approximately 2. This result agrees with previous measurements done by Luntz *et al.*[110] who measured a sticking coefficient a factor 2.5 lower for CD_4 than CH_4 at a surface temperature of 800K. A larger difference was measured by Winters[12], who reported a sticking coefficient 4.5 larger for CH_4 than for CD_4. QCT calculations by Shen *et al.*[38] also predicted the reactivity of the deuterated isotopologues to decrease with increasing deuteration. Figure 4-10 shows the predicted S_0 for all the isotopologues as a function of initial translational energy. In order to confirm that the reason for the reactivities to decrease with further deuteration is the different ZPE, they calculated the reactivities for an artificial CD_4 molecule that they referred to as CD_4* whose ZPE was set equal to that of CH_4. As it is shown in the inset of Figure 4-10, the S_0 calculated for this artificial CD_4* is the same as for CH_4, showing that the difference between ZPE for CH_4 and CD_4 is responsible for this isotope effect observed in the reactivities.

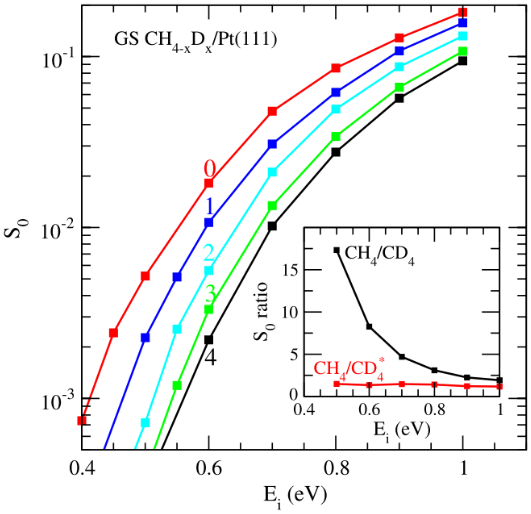

Figure 4-10. Initial sticking probability S_0 of the isotopologues of methane in the vibrational ground state (GS) on Pt(111) as a function of initial incident energy. Inset: ratios $S_0(CH_4)/S_0(CD_4)$ and $S_0(CH_4)/S_0(CD_4{}^*)$ as a function of energy, being CD_4 an artificial molecule CD_4 molecule wose ZPE is set equal to that of CH_4. Reproduced with permission from Ref[38].

4.2.4. Laser-on results

4.2.4.1. Branching ratios

RAIR spectra recorded after 60 minute depositions are shown in Figure 4-11 for CH_3D (left panel), CH_2D_2 (middle panel) and CHD_3 (right panel). The lower black spectrum in each panel corresponds to those recorded without laser excitation, with the peaks observed above 2700 cm^{-1} being due to C-H vibrations and those below 2250 cm^{-1} to C-D vibrations. For all partially deuterated isotopologues both C-H and C-D cleavage are observed at all the translational energies in the present study when there is no laser excitation. The laser-on spectra (show in red) where one quantum of C-H stretch vibration was added to ν_4 in CH_3D, to ν_6 in CH_2D_2 and to ν_1 in CHD_3. The spectrum presented for each of the isotopologues corresponds to the highest translational energy studied for each respective species. This confirms that the C-H bond selectivity measured previously at lower incident translational energies (~25 kJ/mol) is also seen at higher incident kinetic energies up to ~33-38 kJ/mol, demonstrating that the additional translational energy added in these experiments is insufficient to surmount the activation barrier to dissociative chemisorption. Otherwise, if it was, both C-H and C-D bond cleavage would be seen due to the non-selective nature of translational energy, as shown by the spectra obtained without laser excitation.

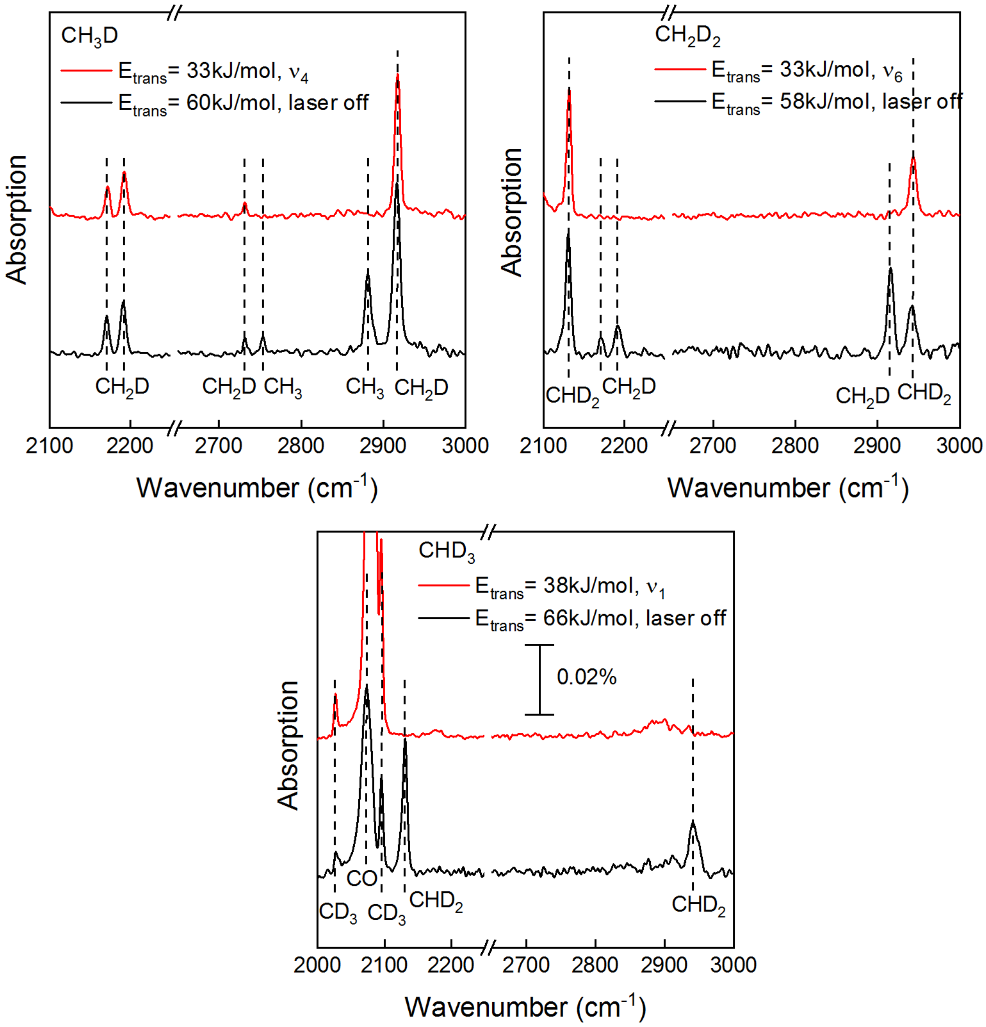

Figure 4-11. RAIR spectra following dissociation of CH_3D (left), CH_2D_2 (middle) and CHD_3 (right) for laser off measurements (black) and with one quantum of C-H stretch vibration (red).

A *loss* of bond selectivity has been predicted by QCT calculations performed by Shen *et al.*[38]. As it can be observed in Figure 4-12, the predicted C-H branching ratio as a function of incident translational energy for the three partially deuterated methanes in ground state (black), C-H stretch excited (red) and C-D stretch excitation (blue). For the range of kinetic energies that we studied, they also predict full C-H bond selectivity when exciting the molecules to ν_4 in CH_3D, to ν_6 in CH_2D_2 and to ν_1 in CHD_3. Further increase of the translational energy is expected to lead a loss of this bond selectivity due to the nonselective nature of the translational energy and by the decreasing role of the initial vibrational energy when the kinetic energy increases.

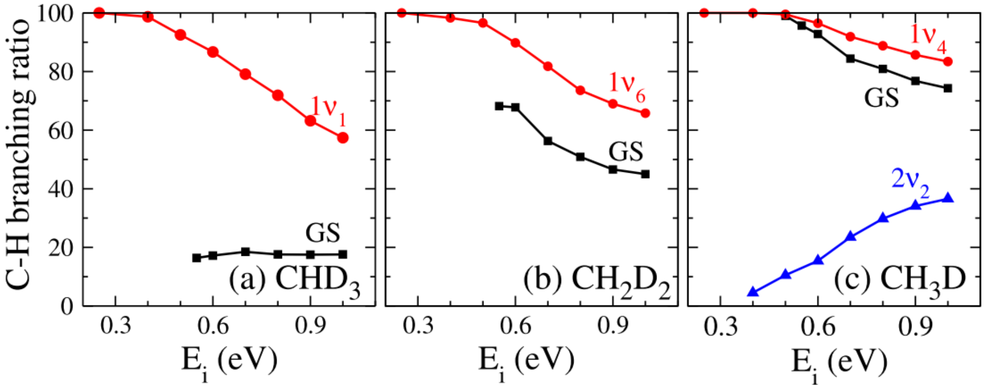

Figure 4-12. C-H branching ratio as a function of incident translational energy for the three partially deuterated methanes on Pt(111) for various initial vibrational states (ground state in black, C-H stretch excitated in red and C-D stretch excited in blue). Reproduced with permission from [38].

4.2.4.2. Sticking coefficients

The effect of C-H vibrational excitation on the reactivities of the methane isotopologues on Pt(111) was studied. Figure 4-13 shows S_0 as a function of incident translational energy for CH_4 (ν_3), CH_3D (ν_4), CH_2D_2 (ν_6) and CHD_3 (ν_1). Although the differences in reactivity fall within experimental error, the general tendency indicated that CH_2D_2 (ν_6) is most reactive isotopologue while CHD_3(ν_1) is found to be the least reactive one.

Several factors such as steric effects, different localization of the C-H stretch amplitude, mode specificity or isotope effects can contribute to the different reactivities of the C-H stretch excited methane reactivities. Localization of the C-H stretch excitation was shown to play an important role in the dissociation of CH_2D_2 on Ni(111)[20]. In this study, the reactivity of the ν_1+ν_6 vibration was found to be greater than that for 2ν_6 even though these two vibrations are nearly isoenergetic. In a local mode basis, these two states resemble the molecule having two quanta of vibration in a single C-H bond in the case of ν_1+ν_6 vibration, while the 2ν_6 vibration would resemble the molecule having a single quantum of C-H stretch in each of the C-H bonds. The experimental results showed that localizing both C-H stretch quanta in a single C-H bond leads to a higher reactivity of CH_2D_2 than if nearly the same total vibrational is distributed over the two C-H bonds. Following this result, one would expect the C-H stretch excited CHD_3 to be the most reactive as the vibrational energy is localized in a single bond, and CH_4 the least reactive as the vibrational energy is distributed over four bonds. However, the orientation of the C-H stretch excited bonds with respect to the surface can also have an effect on the reactivity. Calculations have shown that the transition state corresponds to the dissociating bond being oriented towards the surface[39,43,45]. During the single surface collision, a C-H bond (which is the one that contains most energy) is most likely to be in the correct geometry to dissociate in CH_4 and least likely in CHD_3 simply because the last has only ¼ chances of impinging the surface with its unique C-H bond. Therefore, following steric effects, one would expect the CH_4 molecule to be most reactive and CHD_3 the least reactive. The influence of these two effects together with mode specificity compensates and leads to the small difference in reactivity that is observed in the experiments.

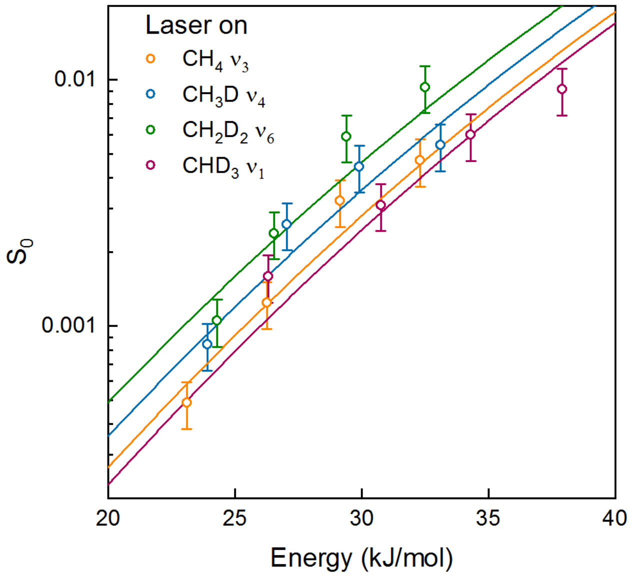

Figure 4-13. Sticking coefficients obtained for laser-on experiments for CH_4 (black), CH_3D (blue), CH_2D_2 (green) and CHD_3 (red). The solid lines are fits to the data obtained using equation (4.2).

Figure 4-14 shows the sticking coefficients predicted by QCT[37] as a function of translational energy for the C-H stretch excited methane isotopologues. The predicted reactivities are also very close to each other as happens to be experimentally, although CH_4 (ν_3) is predicted to be the most reactive one.

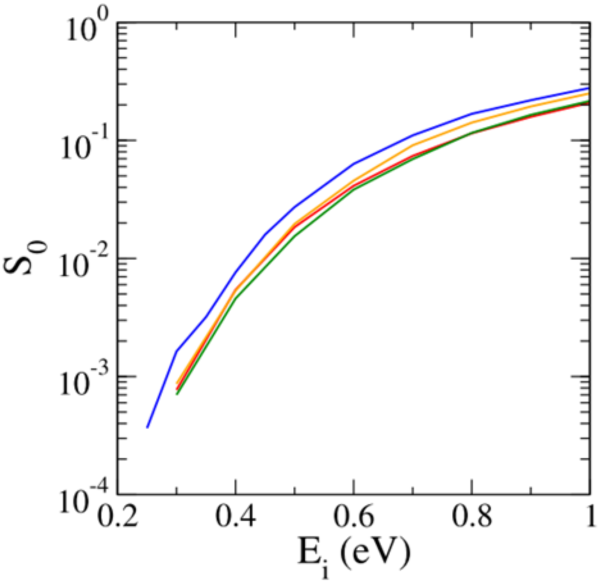

Figure 4-14. Reactive sticking probability, S_0, as a function of the molecular translational energy for CH_4 (ν_3) (blue), CH_3D (ν_4) (orange), CH_2D_2 (ν_6) (green) and CHD_3 (ν_1) (red). Reproduced with permission from[37].

4.2.4.3. Vibrational efficacies

The vibrational efficacy for each particular vibrational mode ν_i was calculated using:

$$\eta(\nu_i) = \frac{(E_0(\text{laser-off}) - E_0(\text{laser-on}))}{E_{\text{vib}}(\nu_i)} \tag{4.2}$$

where $E_{\text{vib}}(\nu_i)$ is the vibrational energy of mode ν_i and E_0 is the barrier height for the dissociation for laser-on and laser-off obtained by fitting the experimental data using equation (3.1). The efficacies for the C-H stretch vibrations in each of the isotopologues of methane are given in Table 4-2.

All the efficacies are lower than unity, indicating that vibrational energy is less efficient in promoting the dissociation of the methane isotopologues on Pt(111) than the translational energy. The value for $CH_4(\nu_3)$ from the current study is in excellent agreement with the value of 0.71 obtained previously[125] and lower than on Ni(111)[140] where the efficacy for $CH_4(\nu_3)$ is 1.25, in agreement with the already predicted earlier barrier for Pt(111) than for Ni(111)[141]. The order for the efficacies obtained is CH_2D_2 (ν_6)> CHD_3 (ν_1)> CH_3D (ν_4)> CH_4 (ν_3). The efficacy of CH_2D_2 (ν_6) was predicted to be higher than that of CH_3D

(ν_4) on Pt(111) using the SVP model[22] in agreement with the results presented here.

Molecule (mode)	$\Delta E_0(\nu_i)$	$E_{vib}(\nu_i)$	$\eta(\nu_i)$
CH_4 (ν_3)	24.7	36.4	0.68
CH_3D (ν_4)	26.4	36.3	0.73
CH_2D_2 (ν_6)	28.8	36.2	0.80
CHD_3 (ν_1)	26.9	36	0.75

Table 4-2. Vibrational efficacies for CH_4 (ν_3), CH_3D (ν_4), CH_2D_2 (ν_6) and CHD_3 (ν_1) on Pt(111).

4.3 Bond and site selective dissociation of CH_3D on Pt(211)

4.3.1. RAIRS detection of methyl isotopologues on the steps and terraces of Pt(211)

Previous RAIRS measurements (see Ref[29] and Figure 4-4) showed that methane isotopologues (CH_4, CH_3D, CH_2D_2, and CHD_3) dissociate on the terrace sites of Pt(111) resulting in the nascent products CD_3(ads), CHD_2(ads), CH_2D(ads), and CH_3(ads) which can readily be distinguished by RAIRS. The Pt(211) surface comprises three different types of surface atoms which we designate as step, terrace, and corner sites, as shown in Figure 2-9. As I have shown in chapter 3, the dissociation product CH_3(ads) can be detected using RAIRS with surface site selectivity on both the step and terrace sites.

Here, I combined both the abilities of RAIRS to distinguish between different dissociation products on the surface with its site-specific detection. Figure 4-15 shows RAIR spectra following dissociation of the five different methane isotopologues on Pt(211). Table 4-3 shows the molecular beam energies used in these experiments. At the incident energies used to get the spectra in Figure 4-15 and following the results presented for CH_4 on Pt(211) in chapter 3, the methane molecules are expected to dissociate on both the steps and the terraces of the Pt(211) surface but not on the corner sites due to the much higher barrier for dissociation predicted on these sites[105].

By comparing the peaks that appear in the different spectra, I identified the products corresponding to each peak. However, as we can see from the assignment at the top of Figure 4-15, overlap of some of the vibrations is observed. On one hand, in the C-D stretch region of the spectrum, there is a peak at 2131 cm^{-1} that is assigned to CD_3(ads) since it appears after the dissociation of CD_4(ads) on the surface, but it is also assigned to CHD_2(ads) since we also detect it after the dissociation of CH_2D_2 (but not of CH_3D). On the other hand, at 2948 cm^{-1}, a slightly broad feature appears to come from both CH_2D(ads) and CHD_2(ads).

Mixture	T_N (K)	E_{trans} (kJ/mol)	<E_{vib}> (kJ/mol)	E_{TOT} (kJ/mol)
3% CH_4 in He	500	40	1.6	41.6
	800	65	8.1	73.1
3% CH_3D in He	500	44	2.0	46.0
	800	66	9.3	75.3
4% CH_2D_2 in He	500	34	2.0	36.0
	800	67	9.0	76.0
3% CHD_3 in He	500	45	2.9	47.9
	800	95	11.9	106.9
2% CD_4 in He	500	48	3.5	51.5
	800	72	13.4	85.4

Table 4-3. Energy (kJ/mol) contents of the molecular beams used for the experiments shown in Figure 4-15 and Figure 4-16.

The assignment of the vibrations associated to the methyl isotopologues adsorbed on the step and terrace sites was obtained by comparison of the spectra after dissociation of every methane isotopologue on Pt(211) with the corresponding spectrum after the dissociation of the same isotopologue on the flat Pt(111) surface where there are only terrace sites. The peaks that appear at similar frequencies on both spectra were assigned to methyl products chemisorbed on the terrace sites. This assignment is confirmed by the site-specific reactivity demonstrated in chapter 3: performing experiments at low incident energies, we expect the reactant molecules to dissociate exclusively on the more reactive steps of the surface.

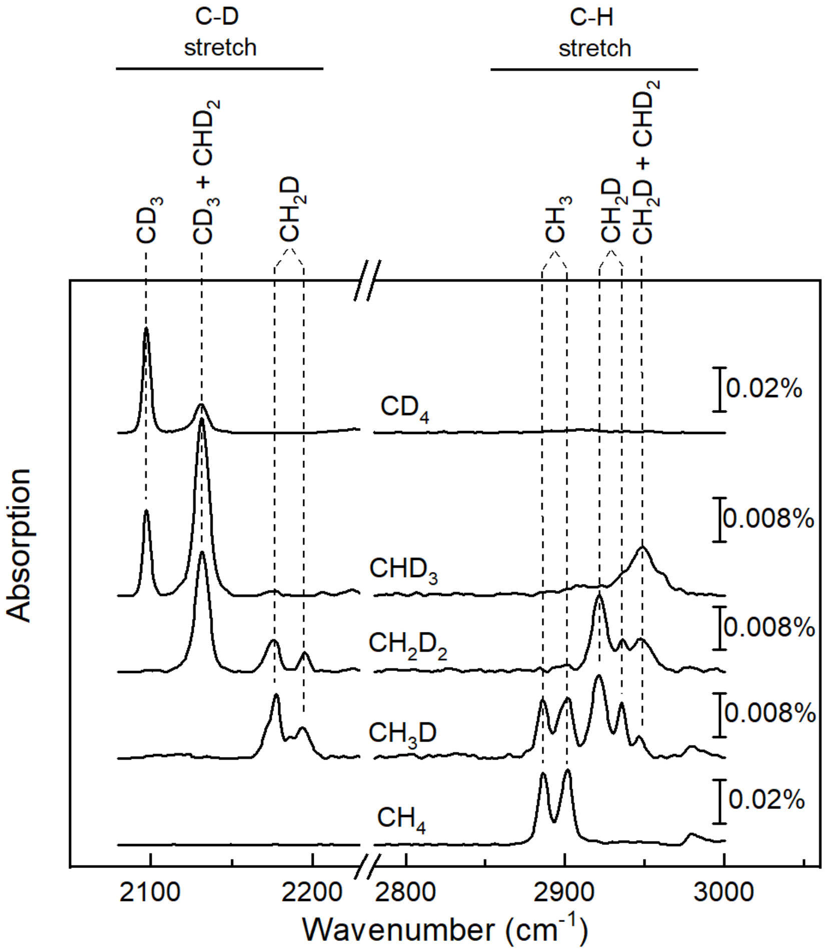

Figure 4-15. RAIRS after deposition of methane isotopologues on Pt(211) at T_S=150 K. All the spectra were taken after 80 min deposition at T_N=800 K. The kinetic energies for the different species are shown in Table 4-3.

Figure 4-16 shows spectra measured after depositions of CD_4, CHD_3 and CH_2D_2 on Pt(111) and on Pt(211) at two incident energies, allowing for the identification of all the peaks. Table 4-4 lists all the observed vibrational frequencies and the mode assignments for all the nascent dissociation methyl products of the five different methane isotopologues on Pt(211). However, due to the overlap of some of the bands, I decided to continue performing the bond selectivity study on Pt(211) for the dissociation of CH_3D, where all the products are readily identified.

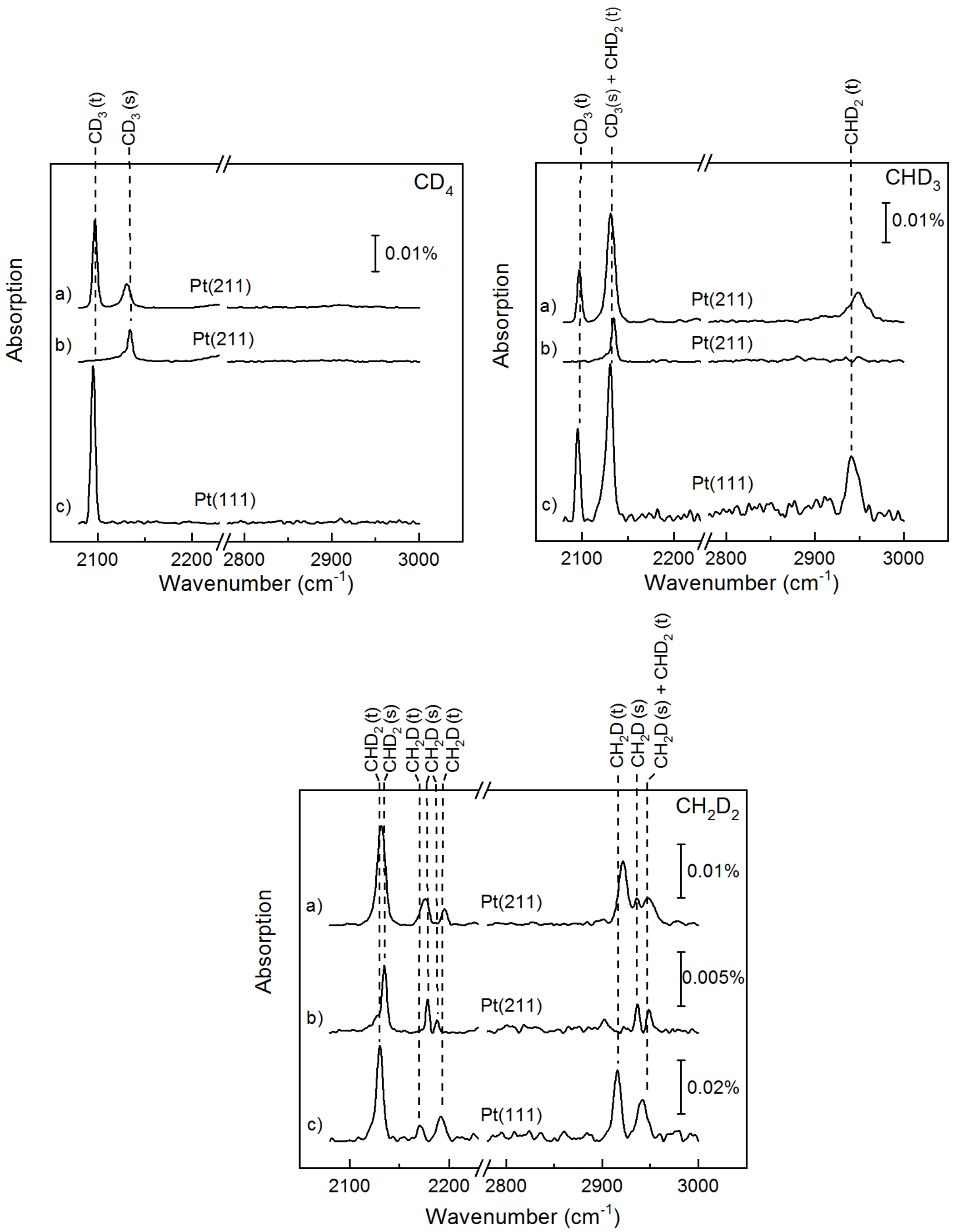

Figure 4-16. RAIR spectra following dissociation of CD_4, CHD_3 and CH_2D_2 on a) the Pt(211) surface at T_N=800 K, b) the Pt(211) surface at T_N=500 K, c) the Pt(111) surface at T_N=800 K. The surface temperature was kept at T_S=150 K in all these experiments.

Figure 4-17 a) displays a RAIR spectrum of the nascent chemisorption products of CH_3D on Pt(211). Comparison with the spectra for CH_3D/Pt(111), CH_4/Pt(211) and CH_4/Pt(111) is also shown. We note that in the C-H stretch region, the absorption due to CH_2D(ads) on the step sites is split into a doublet separate by 11 cm^{-1}. In the C-D stretch region both the step and the terrace peaks due to CH_2D(ads) are split and only partially resolved. Figure 4-18 shows the uptake curves for the two peaks associated to the C-H stretch vibration of CH_2D on the steps (at 2936 and 2948 cm^{-1}). As we can see, both peaks grow in the spectrum at the same rate, confirming their assignment to CH_2D adsorbed on the same surface site. Although the precise origin of the observed splitting is not fully understood, the most likely explanation is that it is due to an anharmonic coupling of CH_2D(ads) vibrations. We exclude any orientation effects of the CH_2D(ads) on the steps with the C-H or the C-D bond pointing toward the step from being responsible for the observed splitting based on DFT calculations that predict the methyl groups to be freely rotating on the surface at T_S=150 K.

Methyl	Frequency (cm^{-1})			Mode assignment
	Pt(111)	Pt(211)		
	terraces	terraces	steps	
CH_3(ads)	2881	2886	2903	Symmetric C-H stretch
	2754	2752	-	First overtone of anti-symmetric C-H bend
CH_2D(ads)	2915	2921	2936 & 2948	C-H stretch
	2733	2730	-	First overtone of C-H bend
	2171 & 2191	2173 & 2194	2178 & 2187	C-D stretch
CHD_2(ads)	2941	2948	?	C-H stretch
	2129	2132	2135	C-D stretch
CD_3(ads)	2094	2097	2132	Symmetric C-D stretch
	2027	2026	-	First overtone of C-D bend

Table 4-4 RAIRS band assignments of all the nascent dissociation methyl products of the five different methane isotopologues on Pt(211) at T_S=150 K. Peak frequencies are taken from comparison of spectra in Figure 4-15, Figure 4-16 and Figure 4-17.

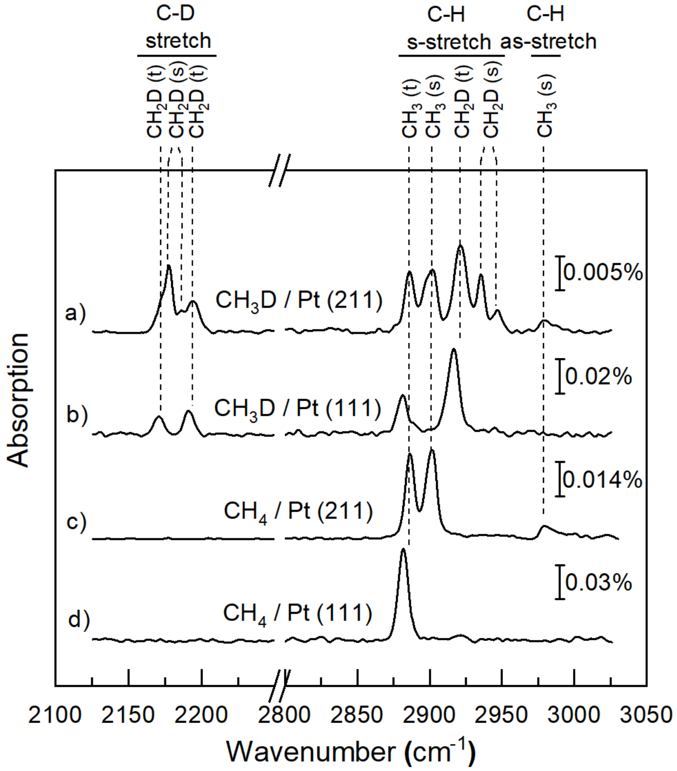

Figure 4-17. RAIR spectra taken at T_S=150 K following deposition of a) CH_3D on Pt(211), b) CH_3D on Pt(111), c) CH_4 on Pt(211), and d) CH_4 on Pt(111).

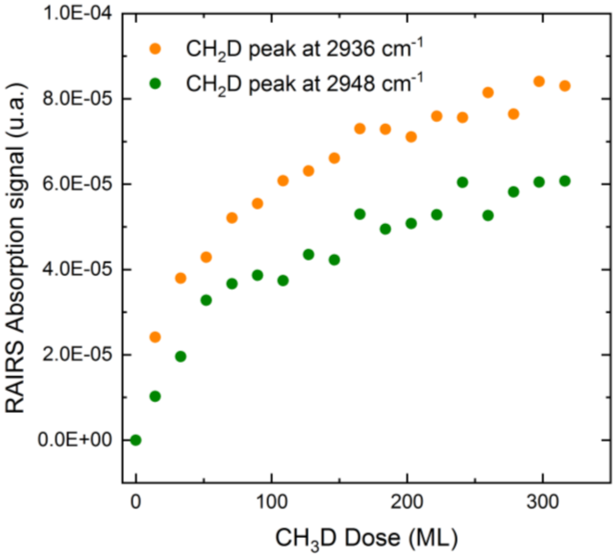

Figure 4-18. Uptake curves (Absorption signal *vs* Dose) of the two peaks associated to CH_2D on the steps in the C-H stretch region of the spectrum. Molecular beam: 3% CH_3D at E_{trans}=53 kJ/mol.

4.3.2. Bond selectivity on Pt(211)

To probe the extent of translational and vibrational activation of CH_3D dissociation on Pt(211), I performed deposition experiments at different translational energies, with and without laser excitation of the C-H stretch mode ν_4. Figure 4-19 a) shows a series of laser-off RAIR spectra, each taken following deposition of a molecular beam of CH_3D at different translational energies (E_{trans}). As we can see, dissociation via C-H and C-D cleavage occurs exclusively on the steps of the surface when the translational energy of the molecular beam is between 25 and 53 kJ/mol. At translational energies E_{trans} ≥58 kJ/mol, the molecules dissociate via both channels on both the steps and the terraces of the surface. This result agrees with the previously shown in chapter 3 lower barrier for dissociation on the steps than on the terraces of the Pt(211) surface.

Figure 4-19 b) shows RAIR spectra obtained after deposition of the CH_3D at the same E_{trans} than on Figure 4-19 a) but using the laser to excite the C-H bonds of the molecule. The CH_3D molecules were excited with one quantum of C-H antisymmetric stretch vibration (ν_4) before reaching the surface. Therefore, in the laser-on experiments, the molecules contained three sources of energy: translational energy, thermal vibrational energy due to the heating of the nozzle, and the extra quantum of vibrational energy (36.3 kJ/mol) added by the laser specifically on the C-H bonds. Since the two first sources of energy are common in the laser-off and laser-on experiments, any difference between the spectra shown in Figure 4-19 a) and b) is due to the effect of ν_4 excitation of the molecules on the dissociation.

As we can see, at the lowest translational energy E_{trans} =10 kJ/mol, where no chemisorbed products were detected after the laser-off deposition, fully bond- and site-specific dissociation occurs for the ν_4-excited CH_3D molecules yielding exclusively the CH_2D(ads) product on the steps of the surface. By increasing the translational energy of the incident molecules (E_{trans} ≥25 kJ/mol), C-D cleavage starts to occur on the steps although an enhancement of the C-H over C-D cleavage is still observable. The full C-H bond selectivity that we observed at 10 kJ/mol on the steps is switched to the terraces of the surface at E_{trans} =39-53 kJ/mol. In this range of translational energies, we only detect the C-H cleavage product CH_2D(ads) on the terraces of the surface (as well as the CH_3(ads) and CH_2D(ads) on the steps). At incident translational energies higher than 53 kJ/mol, both C-H and C-D cleavage products are observed on both, step and terrace sites.

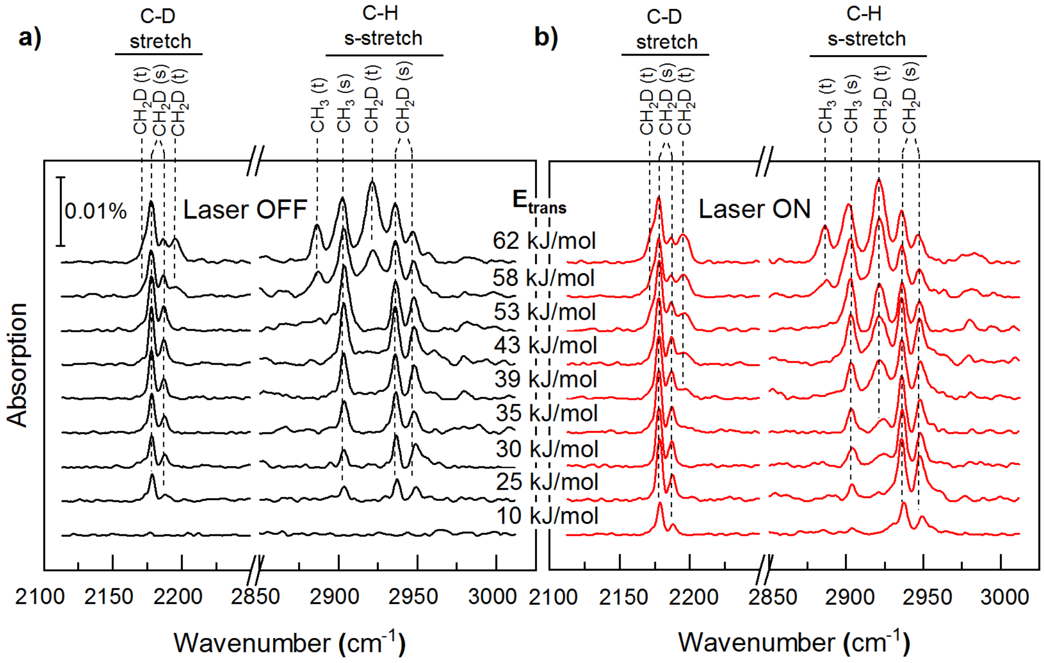

Figure 4-19. Dissociation of CH_3D on the Pt(211) surface at different translational energies (E_{trans}) without (a) left panel) and with (b) right panel) state specific laser excitation of the incident molecules.

4.3.3. Degree of bond selectivity

In Figure 4-19 b) we can see how full bond selectivity is reached either on the step or on the terrace sites of the surface by controlling the translational and state specific vibrational energy. However, since we do not excite 100% of the incident molecules, in all the laser-on experiments we have a contribution from the molecules that are excited to ν_4, and from the non-excited ones. Therefore, the following question arises: *is the fraction of ν_4-excited molecules dissociating exclusively by C-H cleavage at all the translational energies that we studied?*

If the answer is positive, we would say that we have “full-bond selectivity”, and the C-D cleavage products that we detect in Figure 4-19 b) would be just coming exclusively from dissociation of the fraction of non-excited molecules. In other words, the initial reactivity for the C-D cleavage channel (CH_3) would be the same for the laser-on and laser-off experiments taking into account the different fluxes.

$$S_{0_{CH_3}}{}^{laser\ ON} = S_{0_{CH_3}}{}^{laser\ OFF}(1 - f_{exc}) \tag{4.3}$$

If equation (4.3) is fulfilled, the reaction is C-H full bond selective and the fraction of excited molecules dissociate only via C-H cleavage (as it clearly happens at E_{trans} =10 kJ/mol on the step sites).

However, if a fraction of the laser-excited molecules dissociate also via C-D cleavage, the initial sticking coefficient for CH_3 will have the contribution from the non-excited molecules and from the laser-excited ones that dissociate via C-D cleavage. Therefore, the sticking coefficient for CH_3 would be larger in the laser-on than in the laser-off experiment (taking into account again the different fluxes):

$$S_{0_{CH_3}}{}^{laser\ ON} > S_{0_{CH_3}}{}^{laser\ OFF}(1 - f_{exc}) \tag{4.4}$$

Figure 4-20 shows the difference between $S_{0_{CH_3}}{}^{laser\ ON}$ and $S_{0_{CH_3}}{}^{laser\ OFF}(1 - f_{exc})$ as a function of translational energy for the steps. As we can see, for energies below 30 kJ/mol, the reaction is full-bond selective since the laser does not induce any increment in the reactivity for the C-D cleavage channel. For energies higher than 30 kJ/mol, the difference between the sticking coefficients becomes positive, meaning that equation (4.4) is fulfilled and full C-H bond selectivity is lost. Even though there may be an enhancement for the C-H cleavage channel, it becomes clear that a fraction of the laser-excited molecules dissociate via C-D cleavage at high energies.

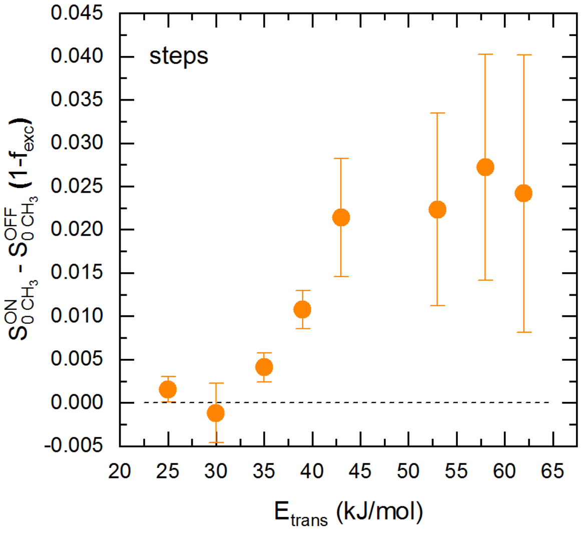

Figure 4-20. Difference between the S_0 (steps) for the C-D cleavage channel in the laser on and the laser off experiment. The dashed line corresponds to the full-bond selectivity condition (eq. 4.3).

A sketch of the energetics for this reaction is shown in Figure 4-21. Without state-specific C-H stretch excitation of the molecules, only translational energy and thermal vibrational energy are available for dissociation of the incident CH_3D molecules. This is the case shown in black in Figure 4-21. If the available energy (E_T) is enough to overcome the barrier for dissociation on a particular site, both C-H and C-D cleavage products are detected with a nearly statistical product branching ratio. A small preference for C-H cleavage at low energies due to the higher ZPE can also be observed, as it was shown in Section 4.2.3. on Pt(111).

Full bond selectivity can easily be observed at translational energies that are well-below the barrier for dissociation when we excite the molecules prior to dissociation. Since by exciting the molecules with one quantum of ν_4 vibration we are selectively adding energy to the C-H bonds of the molecule, only these C-H bonds have sufficient energy to break at the gas-surface interface. If there is no scrambling of the initial C-H vibrational energy in the molecule, the C-D bond only has translational energy and thermal vibrational energy, which is not enough to dissociate. This case is observed on the steps at E_{trans} =10 kJ/mol and on the terraces between E_{trans} =39-53 kJ/mol. When the contribution from the translational energy and thermal energy is sufficient to overcome the barrier on a particular site, the effect of C-H excitation and the degree of bond selectivity decreases. Full bond selectivity is therefore lost at higher translational energies where the incident translational energy is enough for the bond in the most favoured geometry to dissociate, irrespective of whether it is vibrationally excited or not.

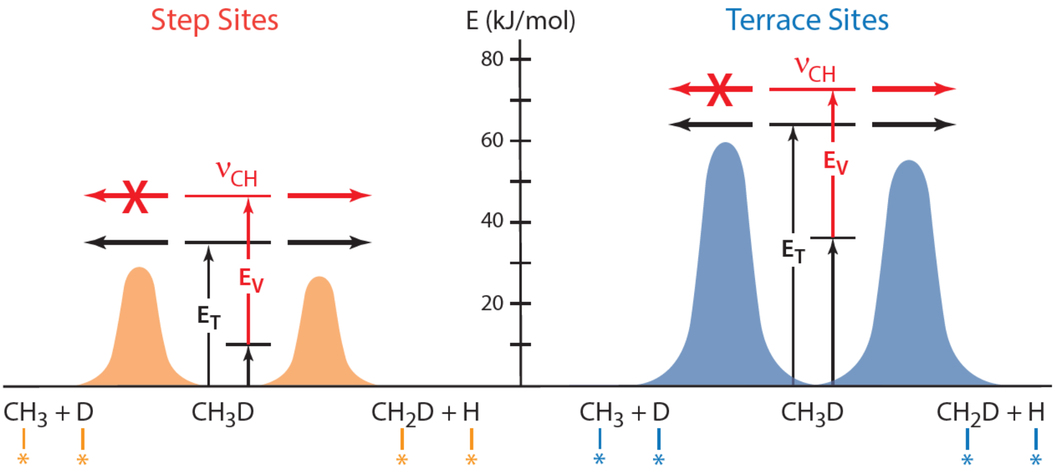

Figure 4-21. Schematics of energetics and dissociation pathways for CH_3D chemisorption on the steps (left) and terraces (right) of Pt(211). For laser-off depositions, the sum of incident translational energy and thermal vibrational energy is indicated in back as E_T. Once E_T exceeds the reaction barrier, both C-H and C-D cleavage are observed with a near statistical branching ratio. State specific laser excitation of the ν_4 C-H antisymmetric stretch normal mode adds E_V=36 kJ/mol selectively to the C-H bonds which enables bond selective C-H cleavage if the dissociation barrier cannot be overcome by E_T alone.

This loss of bond selectivity with increasing translational energy has been predicted theoretically by Lozano *et al.*[37] for the reaction between the three partially deuterated methanes on Pt(111) as it was presented in Figure 4-12. The authors attributed this decrease in bond selectivity to the non-selective character of the translational energy together with the decreasing role of vibrational energy when the translational energy increases.

4.4 Implications of bond selectivity

The implication of bond selectivity has been discussed in detail elsewhere[7,28,50,158]. Here I just briefly discuss it to emphasize the important piece of information that these bond selectivity studies provide about the dynamics of the gas-surface reaction.

In our experiments, excitation of the reactant molecules with single mode infrared radiation with a frequency bandwidth of less than <1 MHz, allows the preparation of the incident molecule in a single rovibrational eigenstate. These eigenstates of the isolated molecule can be obtained by diagonalization of the H_M Hamiltonian. Due to anharmonic couplings and vibration-rotation interaction terms, zero-order state mixing can happen and the vibrational eigenstates that we excite are not necessarily identical to the normal mode vibrations obtained for a harmonic intramolecular potential.

As an eigenstate of the isolated molecule, without any perturbation, it does not evolve in time. Hence, it does not show intramolecular vibrational redistribution (IVR). Moreover, the radiative lifetimes of the states prepared in this thesis are on the scale of milliseconds, longer than the flight time for the molecules to reach the surface from the point of excitation, which is in the order of 100 μs. Therefore, the excited molecule approaches the surface prepared in the vibrational state that we selected. However, once the molecule approaches the surface, the interaction between the molecule and the surface induces a perturbation V_S on the Hamiltonian of the isolated molecule yielding a new Hamiltonian $H_{M-S} = H_M + \lambda V_S$. The rovibrational state that was initially prepared by the laser is no longer an eigenstate of the new system characterized by H_{M-S}, and it can be expressed as a linear combination of the new set of eigenfunctions of H_{M-S}. Thus, the state prepared with the laser starts to evolve in time. This time-evolution of the excited state can induce scrambling of the energy that in the isolated system was localized on the C-H bond(s). This phenomenon, surface-induced intramolecular energy redistribution (IVR), may induce a flowing of energy from the initially excited C-H bonds to the C-D bonds and therefore cause a break-down of the bond selectivity.

The fact that bond selectivity can be observed on the Pt(111) and Pt(211) means that the time that the molecule spends at the interface with the surface is short compared to the time needed for the energy to flow (IVR) between the different bonds. In other words, IVR must be incomplete on the timescale of the collision, and the vibrational amplitude must stay localized in the C-H bond without being transferred to the C-D bonds.

IVR is usually described using the “tier model”[163]: first, the vibrational energy flows from the initial prepared states into the intermediate “doorway” states resulting in a rapid IVR; and then, complete redistribution of the energy to a statistical energy distribution happens when the energy flows from the doorway states to the dense bath of states of the molecule. The first and rapid IVR happens via strong low-order anharmonic interactions with a few almost-degenerate basis set. It has been shown to depend mostly on the molecule itself and not on the chemical environment, being therefore the initial rates of IVR very similar if the molecule is in gas-phase or in solution[164,165]. However, the long-term IVR strongly depends on the chemical environment.

In the experiments described in this chapter, the lowest incident velocity used was about 1000 m/s. Since the molecules start to experience the perturbation from the surface some Å away from the surface[158], they have some 100's of fs for IVR to happen and scramble the initially localized vibrational energy. However, the C-H vibrational states prepared in this chapter present a big mismatch to the C-D stretching. Therefore, there are not close doorway states that involve vibration of the C-D bonds to which the energy can flow.

The second component or tier of IVR happens from these doorway states into other tiers to which these doorway states are coupled. Here, the surface can also offer additional bath of vibrations where energy can flow. However, quenching to the surface is expected to be very slow for these systems due to the large mismatch with the surface phonon bath which is in the order of 200 cm^{-1}. For these reasons but mostly due to the inefficiency of the first and fast IVR, IVR does not happen or is incomplete in our experiments. Thus allowing bond selectivity to occur.

The loss of bond selectivity found at high translational energies for Pt(211) is however not related with IVR. If not, we would expect it to happen more strongly at low incident translational energies when more time is spent approaching the surface and therefore more time is available for the energy scrambling into the C-D bonds. The loss of bond selectivity at high incident energies is attributed to the non-selective character of the incident translational energy.

4.5 Summary

The dissociative chemisorption of partially deuterated methanes on Pt(111) and Pt(211) surfaces was studied by quantum state resolved methods using RAIRS detection of the dissociation products. The ability of this technique to distinguish between different dissociation products on different sites of the surface allows to follow the dissociation of the incident molecules as a function of incident translational energies and measure the site- and state-selective reactivity.

On the Pt(111) surface, we observed how CH_3D, CH_2D_2 and CHD_3 dissociate via C-H and C-D cleavage when no laser excitation was used. The branching ratio between the two channels was shown to be nearly statistical, with a slight preference for the C-H cleavage channel at low incident energies. The reactivity of the molecules without laser excitation was found to decrease with deuteration due to the higher ZPE of the C-H bond.

Full-bond selectivity was observed at all energies studied when the molecules were excited with one quantum of C-H vibrational energy. A comparison of the reactivities of the excited molecules ($CH_4(\nu_3)$, $CH_3D(\nu_4)$, $CH_2D_2(\nu_6)$ and $CHD_3(\nu_1)$) was presented. Factors including the localization of the vibrational energy and steric effects can be used to explain the small difference between the reactivities of the excited methane molecules.

Bond selectivity was also studied for the first time on a stepped surface. The dissociation of CH_3D on a Pt(211) was studied both laser-off and laser-on. Agreeing with the previous results shown in chapter 3, the step sites were found to be more reactive than the terrace sites.

C-H bond selectivity was studied for incident energies in the range of 10-62 kJ/mol. The degree of bond selectivity was shown to decrease with increasing translational energy. The results presented here indicate that once the translational and thermal vibrational energy is above the barrier for dissociation on a particular site, the promotion of bond selectivity on that site decreases. Therefore, the control of a particular bond cleavage on a specific site of the surface is possible by careful tuning of the incident translational energy and the vibrational state of the incoming molecules.

Chapter 5 Surface temperature dependence of methane activation on Pt surfaces

5.1 Introduction

The importance of the surface reaction site has been addressed in the previous two chapters. This last chapter of results also focuses on the surface, but in this case, I will concentrate on its temperature. We find in the literature many experiments concerning the role of the translational and vibrational energy of the incident gas-phase methane, but less attention has been paid to how vibrational energy of the surface (in the form of phonons) influences the reaction between methane and a metal catalyst. This in part because there is no such surface temperature dependence expected for a direct dissociation, since the reaction is very fast and there is no time for the molecules to equilibrate with the surface.

Raising the surface temperature increases the average vibrational energy of the surface due to the excitation of the lattice vibrations (phonons) and electron-hole pairs. Previous studies have reported an increase in the sticking coefficient with increasing surface temperatures for methane reactions on Ni(100)[166], Ni(111)[111], Pt(111)[110,167], and Ir(111)[168] among others. Initial attempts to rationalize a strong surface temperature dependence of the sticking coefficient invoked a reaction mechanism through a tunnelling process via a thermally accommodated molecular precursor[12]. Such a mechanism would be very sensitive to surface temperature because the dissociation rate is limited by the lifetime of the precursor state and this lifetime depends strongly on the surface temperature. However, surface temperature effects were also observed on chemisorption reactions that happen via a direct mechanism, such as CH_4 on Pt(111)[110]. Here, *thermally assisted tunneling* was used to explain the dramatic enhancement of S_0 with T_S[169]. In this model, thermal motion of the substrate influences the tunnelling probability by reducing the tunneling length of the barrier.

Using quantum state resolved experiments, the group of Utz has investigated the effect of surface temperature for the dissociation of methane on Ni(111)[124,170]. CH_4 molecules were excited to ν_3 C-H stretch vibration and the incident translational energy was varied such that the total energy of the incident molecules was near the energy threshold for reaction. Figure 5-1 shows S_0 as a function of incident translational energy for four different surface temperatures. The authors observed a strong increase in the reactivity with increasing surface temperature from 90-475 K at low incident translational energies of the molecular beam. The effect of the surface temperature was seen to decrease with increasing translational energy of the incident methane. These experimental observations were attributed to an increase in the thermally induced surface corrugation with surface temperature predicted by theoretical calculations[36,47,170]. In their model, Jackson and coworkers predict a change in the dissociation barrier height with lattice motion. In a manner, this surface induced corrugation can be pictured as a change in the coordination of the surface atoms, and hence has certain connection with the studies shown in chapters 3 and 4.

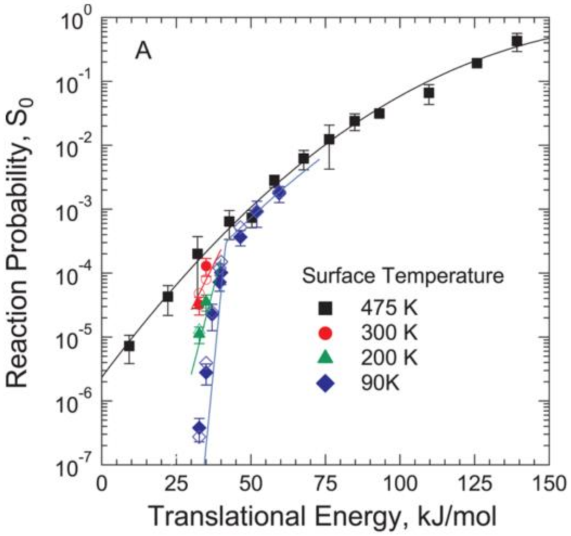

Figure 5-1. State-resolved S_0 for CH_4 (ν_3) dissociation on Ni(111) as a function of incident translational energies for different surface temperatures. Reproduced with permission from[170].

In this chapter 5, I explore the surface temperature dependence for methane dissociation on platinum surfaces. This chapter is divided into two parts depending on the range of incident translational energies studied and the technique used for the detection:

1. A similar experiment to that of Utz's on Ni(111)[124] was performed on Pt(111). The state resolved sticking coefficient of $CH_4(\nu_3)$ was studied as a function of surface temperature for a range of energies between 21 kJ/mol and 34 kJ/mol. AES and RAIRS were used as detection techniques.
2. A study of the effect of surface temperature at high incident energies between 50 kJ/mol and 120 kJ/mol and high surface temperatures for the reaction of methane on Pt(111) and Pt(110)-(1x2) is presented. The K&W method was used as detection technique.

   The experiments presented in the second part of this chapter are continuation of a study published in the Journal of Chemical Physics[9].

5.2 Low incident energy regime – T_S dependence on S_0 (CH_4 (ν_3))/ Pt(111)

The effect of surface temperature on the dissociation of CH_4 (ν_3) on Pt(111) was studied for a range of surface temperatures between 90 K and 800 K for incident translational energies between 21 kJ/mol and 34 kJ/mol. The incident molecules were prepared with one quantum of antisymmetric C-H stretch vibration (ν_3). By doing so, we access total energies (E_{trans} + E_{vib}) near the threshold energy for dissociation (where the effect of surface temperature is expected to be strongest) using low nozzle temperatures, thus limiting the population of thermally vibrationally excited molecules in the incident molecular beam.

Two different techniques were used for the detection of methane chemisorption. For surface temperatures between 90 K and 180 K, RAIRS was used to detect the nascent chemisorption product CH_3(ads) on the surface by its infrared absorption. At higher surface temperatures, CH_3(ads) becomes unstable and dehydrogenates, first to CH(ads), and eventually leading to adsorbed carbon atoms C(ads) for $T_S > 500$ K. The CH(ads) product on the surface is stable up to T_S=500 K[171]. Figure 5-2 shows RAIR spectra following deposition of CH_4 on Pt(111) at T_S=100 K, 200 K and 300 K. At T_S=200 K, the CH_3(ads) has almost dehydrogenated completely into CH(ads). The intermediate dissociation product CH_2(ads) was not detected, in accordance with previous studies that predict that these species are unstable on the Pt(111) surface at T_S>130 K[171]. In principle, we could record the CH(ads) uptake to measure the sticking coefficient of CH_4 at 180 K <T_S< 500 K. However, this would require a calibration of the CH(ads) RAIRS absorption signal in terms of surface coverage. Instead, AES was used to measure the coverage of adsorbed C-atoms (either as CH(ads) or C(ads)) as a result of CH_4 dissociation for surface temperatures between T_S=200-800 K.

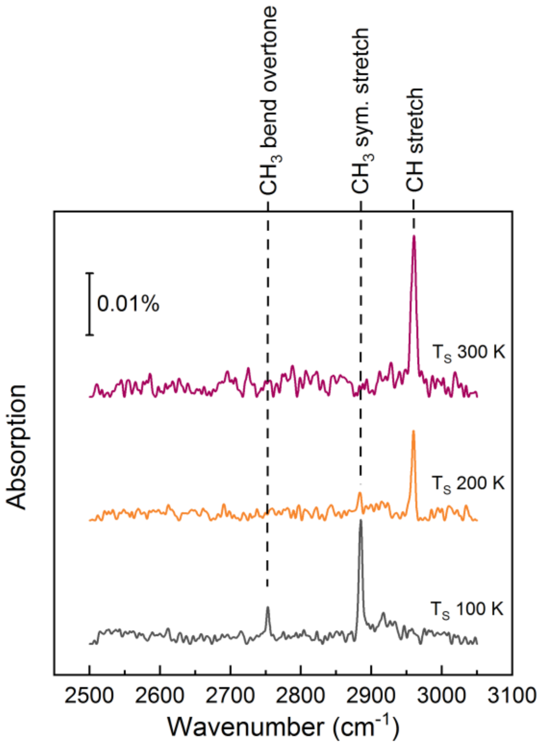

Figure 5-2. RAIR spectra after CH_4 deposition on the Pt(111) surface at 100 K, 200 K, and 300 K.

The state-resolved sticking coefficients for CH_4 (ν_3) were obtained using equation (3.4). The sticking coefficient without laser excitation, $S_0^{laser-off}$, was measured at the highest translational energy (34 kJ/mol) and highest surface temperature (T_S=800 K) used in this study. Under these conditions, the

$S_0^{laser-off}$ was (2.3±0.7) ·10^{-4}. This value contributes 0.3% ML to the measured carbon coverage at laser-on conditions and it is below the sensitivity of our AES setup, which is approximately 1.5% of a ML of C. For the rest of translational energies and surface temperatures studied here, the contribution from the laser-off molecules would be even smaller. For this reason, $S_0^{laser-off}$ was neglected in equation (3.4) and only laser-on experiments were performed for the rest of E_{trans}.

The initial sticking coefficients obtained by RAIRS were calculated following the same procedure explained in chapters 3 and 4: after the correspondent calibration of CH_3(ads) RAIR adsorption signal to coverage, the uptake curves (CH_3(ads) coverage *vs* incident CH_4 dose) were fit by a modified Langmuir uptake curve using equation (4.1) and the S_0 was obtained as the initial slope of the fitting. As an example, Figure 5-3 shows the uptake curves obtained at T_S=90 K for different translational energies.

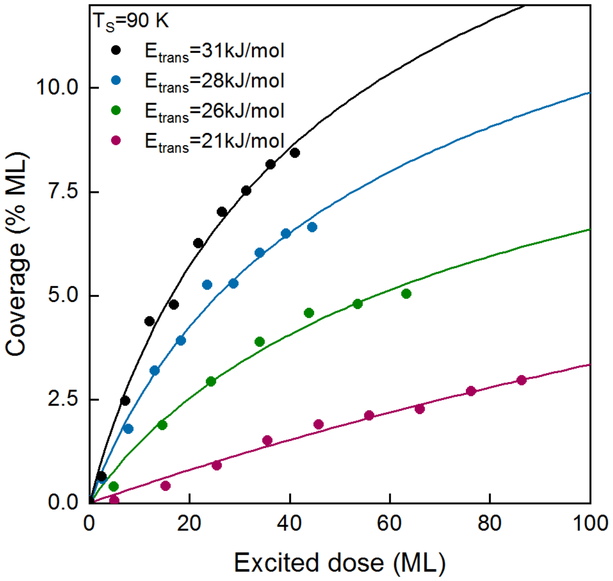

Figure 5-3. RAIRS CH_3(ads) uptake curves obtained at T_S=90 K for different translational energies of the incident $CH_4(v_3)$ beam. The solid lines show the Langmuir uptake fitting to the experimental data points.

At T_S≥200 K, AES was used to obtain the carbon footprints on the surface after the depositions. An example of an Auger profile measured after 60 s deposition of CH_4 (v_3) at 34 kJ/mol and T_S=200 K is presented in Figure 5-4 a). The C/Pt measured with Auger was converted into carbon coverage using the calibration presented in chapter 3.3.3.1. The Auger data shows the carbon footprint of the molecular beam on the surface to be about 7 mm in diameter. The points taken at the edges of the crystal and outside the carbon footprint were used to determine a carbon baseline (red dashed line) due to C adsorption from the chamber background and during the AES analysis. The baseline was subtracted from the profile to give the carbon profile due to the incident molecular beam, as shown in Figure 5-4 b). The carbon coverage was taken as the average of the plateau points in the footprint (those in between the two blue dashed lines in Figure 5-4 b). The sticking coefficient was determined as the ratio between the carbon coverage and the incident dose of state prepared molecules. A disadvantage of AES detection compared to RAIRS detection is the fact that with RAIRS we get the whole uptake curve in a single experiment and we can then fit it with the Langmuir model to extrapolate the initial reactivity. Using AES we only get a single point of the uptake in one experiment. Therefore, since here we wanted to calculate the initial sticking coefficient, it was necessary to work at low carbon coverages where the sticking coefficient is still independent of the coverage (in the linear part of the uptake). For this reason, the final carbon coverage was kept below 8% of a ML in these measurements.

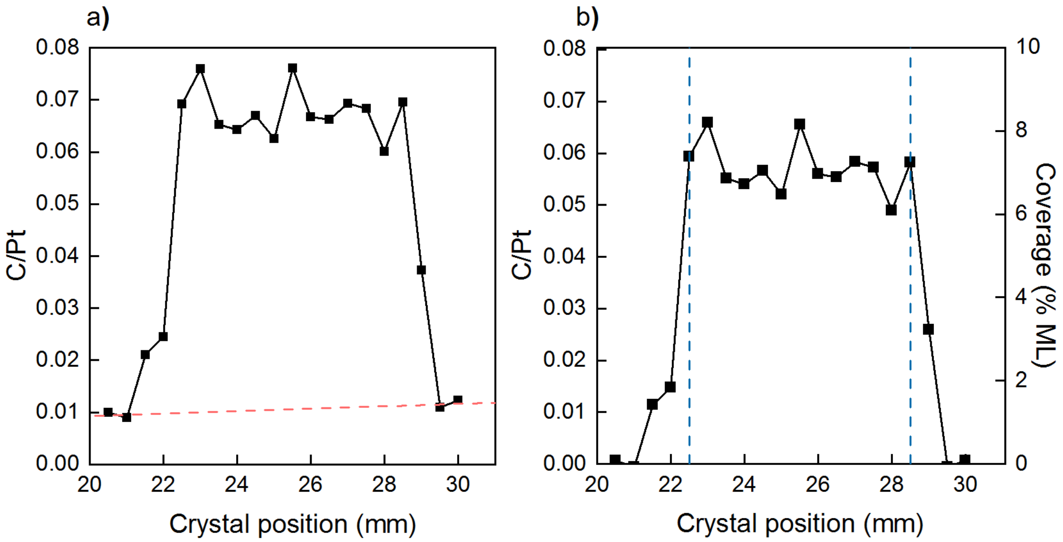

Figure 5-4. a) Auger profile measured following a 60 second deposition of $CH_4(v_3)$ with E_{trans}=34 kJ/mol and T_S=200 K. The red dashed line shows the carbon background. b) Auger profile obtained after background subtraction of the AES profile shown in a). The blue dashed lines show the region of the profile used to determine the average carbon coverage.

Figure 5-5 a) shows the initial sticking coefficients S_0 for CH_4 (ν_3) on Pt(111) as a function of surface temperature for different incident translational energies. At T_S=90 K, S_0 was measured using RAIRS and AES, showing excellent agreement between the values obtained by both techniques. Figure 5-5 b) shows the same set of S_0 for CH_4 (ν_3) but as a function of incident translational energy for the different surface temperatures.

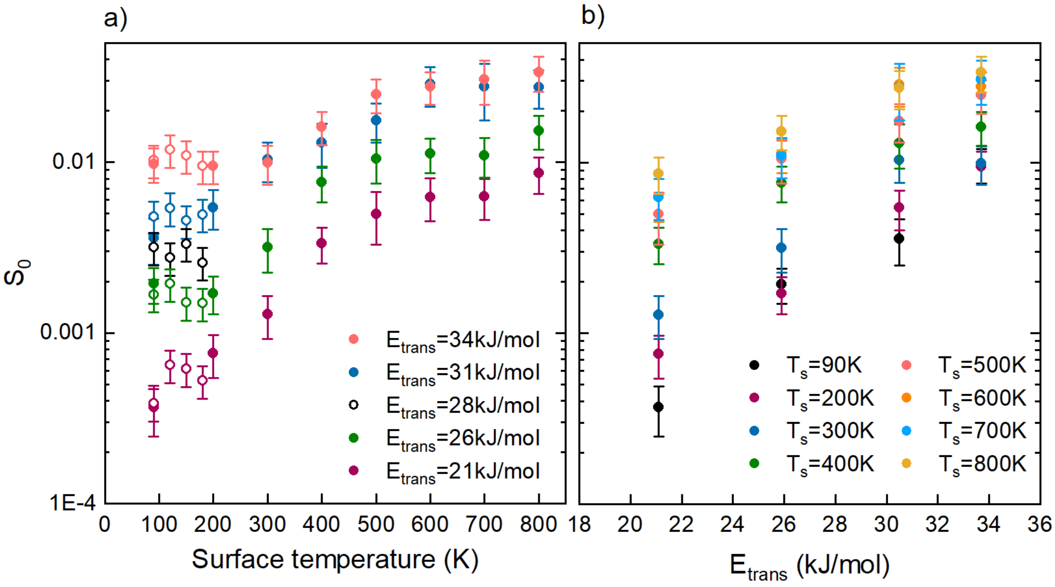

Figure 5-5. S_0 ($CH_4(\nu_3)$) on Pt(111) as a function of: a) surface temperature for different incident translational energies of the molecular beam. The open symbols correspond to sticking coefficients measured using RAIRS and the filled symbols those measured using AES. b) As a function of incident translational energy for different surface temperatures. Only sticking coefficients determined from AES measurements are shown.

The general trend observed in Figure 5-5 is an increasing reactivity with increasing surface temperature, except for T_S=90-200 K where we do not observe a measurable T_S dependence except for the lowest incident energy of 21 kJ/mol. For T_S=200-800 K, the dependence of S_0 with T_S is more important at the lowest incident translational energy: at E_{trans}=21 kJ/mol, the S_0 increases by a factor of 30 raising the temperature from 90 K to 800 K, while it only increases by a factor of 4 for E_{trans}=34 kJ/mol.

Using ab initio quantum reaction dynamics, Jackson and coworkers[36,45,47,170,172,173] have been able to explain the surface temperature dependence in terms of lattice motion, obtaining excellent agreement with experimental studies on the surface temperature dependence on the dissociation of $CH_4(\nu_3)$ on Ni(111)[170]. Here, I will give a short overview of their model, which will help in explaining the results presented in Figure 5-5. An increase in the surface temperature causes the surface atoms to be displaced from their equilibrium position due to their vibrational motion. Since this lattice vibration is relatively slow (phonon frequency of approximately 200 cm^{-1}) in comparison with the timescale of methane-surface collision interaction[101], the authors propose that lattice motion can be treated with a sudden approximation[173]. Therefore, the methane molecules encounter the surface atoms at randomly chosen positions as a result of their vibration motion with respect to the surface plane. This sudden approximation has been further proved in quasi-classical molecular dynamics studies by Lozano *et al.*[37] Computing the sticking coefficients for CH_4 on Pt(111), the authors found no difference when they included the surface atom motion and when they treated the surface atoms as static in a set of distorted configurations determined by the surface temperature.

In their model, Jackson *et al.* account for two different effects of this molecule-lattice coupling[47]. On the one hand, they consider the so-called mechanical coupling, which accounts for a shift in the location of the barrier along the axis perpendicular to the surface as the lattice moves. This coupling is a modified form of the surface mass model developed by Harris and Luntz[34]. This mechanical coupling mimics the effects of energy transfer from the surface to the methane molecule and vice versa that cannot happen in a sudden approximation. At low incident energies of the incident molecule, S_0 tends to increase with surface temperature because the reaction can be “thermally assisted” (i.e. the surface could transfer some of its vibrational energy to the molecule)[169]. At high incident energies of the molecule, the reactant can actually make the surface atom to recoil into the bulk when impinging, losing part of its energy due to this “lattice recoil”[174]. Therefore, the S_0 is expected to decrease with increasing incident kinetic energies.

On the other hand, the electronic coupling, which Jackson and coworkers claim is a more important effect, induces a modulation of the barrier height with lattice motion. The dissociation barrier height depends on the surface atom position relative the surface plane. Moving a surface atom above the surface plane

(Q>0) reduces the dissociation barrier and vice versa. This effect is plot in Figure 5-6, where the calculated total energy along the minimum-energy path for CH_4 dissociation on Ni(111) is shown for three values of Q, which is the displacement of the surface atom perpendicular to the plane of the surface.

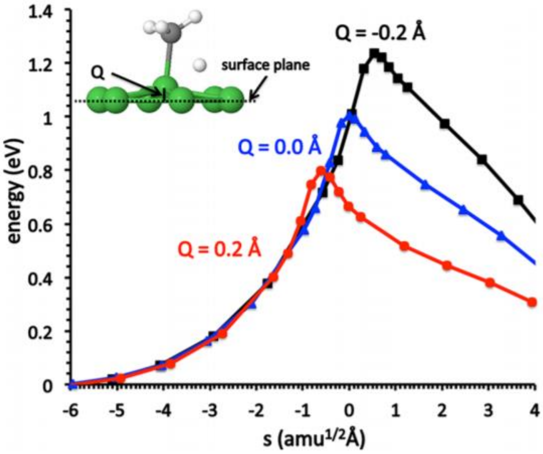

Figure 5-6. Total energy along the minimum-energy path for dissociative chemisorption of methane on Ni(111) for three values of Q, the displacement perpendicular to the plane of the surface, of the Ni atom over which the methane dissociates. Reproduced with permission from[48].

The effect of this modulation of the minimum dissociation barrier is most important at incident energies of the methane reagent near the threshold for dissociation. A methane molecule whose incident translational energy is below the threshold energy for dissociation would not react if it encounters a flat surface. However, if the surface temperature is increased and the methane molecule encounters a surface atom that is displaced above the surface plane (and therefore showing a slightly lower barrier for dissociation), the chances that the methane molecule dissociate increase. On the contrary, if it encounters a surface atom that is below the plane and shows a slightly higher barrier for dissociation, it will not dissociate. But since the methane molecule would not dissociate on the flat surface, the net effect of increasing the surface temperature is to increase the reaction probability. This explains why in Figure 5-5 we observe a more pronounced enhancement of the S_0 with T_S at low incident energies.

At incident energies above the minimum dissociation barrier, we could think at first that the effect of T_S would be the opposite and that S_0 would decrease with increasing T_S due to the increase in the barrier for atoms that are displaced into the bulk. However, this effect is not observed, in part because of the anharmonicity of the potential: DFT calculations show that it requires less energy to displace a surface atom away from the bulk than into the bulk[47]. Therefore the molecules are more likely to hit a surface atom that has been displaced away from the surface, which shows a lower barrier for dissociation than the flat surface.

This explanation for the surface temperature dependence of S_0 does not include tunnelling as it was proposed previously in the literature[12,34]. Jackson claims that adding tunnelling in their model does not change significantly the reactivity[36]. Most of the trajectories are predicted to happen “over the barrier” for methane molecules colliding very near the top sites and when the surface atoms pucker out of the surface plane. It is only at very low incident energies and very low T_S when tunnelling becomes the only possible mechanism for dissociation.

Even though the general effect of the surface temperature is the same for methane reacting on Pt(111) and Ni(111), the T_S dependence observed here for CH_4/Pt(111) is weaker than the one observed on Ni(111)[124,170]. This result can be rationalized as being due to the large mass difference between Ni and Pt and the fact that the Ni(111) surface is stiffer, leading to Ni lattice vibrations with higher frequencies than those of Pt. Furthermore, calculations performed by Nave *et al.*[45] show a weaker electronic coupling between barrier height and Pt atom displacement (0.996 eV/Å) in comparison with Ni (1.158 eV/Å). However, these differences do not explain why we do not observe a measurable T_S dependence for the range between T_S=90-200 K in Figure 5-5 when on Ni, S_0 was observed to increase with increasing T_S for the whole range between T_S=90-475 K[124].

Trying to understand this behaviour, the fractional phonon populations for different T_S on the two surfaces, Ni(111) and Pt(111) were calculated assuming the surfaces behave as harmonic oscillators with masses M_{Ni} and M_{Pt} oscillating with the surface Debye frequency ω_D(Ni(111)) and ω_D(Pt(111)) respectively. The fractional phonon population can be estimated from Boltzmann distribution[169]:

$$P_n = \frac{e^{-n\Theta_D/T_S}}{\sum_n e^{-n\Theta_D/T_S}} \tag{5.1}$$

where Θ_D is the Debye temperature, which is in the range of 222 K to 250 K for Ni(111)[175] and between 110 K and 143 K for Pt(111)[175–177]. For each surface, the average surface Debye temperature was used in equation (5.1).

As shown in Figure 5-7, the range of T_S=90-475 K, covered in the study of Utz *et al.*[124,170], includes temperatures well below and well above the Debye temperature. However, in our study for Pt(111), at T_S=90 K, the lowest surface temperature studied and close to the Debye temperature of the surface, the n=1 phonon state is already populated. This could explain why we do not observe a sharp increase in the S_0 at T_S=90 K as they did on Ni(111). At 90 K, the lattice motions on Pt(111) are not frozen as it happens on Ni(111). Therefore, one would need to work at lower T_S on Pt(111) to make a fair comparison between both studies. However, at T_S<80 K, CH_4 starts to physisorb on Pt(111)[178] and we expect that CH_4 passivates the surface sites for dissociative chemisorption. Nevertheless, Utz *et al.*[170] calculated a higher efficacy in promoting S_0 for the first quantum of surface excitation (n=1) than for the subsequent excited states, and this result seems to be in contradiction with our observation for Pt(111). A more pronounced dependence of the S_0 with T_S is observed at T_S>200 K, temperature at which the n>1 higher vibrational modes start to be populated. Therefore, it seems from our observations that the efficacy of higher vibrational phonon modes is more efficient in promoting the dissociation of CH_4 on Pt. However, this observation is not fully understood yet and more experiments and/or theoretical calculations are needed to clarify the non-dependence of S_0 with T_S at T_S=90-200 K.

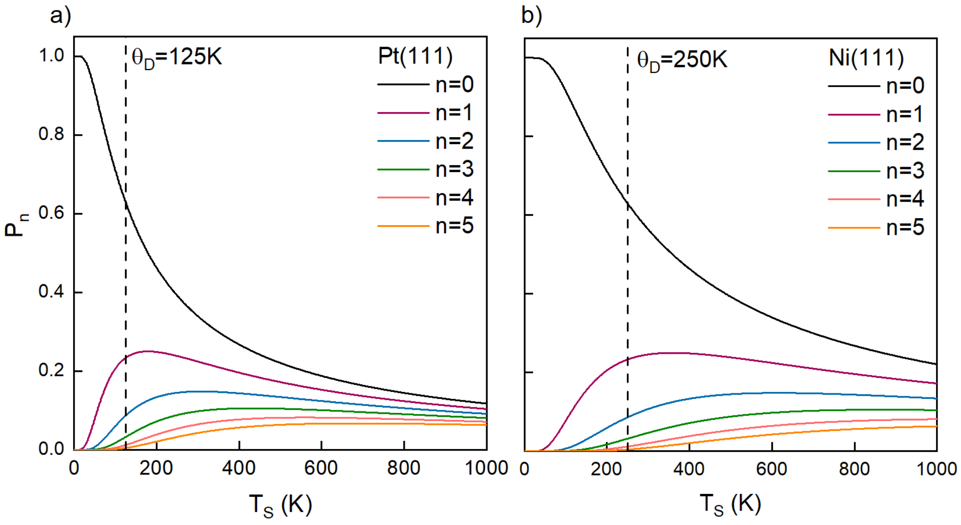

Figure 5-7. Fractional phonon populations as a function of surface temperature for a) Pt(111) and b) Ni(111). n=0 corresponds to the ground state, n=1 with the first excited state, etc. and the fractional populations are calculated using equation (5.1).

For future experiments, it would be interesting to study how the effect of lattice motion affects surfaces with steps or ridges as Pt(211), Pt(110)-(1x2) or for Ni(211) for example and compare with the theoretical predictions[44,179]. The advantage of working with Ni is its lower reactivity and its higher Debye temperature that offers the possibility to work at temperatures below and above the Debye temperature without having CH_4 physisorbing on the surface.

5.3 High incidence energy regime & surface carbon migration at high T_S

In this second part, I will discuss the effect of surface temperature at high incident energies, well above the barrier for dissociation. For these experiments, the K&W method was used, because the initial sticking coefficients at these high E_{trans} are greater than 1%, above the detection limit of the K&W method in our current setup. Sticking coefficient measurements by the K&W technique have the advantage that they are self-calibrating. A gas mixture of 1%CH_4 in H_2 was used to access incident translational energies between 50 and 130 kJ/mol. In order to prevent the adsorption and site blocking by chemisorbed hydrogen atoms, the surface temperature was kept $T_S \geq 500$ K. At these high T_S, the hydrogen atoms quickly leave the surface by recombinative desorption as H_2(g).

On Pt(111), we have reported previously[63] that S_0 for E_{trans} >90 kJ/mol is independent of surface temperature in the range between T_S=500-800 K. This result agrees well with the results presented in the previous section. At E_{trans}>90 kJ/mol, the energy is much greater than the minimum barrier height for dissociation, and so the surface temperature is not expected to affect the initial sticking coefficient (S_0). However, it is interesting to see how the time dependent sticking coefficient S(t), depends on the surface temperature.

Figure 5-8 shows three K&W traces for CH_4 dissociation on Pt(111) at E_{trans}=120 kJ/mol for three different surface temperatures. The initial sticking coefficients S(t=0) are the same within experimental error for the three surface temperatures, and for t< 2s S(t) decreases at a similar rate as the carbon atoms product of CH_4 dissociation block vacant sites on the surface. However, for t>2 s, the time evolution S(t) differs significantly for the different T_S.

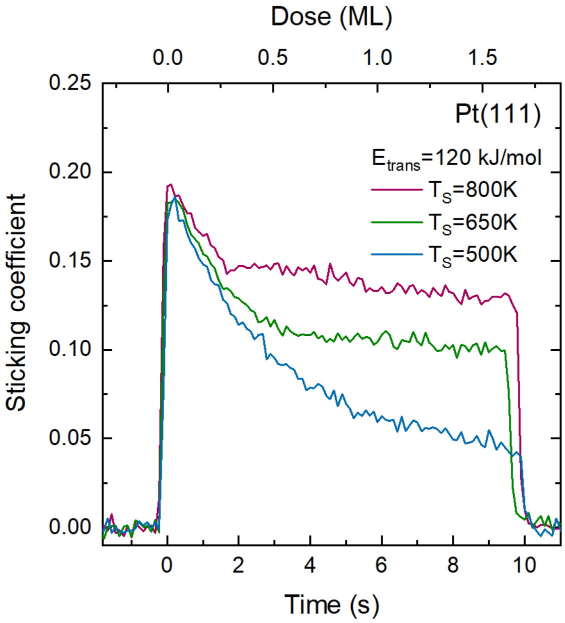

Figure 5-8. Time dependence of the K&W trace for the dissociative chemisorption of CH_4 on Pt(111) at E_{trans}=120 kJ/mol and three surface temperatures (T_S=500 K in blue, T_S=650 K in green, T_S=800 K in purple).

Several possibilities were considered as possible explanations for the behaviour shown in Figure 5-8. One alternative includes recombination of carbon atoms on the surface with CH_4 in the molecular beam or possible contaminants on the surface. Such a process could lead to the desorption of the products of the recombination creating vacant sites for dissociation. One possibility is the formation of CO from the recombination of C(ads) with oxygen contaminant in the UHV chamber. However, no detection of mass 28 amu in the QMS during the measurements indicate that this process is not happening. Another possible product from recombination of the surface carbon atoms could involve the formation of C_2H_4, yet this product was also not observed in the QMS.

The second alternative involves mobility of the C(ads) on the surface that happens more efficiently at high surface temperatures. Carbon migration into the bulk was discarded since it is well-known that happens at T_S>1150 K[180]. Also, carbon migration to the edges of the carbon spot was eliminated since AES probed that the carbon remained on the surface after depositions at high surface temperatures.

The most plausible explanation for the observed behaviour is the surface mobility of C(s) that can lead to the formation of carbon particles on the surface. In this surface temperature range, three-dimensional carbon agglomerates were observed using scanning tunnelling microscopy (STM) by Land *et al.*[181] In their study, they followed the dehydrogenation of ethylidyne on the Pt(111) surface after deposition of ethylene. In the range of T_S=430-700 K, they observed the formation of three dimensional carbonaceous particles on the surface. The size of the carbon particles was observed to increase with increasing surface temperature, consistent with the higher mobility of carbon at high surface temperatures. At T_S>800 K, LEED measurements[182,183] show the formation of graphite through the detection of graphite rings in addition to the (111) spots.

In order to account for these two different processes that happen on the surface during the measurement of the K&W trace (i.e. the CH_4 dissociation and the mobility of the C products on the surface), all the K&W traces were fit with a double exponential using (2.4), as it was shown in Figure 2-10.

In order to check whether the carbon particle formation depends on the surface structure, a similar experiment to the one for Pt(111) shown in Figure 5-8 was performed on Pt(110)-(1x2). Figure 5-9 plots the time dependence of the K&W trace for the dissociation of CH_4 on the more corrugated surface for different surface temperatures and for two incident translational energies (72 kJ/mol in Figure 5-9 a) and 129 kJ/mol in Figure 5-9 b)). As shown in Fig 5-9, S_0 is independent of surface temperature for both incident translational energies. The minimum activation barrier for CH_4 dissociation on the ridges of Pt(110)-(1x2) was calculated by Han *et al.*[44] to be 57.5 kJ/mol. Therefore, at

79 kJ/mol, the CH_4 molecules should have enough energy to surpass the minimum barrier for dissociation and the surface temperature is expected to play a minor role on S_0.

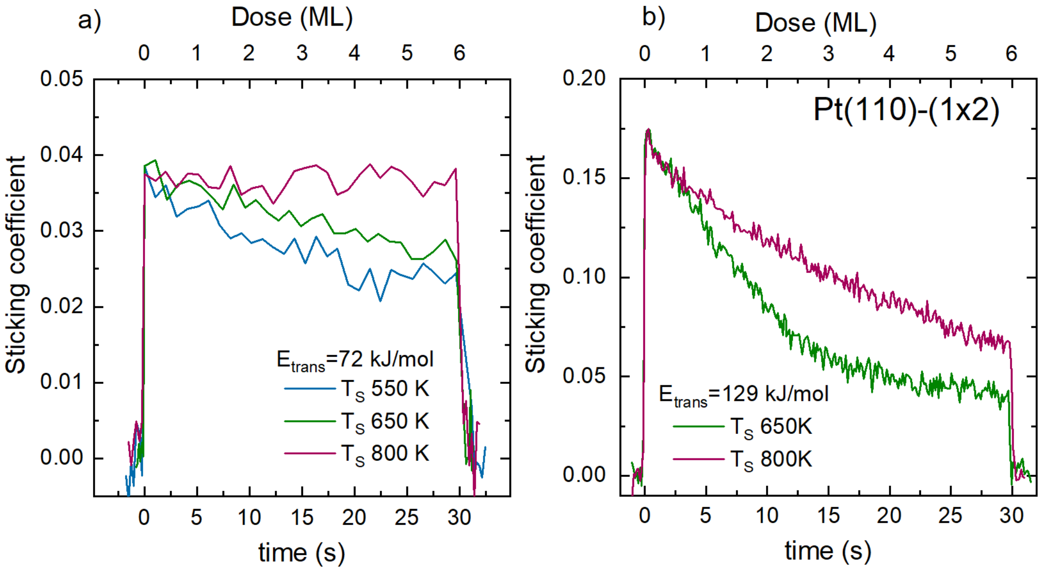

Figure 5-9. Time dependence of the K&W trace for the dissociative chemisorption of CH_4 on Pt(110)-(1x2) at a) E_{trans}=72 kJ/mol and b) E_{trans}=129 kJ/mol for different temperatures (T_S=550 K in blue, T_S=650 K in green, T_S=800 K in purple).

In general, the effect observed for S(t) on Pt(110)-(1x2) as a function of surface temperature is the same as the one observed for Pt(111). By comparing the traces shown in Figure 5-9 measured at different incident energies and surface temperatures, one can see how two processes play a role in the decay of the sticking coefficient trace. On the one hand, for a specific incident translational energy, the S(t) trace is seen to decay more slowly at high surface temperatures because of the more efficient diffusion of the carbon on the surface that frees up vacant sites for dissociation. On the other hand, for a specific surface temperature, the S(t) trace is observed to decay more slowly at lower incident energies. At low incident energies, the sticking coefficient is low, generating less carbon on the surface and so more vacant sites for new methane molecules to dissociate. At high incident energy, the surface is rapidly covered by carbon due to the high initial reactivity of the incident CH_4.

Carbon segregation on the Pt(110)-(1x2) surface into subsurface layers of platinum was observed at T_S>470 K by angle-resolved XPS (ARXPS) at the same time as a complex phase of (1x2)-type was detected by LEED[184]. The most likely explanation for this observation is that carbon atoms accumulate on the valleys of this corrugated surface forming a (1x2) structure since carbon diffusion into the bulk of Pt(110)-(1x2) does not happen at temperatures below 1100 K. Also, the formation of graphite islands has been reported to occur at T_S>700 K[184,185].

5.4 Summary

In this chapter, the effect of surface temperature on the dissociative chemisorption of CH_4 on Pt surfaces has been studied.

At low incident energies, close to the minimum barrier for dissociation, the surface temperature was shown to play a role on the S_0 for $CH_4(\nu_3)$ on Pt(111). The initial reactivity was seen to increase with increasing the surface temperatures for T_S=200-800 K. This effect was observed to be more important at low energies, and explained by a modulation of the dissociation barrier height due to the displacement of surface atoms out of the surface plane with increasing surface temperature (thermally induced corrugation). This modulation of the barrier for atoms moving away for the surface plane mimics in a way a surface with atoms with different coordination, as it was studied in chapters 3 and 4. Surface atoms puckering out would be similar to steps or kinks, while surface atoms moving into the bulk would resemble corner or valley atoms.

A weaker dependence of the surface temperature on the CH_4 reactivity was seen on Pt(111) compared to Ni(111)[124,170]. For T_S=90-200 K, a negligible effect of T_S was observed on S_0 for all the incident energies studied. A possible explanation for this behavior is a higher efficacy of higher excited phonon states on promoting the dissociation on Pt(111), although this idea contradicts previously theoretical predictions[170] and it remains to be established.

At high incident energies, the effect of surface temperature (T_S=500-800 K) on the initial reactivity on Pt(111) and Pt(110)-(1x2) is negligible for $E_{trans} \geq 90$ kJ/mol and $E_{trans} \geq 79$ kJ/mol respectively. However, the time-dependent sticking coefficient measured with K&W is observed to depend on T_S on both surfaces. A slower decay of the sticking coefficient as a function of incident dose was measured at high surface temperatures. This observation was rationalized by a higher mobility of the carbon product of the dissociation on the surface that tends to form carbon particles on the surface and thus continuously create vacant sites for methane dissociation.

Chapter 6 Summary and outlook

This thesis reports an experimental investigation of the dissociative chemisorption of methane on several Pt single crystal surfaces. In all experiments, I used a molecular beam/surface-science apparatus which combines AES, K&W and RAIRS detection with the possibility to perform quantum-state resolved experiments using continuous infrared lasers to prepare the reactant molecules in a specific rovibrational quantum state.

In 2008, Vattuone, Savio and Rocca[71] raised the following question:

"Do defects play any role for direct dissociative chemisorption, i.e. when the molecules dissociate on impact with the surface without having the chance to find a lower energy path by diffusing in search of more active sites?"

At the time, only two experimental studies had investigated the role of low Pt coordinated sites on the dissociation of methane using single crystal surfaces, and both disagreed: while Gee *et al*.[97] suggested a higher reactivity on the steps than on the terraces of Pt(533), Papp *et al.*[99] concluded that the steps are equally reactive as the terraces on the direct CH_4 chemisorption channel for Pt(355) and Pt(322).

I believe that this question is now answered in the third chapter of my thesis. "Defects", or more appropriately, low-coordinated sites such as steps, ridges, or kinks can play an important role in a direct dissociative chemisorption reaction. The determination of the site-specific initial sticking coefficients on the different surface sites allowed for direct comparison of the reactivity of CH_4 on the low- and high- coordinated sites. The experimental sticking coefficients show the highest reactivity on the least coordinated steps (CN=7) and ridges (CN=7) in comparison with the terraces (CN=9). However, the results presented here demonstrate that the coordination number of the surface atoms is not the only factor that determines the site-specific reactivity. This conclusion relies on the different site-specific reactivity found for CH_4 on the steps and on the ridges, being approximately a factor of 2 higher on the step sites. Likewise, the terraces of the Pt(211) were found to be less reactive than the terrace atoms on the flat Pt(111) surface.

On all sites, the dissociation is observed to happen via a direct chemisorption mechanism. Diffusion of CH_3 adsorbed on the terrace sites to the step sites at T_S<150 K as previously proposed by Papp *et al.*[99] can be excluded in our experiments. This is in accordance with DFT calculations, which predict a high barrier for CH_3 diffusion from the terraces to the steps and vice versa. Hence, this absence of diffusion reaffirms the direct chemisorption mechanism: when the CH_4 molecule impinges on a particular surface site, it dissociates on direct impact if it contains sufficient energy to overcome the barrier for dissociation on that specific site.

On Pt(211), dissociation on the highly coordinated corner atoms (CN=10) is not observed in the range of energies studied, again in agreement with DFT calculations predicting a much higher activation barrier for those sites. On the Pt(110)-(1x2) surface, methyl is only detected on the ridge sites. The experimental results show that dissociation does not occur on the facet (CN=9) sites of Pt(110)-(1x2), at least for incident energies lower than 80 kJ/mol. Dissociation in the valleys (CN=11) of Pt(110)-(1x2) was also not observed experimentally, in agreement with AIMD calculations that predict 90% of the reactivity on the ridge atoms and no dissociation on the valleys for incident energies between 70-130 kJ/mol[104].

The presence of these non-reactive sites on the Pt(211), Pt(210), and Pt(110)-(1x2), reduce the “active cross-section” of a particular sample containing several different surface sites. Thus, when comparing the site averaged sticking coefficients for surfaces comprising different surface sites with the reactivity of a Pt(111) surface made up of identical surface atoms, the incident energy plays an important role. At high incident energies of the reactant molecule, Pt(111) is more reactive than the corrugated surfaces because of its larger active cross-section. While the terrace atoms on Pt(111) are less reactive than the steps, kinks and ridges, Pt(111) presents the largest active area of the four studied surfaces. A compromise between low-coordinated sites and their abundance needs to be taken into account in the design of a good catalyst.

Furthermore, I explored the effect of rovibrational excitation of the incident methane on the chemisorption on different surface sites in chapter 3. By exciting the antisymmetric C-H stretch vibration (ν_3) of CH_4 and detecting the methyl product of the dissociation using RAIRS, I report in this thesis for the first time quantum state- and surface-site-specific sticking coefficients of CH_4 on corrugated Pt surfaces. Excitation of the reactant molecules with one quantum of ν_3 was found to be less efficient than an equivalent amount of translational energy normal to the surface for promoting the dissociation on all the surface sites studied. In addition, the vibrational efficacy is lower for dissociation on the low coordinated step and ridge sites in comparison with the terraces. This observation is rationalized based on the different barrier heights for methane dissociation on each surface site, and on the different transition state geometries. As previously reported in a comparison of the efficacy of $CH_4(\nu_3)$ on Ni(111) and Pt(111), the efficacy is higher in a system that is “starved for energy”[141]. Here, the reaction on the terraces with its higher barrier clearly needs more energy than the reaction on the steps or ridges. Moreover, transition state geometry calculations predict the C-H reactive bond to be more stretched at the TS for dissociation on the steps than on the terraces[105].

The effect of rovibrational excitation of the incident molecules is also reported in chapter 4. In this chapter, the rovibrational energy is used to control the outcome of the methane chemisorption reaction. In particular, bond selectivity for methane isotopologues on Pt(111) and Pt(211) is presented.

CH_3D, CH_2D_2 and CHD_3 are shown to dissociate on the Pt(111) surface yielding C-H and C-D cleavage products in a nearly statistical product branching ratio. A small preference for the C-H bond cleavage is observed at low energies due to the higher zero point energy of the C-H bond. This isotope effect decreases the barrier to break a C-H bond compared to a C-D bond, and is also responsible for the higher sticking coefficient observed when decreasing deuteration of the incident methane molecules. Excitation of the C-H stretch bond(s) prior to the chemisorption reaction is shown to induce a strong preference for C-H cleavage, yielding bond selectivity on the Pt(111) at all incident translational energies studied.

On Pt(211), a combined study of bond selectivity and surface-site-specificity is reported. The ability of RAIRS to distinguish between C-H and C-D cleavage products adsorbed on step and terrace sites allowed me to study the dissociation of CH_3D on Pt(211) as a function of translational energy. When the incident reagent CH_3D was prepared with one quantum of antisymmetric C-H stretch excitation, an enhancement of the C-H cleavage was observed. Full bond selectivity is reported on the steps and on the terraces of the surface, although at different ranges of energy, in accordance with the different activation barriers on both surface sites. Using a slow molecular beam of C-H stretch excited CH_3D, I obtained both bond- and site-specific methane chemisorption where only the steps are covered by the C-H cleavage product CH_2D(ads). The bond selectivity decreases with incident translational energy, as previously predicted by quasi-classical trajectory calculations[37]. When the incident translational energy is below the activation barrier for dissociation on a particular site, the vibrational energy added in the quantum of C-H stretch excitation provides the extra amount of energy to the C-H bonds needed for the molecule to dissociate on that specific site. Once the translational energy alone becomes sufficient to overcome the dissociation barrier, the effect of C-H excitation and therefore the degree of bond selectivity is reduced.

Chapter 5 focuses on the effect of surface temperature on the reactivity of CH_4 on Pt(111). Since the dissociation of methane requires the crossing of a large energy barrier and the reaction is known to be direct, the question was whether such a barrier could be lowered by increasing the surface temperature. At low incident energies, close to the minimum barrier for dissociation, I observed a strong effect of surface temperature on the dissociation probability where the sticking coefficient increases with increasing surface temperature. This observation could be rationalized as being due to a thermally induced corrugation. Increasing the surface temperature increases the vibrational amplitude of the Pt surface atoms, resulting in atoms being temporally displaced above and below the surface plane. DFT calculations show that a methane molecule which collides with a Pt atom displaced above the surface plane experiences a lower barrier than for an atom in or below the surface plane. This thermally induced puckering of the surface atoms out of the surface plane results in a transient reduction of the coordination number decreasing the dissociation barrier. There seems to be a connection between the surface temperature dependence and surface site dependence of the methane reactivity: in the same way that step sites have a lower activation barrier than the terraces, the atoms puckering out of the surface plane are predicted and observed to be more reactive than atoms in or below the surface plane. Consistent with this interpretations of the surface temperature effect, I observe that at high incident energy, significantly above the minimum barrier, the surface temperature dependence of the reactivity is reduced and finally disappears.

King and Wells data for surface temperatures higher than 500 K indicates that the carbon atoms on the surface product of the dissociation of CH_4 on Pt(111) and Pt(110)-(1x2) are mobile. This diffusion of the carbon atoms has been reported before, and the carbon atoms were observed to agglomerate forming particles of 10-40 atoms/particle depending on the surface temperature. This agglomeration of the carbon atoms in three dimensional particles frees up vacant sites on the surface for more methane to dissociate.

Taken together, the experimental results shown in this thesis are highly valuable for testing the validity of current dynamical models. In particular, the new quantum state and surface-site resolved sticking coefficients contribute to advancing the understanding of methane dissociation toward surfaces that resemble the catalysts used in industry, where defects and atoms with different terminations are used.

Future experiments

The ability of RAIRS to distinguish between dissociation of methane on different surface sites opens a range for possible future experiments that could make use of the site-specific detection of this technique. Here I will suggest and discuss some promising future experiments:

CH_4 dissociation on stepped Ni surfaces

Until now we have used RAIRS to study the dissociation of methane on Pt surfaces. However, Ni based catalysts remain the most feasible, economically. Therefore, exploring how the rates of methane dissociation on Ni are affected by the coordination of the surface atom is very interesting since its relevance in catalysis. For this reason, a Ni(211) surface is now being under investigation in our RAIRS setup. Previous attempts to detect methane dissociation on Ni(111) by RAIRS were unsuccessful, presumably because on Ni(111) the methyl groups adsorbs in the three-fold hollow sites instead of the terrace top site as is the case for Pt(111). Nevertheless, very recent theoretical calculations predict the CH_3 product of CH_4 dissociation to adsorb on the step edge top sites[179], so it may still be possible to detect the chemisorbed methyl species on the steps a Ni(211) surface by RAIRS. Moreover, these calculations predict the steps of the surface to be much more reactive than the terraces, with a contribution of the terraces to the sticking coefficient of only 3% at incident energies of 96 kJ/mol.

Exploring steric effects in the chemisorption of methane on stepped surfaces

Using linearly polarized infrared light one can align methane's angular momentum and vibrational transition dipole moment in the laboratory frame. Yoder *et al.*[30] observed an initial sticking coefficient that was 60% higher when the laser polarization was parallel rather than normal to the surface. The authors attributed this steric effect to the alignment of the transition dipole moment of the incident methane with respect to the surface. Using such laser induced alignment of the incident methane one could probe for steric effects on a stepped Pt surface. From the site-specific experiments reported in this thesis, we know that, at low incident energies, methane dissociates exclusively on the step sites of Pt(211). At these energies, one can investigate if there are any differences in the reactivity for molecules whose vibrational transition dipole moment is parallel or perpendicular to the step edges revealing further information about the reactive potential energy surface.

CH_4 dissociation on early transition metal surfaces

As mentioned in chapter 3, the *d*-band model predicts low coordinated sites such as steps or kinks on early transition metal surfaces to be less reactive than terrace sites. In order to check if this theory holds, one could study site-specific reactivities for CH_4 on a stepped W surface by RAIRS, and compare with the results presented in this thesis.

CO_2 reaction on stepped surfaces

Other gas-surface systems can be potentially studied in our setup. One of them is the adsorption of CO_2 on solid surfaces. Removal of CO_2 from the atmosphere to limit greenhouse emissions, and the conversion of CO_2 into useful chemicals such as methanol or small hydrocarbons are two good motivations to study this reaction. CO_2 chemisorption on transition metal surfaces has been shown to be structure dependent[186]. Dissociative chemisorption of CO_2 has been observed on stepped Cu surfaces[187] while no such dissociation happened on flat Cu surfaces. This reaction was believed to be "strictly site dependent" due to the special electronic properties of the step sites. On Ni and Fe metal surfaces, the chemisorption reaction was also observed to be structure sensitive[186,188]. Our surface-site selective detection method together with the ability to perform quantum state resolved studies would provide highly detailed reactivity measurements for this important reaction.

Gas surface reactions on model catalysts

As a future goal or direction of this thesis research, I would also propose the study of reactions between gas phase molecules and metal nanoparticles instead of metal single crystals. These experiments would definitely help us closing the "structure gap" between atomically smooth single crystals and real catalysts by the use of model catalysts[72]. Typical model catalysts are based on a thin oxide support material film (for example SiO_2 or Al_2O_3) onto which metal particles of few nanometers are deposited in UHV. For the growth of metal nanoparticles on the surface, either physical vapor deposition (PVD) or chemical vapor deposition (CVD) can be used in the UHV chamber.

The state-of-the-art of molecular beam studies on model catalysts has been reviewed by Libuda and Freund[72]. RAIRS studies on CO adsorption and oxidation on Pt or Pd nanoparticles, adsorption of methanol on Pd nanoparticles, or NO adsorption and dissociation on model catalysts are some examples of reactions that have been investigated on model catalysts. Hence, it has been demonstrated that RAIRS is a powerful technique to study reactions on metal nanoparticles when the oxide film is very thin and relatively high reflected signal is obtained due to the optical properties of the metal.

We could potentially study the reaction between methane and Pt nanoparticles, and compare the behaviors observed on the nanoparticles with the results we do have on different Pt single crystals. By doing so, we would be able to study site-specific properties of particles in the nanometer size regime that are not always observed using stepped single crystals.

Unresolved observations during this thesis work

Furthermore, this thesis work leaves also some issues unresolved. Due to time restrictions, these observations or results could not be investigated in more detail. However, I would like to mention them here for possible future experiments:

1. CH_3(ads) formation on the steps of Pt(211)

After a 30 min deposition of a methane molecular beam at incident energy of 22 kJ/mol, no dissociation was observed on the steps or terraces of the Pt(211) surface using RAIRS. This result is in agreement with the barriers for dissociation predicted on the steps (42 kJ/mol) and terraces (84 kJ/mol)[105] and the results presented in chapters 3 and 4. The only species observed on the surface after the methane deposition is CO(ads) from contamination in the molecular beam and the UHV chamber. However, after having stopped the molecular beam deposition, I followed the spectra on the surface for three more hours. Surprisingly, the peak associated to CH_3(ads) on the steps, grows at a slow rate, as it is presented in Figure 6-1. At the same time as the CH_3(ads) on the steps grows, the CO adsorbed on the top sites of the step edges decreases and diffuses to the bridge sites on the steps. Moreover, the rate at which the CH_3(ads) grows after the molecular beam has been stopped was found to decrease with decreasing surface temperature.

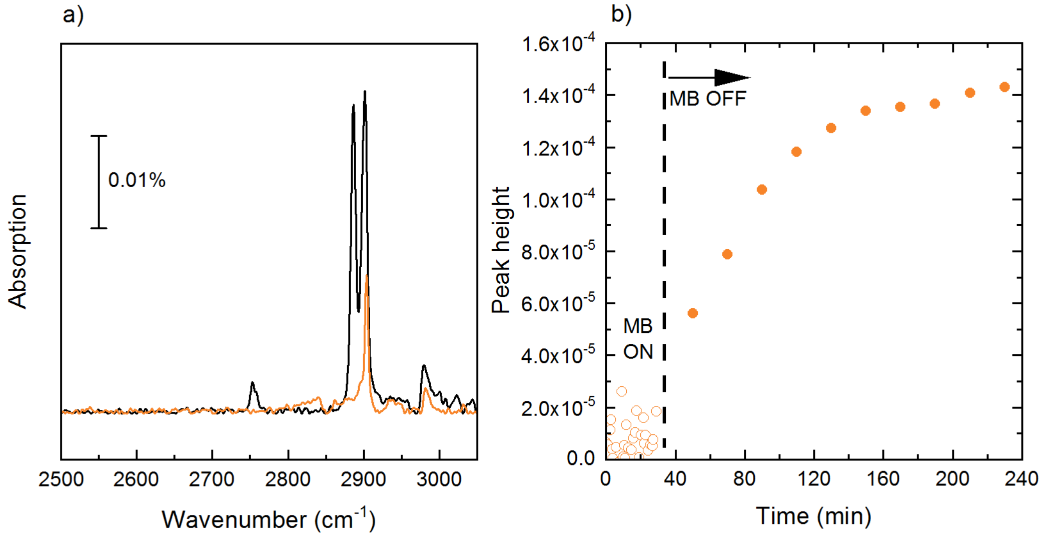

Figure 6-1. a) Comparison of a spectrum taken after a 30 min deposition of CH_4 at E_{trans}= 65 kJ/mol (black) on Pt(211), and a spectrum measured 90 min after the molecular beam has been turned off once CH_4 was deposited at E_{trans}= 22 kJ/mol (orange). b) Uptake measured for CH_3(ads) on the step sites for a CH_4 deposition at E_{trans}= 22 kJ/mol. During the deposition (MB ON), no CH_3(ads) was observed on the surface. After the molecular beam deposition has been stopped (MB OFF), CH_3 adsorbed on the steps was observed.

At first, we thought that a precursor mediated pathway could be responsible for this observation. However, physisorbed CH_4 was not detected on the surface. Moreover, if there was a precursor mediated pathway for CH_4 dissociation on the steps of the surface, at lower incident energies this channel should be favored. Instead, I did not observe CH_3(ads) on the step sites when exposing the Pt(211) to a CH_4 static gas.

This result has not been yet understood. A more complete report with the experiments that I have tried to investigate the origin of this CH_3(ads) on the steps can be found in (*Z:\Surface\Ana\Reports\Not resolved issues*).

One of the possibilities that we currently consider is that the reverse reaction of the steam reforming process could be happening on the step sites of the surface:

$$\mathrm{CO} + 3\mathrm{H}_2 \rightarrow \mathrm{CH}_4 + \mathrm{H}_2\mathrm{O} \tag{6.1}$$

A sequence of breaking CO and H_2 followed by hydrogenation of the surface carbon to produce methyl. Even though CO is generally unable to dissociate on low Miller indices faces of Pt under UHV conditions, few studies have shown that CO can dissociate on Pt surfaces that present low coordinated sites such as steps or kinks[189–191]. The ability of low coordinated sites to break the CO molecule is related to the strong weakening of the intramolecular CO bond on those sites due to the filling of the $2\pi^*$ antibonding orbital caused by an induced lateral Stark effect on the surface[122]. On the other hand, surface hydrocarbon (CH(ads)) formation from hydrogenation of carbon on the surface has been observed on a Pt(111) surface[171].

To prove if this possibility is feasibly happening, more experiments would be needed. First of all, one would need to check if CO can dissociate on the step sites of Pt(211). For that, Auger could be used to detect C after CO depositions on the surface at different surface temperatures. Also, hydrogenation of surface carbon on the surface should be tested by dosing H_2 in the UHV chamber with the surface partially covered with C(ads).

2. RAIRS on Pt(210)/Pt(531)

As shown in chapters 3 and 4, RAIRS is able to distinguish between CH_4 dissociation on the steps, terraces and ridges. However, RAIR spectra following deposition of CH_4 on Pt(210) and Pt(531) surfaces, both surfaces presenting kink atoms, present a broad band in the CH stretch region, instead of well-defined and sharp peaks as it happened for Pt(111), Pt(110)-(1x2) and Pt(211). Spectra following deposition on the different surfaces is shown in Figure 6-2.

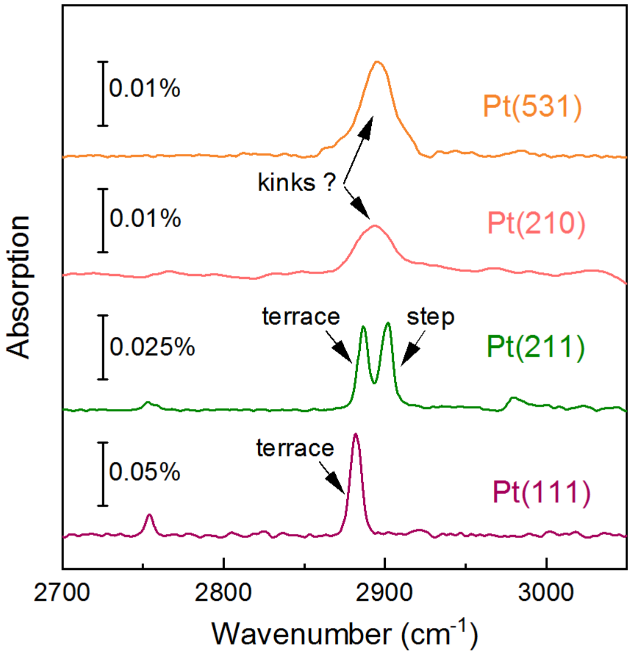

Figure 6-2. RAIR spectra following CH_4 deposition at Etrans~65 kJ/mol on P(111), Pt(211), Pt(210), and Pt(531) at T_S=150 K.

On both Pt(531) and Pt(210) the broad band was observed at different incident energies of the beam. As an example, Figure 6-3 presents a comparison of spectra taken after 30 min deposition of CH_4 on Pt(531) at different incident energies. This observation excludes the possibility of being CH_3(ads) on the different sites of the surfaces, since we would expect the CH_4 to dissociate only on the kinks of the surface at the lowest incident energy.

The explanation for this broad band observed on the two kinked surfaces is missing. On the Pt(531), we justified the broad band with possible roughening of the surface. Due to this roughening, the Pt(531) surface could consist of kinks formed at different length steps and terraces. Having the CH_3 adsorbed on the different atoms could lead to slightly different CH_3 stretch frequencies, which altogether form the broad band that we observe. However, on the Pt(210), LEED indicates no faceting or roughening of the surface. Therefore, the broad feature seen by RAIRS is still not understood.

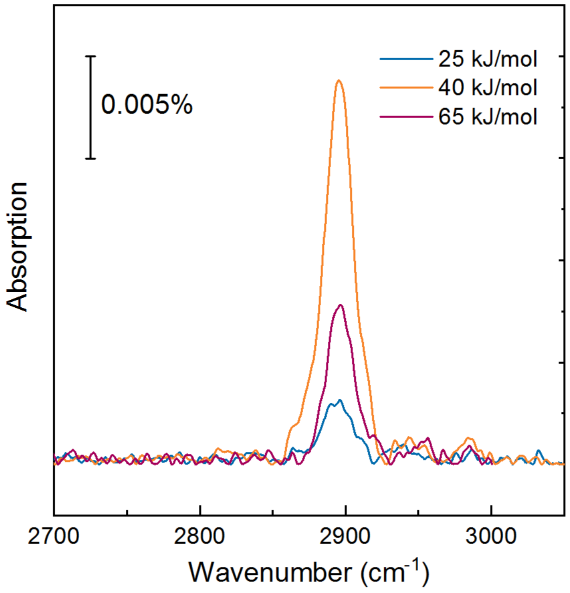

Figure 6-3. RAIR spectra following CH_4 deposition at three different incident translational energies on Pt(531).

3. Stability of CH_3 on the ridges of Pt(110)-(1x2)

Deposition of CH_4 on the Pt(110)-(1x2) at T_S=120 K led to a single peak assigned to CH_3(ads) on the ridge sites, as it presented in Figure 3-10. Dehydrogenation of CH_3(ads) on the ridge sites was seen to happen at T_S>180 K by increasing the surface temperature and measuring RAIR spectra. However, when the deposition was performed at T_S=150 K, no CH_3(ads) was detected on the surface using RAIRS.

At the moment it is not understood why the CH_3(ads) on the ridge sites was not observed at T_S=150 K. Several possible explanations for this observation were tested and summarized in a report that can be found in *Z:\Surface\Ana\Reports\Not resolved issues*.

References

[1] K.W. Kolasinski, *Surface Science: Foundations of Catalysis and Nanoscience* (JohnWiley & Sons, Ltd, Chichester, 2012).

[2] I. Chorkendorff and J.W. Niemantsverdriet, *Concepts of Modern Catalysis and Kinetics* (Wiley-VCH, Weinheim, 2003).

[3] V. Smil, *Enriching the Earth: Fritz Haber, Carl Bosch, and the Transformation of World Food Production* (Production,MIT Press, Cambridge, MA, 2001).

[4] M.J. Overett, R. Oliver Hill, and J.R. Moss, Coord. Chem. Rev. **206-207**, 581 (2000).

[5] H.S. Gandhi, G.W. Graham, and R.W. McCabe, J. Catal. **216**, 433 (2003).

[6] D.D. Ebbing and S.D. Gammon, *General Chemistry*, 9th ed. (Houghton Mifflin Company, 2007).

[7] L.B.F. Juurlink, D.R. Killelea, and A.L. Utz, Prog. Surf. Sci. **84**, 69 (2009).

[8] A.L. Utz, Curr. Opin. Solid State Mater. Sci. **13**, 4 (2009).

[9] H. Chadwick and R.D. Beck, Chem. Soc. Rev. **45**, 3576 (2016).

[10] H. Chadwick and R.D. Beck, Annu. Rev. Phys. Chem. **68**, 39 (2017).

[11] A.C. Luntz and R.D. Beck, J. Vac. Sci. Technol. A Vacuum, Surfaces, Film. **35**, 05C201 (2017).

[12] H.F. Winters, J. Chem. Phys. **64**, 3495 (1976).

[13] J.T. Yates, Surf. Sci. **28**, 437 (1971).

[14] D.K. Bronnikov, D. V. Kalinin, V.D. Rusanov, Y.G. Filimonov, Y.G. Selivanov, and J.C. Hilico, J. Quant. Spectrosc. Radiat. Transf. **60**, 1053 (1998).

[15] C.T. Rettner, H.E. Pfnür, and D.J. Auerbach, Phys. Rev. Lett. **54**, 2716 (1985).

[16] C.T. Rettner, H.E. Pfnür, and D.J. Auerbach, J. Chem. Phys. **84**, 4163 (1986).

[17] L. Juurlink, P. McCabe, R. Smith, C. DiCologero, and A.L. Utz, Phys. Rev. Lett. **83**, 868 (1999).

[18] J.C. Polanyi, Acc. Chem. Res. **161**, 680 (1972).

[19] P. Maroni, D.C. Papageorgopoulos, M. Sacchi, T.T. Dang, R.D. Beck, and T.R. Rizzo, Phys. Rev. Lett. **94**, 246104 (2005).

[20] R.D. Beck, P. Maroni, D.C. Papageorgopoulos, T.T. Dang, M.P. Schmid, and T.R. Rizzo, Science **302**, 98 (2003).

[21] R. Bisson, M. Sacchi, and R.D. Beck, Phys. Rev. B **82**, 121404 (2010).

[22] P.M. Hundt, H. Ueta, M.E. van Reijzen, B. Jiang, H. Guo, and R.D. Beck, J. Phys. Chem. A **119**, 12442 (2015).

[23] R.A. Marcus, J. Chem. Phys. **20**, 359 (1952).

[24] H. Guo and B. Jiang, Acc. Chem. Res. **47**, 3679 (2014).

[25] B. Jiang and H. Guo, J. Phys. Chem. C **117**, 16127 (2013).

[26] B. Jiang, R. Liu, J. Li, D. Xie, M. Yang, and H. Guo, Chem. Sci. **4**, 3249 (2013).

[27] L.B.F. Juurlink, R.R. Smith, D.R. Killelea, and A.L. Utz, Phys. Rev. Lett. **94**, 1 (2005).

[28] D.R. Killelea, V.L. Campbell, N.S. Shuman, and A.L. Utz, Science **319**, 790 (2008).

[29] L. Chen, H. Ueta, R. Bisson, and R.D. Beck, Faraday Discuss. **157**, 285 (2012).

[30] B.L. Yoder, R. Bisson, and R.D. Beck, Science **329**, 553 (2010).

[31] B.L. Yoder, R. Bisson, P. Morten Hundt, and R.D. Beck, J. Chem. Phys. **135**, 224703 (2011).

[32] H.L. Abbott, a. Bukoski, and I. Harrison, J. Chem. Phys. **121**, 3792 (2004).

[33] S.B. Donald and I. Harrison, Phys. Chem. Chem. Phys. **14**, 1784 (2012).

[34] A.C. Luntz and J. Harris, Surf. Sci. **258**, 397 (1991).

[35] G.J. Kroes, Phys. Chem. Chem. Phys. **14**, 14966 (2012).

[36] S. Nave, A.K. Tiwari, and B. Jackson, J. Phys. Chem. A **118**, 9615 (2014).

[37] A. Lozano, X.J. Shen, R. Moiraghi, W. Dong, and H.F. Busnengo, Surf. Sci. **640**, 25 (2015).

[38] X.J. Shen, A. Lozano, W. Dong, H.F. Busnengo, and X.H. Yan, Phys. Rev. Lett. **112**, 046101 (2014).

[39] F. Nattino, H. Ueta, H. Chadwick, M.E. Van Reijzen, R.D. Beck, B. Jackson, M.C. Van Hemert, and G.J. Kroes, J. Phys. Chem. Lett. **5**, 1294 (2014).

[40] G. Füchsel, K. Cao, S. Er, E.W.F. Smeets, A.W. Kleyn, L.B.F. Juurlink, and G.J. Kroes, J. Phys. Chem. Lett. **9**, 170 (2018).

[41] D. Migliorini, H. Chadwick, F. Nattino, A. Gutiérrez-González, E. Dombrowski, E.A. High, H. Guo, A.L. Utz, B. Jackson, R.D. Beck, and G.J. Kroes, J. Phys. Chem. Lett. **8**, 4177 (2017).

[42] B. Jackson, F. Nattino, and G.J. Kroes, J. Chem. Phys. **141**, 054102 (2014).

[43] F. Nattino, D. Migliorini, M. Bonfanti, and G.J. Kroes, J. Chem. Phys. **144**, 044702 (2016).

[44] D. Han, S. Nave, and B. Jackson, J. Phys. Chem. A **117**, 8651 (2013).

[45] S. Nave, A.K. Tiwari, and B. Jackson, J. Chem. Phys. **132**, 054705 (2010).

[46] H. Guo and B. Jackson, J. Phys. Chem. C **119**, 14769 (2015).

[47] B. Jackson and S. Nave, J. Chem. Phys. **138**, 174705 (2013).

[48] H. Guo, A. Farjamnia, and B. Jackson, J. Phys. Chem. Lett. **7**, 4576 (2016).

[49] H. Guo and B. Jackson, J. Chem. Phys. **144**, 184709 (2016).

[50] L. Chen, Vibrationally Bond-Selective Chemisorption of Methane Isotopologues on Pt (111) Studied by Reflection Absorption Infrared

Spectroscopy, Ph.D. thesis, École Polytechnique fédérale de Lausanne, Lausanne, 2012.

[51] L. Chen, H. Ueta, R. Bisson, and R.D. Beck, Rev. Sci. Instrum. **84**, 053902 (2013).

[52] G. Scoles, *Atomic and Molecular Beam Methods* (Oxford University Press, New York, 1988).

[53] M.R. Tate, D. Gosalvez-Blanco, D.P. Pullman, A.A. Tsekouras, Y.L. Li, J.J. Yang, K.B. Laughlin, S.C. Eckman, M.F. Bertino, and S.T. Ceyer, J. Chem. Phys. **111**, 3679 (1999).

[54] M. Sander, R. Imbihl, R. Schuster, J. V. Barth, and G. Ertl, Surf. Sci. **271**, 159 (1992).

[55] C. Badan, M.T.M. Koper, and L.B.F. Juurlink, J. Phys. Chem. C **119**, 13551 (2015).

[56] M. Sacchi, The Effect of Molecular Vibrations and Surface Structure on the Chemisorption of Methane on Platinum, Ph.D. thesis, École Polytechnique fédérale de Lausanne, Lausanne, 2008.

[57] M. Berdau, S. Moldenhauer, A. Hammoudeh, J.H. Block, and K. Christmann, Surf. Sci. **446**, 323 (2000).

[58] M.J. Gladys, I. Ermanoski, G. Jackson, J.S. Quinton, J.E. Rowe, and T.E. Madey, J. Electron Spectros. Relat. Phenomena **135**, 105 (2004).

[59] J.W. Arblaster, Platin. Met. Rev. **41**, 12 (1997).

[60] M.A. Van Hove and G.A. Somorjai, Surf. Sci. **92**, 489 (1980).

[61] S. Speller, J. Kuntze, T. Rauch, J. Bömermann, M. Huck, M. Aschoff, and W. Heiland, Surf. Sci. **366**, 251 (1996).

[62] D.A. King, Surf. Sci. **47**, 384 (1975).

[63] H. Chadwick, A. Gutiérrez-González, and R.D. Beck, J. Chem. Phys. **145**, 174707 (2016).

[64] J.C. Vickerman and I.S. Gilmore, *Surface Analysis: The Principal Techniques* (John Wiley & Sons Ltd Registered, 2009).

[65] P.M. Hundt, Quantum-State Resolved Gas / Surface Reaction Dynamics of Water and Methane PAR, Ph.D. thesis, École Polytechnique fédérale de Lausanne, Lausanne, 2014.

[66] B.L. Yoder, Steric Effects in the Chemisorption of Vibrationally Excited Methane on Nickel, Ph.D. thesis, École Polytechnique fédérale de Lausanne, Lausanne, 2010.

[67] M.E. Van Reijzen, State-to-State Scattering of CH4 from Ni(111) and Gr/Ni(111), Ph.D. thesis, École Polytechnique fédérale de Lausanne, Lausanne, 2016.

[68] J. Werdecker, Vibrationally and Rotationally Inelastic Scattering of Methane from Ni(111), Ph.D. thesis, École Polytechnique fédérale de Lausanne, Lausanne, 2018.

[69] H. Chadwick, P.M. Hundt, M.E. van Reijzen, B.L. Yoder, and R.D. Beck, J. Chem. Phys. **140**, 034321 (2014).

[70] T. Zambelli, J. Wintterlin, J. Trost, and G. Ertl, Science **273**, 1688 (1996).

[71] L. Vattuone, L. Savio, and M. Rocca, Surf. Sci. Rep. **63**, 101 (2008).

[72] J. Libuda and H.J. Freund, Surf. Sci. Rep. **57**, 157 (2005).

[73] L. Juurlink, J. Phys. Condens. Matter **30**, 090301 (2018).

[74] I.M.N. Groot, a W. Kleyn, and L.B.F. Juurlink, J. Phys. Chem. C **117**, 9266 (2013).

[75] K.E. Lu and R.R. Rye, Surf. Sci. **45**, 677 (1974).

[76] R.J. Gale, M. Salmeron, and G.A. Somorjai, Phys. Rev. **38**, 1027 (1977).

[77] A.T. Gee, B.E. Hayden, C. Mormiche, and T.S. Nunney, J. Chem. Phys. **112**, 7660 (2000).

[78] D.A. McCormack, R.A. Olsen, and E.J. Baerends, J. Chem. Phys. **122**, 1 (2005).

[79] I.M.N. Groot, A.W. Kleyn, and L.B.F. Juurlink, Angew. Chemie - Int. Ed. **50**, 5174 (2011).

[80] I.M.N. Groot, K.J.P. Schouten, A.W. Kleyn, and L.B.F. Juurlink, J. Chem. Phys. **129**, 4274 (2008).

[81] K.D. Rendulic, Appl. Phys. A Solids Surfaces **47**, 55 (1988).

[82] R. van Lent, S. V. Auras, K. Cao, A.J. Walsh, M.A. Gleeson, and L.B.F. Juurlink, Science **363**, 155 (2019).

[83] A.T. Gee and B.E. Hayden, J. Chem. Phys. **113**, 10333 (2000).

[84] A. Winkler, X. Guo, H.R. Siddiqui, P.L. Hagans, and J.T. Yates, Surf. Sci. **201**, 419 (1988).

[85] R.J. Mukerji, A.S. Bolina, and W.A. Brown, Surf. Sci. **527**, 198 (2003).

[86] B. Tränkenschuh, C. Papp, T. Fuhrmann, R. Denecke, and H.P. Steinrück, Surf. Sci. **601**, 1108 (2007).

[87] F. Zaera, Nat. Chem. **7**, 279 (2015).

[88] T. Sugisawa, D. Shiraishi, D. Machihara, K. Irokawa, H. Miki, C. Kodama, T. Kuriyama, T. Kubo, and H. Nozoye, Appl. Surf. Sci. **169-170**, 292 (2001).

[89] J.M. Gohndrone and R.I. Masel, Surf. Sci. **209**, 44 (1989).

[90] E.H.G. Backus, A. Eichler, M.L. Grecea, A.W. Kleyn, and M. Bonn, J. Chem. Phys. **121**, 7946 (2004).

[91] C.E. Tripa, T.S. Zubkov, J.T. Yates, M. Mavrikakis, and J.K. Nørskov, J. Chem. Phys. **111**, 8651 (1999).

[92] C.E. Tripa, T.S. Zubkov, and J.T. Yates, J. Phys. Chem. B **105**, 3724 (2001).

[93] C. Hahn, J. Shan, Y. Liu, O. Berg, A.W. Kleijn, and L.B.F. Juurlink, J. Chem. Phys. **136**, 114201 (2012).

[94] J. Janlamool, D. Bashlakov, O. Berg, P. Praserthdam, B. Jongsomjit, and L.B.F. Juurlink, Molecules **19**, 10845 (2014).

[95] A.J. Walsh, R. van Lent, S. V. Auras, M.A. Gleeson, O.T. Berg, and L.B.F. Juurlink, J. Vac. Sci. Technol. A Vacuum, Surfaces, Film. **35**, 03E102 (2017).

[96] A.L. Walter, F. Schiller, M. Corso, L.R. Merte, F. Bertram, J. Lobo-Checa, M. Shipilin, J. Gustafson, E. Lundgren, A.X. Brión-Ríos, P. Cabrera-Sanfelix, D. Sánchez-Portal, and J.E. Ortega, Nat. Commun. **6**, 1 (2015).

[97] A.T. Gee, B.E. Hayden, C. Mormiche, A.W. Kleyn, and B. Riedmüller, J. Chem. Phys. **118**, 3334 (2003).

[98] D.A. King and M.G. Wells, Surf. Sci. **29**, 454 (1972).

[99] C. Papp, B. Tränkenschuh, R. Streber, T. Fuhrmann, R. Denecke, and H.P. Steinrück, J. Phys. Chem. C **111**, 2177 (2007).

[100] A.V. Walker and D.A. King, Phys. Rev. Lett. **82**, 5156 (1999).

[101] R. Bisson, M. Sacchi, and R.D. Beck, J. Chem. Phys. **132**, 094702 (2010).

[102] F. Viñes, Y. Lykhach, T. Staudt, M.P.A. Lorenz, C. Papp, H.P. Steinrück, J. Libuda, K.M. Neyman, and A. Görling, Chem. - A Eur. J. **16**, 6530 (2010).

[103] H. Chadwick, A. Gutiérrez-González, D. Migliorini, R.D. Beck, and G.J. Kroes, J. Phys. Chem. C **122**, 19652 (2018).

[104] H. Chadwick, A. Gutiérrez-González, R.D. Beck, and G.J. Kroes, J. Chem. Phys. **150**, 124702 (2019).

[105] H. Chadwick, H. Guo, A. Gutiérrez-González, J.P. Menzel, B. Jackson, and R.D. Beck, J. Chem. Phys. **148**, 014701 (2018).

[106] A. Gutiérrez-González, M.E. Torio, H.F. Busnengo, and R.D. Beck, Top. Catal. https://doi.org/10.1007/s11244-019-01170-5 (2019).

[107] A.T. Anghel, D.J. Wales, S.J. Jenkins, and D.A. King, Phys. Rev. B - Condens. Matter Mater. Phys. **71**, 2 (2005).

[108] D. Migliorini, H. Chadwick, and G.J. Kroes, J. Chem. Phys. **149**, 094701 (2018).

[109] H. Chadwick, H. Guo, A. Gutiérrez-González, J.P. Menzel, B. Jackson, and R.D. Beck, J. Chem. Phys. **148**, (2018).

[110] A.C. Luntz and D.S. Bethune, J. Chem. Phys. **90**, 1274 (1989).

[111] M.B. Lee, Q.Y. Yang, and S.T. Ceyer, J. Chem. Phys. **87**, 2724 (1987).

[112] S.L. Tait, Z. Dohnálek, C.T. Campbell, and B.D. Kay, Surf. Sci. **591**, 90 (2005).

[113] M.C. McMaster and R.J. Madix, J. Chem. Phys. **98**, 9963 (1993).

[114] D.J. Oakes, M.R.S. Mccoustra, and M.A. Chesters, Faraday Discuss. **96**, 325 (1993).

[115] D.H. Fairbrother, X.D. Peng, M. Trenary, and P.C. Stair, **91**, 3619 (1995).

[116] T. Jacob and William A. Goddard III, J. Phys. Chem. B **109**, 297 (2005).

[117] F. Hoffmann, Surf. Sci. Rep. **3**, 107 (1983).

[118] D.H. Fairbrother, X.D. Peng, R. Viswanathan, P.C. Stair, M. Trenary, and J. Fan, **285**, L455 (1993).

[119] R.K. Brandt, R.S. Sorbello, and R.G. Greenler, Surf. Sci. **271**, 605 (1992).

[120] H. Orita and Y. Inada, J. Phys. Chem. B **109**, 22469 (2005).

[121] J. Xu and J.T. Yates, Surf. Sci. **327**, 193 (1995).

[122] K. Wandelt, Surf. Sci. **251-252**, 387 (1991).

[123] B. Gumhalter, K. Hermann, and K. Wandelt, Vacuum **41**, 192 (1990).

[124] D.R. Killelea, V.L. Campbell, N.S. Shuman, R.R. Smith, and A.L. Utz, J. Phys. Chem. C **113**, 20618 (2009).

[125] H. Ueta, L. Chen, R.D. Beck, I. Colón-Dìaz, and B. Jackson, Phys. Chem. Chem. Phys. **15**, 20526 (2013).

[126] K. Griffiths, W.N. Lennard, I. V Mitchell, P.R. Norton, G. Pirug, and H.P. Bonzel, Surf. Sci. **284**, L389 (1993).

[127] C.R. Arumainayagam, M.C. McMaster, and R.J. Madix, J. Phys. Chem. **95**, 2461 (1991).

[128] A.F. Carlsson and R.J. Madix, J. Chem. Phys. **115**, 8074 (2001).

[129] A.F. Lee and K. Wilson, J. Vac. Sci. Technol. A Vacuum, Surfaces Film. **21**, 563 (2003).

[130] F. Calle-Vallejo, J. Tymoczko, V. Colic, Q.H. Vu, M.D. Pohl, K. Morgenstern, D. Loffreda, P. Sautet, W. Schuhmann, and A.S. Bandarenka, **350**, 185 (2015).

[131] J.K. Nørskov, Rep. Prog. Phys. **53**, 1253 (1996).

[132] B. Hammer and J.K. Nørskov, Surf. Sci. **343**, 211 (1995).

[133] A. Groß, *Theoretical Surface Science* (Springer, 2009).

[134] B. Hammer, Top. Catal. **37**, 3 (2006).

[135] S. Schnur and A. Groß, Phys. Rev. B - Condens. Matter Mater. Phys. **81**, 033402 (2010).

[136] M.G. Evans and M. Polanyi, Trans. Faraday Soc. **34**, 0011 (1938).

[137] J.N. Bronsted, Chem. Rev. **5**, 231 (1928).

[138] L. Bianchettin, A. Baraldi, S. De Gironcoli, E. Vesselli, S. Lizzit, L. Petaccia, G. Comelli, and R. Rosei, J. Chem. Phys. **128**, 114706 (2008).

[139] M.P. Schmid, P. Maroni, R.D. Beck, and T.R. Rizzo, J. Chem. Phys. **117**, 8603 (2002).

[140] R.R. Smith, D.R. Killelea, D.F. DelSesto, and A.L. Utz, Science **304**, 992 (2004).

[141] R. Bisson, M. Sacchi, T.T. Dang, B. Yoder, P. Maroni, and R.D. Beck, **4**, 12679 (2007).

[142] L. Halonen, S.L. Bernasek, and D.J. Nesbitt, J. Chem. Phys. **115**, 5611 (2001).

[143] A.B. Anderson and J.J. Maloney, J. Phys. Chem. **92**, 809 (1988).

[144] B. Jiang and H. Guo, J. Chem. Phys. **138**, 234104 (2013).

[145] F.F. Crim, J. Phys. Chem. **100**, 12725 (1996).

[146] N.H. Damrauer, C. Dietl, G. Krampert, S.H. Lee, K.H. Jung, and G. Gerber, Eur. Phys. J. D **20**, 71 (2002).

[147] P. Brumer and M. Saphiro, Annu. Rev. Phys. Chem. **43**, 257 (1992).

[148] F.F. Crim, Proc. Natl. Acad. Sci. U. S. A. **105**, 12654 (2008).

[149] R.L. Vander Wal, J.L. Scott, and F.F. Crim, J. Chem. Phys. **92**, 803 (1990).

[150] A. Sinha, M.C. Hsiao, and F.F. Crim, J. Chem. Phys. **92**, 6333 (1990).

[151] M.J. Bronikowski, W.R. Simpson, B. Girard, and R.N. Zare, J. Chem. Phys. **95**, 8647 (1991).

[152] S. Yoon, R.J. Holiday, and F.F. Crim, J. Phys. Chem. B **109**, 8388 (2005).

[153] S. Yoon, R.J. Holiday, E.L. Sibert, and F.F. Crim, J. Chem. Phys. **119**, 9568 (2003).

[154] R.J. Holiday, C.H. Kwon, C.J. Annesley, and F. Fleming Crim, J. Chem. Phys. **125**, 133101 (2006).

[155] H.A. Bechtel, Z.H. Kim, J.P. Camden, and R.N. Zare, J. Chem. Phys. **120**, 791 (2004).

[156] Z.H. Kim, H.A. Bechtel, and R.N. Zare, J. Am. Chem. Soc. **123**, 12714 (2001).

[157] J.P. Camden, H.A. Bechtel, D.J.A. Brown, and R.N. Zare, J. Chem. Phys. **124**, 034311 (2006).

[158] D.R. Killelea and A.L. Utz, Phys. Chem. Chem. Phys. **15**, 20545 (2013).

[159] A.M. Wodtke, D. Matsiev, and D.J. Auerbach, Prog. Surf. Sci. **83**, 167 (2008).

[160] R. Diez Muiño and H.F. Busnengo, *Dynamics of Gas-Surface Interactions* (Springer, 2013).

[161] A. Gutiérrez-González, F.F. Crim, and R.D. Beck, J. Chem. Phys. **149**, 074701 (2018).

[162] H. Guo and B. Jackson, J. Phys. Chem. C **119**, 14769 (2015).

[163] D.J. Nesbitt and R.W. Field, J. Phys. Chem. **100**, 12735 (1996).

[164] C.G. Elles, M.J. Cox, and F.F. Crim, J. Chem. Phys. **120**, 6973 (2004).

[165] H.S. Yoo, M.J. DeWitt, and B.H. Pate, J. Phys. Chem. A **108**, 1348 (2004).

[166] P.M. Holmblad, J. Wambach, and I. Chorkendorff, J. Chem. Phys. **102**, 8255 (1995).

[167] K.M. DeWitt, L. Valadez, H.L. Abbott, K.W. Kolasinski, and I. Harrison, J. Phys. Chem. B **110**, 6705 (2006).

[168] D.C. Seets, C.T. Reeves, B.A. Ferguson, M.C. Wheeler, and C.B. Mullins, J. Chem. Phys. **107**, 10229 (1997).

[169] J. Harris, J. Simon, A.C. Luntz, C.B. Mullins, and C.T. Rettner, Phys. Rev. Lett. **67**, 652 (1991).

[170] V.L. Campbell, N. Chen, H. Guo, B. Jackson, and A.L. Utz, J. Phys. Chem. A **119**, 12434 (2015).

[171] R. Deng, E. Herceg, and M. Trenary, Surf. Sci. **573**, 310 (2004).

[172] S. Nave and B. Jackson, J. Chem. Phys. **130**, 054701 (2009).

[173] A.K. Tiwari, S. Nave, and B. Jackson, J. Chem. Phys. **132**, 134702 (2010).

[174] M. Hand and J. Harris, J. Chem. Phys. **92**, 7610 (1990).

[175] C.L. Kao and R.J. Madix, Surf. Sci. **557**, 215 (2004).

[176] H.B. Lyon and G.A. Somorjai, J. Chem. Phys. **44**, 3707 (1966).

[177] W. Takeuchi and Y. Yamamura, Surf. Sci. **277**, 351 (1992).

[178] L. Chen, H. Ueta, H. Chadwick, and R.D. Beck, J. Phys. Chem. C **119**, 14499 (2014).

[179] H. Guo, J.P. Menzel, and B. Jackson, J. Chem. Phys. **149**, 244704 (2018).

[180] J.C. Hamilton and J.M. Blakely, J. Vac. Sci. Technol. **15**, 559 (1978).

[181] T.A. Land, T. Michely, R.J. Behm, J.C. Hemminger, and G. Comsa, J. Chem. Phys. **97**, 6774 (1992).

[182] T. Kondo, T. Sasaki, and S. Yamamoto, J. Chem. Phys. **116**, 7673 (2002).

[183] H. Ueta, M. Saida, C. Nakai, Y. Yamada, M. Sasaki, and S. Yamamoto, Surf. Sci. **560**, 183 (2004).

[184] A.I. Boronin, V.I. Bukhtiyarov, R. Kvon, V. V. Chesnokov, and R.A. Buyanov, Surf. Sci. **258**, 289 (1991).

[185] E. Janin, M. Göthelid, and U.O. Karlsson, Appl. Surf. Sci. **162**, 184 (2000).

[186] M.C.J. Bradford and M.A. Vannice, Catal. Rev. **41**, 1 (2002).

[187] I.A. Bönicke, W. Kirstein, and F. Thieme, Surf. Sci. **307-309**, 177 (1994).

[188] S.G. Wang, D.B. Cao, Y.W. Li, J. Wang, and H. Jiao, J. Phys. Chem. B **109**, 18956 (2005).

[189] Y. Iwasawa, R. Mason, M. Textor, and G.A. Somorjai, **44**, 5 (1976).

[190] X.Q.D. Li, T. Radojicic, and R. Vanselow, Surf. Sci. Lett. **225**, L29 (1990).

[191] Y.O. Park and R.I. Masel, Surf. Sci. Lett. **131**, 385 (1983).

Appendix

During my thesis work a new separation valve was designed and installed between the second and third chambers in order to the UHV chambers from molecular beam source in the first and second chambers. The original separation valve which was part of the commercial molecular beam source manufactured by Thermionics was unreliable. The valve did not properly seal between the second and third stage during venting of the molecular beam source because a pressure difference was need to properly compress the O-ring seal. Also the mechanical actuator for the separation valve consisting of a rotation motion feedthrough and several gears with unreliable. Therefore, we decided to replace the original separation valve with an improved version which is actuated by stepper motor. All the Solidworks designs can be found on the server of our group in the following address:

Z:\Surface\all data\Equipment Solidworks Design\RAIRS machine\Separation valve (Ana)

A schematic of the separation valve is shown in Figure. A stainless steel sliding sheet (1) is translated in the vertical axis in a linear guide that is defined by two guides (2). The movement is provided by a stepper motor (UDB11-12V) with a reducing gear (UGM20CNN) that is attached to the axis (3) that connects with the sheet through a mechanical joint (4).

The separation valve has two well-defined positions that are fixed by the length of two slots (5) in the sliding sheet. Four bronze bolts (6) screwed trough the guides (2) act as mechanical end stops for the translation of the sheet. Moreover, the bottom of the slots has been designed with two small ramps (7), so that in the closed position the sheet is pressed against the wall of the chamber with an o-ring made of PTFE.

A limit switch is installed to indicate when the motor has reached the closed position. The motor controller (trinamic TMCM-1141) sits outside the vacuum chamber and it has two input buttons: “open” and “close”. When the limit switch is active, a LED light turns on indicating that the valve is in the close position.

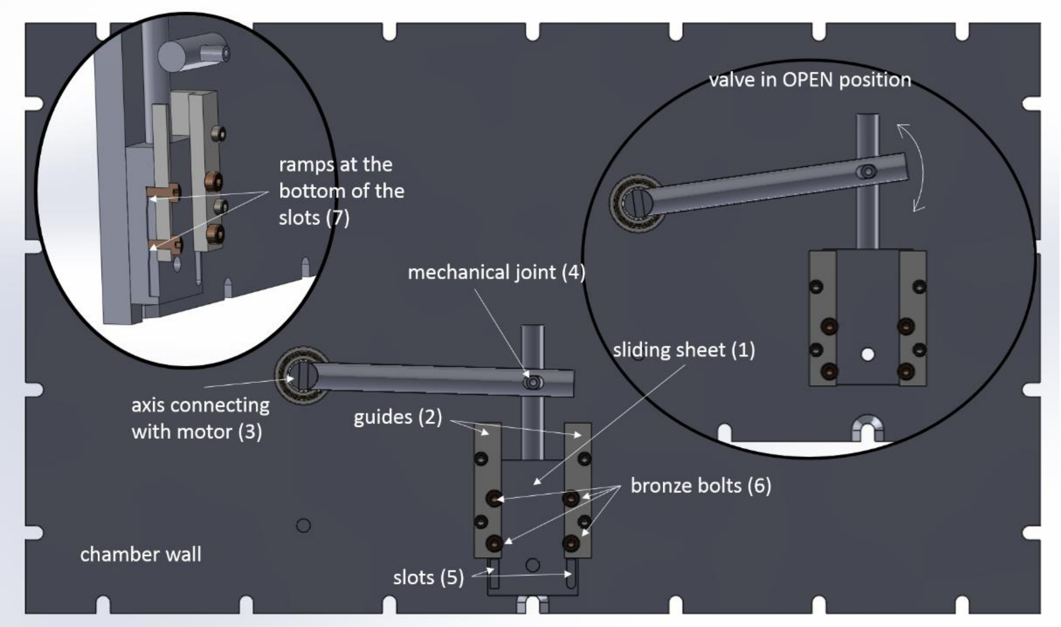
valve in OPEN position
ramps at the bottom of the slots (7)
mechanical joint (4)
sliding sheet (1)
axis connecting with motor (3)
guides (2)
bronze bolts (6)
chamber wall
slots (5)

Figure A-1. Schematic of the separation valve from the Solidworks assembly.

List of Figures

Figure 1-1. Cartoon of a CH_4 molecule striking a Pt(211) surface that is composed of different types of surface atoms. Some of the parameters that influence the probability of adsorption are indicated: the translational energy (E_{trans}), the rotational and vibrational quantum number (ν, J), the angle of incidence (Θ), or the surface temperature (T_S). 2

Figure 1-2. Schematic contour plots of the PES for the $A + BC \rightarrow AB + C$ reaction as a function of the interatomic distance of the reagent BC and the product AB. The saddle points are represented by solid green circles. The initial and final states are indicated in the bottom right plot. Adapted from [9]. 5

Figure 1-3. Frequencies of the 9 vibrational modes of CH_4 (the triply degenerate antisymmetric stretch, ν_3, the symmetric stretch, ν_1, the doubly degenerate bend, ν_2, and the triply degenerate bend, ν_4) and other five modes corresponding to rotational and translational motion along the reaction path (s). s=0 corresponds to the transition state. Reproduced with permission from[49] 11

Figure 2-1. SolidWorks 3-D model of the molecular beam/surface-science apparatus. Taken from [50] 15

Figure 2-2. Schematic overview of the molecular beam/surface-science apparatus. In the first chamber, P1, the supersonic jet expansion is produced and skimmed. In the second chamber, P2, a chopper wheel modulates the molecular beam for TOF measurements using the on-axis QMS (1). In the third chamber, P3, a pyroelectric detector that can be translated into the molecular beam to measure the excited fraction of molecules by the OPO light source. Finally, the molecular beam enters into the UHV chamber and collides with the sample surface where the adsorbed dissociation products can be detected by RAIRS, AES, K&W (using QMS(2) in combination with the flag) or TPD (using QMS(2)). 17

Figure 2-3. QMS signal calibration in terms of CH_4 partial pressure using a pure CH_4 molecular beam. The slope of the linear regression (56 mbar/A) is used to convert between the QMS signal and CH_4 partial pressure. 21

Figure 2-4. Measurement of the pump-out time for CH_4. QMS signal decays exponentially as a function of time once the molecular beam is turned off. Inset shows the linear fitting for the ln(QMS) vs time. The inverse of the slope, 85 ms, is the pump-out time. 22

Figure 2-5. Photograph of the sample mount inside the UHV chamber (a)), and of the sample glowing when it is being heated at a surface temperature of 1100 K (b)). 23

Figure 2-6. LEED images of the Pt(210) sample at different electron energies: a) 53 eV, b) 65 eV, and c) 95 eV. 25

Figure 2-7. Sketch of a fcc conventional cubic cell. “a” refers to the conventional lattice parameter, which for Pt is 3.92 Å[59]. 25

Figure 2-8. Sketches of different planes along which Pt was cut to obtain the Pt(111), Pt(110), Pt(211) and Pt(210) surfaces. On the second layer, only the atoms that are centered on the specified planes are shown. 26

Figure 2-9. Models of the a) Pt(111), b) Pt(211), c) Pt(110)-(1x2), and d) Pt(210) with the different surface sites labeled in the side view of the surfaces with the corresponding coordination numbers. 27

Figure 2-10. a) King and Wells QMS trace for the dissociative chemisorption of CHD_3 on Pt(110)-(1x2) at 123 kJ/mol and a surface temperature of 650K. b) Time dependence of the sticking coefficient. The dashed blue corresponds to the fit to the data with a double exponential using equation (2.4). 30

Figure 2-11. Auger electron spectra measured on Pt(211). In red, AES spectrum taken on the surface contaminated with carbon and oxygen; In green, AES of a clean surface after cleaning in a O_2 atmosphere at T_S= 700 K. 31

Figure 2-12. a) Example of an Auger profile measured following a CH_4 deposition on Pt(111). The red dashed line shows the carbon background generated from the UHV background contamination and the electron gun. b) Auger profile obtained after background subtraction of the AES profile shown in a). 32

Figure 2-13. Optical layout of the RAIRS setup. S_1: MIR Globar source; A: Aperture wheel; BS: Beam Splitter; W_1, W_2 and W_3: KBr windows; M_1 and M_2: gold-coated plane mirrors; P_1,P_2 and P_3: praboloidal mirrors; P: wire-grid linear polarizer; B: bellows; D_1: InSb IR detector. 34

Figure 2-14. a) Schematic representation of the plane of incidence and the definition of the s and p polarized radiation; b) Destructive and constructive interference for the s and p components of the electric field at the surface; c) Illustration of the surface selection rule: the interaction of the vibrational dipole moment with its image dipole moment on the metal surface leads to a destructive interference for dipole moments parallel to the surface plane. 35

Figure 2-15. SNR from 100% line measurements as a function of $t^{1/2}$, being t the measurement time. Two different apertures (A in Figure 2-13) for the IR beam were used. The IR beam shapes on the sample surface for both apertures are shown on the right. 37

Figure 2-16. Schematic of the Argos 2400 SF tunable light source. See text for details. Drawing provided by Lockheed Martin Aculight. 39

Figure 2-17. Doppler broadened profile of the R(1) transition of the ν_3 antisymmetric stretch transition of CH_4 with the Lamb dip in the center (at 3038.491 cm^{-1}). The gas cell was filled with 30 μbar of CH_4. Inset: Magnification of the Lamb dip. In this case, the x axis is expressed in terms of the frequency detuning $\omega L - \omega 0$. 41

Figure 2-18. Schematic drawing of the transfer cavity setup. The IR and HeNe lasers are aligned through the confocal Fabry-Pérot cavity. The cavity length is scanned by periodically applying a voltage ramp to the PZT mount of one cavity mirror. After passing through the cavity, the IR and visible beams are separated and detected by two different photodiodes. The relative position between two fringes of the IR and HeNe laser are measured by a LabView program and used to correct for any drift in the wavelength of the IR laser. Taken from [68]....43

Figure 2-19. Fluence curves for the ν_3 R(0) and R(1) transitions for a 3% CH_4 in He mixture....45

Figure 2-20. A comparison of the excited fraction determined using equation (2.8) and calculated assuming that the pyroelectric detector signal is proportional to the flux of excited molecules using equation (2.10). For each of the gas mixtures and nozzle temperatures, the excited fraction for transitions involving different initial J levels are shown....47

Figure 3-1. (*center*) Sketch of an idealized metallic catalytic nanoparticle. (*outer*) Top and side views of small parts of atomic arrangements on low- and high- Millex indices single crystal surfaces. Reproduced with permission from[74]. 50

Figure 3-2. Initial sticking coefficient as a function of incident energy for CH_4 dissociation: on Pt(533) at T_S=600 K (empty symbols and crosses), and on Pt(111) at T_S=550 K and T_S=800 K (filled symbols). Reproduced with permission from[97]....51

Figure 3-3. Relative initial sticking coefficient as a function of incident kinetic energy for CH_4 dissociation on Pt(355), Pt(322) and Pt(111) at T_S=125 K. The inset shows the coverage on the steps and terraces as a function of adsorption time for an incident kinetic energy of methane of 0.54 eV. Reproduced with permission from[99]. 52

Figure 3-4. Comparison of the sticking coefficients measured using the K&W method for CHD_3 on Pt(111) (T_S 500 K, purple), Pt(211) (T_S 650 K, green), Pt(110)-(1x2) (T_S 650 K, blue) and Pt(210) (T_S 650 K, pink). 55

Figure 3-5. Comparison of the sticking coefficients from K&W experiments (filled symbols) and from AIMD calculations (empty symbols) for CHD_3 dissociation on a) Pt(111), b) Pt(211), c) Pt(110)-(1x2) and d) Pt(210) On the Pt(110)-(1x2) surface AIMD S_0 including (empty circles) and excluding (star symbols) reactivity from “trapped trajectories” is presented. 59

Figure 3-6. Schematic illustration of the Pt(211) surface indicating the polar (Θ) and azimuthal (ϕ) angle. For the experiments presented here, only the polar angle of incidence was modified, keeping ϕ=0 so the plane of incidence is perpendicular to the step rows. 61

Figure 3-7. Sticking coefficients as a function of polar angle of incidence measured using K&W for CHD_3 dissociation on Pt(211) at incident translational energy of 96.8 kJ/mol and T_S 650 K. 62

Figure 3-8. a) Fraction of CHD_3 molecules that impact closest to the step (red), terrace (blue) and corner (green) sites of the Pt(211) surface; b) Fraction of molecules that lead to dissociation of CHD_3 on the step and terrace sites; c) Calculated site-specific sticking coefficient for CHD_3 on the step and terrace sites. Reproduced from [103]. 63

Figure 3-9. Configurations for the transition state (a)) and product state of minimum energy (b)) for dissociation of CH_4 on Pt(111). Reproduced with permission from[45]. 65

Figure 3-10. RAIRS detection of CH_3 adsorbed on a) Pt(111), b) Pt(211) and c) Pt(110)-(1x2) at T_S=120 K. CH_3(ads) was generated by dissociative chemisorption of CH_4 with incident translational energies in the range of 62-65 kJ/mol. 66

Figure 3-11. RAIR spectra following adsorption of CO on Pt(211) at T_S=150 K at different doses (in Langmuir). 68

Figure 3-12. RAIR spectra following annealing to different surface temperatures after saturation of the Pt(211) surface with CO at T_S=150 K. 69

Figure 3-13. RAIR spectra following 45 min deposition of a 3% CH_4 in He molecular beam at E_{trans}=65 kJ/mol at T_S=150 K: a) on the Pt(211) whose steps were previously passivated with CO, b) on a clean Pt(211) surface. 70

Figure 3-14. a) RAIR spectra taken during exposure of the Pt(211) surface at different incident doses of CH_4 at E_{trans}=65 kJ/mol and T_S=120 K. b) Uptake curves for CH_3(ads) on the steps (orange) and on the terraces (blue). The solid lines are fits to the data obtained using eq. (3.2) with $\xi = 1$. 73

Figure 3-15. RAIRS uptake curve for methane dissociation on the terraces (blue) and steps (orange) at T_S=120 K. During the first 15 min, the incident CH_4 had an incident energy E_{trans}=56 kJ/mol and CH_3 is detected only on the steps. The molecular beam was then stopped and the incident energy was increased to E_{trans}=65 kJ/mol. At this incident energy, CH_3 is observed also on the terraces.....74

Figure 3-16. Steps of the calibration needed to convert our RAIR signal to absolute coverage. 75

Figure 3-17. AES peak-to-peak ratio C(272 eV)/Pt(237 eV) as a function of C_2H_4 dose on Pt(111) at T_S=140 K. The solid line is a fit of the data based on a modified-Kisliuk model that gives a C/Pt at the plateau of 0.4 which corresponds with the known 0.5 ML carbon saturation coverage (right axis). 76

Figure 3-18. CH_3 RAIRS calibration on Pt(111): a) The final RAIR spectra for different incident doses, each of them obtained by averaging 4096 scans; b) CH_3 uptake curves recorded during the depositions; c) Auger scans taken after every deposition measurement; d) C/Pt AES signal ratio *vs* RAIRs absorption peak signal for the CH_3 symmetric stretch peak at 2881 cm^{-1}. 77

Figure 3-19. The dissociation of CH_4 at E_{trans}=62 kJ/mol on Pt(110)-(1x2) at T_S=120 K was studied by K&W and RAIRS in the same experiment: a) shows the time dependence trace of the Sticking coefficient measured by K&W. The dashed red line corresponds to the fit to the data using a double exponential decay; b) RAIRS uptake curve fit using equation (3.2). 78

Figure 3-20. Site-specific initial sticking coefficient S_0 vs. incident translational energy (E_{trans}): terrace sites of Pt(111) (T_S=150 K, green), the ridges of the Pt(110)-(1x2) surface (T_S=120 K, red), and the steps (orange) and terraces (blue) of the Pt(211) surface (T_S=120 K). The solid symbols are S_0 as a function E_{trans} measured normal to the macroscopic surfaces. The open symbol S_0 vs. E_{trans} normal to the (111) terrace of the Pt(211) surface which are tilted by 19.5° relative to the 211 crystal plane. The solid lines corresponds to the fit to the experimental data points obtained using equation (3.1.) 81

Figure 3-21. Schematic drawing of the interaction of an atomic level with the metallic states of a transition metal surface. The atomic level is broadened and shifted down due to the interaction with the s and p states (*jellium model*). The interaction with the center of the *d*-band splits the atomic level into a molecule-surface bonding and anti-bonding contributions. Reproduced with permission from[133]....................85

Figure 3-22. Schematic illustration of the effect of reducing the coordination of the surface atoms. From the right to the left: a) a more than half-filled *d*-band; b) the reduced width of the *d*-band due to the lower coordination of the surface atoms; c) up-shift of the *d*-band because of charge conservation; d) the molecule-surface bonding and anti-bonding orbitals; e) a free molecule orbital....................86

Figure 3-23. State-resolved sticking coefficients for CH_4 prepared with a single quantum of ν_3 (red symbols) and under laser-off conditions (black symbols) for dissociation on the ridges of Pt(110)-(1x2). 90

Figure 4-1. Schematic of a bond selective bimolecular reaction. A particular bond of the polyatomic reactant molecule is vibrationally excited. This localized excitation leads to the breaking of that particular excited bond during the reaction, inhibiting the other channel of the reaction to occur. 96

Figure 4-2. Illustration of subsurface D titration method for quantifying bond selectivity. 1) clean Ni(111) surface (side view), 2) D atoms occupy surface and subsurface sites, 3) Xe atoms induce recombinative desorption of surface-bound D leaving a clean surface, 4) CHD_3 impinges on the surface and some CHD_3 molecules dissociative chemisorb, 5) Temperature Programmed Desorption measurement of deuterated adsorbed methyl species. Reproduced with permission from [160]........ 98

Figure 4-3. RAIR spectra measured after 80 minutes molecular beam deposition on Pt(111) at T_s 150 K for CH_3D, CH_2D_2 and CHD_3. The black lines correspond to molecules with high kinetic energies (but without laser excitation) and the red lines to C-H stretch vibrationally excited molecules. Adapted from[50]..........100

Figure 4-4. RAIRS of methane isotopologues on Pt(111) at T_S=150 K. All the spectra were taken after 60 min deposition at T_N=700 K. The kinetic energies for the different species were: 57 kJ/mol (CH_4), 60 kJ/mol (CH_3D), 58 kJ/mol (CH_2D_2) and 66 kJ/mol (CHD_3)..........103

Figure 4-5. CH_2D RAIRS calibration measurements: a) The final RAIRS spectra for different incident doses, each obtained by averaging 4096 scans; b) CH_2D uptake curves recorded during the deposition following the growth of the C-H stretch; c) Auger scans taken after every deposition measurement; d) C/Pt AES signal ratio *vs* RAIRs absorption peak signal for the C-H stretch peak at 2917 cm^{-1} peak. 105

Figure 4-6. RAIRS uptakes for the dissociation of CH_3D, CH_2D_2 and CHD_3 measured at 60, 58 and 66 kJ/mol of translational energy respectively. The open triangles show the uptake for the C-D cleavage product and the filled triangles the one for the C-H cleavage product..........107

Figure 4-7. Branching ratios as a function of translational energy for CH_3D, CH_2D_2 and CHD_3. The dashed lines in each plot show the values that correspond to the statistical branching ratio. 109

Figure 4-8. C-H:C-D branching ratio for CHD_3 molecules in either the ground state (gs) or one of the vibrational states indicated. ν_1 is the C-H symmetric stretch normal mode, ν_2 the C-D symmetric stretch and ν_4 corresponds to the C-D antisymmetric stretch. The lines correspond to a quantum approach[36] while circles are results from quasi-classical calculations[25]. Figure adapted with permission from[46]. 110

Figure 4-9. Sticking coefficients obtained for laser-off experiments for CH_4 (black), CH_3D (blue), CH_2D_2 (green) and CHD_3 (red) on Pt(111) at T_S=150 K. 111

Figure 4-10. Initial sticking probability S_0 of the isotopologues of methane in the vibrational ground state (GS) on Pt(111) as a function of initial incident energy. Inset: ratios $S_0(CH_4)/S_0(CD_4)$ and $S_0(CH_4)/S_0(CD_4^*)$ as a function of energy, being CD_4 an artificial molecule CD_4 molecule wose ZPE is set equal to that of CH_4. Reproduced with permission from Ref[38]. 112

Figure 4-11. RAIR spectra following dissociation of CH_3D (left), CH_2D_2 (middle) and CHD_3 (right) for laser off measurements (black) and with one quantum of C-H stretch vibration (red). 113

Figure 4-12. C-H branching ratio as a function of incident translational energy for the three partially deuterated methanes on Pt(111) for various initial vibrational states (ground state in black, C-H stretch excitated in red and C-D stretch excited in blue). Reproduced with permission from [38]. 114

Figure 4-13. Sticking coefficients obtained for laser-on experiments for CH_4 (black), CH_3D (blue), CH_2D_2 (green) and CHD_3 (red). The solid lines are fits to the data obtained using equation (4.2). 115

Figure 4-14. Reactive sticking probability, S_0, as a function of the molecular translational energy for CH_4 (ν_3) (blue), CH_3D (ν_4) (orange), CH_2D_2 (ν_6) (green) and CHD_3 (ν_1) (red). Reproduced with permission from[37]. 116

Figure 4-15. RAIRS after deposition of methane isotopologues on Pt(211) at T_S=150 K. All the spectra were taken after 80 min deposition at T_N=800 K. The kinetic energies for the different species are shown in Table 4-3. 119

Figure 4-16. RAIR spectra following dissociation of CD_4, CHD_3 and CH_2D_2 on a) the Pt(211) surface at T_N=800 K, b) the Pt(211) surface at T_N=500 K, c) the Pt(111) surface at T_N=800 K. The surface temperature was kept at T_S=150 K in all these experiments. 120

Figure 4-17. RAIR spectra taken at T_S=150 K following deposition of a) CH_3D on Pt(211), b) CH_3D on Pt(111), c) CH_4 on Pt(211), and d) CH_4 on Pt(111). 122

Figure 4-18. Uptake curves (Absorption signal *vs* Dose) of the two peaks associated to CH_2D on the steps in the C-H stretch region of the spectrum. Molecular beam: 3% CH_3D at E_{trans}=53 kJ/mol. 122

Figure 4-19. Dissociation of CH_3D on the Pt(211) surface at different translational energies (E_{trans}) without (a) left panel) and with (b) right panel) state specific laser excitation of the incident molecules. 124

Figure 4-20. Difference between the S_0 (steps) for the C-D cleavage channel in the laser on and the laser off experiment. The dashed line corresponds to the full-bond selectivity condition (eq. 4.3). 126

Figure 4-21. Schematics of energetics and dissociation pathways for CH_3D chemisorption on the steps (left) and terraces (right) of Pt(211). For laser-off depositions, the sum of incident translational energy and thermal vibrational energy is indicated in back as E_T. Once E_T exceeds the reaction barrier, both C-H and C-D cleavage are observed with a near statistical branching ratio. State specific laser excitation of the ν_4 C-H antisymmetric stretch normal mode adds E_V=36 kJ/mol selectively to the C-H bonds which enables bond selective C-H cleavage if the dissociation barrier cannot be overcome by E_T alone. 127

Figure 5-1. State-resolved S_0 for CH_4 (ν_3) dissociation on Ni(111) as a function of incident translational energies for different surface temperatures. Reproduced with permission from[170]. 132

Figure 5-2. RAIR spectra after CH_4 deposition on the Pt(111) surface at 100 K, 200 K, and 300 K. 134

Figure 5-3. RAIRS CH_3(ads) uptake curves obtained at T_S=90 K for different translational energies of the incident $CH_4(\nu_3)$ beam. The solid lines show the Langmuir uptake fitting to the experimental data points. 135

Figure 5-4. a) Auger profile measured following a 60 second deposition of $CH_4(\nu_3)$ with E_{trans}=34 kJ/mol and T_S=200 K. The red dashed line shows the carbon background. b) Auger profile obtained after background subtraction of the AES profile shown in a). The blue dashed lines show the region of the profile used to determine the average carbon coverage. 136

Figure 5-5. S_0 ($CH_4(\nu_3)$) on Pt(111) as a function of: a) surface temperature for different incident translational energies of the molecular beam. The open symbols correspond to sticking coefficients measured using RAIRS and the filled symbols those measured using AES. b) As a function of incident translational energy for different surface temperatures. Only sticking coefficients determined from AES measurements are shown. 137

Figure 5-6. Total energy along the minimum-energy path for dissociative chemisorption of methane on Ni(111) for three values of Q, the displacement perpendicular to the plane of the surface, of the Ni atom over which the methane dissociates. Reproduced with permission from[48]. 139

Figure 5-7. Fractional phonon populations as a function of surface temperature for a) Pt(111) and b) Ni(111). n=0 corresponds to the ground state, n=1 with the first excited state, etc. and the fractional populations are calculated using equation (5.1). 142

Figure 5-8. Time dependence of the K&W trace for the dissociative chemisorption of CH_4 on Pt(111) at E_{trans}=120 kJ/mol and three surface temperatures (T_S=500 K in blue, T_S=650 K in green, T_S=800 K in purple). 143

Figure 5-9. Time dependence of the K&W trace for the dissociative chemisorption of CH_4 on Pt(110)-(1x2) at a) E_{trans}=72 kJ/mol and b) E_{trans}=129 kJ/mol for different temperatures (T_S=550 K in blue, T_S=650 K in green, T_S=800 K in purple) 145

Figure 6-1. a) Comparison of a spectrum taken after a 30 min deposition of CH_4 at E_{trans}= 65 kJ/mol (black) on Pt(211), and a spectrum measured 90 min after the molecular beam has been turned off once CH_4 was deposited at E_{trans}= 22 kJ/mol (orange). b) Uptake measured for CH_3(ads) on the step sites for a CH_4 deposition at E_{trans}= 22 kJ/mol. During the deposition (MB ON), no CH_3(ads) was observed on the surface. After the molecular beam deposition has been stopped (MB OFF), CH_3 adsorbed on the steps was observed. 156

Figure 6-2. RAIR spectra following CH_4 deposition at Etrans~65 kJ/mol on P(111), Pt(211), Pt(210), and Pt(531) at T_S=150 K 158

Figure 6-3. RAIR spectra following CH_4 deposition at three different incident translational energies on Pt(531) 159

List of Tables

Table 2-1. Overview of the turbomolecular pumps used in the molecular beam/surface-science apparatus and typical vacuum conditions. 18

Table 2-2. Some examples of molecular beam conditions used through this thesis work. 20

Table 2-3. Summary of the surfaces used in this thesis, the different surface atoms that each of the surface exposes with their fractional occurrence (f^{site}) and coordination number (CN), the density of each of the surface atoms and the total surface atom density. 28

Table 3-1. Summary of the values obtained for A, W and E_0 in equation (3.1) that gave the best fit to the experimental data points 55

Table 3-2. Computed lowest activation barriers E_b using the SRP32-vdW functional for different sites of the Pt(111), Pt(211), Pt(110)-(1x2) and Pt(210) surfaces. ..57

Table 3-3. Assignments of RAIRS peaks observed for nascent methyl products of CH_4 dissociation on Pt(111), Pt(211), and Pt(110)-(1x2) at T_S=150 K. Peak frequencies are taken from spectra in Figure 3-10. 67

Table 3-4. Conversion factors from CH_3 absorption signal (using the peak height of the CH_3 symmetric stretch peak) to coverage (in ML, taking into account the different surface atom densities of the different surfaces). 79

Table 3-5. Vibrational efficacies of $\nu3$ vibration for the dissociation of CH_4 on different surface sites of Pt(111), Pt(211) and Pt(110)-(1x2) surfaces. 91

Table 4-1. Measured absorption peak height to coverage factors obtained from the calibration measurements. The calibration factors obtained previously by Li Chen are also shown, being both calibrations in agreement with a maximum deviation of 18% for the CD_3 calibration factor. 106

Table 4-2. Vibrational efficacies for CH_4 (ν_3), CH_3D (ν_4), CH_2D_2 (ν_6) and CHD_3 (ν_1) on Pt(111). 117

Table 4-3. Energy (kJ/mol) contents of the molecular beams used for the experiments shown in Figure 4-15 and Figure 4-16. 118

Table 4-4 RAIRS band assignments of all the nascent dissociation methyl products of the five different methane isotopologues on Pt(211) at T_S=150 K. Peak frequencies are taken from comparison of spectra in Figure 4-15, Figure 4-16 and Figure 4-17. 121

Acknowledgements

Looking back at these last four years brings me mixed feelings. I realize how lucky I was to have come to Switzerland, and how this opportunity let me travel and meet people from all over the world who have very much enriched my experience of PhD life. This thesis work is by no means an individual effort and here I would like to thank all of those who have supported, helped and guided me during this journey.

First of all, I would like to thank **Prof. Rainer Beck** for accepting me in his group. You have been of enormous help through this thesis work: lending a hand in the lab whenever it was needed, explaining in detail and with enthusiasm when something was not clear, and pushing me when things did not seem to be working and this thesis goal seemed nigh impossible.

I also want to thank **Dr. Ludo Juurlink**, **Dr. Magali Lingenfelder** and **Prof. Jacques Moser** for agreeing to join my thesis committee. Special thanks to **Prof. Dan Auerbach**, not only for agreeing to be part of the jury but also for the many discussions we had during your visits to our group.

I am very grateful to all the former and current members of the GGSD group. In particular, I must thank **Dr. Helen Chadwick** for teaching me how to operate the “new machine”, for being always willing to answer any question that would come to my mind at any random moment, and for the good (and sometimes frustrating, let’s be honest…) moments that we had together in the lab. Thanks as well to **Dr. Jörn Werdecker**, for teaching me most of the laser setup, for the help in the lab whenever it was needed and for the fun we had travelling together to conferences. A big thanks goes also to **Bojung Chen**: you have brought a very nice atmosphere to the group! I am sure you will succeed in your research and I would like to continue celebrating with you by climbing more Swiss mountains! I would also like to thank **Milica Vasilevik** and **Harmina Vajayan** for being always nice and supportive with me during the last year of my PhD.

Thanks to **Prof. Thomas Rizzo** for accepting me in the LCPM group and for his helpful feedback during the group meetings. I also extend this thanks to all the members of the LCPM and LND groups for the fun group days, PhD defenses, and just for being nice corridor-mates ☺. In particular, I must thank **Dr. Sean Gordon**, for reading through the introduction to this thesis, **Dr. Marcel Drabbels** for giving me the chance to teach in your Quantum Chemistry and Spectroscopy courses, and **Dr. Chiara Masellis**, for being such a good teaching partner and for the good conversations, both work and not-work related. And of course thanks to **Angeles Alarcon**, the secretary of the LCPM group. Gracias por estar siempre sonriente y dispuesta a hacernos la vida un poco más fácil.

Thanks to **Prof. Fleming Crim** for sharing his passion for science and for the discussions during his sabbatical time at EPFL. I feel very lucky for having had the chance to collaborate with you.

A big thanks goes to **Prof. Fabio Busnengo**. Muchísimas gracias por la buena acogida durante mi estancia en Rosario (gracias también a Dr. Mariu Torio). Estoy enormemente agradecida por haber tenido la oportunidad de colaborar contigo y te debo un enorme “gracias” por haber tenido la paciencia de contestar a todas mis preguntas sobre teoría!

Merci beaucoup à tout le personnel de l’atelier mecanique et électronique, et le personnel IT, surtout à **Yves Mourier**, **Benjamin Charles Le Geit** et **Antonio Oliveira**.

I would not have landed in Switzerland without the support of **Prof. Nerea Bordel** and **Prof. Jorge Pisonero**, who introduced me into research when I was still in the final year of my bachelor studies. A big thank you goes to **Prof. Thomas Nelis**. I am extremely grateful for your valuable help and guidance in gaining admission to EPFL.

Thanks to the EPFL-MPS center for providing me the opportunity to meet awesome friends: **Eleonora**, **Murari**, **Dani** and **Bart**. It was just a pleasure to have you around (not anymore now that you are spread over the world). Thanks for the chats over coffee and beers, barbecues, my favourite Ricotta-cake, and for the fun trips to Lisbon and Riga. A special thanks goes to Murari for reading through most of these pages, and for your continuous english corrections ☺ I learnt a lot from you!

My PhD would not have been the same without having started just one month after **Verónica Oliver**. Has estado ahí, para celebrar lo bueno, y para apoyar

en lo malo durante estos años. Que nos quiten las risas echadas en la coffee-corner! ¡Muchas gracias por todo y mucho ánimo en estos últimos pasos que nos quedan a las dos!

Un enormísimo gracias a **Rebe** y **Javi**. No solo por haberse encargado del “resumé” de esta tesis, sino por haberse convertido en mi mayor apoyo en este país. Habéis estado ahí desde aquel 29 de septiembre de 2014 hasta hoy, pasando por karaokes, findes en Lyon, viajes en madriguera, la famosa Fête de la lutte,… y también en momentos no tan fáciles de esta tesis…nunca os estaré suficientemente agradecida!

Hace 4 años que dejé Asturias, pero las amistades no conocen de distancias. Muchas gracias por el ánimo que recibí durante este tiempo a mis **Luankings**, a **Laura**, a **Javi** y a **Aurora**. Gracias por las visitas, y también por aguantar mis quejas ☺. Un gracias especial para **Sonia**, no solo por el record en visitas, sino también por el viaje post-tesis que nos espera a Islandia!

Finalmente, me gustaría agradecer a mi **familia**, por estar siempre ahí. Me siento muy afortunada de teneros a todos. Gracias a **Marta**, mi eterna compañera, por todo tu apoyo y por haberte esforzado tanto en estos cuatro años en hacer que la distancia fuese secundaria. Finalmente, no tengo palabras para agradecer el apoyo recibido por **mis padres**. Estos cuatro años te convalidan por una licenciatura en física, mamá. Simplemente sois el motor de mi vida, y nada de lo que yo soy o consigo sería posible sin vosotros.

A **Julio**. Gracias por apostar por este viaje, sé muy bien que no fue fácil y nunca podré agradecértelo lo suficiente. Muchas gracias por todo lo que dejaste por mí y haces por mí cada día. Te quiero.

Lausanne, 10th March 2019

Avenue de Béthusy, 54 bis
1012 Lausanne
Switzerland
anllandejo@gmail.com
Nationality : Spanish

Ana Gutiérrez González

EDUCATION

Swiss federal institute of technology, Lausanne (EPFL), Switzerland **2015-2019**

Ph.D. in Physical Chemistry

Supervisor: Prof. Rainer D. Beck

Thesis title: “*Bond Selective and Surface-Site Specific Dissociation of Methane on Pt Surfaces*”

Doctoral program in collaboration with the Max Planck Society (MPS)

University of Oviedo, Spain **2013-2014**

Master’s Degree in Analytical and Bioanalytical Chemistry

University of Oviedo, Spain **2008-2012**

Bachelor and Master’s Degree in Physics

TEACHING EXPERIENCE

Swiss federal institute of technology, Lausanne (EPFL), Switzerland **2015-2018**

Class exercises for the courses of the Bachelor Program in Chemistry and Chemical Engineering:

- Quantum Chemistry
- Spectroscopy

LANGUAGES

SPANISH NATIVE **ENGLISH** FLUENT **FRENCH** INTERMEDIATE

PUBLICATIONS

[1] Chadwick, H; Gutiérrez-González, A; Beck, R.D. and Kroes, G.J. “Dissociation on the Kinked Pt(210) Surface: A Comparison of Experiment and Theory”; *J. Phys. Chem. C*, in review status.

[2] Gutiérrez-González, A; Torio, M.E.; Chadwick, H; Busnengo, F and Beck, R.D. “Site Selective Detection of Methane Dissociation on Stepped Platinum Surfaces”; *Top. Catal*. https://doi.org/10.1007/s11244-019-01170-5 (2019).

[3] Chadwick, H; Gutiérrez-González, A; Beck, R.D. and Kroes, G.J. “Transferability of the SPR32-vdW specific reaction parameter function to CHD_3 dissociation on Pt(110)-(2x1)”; *J. Chem. Phys.,* 150 (12), 124702 (2019).

[4] Chadwick, H; Gutiérrez-González, A; Migliorini, D; Beck, R.D. and Kroes, “G.J. Incident Angle Dependence of CHD_3 Dissociation on the Stepped Pt(211) Surface”; *J. Phys. Chem*. C, 122 (34), 19652–19660 (2018).

[5] Gutiérrez-González, A; Crim, F.F. and Beck, R.D. "Bond selective dissociation of methane (CH_3D) on the steps and terraces of Pt(211)". *J. Chem. Phys*., 149, 074701 (2018).

[6] Chadwick, H; Guo, H; Gutiérrez-González, A; Menzel, J.P.; Jackson, B. and Beck, R.D. "Methane dissociation on the steps and terraces of Pt(211) resolved by quantum state and impact site". *J. Chem. Phys*., 148, 014701-9 (2018).

[7] Migliorini, D; Chadwick, H; Nattino, F; Gutiérrez-González, A; Drombrowski, E; High, E.A.; Guo, H; Utz, A.L.; Jackson, B; Beck, R.D. and Kroes, G.J. "Surface reaction barriometry: Methane dissociation on flat and stepped transition-metal surfaces”. *J. Phys. Chem. Lett*., 8, 4177-4182 (2017).

[8] Chadwick, H; Gutiérrez-González, A and Beck, R.D. "Quantum state resolved molecular beam reflectivity measurements: CH_4 dissociation on Pt(111)". *J. Chem. Phys*., 145, 174707 (2016).

[9] Gutiérrez-González, A; González-Gago, C; Pisonero, J; Tibbetts, N; Menéndez, A; Vélez, M. and Bordel, N. "In-depth resolved analysis of multi-layer CdTe photovoltaic devices using LA-ICPMS". *J. Anal. At. Spectrom.,* 30, 191 (2015).

CONFERENCE CONTRIBUTIONS

ORAL

2019 "Bond selective and surface-site specific dissociation of methane on platinum surfaces”. *SAOG Meeting,* Fribourg; 31/1/2019

2018 "Molecular vibrations in solids and interfaces”. *Annual meeting of the Max Planck-EPFL Center for Molecular Nanoscience and Technology*; Lausanne; 11/10/2018

2018 "Site- and bond-selective dissociation of methane on the steps and terraces of Pt(211)". Invited seminar at the *National Scientific and Technical Research Council (CONICET);* Rosario, Argentina; 31/05/2018

2014 "Depth profile analysis of multi-layer photovoltaic devices using LA-ICPMS: Pros and cons". *European Workshop on Laser Ablation*; 11/07/2014*.*

POSTER

2018 *VI San Luis Conference on Surfaces, Interfaces and Catalysis*, Santa Fe (Argentina).

2017 *Molecules at Surfaces and Interfaces- from Structure to Interactions. Max-Planck-EPFL Center for Molecular Nanoscience and Technology*; Zeuthen, Berlin (Germany).

2017 *Fundamentals of Chemical and Physical Change at Surfaces and Interfaces. Gordon Research Conferences*; Salve Regina University, Newport (Rhode Island, EEUU).

2017 *Conference on Molecular Nanostructures 2017.* Monte Verità, Ascona (Switzerland).

2016 *Interfaces and Energy; Max-Planck-EPFL Center for Molecular Nanoscience and Technology and the International Center for Advanced Studies of Energy Conversion*; Göttingen (Germany).

2015 *Reaction Dynamics, Scattering Dynamics, and Molecular and Structural Dynamics at Surfaces and Interfaces. Gordon Research Conferences*; Salve Regina University, Newport (Rhode Island, EEUU).

2015 *Summer School of the Max-Planck-EPFL Center for Molecular Nanoscience & Technology*; Schloss Ringberg (Germany).

Ce document a été imprimé au Centre d’impression EPFL,
imprimerie climatiquement neutre, certifiée myClimate.